Dipl.-Ing. Denise Tapler, BSc

Electrochemical Characterization of Nanostructured Anode Materials and Solid-State Electrolytes for Sodium-Ion and Lithium-Ion Batteries

DOCTORAL THESIS

to achieve the university degree of

Doktorin der technischen Wissenschaften

submitted to

Graz University of Technology

Supervisor

Univ.-Prof. Dr. Martin Wilkening

Institute for Chemistry and Technology of Materials

Dr. Ilie Hanzu

Institute for Chemistry and Technology of Materials

Graz, November 2018

Affidavit

I declare that I have authored this thesis independently, that I have not used other than the declared sources/resources, and that I have explicitly indicated all material which has been quoted either literally or by content from the sources used. The text document uploaded to TUGRAZonline is identical to the present doctoral dissertation.

Eidesstattliche Erklärung

Ich erkläre an Eides statt, dass ich die vorliegende Arbeit selbstständig verfasst, andere als die angegebenen Quellen/Hilfsmittel nicht benutzt, und die den benutzten Quellen wörtlich und inhaltlich entnommenen Stellen als solche kenntlich gemacht habe. Das in TUGRAZonline hochgeladene Textdokument ist mit der vorliegenden Dissertation identisch.

Date / Datum

Signature / Unterschrift

Eine wirklich gute Idee erkannt man daran,

dass ihre Verwirklichung von vornherein ausgeschlossen erschien.

Albert Einstein

Abstract

Rechargeable lithium-ion batteries have become an integral part of our everyday life since they play a significant role as prominent power components in portable electronic devices and advanced technologies. Due to their high power capability and energy density, they are also considered as technology of choice in future energy storage for automotive applications such as electric vehicle propulsion and for stationary electric grid storage of energy from renewable sources. However, implementation of Li-ion based systems on large-scale faces challenges in terms of lithium availability and cost, life-time and safety.

When considering availability and cost the most appealing alternative to lithium is sodium. Na-ion based technologies are expected to be a near-term solution for stationary large-scale energy storage applications. Although, so far, many materials have been successfully reported to be suitable as positive electrode materials, there is a limited choice of appropriate compounds serving as negative electrodes. Here, in the first part of this doctoral thesis we investigated amorphous TiO_2 nanotubes prepared by anodic oxidation as promising anode material for sodium-ion based systems. Several titania nanotubes samples, having different lengths and diameters in accordance to the chosen anodization conditions, were tested in Na half-cells in the absence of any conductive agents and binder using electrochemical techniques such as galvanostatic cycling and cyclic voltammetry. It was found that sodium storage preferentially occurs on the surface of the titania nanotube walls in contrast to lithium insertion into TiO_2, where most of the stored Li^+ ions can be found in the bulk regions. In addition, it was noticed that these materials can withstand a large number of cycles without significant loss of capacity. The highly ordered and vertically aligned geometry of the titania nanotubes allows for the introduction of a second active material into their inner volume leading to nanotubes with either improved or new functional properties. Hence, we tried to embed different metals inside the tubes making use of a pulsed-current electrodeposition approach. It was possible to successfully fill the highly ordered TiO_2 nanotubes with metallic tin, antimony and nickel. For the tin-titania nanocomposites we propose that tin is deposited via an indirect, redox-mediated mechanism and that deposition starts at the tube tops, which is in contradiction to already existing observations in the literature. These tin-titania nanotubular arrays were also investigated with respect to their Na^+ and Li^+ storage behavior, since Sn, as high-capacity anode material, can have a positive effect on the achievable capacity values.

One option to overcome the durability and safety problems that go along with current Li-ion based technologies is the use of a solid electrolyte instead of a flammable liquid electrolyte. The search for appropriate materials has driven the development of ionic conductors to an exceptional unprecedented level. Ionic transport in such ceramic materials is one of the most important properties that determine whether a solid ion conductor is applicable as electrolyte. In the second part of this doctoral thesis we studied ion dynamics and diffusion-induced parameters of two Li-bearing sulfide-based solid electrolytes (β-Li_3PS_4 and $LiTi_2(PS_4)_3$) and one Na-ion conducting material (NASICON compound $Na_{3.4}Sc_{0.4}Zr_{1.6}SiP_4O_{12}$) on different length-scales taking advantage of impedance and solid-state NMR spectroscopy. Regarding the

β-form of Li_3PS_4 we identified a low-dimensional Li-ion diffusion pathway involving regular and interstitial sites in the structure, which is mainly responsible for ion transport in its three-dimensional network. ^{7}Li NMR line shape and spin-lattice relaxation measurements revealed the presence of two extremely fast jump processes in $LiTi_2(PS_4)_3$ (LTPS) characterized by self-diffusion coefficients in the order of 2.4×10^{-11} m^2s^{-1} (340 K) and 6.4×10^{-12} m^2s^{-1} (214 K), respectively. For the study on the NASICON-type compound we combined ^{23}Na spin-lattice relaxation NMR and broadband impedance spectroscopy to clarify the interrelation of long-range ion transport with the elementary steps of fast ion hopping in $Na_{3.4}Sc_{0.4}Zr_{1.6}SiP_4O_{12}$. It turned out that extremely fast Na ion dynamics are present that trigger successful ion jump processes between the different crystallographic positions in the three-dimensional NASICON framework and facilitate macroscopic diffusion. Finally, we considered the ion transport and electrochemical properties of a broad range of nano-sized ceramics. In particular, we studied the effect of structural disorder on Li and Na ion dynamics in nanocrystalline ceramics.

Kurzfassung

Wiederaufladbare Li-Ionen-Batterien sind zu einem unverzichtbaren Bestandteil unseres täglichen Lebens geworden, da sie eine bedeutende Rolle als Energiespeicher in tragbaren elektronischen Geräten und fortschrittlichen Technologien einnehmen. Aufgrund ihrer hohen Leistungs- und Energiedichte werden sie auch als bevorzugte Technologie für zukünftige Energiespeicherung im Bereich der Automobilindustrie für den Antrieb von Elektrofahrzeugen und für die stationäre Speicherung von Strom aus erneuerbaren Energiequellen angesehen. Die Implementierung von Systemen auf der Basis von Li^+ als Ladungsträger im großen Maßstab ist allerdings mit Herausforderungen hinsichtlich Verfügbarkeit von chemischen Elementen und -kosten, Lebensdauer und Sicherheit verbunden.

In Bezug auf Verfügbarkeit und Kosten stellt Natrium die attraktivste Alternative zu Lithium dar. Na-Ionen basierte Technologien werden als kurzfristige Lösungen für stationäre Energiespeicheranwendungen gehandelt. Obwohl bereits eine große Anzahl an geeigneten positiven Elektrodenmaterialien zur Verfügung steht, ist die Auswahl an möglichen Anodenmaterialien noch limitiert. Deshalb beschäftigt sich der erste Teil dieser Doktorarbeit mit amorphen TiO_2-Nanoröhren, hergestellt durch anodische Oxidation, welche als mögliches negatives Elektrodenmaterial für Natrium-Ionen basierte Systeme in Betracht gezogen werden. Die elektrochemische Charakterisierung dieser Titandioxid Nanoröhrchen – wobei Proben unterschiedlichster Länge und Durchmesser hergestellt wurden – erfolgte in Natrium-Halbzellen in Abwesenheit von Leitruß und Bindemitteln unter Verwendung üblicher Techniken wie galvanostatische Zyklisierung und zyklische Voltammetrie. Im Gegensatz zur Lithium-Insertion, wo sich die meisten der gespeicherten Li-Ionen im bulk-Bereich befinden, wurde festgestellt, dass Natrium bevorzugt auf der Oberfläche der Wände der Nanoröhrchen gespeichert wird. Darüber hinaus wurde erkannt, dass dieses Material einer großen Anzahl an Zyklen ohne erheblichen Kapazitätsverlust standhalten kann. Die hochgeordnete Struktur der Titandioxid Nanoröhrchen ermöglicht außerdem die Einbettung eines zweiten aktiven Materials in das Innere der Röhrchen, um entweder ihre funktionellen Eigenschaften zu verbessern oder neue zu erschaffen. Deshalb wurde weiter versucht, die Röhrchen mittels gepulster elektrolytischer Abscheidung mit verschiedensten Metallen zu füllen. Metallisches Zinn, Antimon und Nickel konnten dabei erfolgreich in die TiO_2-Nanoröhrchen abgeschieden werden. Der zugrundeliegende Mechanismus für die Abscheidung von Sn in die Röhrchen wurde genauer untersucht. Es war offensichtlich, dass sich metallisches Zinn zunächst im oberen Bereich der Röhrchen bildet und die Abscheidung indirekt erfolgt. Diese Sn/TiO_2 Nanokomposite wurden auch hinsichtlich ihres Li^+- und Na^+-Insertionsverhaltens studiert, da Zinn, als hochkapazitives Speichermaterial, die erreichbaren Kapazitäten positiv beeinflussen kann.

Eine Möglichkeit, um die Lebensdauer und Sicherheit derzeit verwendeter Li-Ionen basierter Technologien zu erhöhen, ist die Verwendung eines Festkörperelektrolyten anstelle eines brennbaren, flüssigen Elektrolyten. Die Suche nach geeigneten Materialien hat die Entwicklung von Ionenleitern intensiv vorangetrieben. Der Ionentransport in solchen keramischen

Materialien ist eine der wichtigsten Eigenschaften, die bestimmt, ob ein fester Ionenleiter als Elektrolyt in Frage kommt. Im zweiten Teil dieser Arbeit wurde die Ionendynamik in zwei lithiumhaltigen Festkörperelektrolyten auf Basis von Sulfiden (β-Li_3PS_4 and $LiTi_2(PS_4)_3$) und einem Na-Ionen leitenden Material über einen weiten Längen- und Temperaturbereich untersucht sowie deren dynamischen Parameter mittels Festkörper-NMR und Impedanzspektroskopie bestimmt. In der β-Form von Li_3PS_4 wurde ein niedrigdimensionaler Diffusionsweg für die Lithium Ionen identifiziert, welcher hauptsächlich für den Ionentransport im dreidimensionalen Netzwerk verantwortlich ist. Dabei sind reguläre aber auch Zwischengitterplätze in der Struktur beteiligt. ^{7}Li-NMR-Spin-Gitter-Relaxationsmessungen sowie Messungen der Linienform zeigten das Vorhandensein zweier extrem schneller Sprungprozesse in $LiTi_2(PS_4)_3$ (LTPS), welche durch Selbstdiffusionskoeffizienten in der Größenordnung von 2.4×10^{-11} m^2s^{-1} (340 K) beziehungsweise 6.4×10^{-12} m^2s^{-1} (214 K) gekennzeichnet sind. Für die Untersuchung der NASICON Probe wurden beide Methoden, die Breitbandimpedanzspektroskopie sowie die Festkörper-NMR, in Kombination verwendet, um einerseits Informationen über die langreichweitige Ladungsträgerbewegung zu erhalten, aber auch die elementaren Sprungprozesse genauer zu betrachten. Es stellte sich heraus, dass extrem schnelle Transportprozesse in $Na_{3.4}Sc_{0.4}Zr_{1.6}SiP_4O_{12}$ vorhanden sind, die zu erfolgreichen Sprüngen zwischen den verschiedensten, kristallographischen Positionen im dreidimensionalen NASICON-Gerüst führen und somit die makroskopische Diffusion erleichtern. Zum Schluss betrachteten wir die elektrochemischen und Ionentransporteigenschaften von einer Reihe von nanostrukturierten Keramiken. Insbesondere widmen wir uns der wichtigen Frage nach dem Einfluss von struktureller Unordnung auf die Ionendynamik in nanokristallinen Keramiken.

Contents

1 Introduction

Increasing energy demand in combination with environmental concerns and the scarcity of fossil resources has led to calls for alternative energy sources, especially in the field of grid-related and automotive applications. Over the past few years, electricity generated by sun, wind or tidal has become more and more popular. But as these are intermittent renewable energy sources and thus cannot provide power in a constant and reliable way, electric energy storage on a large-scale is of utmost important. It allows for the storage of energy during peak hours and its release during periods of high demand. The electrification of transportation also promotes research on large-scale electric energy storage systems. Among already existing systems, the electrochemical storage of energy based on the rechargeable secondary battery technology is the most promising solution for this purpose at least on the medium-term [1-5].

Lithium-ion batteries (LIB)s, for instance, have revolutionized the market of portable electronic devices. They are attractive in terms of long cycle-life, good rate capability, high output voltage and high energy density [6]. Therefore, Li-ion based technologies are currently considered and developed as the technology of choice for electric vehicle propulsion and also show a great potential for use in stationary and electric grid storage systems [7-11]. However, it is feared that the global available lithium resources cannot cope with the foreseen increasing demand for large-scale lithium-ion storage batteries in the near future. As a consequence, the price of Li-based raw materials will possibly rise limiting its application in renewable energy storage [12, 13].

The most appealing alternative to lithium in terms of availability and cost is sodium. Its unlimited and inexhaustible resources combined with a low reduction potential and electrochemical equivalent to lithium make sodium-ion based systems attractive for large-scale energy storage applications with respect to renewable resources [14-16]. It is worth noting that sodium chemistry tends to differ from lithium in matters of ionic properties making the development and optimization of new electrode materials and new stable electrolytes necessary [6]. Although, so far, many successful reports exist on suitable positive electrode materials, there is a lack of appropriate compounds operating as negative electrodes.

Thus, the first part of this doctoral thesis deals with amorphous TiO_2 nanotubes as possible anode material for sodium-ion based systems. Such self-organized titania nanotubular arrays can be simply grown on metallic titanium substrates from fluoride containing viscous electrolytes by a conventional electrochemical oxidation (anodization) process. We present a detailed electrochemical study on Na^+ insertion into several titania nanotubes samples, which differed in

lengths and diameter taking advantage of common techniques such as cyclic voltammetry and galvanostatic cycling with potential limitation.

In addition to the electrochemical characterization of these titania nanotubes, the second aim was to fill the titania nanotubes with different metals. This is generally done either to enhance their functional properties or to create entirely new ones broadening their range of possible applications. We report on the successful embedding of metallic Sn, Sb and Ni into the inner volume of the tubes using a pulsed-current electrodeposition approach. The prepared tin-titania nanocomposites were investigated in terms of their Li^+ and Na^+ storage capability.

Due to the increased use of lithium-ion batteries for electric vehicle propulsion and in large-scale energy storage systems that goes along with a larger battery size, special emphasis must be paid on safety issues. Current Li-ion and Na-ion based technologies mainly use organic liquids as electrolyte [8,17]. But, despite their excellent wetting properties and their high ionic conductivities, these electrolytes often suffer from flammability and leakage, and inadequate electrochemical and thermal stabilities, thus complicating its application in large-scale systems and electric vehicles [18]. The replacement of liquid organic electrolytes by solid-state electrolytes represents one option to overcome these safety and stability problems due to diminished flammability, enhanced thermal stability and the wider electrochemical voltage stability window [19]. Furthermore, such all-solid state batteries are expected to withstand a large number of cycles at full storage capacity, which is indispensable for large-scale stationary energy storage applications [20].

A key property materials have to fulfill in order to be considered as suitable solid electrolyte is a high lithium-ion diffusion or conductivity at ambient temperature. Further requirements are a vanishing electron transport, a wide electrochemical and thermal stability window, no reactivity with other components, good interfacial compatibility, good mechanical properties and low cost [21, 22]. Unfortunately, solid electrolytes reported so far for lithium and sodium systems are not able to meet all these prerequisites. Especially, their low room temperature ionic conductivities and poor stabilities limit the commercial application of all-solid state batteries. Thus, the search for appropriate materials that show fast ion dynamics and higher stability has driven the development of ionic conductors to an exceptional unprecedented level. A fundamental understanding of the elementary diffusion processes in solids, that can be acquired by an in-depth study on both structure and ion dynamics, is crucial for the implementation of new concepts or the improvement of already existing systems.

Knowledge about ionic diffusion in solid-state matters can be obtained by applying complementary methods that study ion dynamic properties on different length-scales. Solid-state nuclear magnetic resonance spectroscopy, for example, especially NMR spin-lattice relaxometry (SLR) provides information about both, short-range/local and long-range ion transport and helps to understand the relationship between dynamic parameters and local structures. Besides the determination of some relevant diffusion-induced parameters, such as jump rates and activation energies, it is also possible to draw conclusions regarding the diffusion pathways (dimensionality) through the crystal lattice [23]. In contrast, impedance spectroscopy

studies ion dynamics on a long-range scale. It allows the determination of some important parameters such as the impedance, the dielectric permittivity and the ionic conductivity at different temperatures as a function of the frequency. Information about activation energies and the contribution of grain boundary or bulk diffusion to the overall conductivity are also available.

Thus the second part of this doctoral thesis focuses on the study of ion dynamics in two Li-containing sulfide-based solid electrolytes (β-Li_3PS_4 and $LiTi_2(PS_4)_3$) and one Na-ion conducting material (scandium-substituted NASICON compound $Na_{3.4}Sc_{0.4}Zr_{1.6}SiP_4O_{12}$) using either impedance or solid-state NMR spectroscopy or the combination of both. The results obtained (diffusion mechanisms, dynamical parameters) are related to the structure of the compounds.

2 Rechargeable Li- and Na-ion batteries

Rechargeable secondary batteries have become an integral part of our everyday life since they play a significant role as prominent power components in many devices and advanced technologies. Lithium-ion (Li-ion) batteries, for instance, have revolutionized the market of portable electronics and are therefore considered and currently developed as the technology of choice for automotive applications including full/hybrid electric vehicles [1, 8-10, 24]. They also show a great potential for use in stationary and electric grid storage systems [11]. The attractiveness of Li-ion batteries (LIB)s for these applications resides in the high output voltage and energy density as well as the high specific capacity they can provide in comparison to other rechargeable systems. This outstanding electrochemical performance is a direct consequence of the small crystallographic ionic radius (0.76 Å) and molar mass (6.941 g/mol) of lithium and the very low reduction potential of E^0 = –3.04 V *vs.* SHE of the corresponding Li^+/Li redox couple [6]. Moreover, a long cycle-life and a good rate capability combined with the availability of a versatile and rich chemistry concerning electrode materials makes the lithium-ion technology indispensable [12, 25].

However, in recent years, sodium-ion based batteries (NIB)s, where sodium instead of lithium ions are used, have attracted particular attention due to controversies on available Li resources and costs. The foreseen increasing demand for lithium-ion storage batteries in grid-related and automotive applications is expected to lead to a major and sustained Li consumption in the near future. Since the amount of available lithium is low and most of the untapped global reserves are located in politically sensitive and remote areas, the price of Li-based raw materials will possibly rise limiting its application in renewable energy storage [12, 13]. The use of sodium instead of lithium in rechargeable batteries is one appealing option to mitigate the shortage of Li resources in an economically effective way. Sodium is a highly abundant, low cost element showing virtually unlimited resources and being easy to recover. Thanks to the similar intercalation chemistry to lithium and the low reduction potential of the corresponding Na^+/Na redox couple (E^0 = –2.71 V *vs.* SHE) [14, 15], sodium-ion based systems may be a substituting or complementary alternative to common Li-based technologies intended for large-scale stationary energy storage applications [16]. Until now, sodium storage technology has been applied to high temperature working Na/$NiCl_2$ ZEBRA and Na/S batteries, respectively [26].

It must be pointed out that Na-ion batteries cannot compete against Li-based systems in terms of energy density and specific capacity due to the three times larger molar mass and approximately 30 % larger crystallographic ionic radius of sodium (1.02 Å) compared to lithium (0.76 Å) and the 0.3 V higher reduction potential [17]. Thus, Na-ion systems may be an option for applications, in which extended cycle-life and low costs represent valuable assets [16]. Moreover, sodium chemistry also tends to differ from lithium in matters of ionic properties such as diffusion properties, ionic and solvation mobility, ionic radius etc. and chemical reactivity making it rarely possible to directly adopt the electrode materials and electrolyte formulations used in LIBs to sodium-based systems [6]. Therefore, finding and optimization of new electrode materials (especially on the negative side) and new stable electrolytes is the key to obtain commercially viable NIBs. Taking into account all these considerations combined with the knowledge already gained in Li-ion systems, the development of room temperature sodium-ion batteries showing the same working principle as lithium-ion batteries is not only realistic but certainly feasible.

2.1 Components and working principle of Li- and Na-ion batteries

A battery is an electrochemical energy storage and conversion system that directly converts stored chemical energy into electrical energy through an electrochemical reduction and oxidation (redox) reaction. In rechargeable systems, the overall process is reversible in order to recharge the battery. In principle a battery consists of an assembly of galvanic cells that are electrically connected in such a way (series and/or in parallel) to meet the desired electrical output depending on the application. Each of these cells is composed of at least a negative and a positive electrode, an ion-conductive electrolyte and a separator. The positive and the negative electrode materials, generally consisting of intercalation compounds in Li- and Na-ion batteries, are the sites of the (electro)chemical reactions. The electrolyte, which should have a good ionic conductivity without being electronically conductive, allows the ion transport between the electrodes. It usually consists of a mixture of organic solvents and dissociated salts. The separator avoids direct contact of the two electrodes, as this would lead to internal short-circuit, while being permeable to the Li/Na-ions and the electrolyte [27, 28]. To get further information about the components of the battery the reader is referred to the following literature [27-31].

The working principle of rechargeable Li-and Na-ion batteries, as graphically illustrated in Fig. 1, is based on a reversible intercalation process. This implies that the lithium or the sodium ions, the so-called guest ions, are reversibly inserted or extracted into/from a host material during charging and discharging. Both the positive and the negative electrode material are acting as intercalation hosts. When the cell is charged, the guest ions are extracted from the positive material and migrate through the separator and the electrolyte towards the negative electrode material, where insertion takes place. At the same time electrons are released from the positive electrode due to oxidation of the active material on this side. These free electrons flow through

an external circuit to the negative electrode, where the active material is reduced. Charging of a galvanic cell is a non-spontaneous process, requiring electric energy from an external source in order to proceed. When discharging the cell, the processes are reversed resulting in a reduction of the positive material and an oxidation of the negative active material. In this case the guest ions are extracted from the negative host material and intercalated in the positive material. The discharging process allows the conversion of the stored chemical energy into electrical energy [27, 28]. This is a spontaneous process; during discharge the cell is able to supply electrical energy to an external circuit.

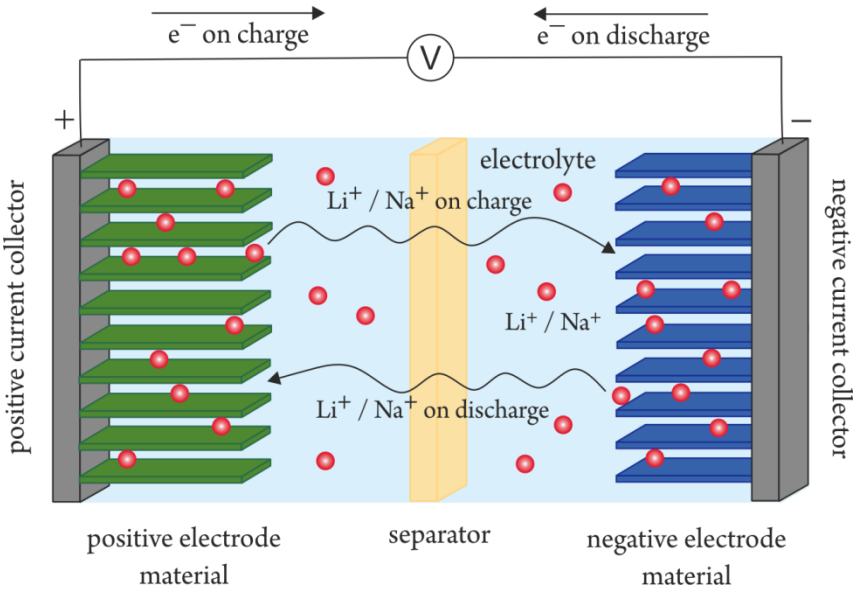

Fig. 1 Schematic representation of insertion/de-insertion processes in lithium- and sodium-ion batteries.

The maximum amount of energy, either expressed per mass unit as the specific energy (in Wh/kg) or expressed per volume unit as the energy density (in Wh/l), that a battery system can deliver depends on the specific capacity (Ah/kg) and the cell voltage (V) and is directly linked to the characteristics and properties of the cell components [27, 28]. To obtain high capacity values the intercalation electrode material should enable the insertion and extraction of a large number of charge carriers per mass of the material. To maximize the cell voltage, a negative electrode material with a low oxidation potential and a positive electrode active material with a high reduction potential is used [29, 32]. Much research has already been done on the design of high capacity negative and positive electrode materials as well as on high voltage positive electrodes. However, the use of high voltage positive active materials is, at the moment, limited by the stability of the electrolyte making the development of new electrolyte formulations with

an extended electrochemical window necessary [33]. Furthermore, the insertion and extraction reaction at both electrodes should be highly reversible, preferably without changing the structure of the intercalation host material, leading to a high efficiency and a long cycle-life of the battery [29, 32].

2.2 Negative electrode materials

Materials that are able to reversibly insert and extract sodium or lithium ions at low potentials are considered as suitable negative electrode materials for Li- and Na-ion batteries, respectively. Moreover, high capacity, high diffusion rate of the charge carriers into the corresponding active material, good electrical and ionic conductivity along with a good cycle-life and low costs are also important requirements that should be taken into account in the design of the electrode material [25]. Fig. 2 gives a synthetic view of the potential negative active materials reported for Li- and Na-ion batteries. Apparently, just a few materials have been proposed to be suitable for sodium-ion based systems in comparison to lithium. Since structures, chemistries and reaction pathways differ when Na instead of Li is used, the development of acceptable negative host materials for NIBs is much more challenging [14, 15, 17].

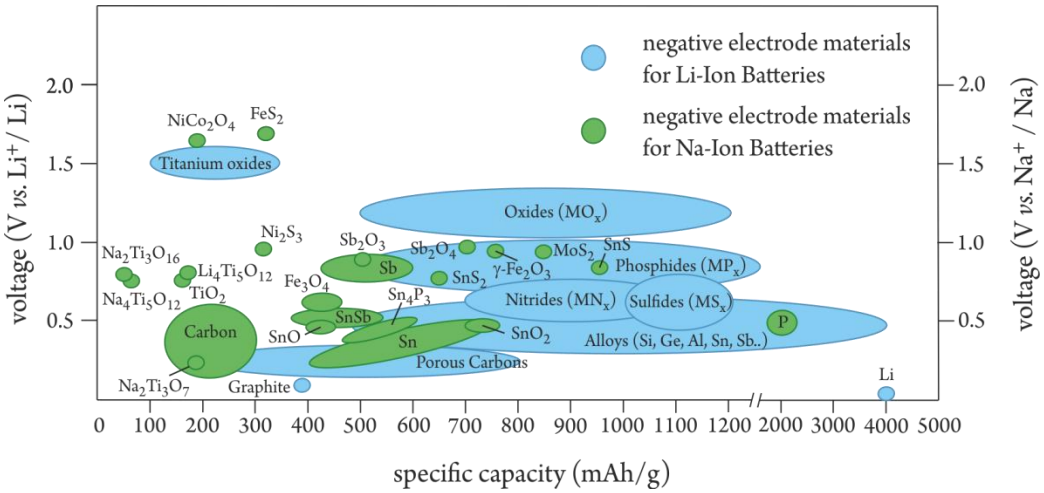

Fig. 2 Most important negative active electrode materials presently used or under investigation for rechargeable Na- and Li-ion batteries, represented by their operating voltage *vs.* lithium or sodium metal and specific capacity (adopted from references [6, 14, 25, 26]).

Generally, these active materials can be classified into three groups according to their reaction mechanism [25]

- *Intercalation materials* – carbon and titanium-based materials such as graphite, hard carbon, titanates, TiO_2, etc.,
- *Alloy materials* – silicon, germanium, tin, aluminum, antimony, etc.,
- *Conversion materials* – transition metal -oxides, -sulfides, -phosphides and -nitrides.

The following section should provide a concise overview of the most important negative electrode materials for Li- and Na-ion batteries. For further information, more detailed reviews dealing with electrode materials for sodium-ion [6, 14-17, 26] and lithium-ion batteries [7, 12, 25, 32] are recommended.

2.2.1 Intercalation materials

Carbon-based materials

At the present state of the art, carbon-based materials are mainly used as negative electrodes in room-temperature rechargeable secondary batteries due to some good features such as (i) the good availability and low costs of carbons; (ii) the good thermal, chemical and electrochemical stability; (iii) the highly reversible insertion/extraction reaction without significant volume changes leading to a good cycling performance; and (iv) the low reduction potential of carbons compared to other active materials. Thus, carbon-based materials show a good balance between costs, availability, moderate energy density and cycle-life [12, 25]. The intercalation of the guest ions into carbon host materials can be described by the following equation:

$$x\mathrm{Li}^+ / \mathrm{Na}^+ + x\mathrm{e}^- + n\mathrm{C} \rightleftharpoons \mathrm{Li}_x / \mathrm{Na}_x\mathrm{C}_n \qquad (2.1)$$

Since the carbon host is reduced during charging, the lithium or sodium ions insert into the carbon leading to the formation of an intercalation compound Li_xC_n and Na_xC_n, respectively. This reaction is reversible [32].

For lithium-ion batteries

Graphite is the most commonly used negative electrode material in LIBs showing a theoretical capacity of 372 mAh/g [34]. It has an ordered layer structure consisting of stacked parallel graphene planes, which allow fast Li diffusion, high mechanical stability and good electronic conductivity. The Li-ions can be reversibly intercalated between the graphene layers at a low potential of 0.1 V *versus* Li^+/Li. For highly structured, crystalline graphitic carbons up to one Li atom per six C atoms can be inserted at low cycling rates leading to the lithium-rich phase LiC_6 [27, 32]. However, the low lithium intercalation potential of graphite can lead to the formation of dendritic Li above all during overcharging, at high cycling rates and low temperatures. These dendrites can cause internal short-circuits resulting, in the worst case, in a thermal runaway of the cell [35]. Moreover, graphite electrodes suffer from volume changes of about 10 % during Li

insertion and extraction leading to cracks and electrical contact loss between the particles and thereby to a decrease in capacity over time [36]. Additionally, graphitic carbons are thermodynamically not stable in most electrolytes. Therefore, a protective film, the so-called Solid Electrolyte Interphase (SEI), forms on the surface of the negative electrode during the first Li^+ intercalation reaction into the graphite active material. This SEI film consists of electrolyte decomposition products and lithium from the positive electrode material inducing irreversible loss of capacity during the first cycle [32]. The quality of the passivating layer significantly influences the cycle stability, the cycle-life, the performance and the safety of the lithium-ion cell [27].

Since higher capacity values are required for the use of carbon-based materials in the next generation of Li-ion batteries, research has focused on the development of porous carbon materials. In contrast to graphite, hard carbon shows a disordered orientation of the graphene layers with variable interplanar distances providing a large number of pores that can accommodate Li^+ [25]. Furthermore, these void spaces prevent large volume changes during charging and discharging leading to a high cycle-life of the battery [12]. Recently, high reversible capacity values up to 500 mAh/g have been reported [37, 38]. However, hard carbons exhibit large voltage hysteresis during lithium extraction and suffer from high irreversible losses of capacity limiting their application in commercialized systems [12].
Presently, many other non-graphitic carbon materials, such as nanofibers, carbon nanotubes and graphene have been demonstrated as possible negative electrodes for LIBs [25].

For Na-ion batteries
Unlike lithium, Na^+ cannot be intercalated between the ordered graphene planes due to its larger size, unfavorable thermodynamics of the insertion process and its lower reactivity with graphite making the formation of intercalation compounds almost impossible [39-41].

Instead, hard carbon seems to be the most promising candidate as negative electrode material as sodium ions can successfully intercalate between the disordered layers of the graphene stacks and also into the nanopores. This porous structure allows short diffusion path lengths and fast Na-ion transport leading to an initial capacity of about 300 mAh/g at a low cycling rate, a value close to that obtained for lithium insertion into graphite [42]. However, hard-carbon based electrodes show poor cycle performance and significant irreversible loss of capacity during the first cycles due to side reactions of the highly reactive sodiated hard carbon active material with the electrolyte [6]. However, through optimization of the used electrolyte composition a reversible capacity value as high as 240 mAh/g can be achieved [43].

To date, many other electro-active carbonaceous materials such as petroleum coke [44, 45], carbon black [46] and carbon fibers [47] as well as porous nanosheets [48], hollow nanospheres [49] and nanowires [50] have been demonstrated to successfully insert Na.

Titanium-based materials

Titanium-based oxides have attracted particular attention as potential alternative to conventional carbon-based materials, since they allow a highly reversible insertion/extraction reaction at higher operating potentials with only slight changes in volume along with low toxicity and an excellent cycle-life [36]. In addition, the higher intercalation potential ensures a safe battery operation by largely avoiding sodium and lithium plating and the formation of a SEI film. However, this class of materials exhibit relatively low theoretical capacities and electronic conductivity and slow ionic diffusion [12] .

The electrochemical performance strongly depends on the morphology, size and structure of the Ti-based oxides. In recent years, nanostructuring of these materials has been intensively explored, as this can lead to higher capacity values and rate capabilities as well as longer cycle-life compared to the bulk materials [25].

The insertion reaction of lithium or sodium ions into titanium-based oxides occurs according to the following equation [6]:

$$Ti_yO_z + xLi^+ / Na^+ + xe^- \rightleftharpoons Li_x / Na_xTi_yO_z \qquad (2.2)$$

For Li-ion batteries

Lithium titanium oxide $Li_4Ti_5O_{12}$ (LTO) is the most commonly used alternative negative electrode to carbon-based materials. The spinel $Li_4Ti_5O_{12}$ can reversibly insert three lithium ions per mole of active material at 1.55 V *vs.* Li^+/Li with a theoretical capacity of 175 mAh/g leading to a $Li_7Ti_5O_{12}$ stoichiometry [36]. LTO is treated as a zero strain electrode material showing high cycling stability, since the phase change, which is caused by the insertion and extraction of lithium into LTO occurs with negligible changes in volume [12]. In order to reduce the lithium diffusion path lengths and to increase the number of active sites in LTO, nano-sized LTO particles are used leading to improved Li-ion diffusion and higher capacity values [25].

Titanium dioxide (titania, TiO_2) has attracted significant interest as promising negative active material due to some advantages such as high power density, reversibility and availability, low toxicity and cost effectiveness. Moreover, titania exhibit excellent stability and safety conditions. Theoretically, titanium dioxide can intercalate one lithium ion per mol TiO_2 ($LiTiO_2$) resulting in maximum theoretical capacity values of 330 mAh/g. However, the insertion reaction of lithium into TiO_2 is strongly influenced by its structure, crystallinity and particle size. The most common allotropic forms of TiO_2 are rutile, anatase and brookite [25]. Among these allotropes, anatase titania presents the highest electro-activity [51]. Recently, it has been shown that nanostructured rutile particles are also able to reversible intercalate lithium with moderate capacities [52]. Presently, anatase TiO_2 nanotubes [53] and nanostructured TiO_2(B) [54] were proven as insertion materials for Li-ion based systems.

For Na-ion batteries

So far, $Na_4Ti_5O_{12}$, the Na analogue of the spinel-type $Li_4Ti_5O_{12}$, has not yet been prepared. However, sodium insertion into lithium titanium oxide has been extensively studied, which shows a reversible capacity value of about 150 mAh/g at a potential of 1 V *vs.* Na^+/Na. This study suggests a three-phase reaction, in comparison to Li uptake into LTO, where a two-phase reaction takes place, resulting in a mixture of $Li_7Ti_5O_{12}$ and $Na_6LiTi_5O_{12}$ as final products [55].

Sodium titanate, $Na_2Ti_3O_7$, has attracted particular attention as possible negative electrode material, since reversible insertion of two additional Na-ions per mol $Na_2Ti_3O_7$ can occur at a low potential of 0.3 V *vs.* Na^+/Na with a capacity of 200 mAh/g. However, this active material suffers from poor cycle-life and poor rate performance [56].

Reversible Na-ion uptake has also been reported for amorphous TiO_2 nanotubes. These electrodes show excellent cycle-life without considerable loss of capacity over 300 cycles. Stable reversible capacity values are reached after a few cycles and strongly depend on the dimensions of the titania nanotubes. Additionally, it is found that a pseudocapacitive behavior is responsible for the electrochemical storage mechanism of Na^+ in these nanotubular structures [57].

Among the other titania polymorphs, anatase TiO_2 nanoparticles [58] and TiO_2(B) nanotubes [59] have been demonstrated to successfully insert sodium.

2.2.2 Alloy materials

Alloy-based materials have the potential to accommodate more lithium or sodium per unit volume compared to intercalation materials offering higher specific theoretical capacities [33]. In addition, they are attractive in terms of safe operation potential, environmental compatibility and relatively low costs. Alloy materials apply to elements that are able to electrochemically insert Li or Na into its crystal structure through an alloying mechanism forming stoichiometric compound phases Li_xM and Na_xM, respectively:

$$xLi^+ / Na^+ + xe^- + M \rightleftharpoons Li_x / Na_xM \tag{2.3}$$

Since the formation of these binary phases is reversible, extraction of the alkali ions occur through a corresponding de-alloying mechanism [12, 32].

However, the reaction of the elemental host with lithium or sodium is associated with very high volume changes, which creates detrimental mechanical stress in the alloy material. This leads to severe fracturing and subsequently to the disintegration of the electrode resulting in electrical contact loss between the particles [60]. A large irreversible capacity during the first few cycles and shorter cycle-life are the unavoidable consequences.

To overcome the above-specified problems, various approaches have been considered. One possibility is the reduction of the particle size of the elemental host material to the nanoscale, since smaller particles are more tolerant to mechanical strain. Thus, particle cracking and electrode deformation can be suppressed leading to an improved cycle-life [61]. Much attention has also been paid to nanostructured alloy-based materials showing different morphologies. Due

to their structure free volume is available for expansion and contraction resulting in better cycling stability [62]. The most promising approach is the preparation of composites consisting of both electrochemically inactive (mostly carbon) and active components. The inactive material acts as buffer matrix that can compensate the volume changes during the alloying/de-alloying process and plays a part in the mechanical stability and electronic conductivity of the electrode, while the active material provides the high capacity [61, 63]. In addition, embedding of the host elements into a matrix prevents aggregation of the active particles and thus avoids changes in the microstructure of the electrode [64]. Buffer action can also be obtained by using intermetallic compounds consisting of elements that are electrochemically active at different potentials [61, 63]. Other possibilities to reduce volume expansion are the use of multi-phase materials or compound alloys that exhibit a strong structural connection to their sodiated or lithiated phases [65].

For Li-ion batteries

Among all alloy materials, silicon (Si) has attracted the most attention, since it shows the highest theoretical specific capacity (4200 mAh/g for $Li_{22}Si_5$) known today along with a low intercalation potential (close to graphite) and high chemical stability. In addition, Si is a low cost, non-toxic element of high natural abundance. Lithiation of silicon occurs via the formation of well-defined intermetallic Li-Si binary phases. However, insertion and extraction of lithium goes along with huge volume changes of up to 400 % resulting in high irreversible capacities and poor cycle-life limiting its application as negative electrode material in next-generation LIBs [25]. Therefore, large effort is put in the development of nanostructured Si, especially with different morphologies [62]. SiO is also considered as possible alternative to pure silicon [25].

Tin (Sn) has also drawn interest as possible elemental host material in lithium-ion batteries. Even though Sn shows some advantages such as high theoretical Li storage capability (993 mAh/g for the $Li_{4.4}Sn$ stoichiometry) [27], high electronic conductivity and relatively low operation potential of 0.6 V *vs.* Li^+/Li, Sn electrodes are susceptible to fracturing leading to a severe degradation of the electrode upon cycling [25]. To overcome this problem, Sn nanostructures and Sn/carbon-based nanocomposites have been investigated resulting in a better battery performance in terms of cycle-life and reversible capacity [27].

Germanium (Ge) is also reported as potential Li alloy material due to its high theoretical specific capacity of 1623 mAh/g, reversible alloying/de-alloying reactions and high electronic conductivity. Moreover, Ge shows much faster Li kinetics compared to silicon and thus higher rate and power capability. However, high costs and extremely large volume changes impede the practical use of germanium as negative electrode material for LIBs [25].

Furthermore, electrochemical insertion of lithium into Zn [66], Al [67], Pb and Sb [63] have been widely studied, but these materials show some disadvantages such as low specific capacity values, high operation potentials, low abundance or high toxicity.

For Na-ion batteries

Although Li alloy materials are well researched, only a limited choice of suitable alloy compounds has been proposed for Na-ion based systems. Silicon, for example, the most studied alloy material for LIBs, does not show electrochemical activity with sodium. Therefore, much research has focused on tin or antimony-based compounds [6].

Pure elemental Sn can react with up to 3.75 Na delivering reversible capacities of about 500 mAh/g [68]. The electrochemical insertion of sodium into tin proceeds through several phase transformations forming the crystalline binary phase $Na_{15}Sn_4$ at full sodiation. The composition of the three intermediate amorphous Na-Sn binary compounds is still not clear, since these phases do not correspond to any known Na-Sn binary system at equilibrium [69,70]. Interestingly, no particle cracking or fracture was observed during the alloying/de-alloying reaction, despite the extremely large volume modification of about 420 %, resulting in a good cyclability [69].

Surprisingly, Sb-based electrodes exhibit better cycling performance for Na-ion batteries in comparison to lithium-ion based systems. This alloy material can incorporate three additional Na ions, which corresponds to a reversible specific capacity value of 600 mAh/g [71].

Furthermore, carbon-based nanocomposites Sb/C [72], Sn/C [73] and SnSb/C [74] were proven as possible negative active material due to some good features such as high capacities, good cycling stability as well as good rate capability.

2.2.3 Conversion materials

Some transition metal compounds of the general composition M_xN_y (with M= Fe, Ni, Cu, Co, Mn and combinations thereof and N = O, S, P and N) can react with lithium or sodium through a conversion reaction mechanism according to the following equation:

$$M_yN_z + xLi^+ / Na^+ + xe^- \rightleftharpoons Li_x / Na_xN_z + yM \qquad (2.4)$$

The electrochemical reaction involves the complete reduction of the transition metal to metallic nanoparticles and the formation of lithium or sodium compounds. The metal nanoparticles formed are dispersed in the Li_x/Na_xN_z matrix. This conversion reaction is reversible [25].

Since a large number of electrons participate in the above-described conversion reaction, high specific capacity values in the range of 500 – 1000 mAh/g can be achieved [75]. On the other hand, conversion-based materials show large voltage hysteresis and slow ionic diffusion [25].

For Li-ion batteries
Regarding the oxides, Fe_2O_3 and Fe_3O_4 as well as Co_3O_4 and CoO have been extensively studied as host materials for LIBs. Iron-based oxides are advantageous in terms of non-toxicity, high availability and low costs [25,75]. Due to their low insertion potential for lithium, metal phosphides M_xP_y (M = Fe, Co, Cu, Ni and Sn) have also attracted attention, but they exhibit low electronic conductivity and high changes in volume during the conversion reaction [25]. Metal nitrides MN_x and sulphides MS_y with transition metals of Fe, Mo, Sn, Sb, Ni, Co and W are of highly interest as negative active material too, due to some structural advantages and their high Li storage capacity [25, 75].

For Na-ion batteries
Among the oxides, the spinel $NiCo_2O_4$ [76] and Sb_2O_4 [77] as well as iron-based oxides such as nanocrystalline Fe_2O_3 [78] and Fe_3O_4 [79] were proven as conversion materials for sodium storage. Recently, metal sulphides including Ni_3S_2 [80] and FeS_2 [81] have attracted significant attention, since the conversion reactions with Na occur at relatively low potentials. Unfortunately, these sulphides exhibit poor cyclic stability. Other transition metal sulphides such as TaS_2 [82], TiS_2 [82] and MoS_2 [83], are also a possible option to be used as negative electrode material in NIBs.

2.3 Positive electrode materials

This topic is not subject of this doctoral thesis and therefore only the most important principles will be described without an extended coverage. To get more insight, the following review articles [6, 12, 15-17, 26, 32] and books [27-29] are recommended.

Positive electrode materials serve as lithium or sodium source in a rechargeable secondary Li- and Na-ion battery, because the corresponding negative active materials do not contain any lithium or sodium after their synthesis. These Li- and Na-based compounds should allow the electrochemical insertion and extraction of the alkali ions at relatively high potentials resulting in a high cell voltage. To permit good cycling performance and long cycle-life, structural and volume changes during reversible insertion of the guest ions should be as small as possible. High ionic diffusivity, good electronic conductivity and low costs also represent valuable assets [28]. Generally, insertion materials are used as positive electrode materials for both Li- and Na-ion based systems. Due to their high operation potential and related high lithium and sodium storage capability, most research work is focused on transition metal oxide- and phosphate-based intercalation materials. Typically, these active materials provide specific capacity values in the range of 100 – 200 mAh/g [12].

For lithium-ion batteries the most important positive electrode materials are: layered oxides ($LiMO_2$, M = Co, Ni, Mn, Al) such as LCO ($Li_{1-x}CoO_2$), NMC ($LiNi_{0.33}Co_{0.33}Mn_{0.33}O_2$),

NCA ($LiNi_{0.8}Co_{0.15}Al_{0.05}O_2$); spinels ($LiM_2O_4$, M = Ni, Mn) such as LMO ($Li_{1-x}Mn_2O_4$) and phosphates ($LiMPO_4$, M = Fe, Co, Ni, Mn) such as LFP ($LiFePO_4$) [27, 30].

Since research on active materials for the positive side has been more successful than for the negative side, numerous intercalation materials have been proposed as appropriate positive electrode materials for Na-ion batteries. Among the oxides, Na_xCoO_2 [84], $NaNiO_2$ [85], $NaCrO_2$ [86] and transition metal combinations such as $Na_{0.58}Ni_{0.6}Co_{0.4}O_2$ [87] with a layered structure as well as $Na_{0.44}MnO_2$ [88] showing a tunnel-type structure have attracted attention. Vanadium oxides, either with a channel (beta–$Na_xV_2O_5$) or layered (alpha–V_2O_5) structure have been also demonstrated to reversibly insert Na [89]. Concerning the phosphate-based materials, olivine $NaFePO_4$ [90] and NASICON compounds of the type $Na_xM_2(PO_4)_3$ (M = Fe, Ti, Nb, V) [91] were proven as positive electrode materials. Recently, a number of sodium fluorophosphates such as $Na_3V_2(PO_4)_2F_3$ [92], Na_2FePO_4F [93] and $NaVPO_4F$ [94], have emerged as promising candidates.

2.4 Electrolytes

Electrolytes not only serve as transport medium for the alkali ions between the electrodes, but also play a significant role for the overall battery performance. Since they influence the electrochemical properties of a cell, they are crucial for its cycle and shelf life and even determine the overall intrinsic safety features and limitations of a battery. Generally, liquid non-aqueous electrolytes, which are primarily used in Li- and Na-ion based systems, consist of a conducting salt Li^+X^- dissolved in an organic aprotic solvent or a solvent mixture thereof. Sometimes small amounts of a functional additive are added to enhance the cell performance. To be regarded as good electrolyte the following requirements should be met: (i) high ionic conductivity along with an insignificant electronic conductivity over a wide temperature range, (ii) a large thermal as well as electrochemical stability window to enable cell operation and (iii) chemical and electrochemical compatibility with the other cell components [27, 29]. The ionic conductivity of an electrolyte is one of the most important critical factors that affect the battery performance and depends on the number of ions transported, the viscosity of the electrolyte (low viscosity is required for high ionic mobility) and the degree of solvation of the conducting salt (solvents with a high dielectric constant can dissolve salts in high concentration). To achieve a sufficient electrochemical stability window, electrolyte decomposition through reduction or oxidation should not occur within the potential range of the negative and positive electrode. For liquid electrolytes it is also important that both the boiling and melting points are outside the battery operation temperatures in order to provide a large usable liquid range and to ensure safe behavior. Additionally, costs and toxicity of the electrolyte have to be considered [27, 95].

The aforementioned features strongly depend on the nature of the solvent(s) and the salt used. Due to their highly polar and aprotic behavior, good compatibility with the cell components and excellent stability, carbonates including propylene carbonate (PC), ethylene

carbonate (EC), dimethyl carbonate (DMC), ethyl methyl carbonate (EMC) and diethyl carbonate (DEC) are mainly employed as solvents in current electrolyte formulations. Usually, mixtures of these solvents are used, as they can provide a higher ionic conductivity, a better cell performance and an extended operating temperature range compared to a single solvent [28]. The number of inorganic conducting salts, which show a sufficient solubility and a high degree of dissociation in the above-mentioned solvents without increasing the viscosity, is very limited. Salts with anions based on a Lewis base XF_n^-, such as PF_6^-, BF_4^-, and AsF_6^- or with a large monovalent anion, for example ClO_4^-, were proven to be suitable [29]. Organic salts based on sulfonylimides have also been developed [27, 29].

One of the most common used electrolyte for commercially available Li-ion batteries consists of a 1 M solution of $LiPF_6$ in a 1:1 mixture of EC:DMC (referred to as LP 30). Other binary solvents including EC:DEC and EC:EMC also deliver high ionic conductivities and show low capacity fading. Indeed, propylene carbonate cannot be used in combination with graphite-based electrodes, since it co-intercalates with Li^+ between the graphene layers and causes degradation of the electrode [28]. For low temperature operation ternary solvent mixtures have been developed – they are highly relevant for batteries designed for electric vehicles.

For sodium-ion batteries $NaPF_6$ or $NaClO_4$ as electrolyte salts dissolved in PC or in a EC:PC solvent mixture were proven to be most suitable [95]. Compared to LIBs, propylene carbonate is the most attractive solvent for Na-ion based systems due to some excellent features such as high dielectric constant, wide electrochemical stability window, high boiling point as well as low melting point, good chemical stability and above all good compatibility with the electrode materials available for NIBs [16]. Recently, NaFSI in DME or in a mixture of EC:DEC was proposed as possible electrolyte formulation for sodium-ion batteries [96].

Since these organic electrolytes are rather expensive, often toxic, easily inflammable and show a limited electrochemical and thermal stability window, in recent years intensive research has been focused on solid-state electrolytes. This topic will be discussed in more detail in chapter 4.

3 Titania Nanotubes

One-dimensional (1D) nanostructured materials in form of nanorods, nanowires, nanofibers and nanotubes have stimulated intense research activities within the past decade as they can provide outstanding geometrical features combined with exciting chemical and physical properties [97-99]. Special emphasis is paid on the synthesis and characterization of nanostructured transition metal-oxides, since they open the way for applications in the environmental, biomedical, electronic and photochemical sector [100, 101]. Particularly, self-organized TiO_2 nanotubular structures formed on titanium are today of major importance. These nanotube layers, that commonly feature a controllable, defined geometry with a relatively high surface area, show a variety of unique properties such as high mechanical strength, good chemical stability, high corrosion resistance, semiconductive behavior, photocatalytic activity along with environmental-friendliness and non-toxicity [102-104]. These extraordinary features enable their use in a wide range of applications including solar cells [105], rechargeable batteries [106], gas sensing [107], catalysis [108, 109], self-cleaning coatings [110] and even biomedical [111] and electrochemical devices [112].

3.1 Growth mechanism of TiO_2 nanotubes

3.1.1 Stages of growth

Among various techniques that have been developed to synthesize self-organized TiO_2 nanotubes, electrochemical oxidation (anodization) of metallic titanium in fluoride containing electrolytes is proven to be the most simple and cost-effective approach. Under optimized experimental conditions, formation of self-organized, highly ordered and vertically aligned tubes can be achieved. Today, the typical anodization process of Ti is usually carried out at a constant voltage in ethylene glycol or glycerol-based organic electrolytes with small content of water and ammonium fluoride NH_4F as fluoride ion source using a simple two-electrode configuration as schematically depicted in Fig. 3 [103, 104, 113].

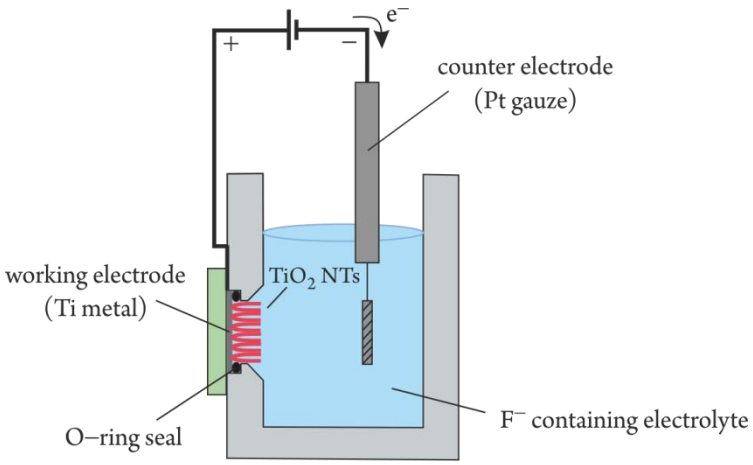

Fig. 3 Schematic representation of the experimental set-up used for the anodization process.

For the following discussion on the stages in TiO_2 growth, the published articles of Roy [103], Macak [104], Berger [114] and Kowalski [115] served as the basis.

During the initial stage of anodization, a thin oxide layer is formed on the Ti metal due to the reaction of the oxidized titanium species with the oxygen ions provided by the H_2O in the electrolyte according to the following equations:

$$Ti \rightarrow Ti^{4+} + 4e^- \tag{3.1}$$

$$2H_2O \rightarrow 2O^{2-} + 4H^+ \tag{3.2}$$

$$Ti + 2H_2O \rightarrow TiO_2 + 4H^+ + 4e^- \tag{3.3}$$

After initiation, further growth of this anodic oxide layer is governed by the field-assisted transport of the mobile ionic species (O^{2-} and Ti^{4+}) through the formed TiO_2 film (Fig. 4(a)). This is due to the fact that a high electric field is established within the oxide by the applied voltage leading to a simultaneous migration of the titanium ions towards the TiO_2/electrolyte interface and the oxygen ions towards the titanium/TiO_2 interface. Thus, new oxide growth occurs at both interfaces depending only on the rate of the migrating ions. The O^{2-} ions arriving at the titanium/TiO_2 interface can react with the titanium metal [Eq. (3.4)] forming a stable and dense TiO_2 layer, while at the TiO_2/electrolyte interface, where reaction of the outward migrating Ti^{4+} ions with water occurs, a less-dense oxide film is grown [Eq. (3.5)].

$$Ti + 2O^{2-} \rightarrow TiO_2 + 4e^- \tag{3.4}$$

$$Ti^{4+} + 2H_2O \rightarrow TiO_2 + 4H^+ \tag{3.5}$$

Simultaneously, hydrogen evolution occurs on the cathode side:

$$2H_2O + 2e^- \rightarrow H_2(g) + 2OH^- \tag{3.6}$$

However, with increasing TiO_2 layer thickness, the electric field involved in the ion transport drops progressively, making the growth process self-limiting. Thus, the thickness of the formed compact oxide layer is directly determined by the applied voltage.

This early stage in the anodic formation of nanotubular structures is very similar to the high field growth of barrier-type oxides described for example for Al and takes place independently of the F^- ions that are present in the organic electrolyte. But, these fluoride ions are indispensable for the subsequent formation of the self-organized nanotubes, as they can influence the following anodization stage in two ways. On the one hand, they can form complexes with the Ti^{4+} ions arriving at the TiO_2/electrolyte interface in form of water-soluble $[TiF_6]^{2-}$ species according to the following reaction:

$$Ti^{4+} + 6F^- \rightarrow [TiF_6]^{2-} \tag{3.7}$$

On the other hand, chemical dissolution of the already formed TiO_2 layer is possible:

$$TiO_2 + 6F^- + 4H^+ \rightarrow [TiF_6]^{2-} + 2H_2O \tag{3.8}$$

Additionally, the fluoride ions are very small and can therefore migrate under the electric field through the TiO_2 layer in competition with the O^{2-} ions. As the field-aided transport of the fluoride species is twice as fast as that of the oxygen ions, a fluoride-rich layer [116] develops at the interface between the titanium metal and the oxide. The role of these accumulated fluoride species at the interface for the tube shape formation will be discussed later. The processes involved in this stage of anodization are outlined in Fig. 4(b).

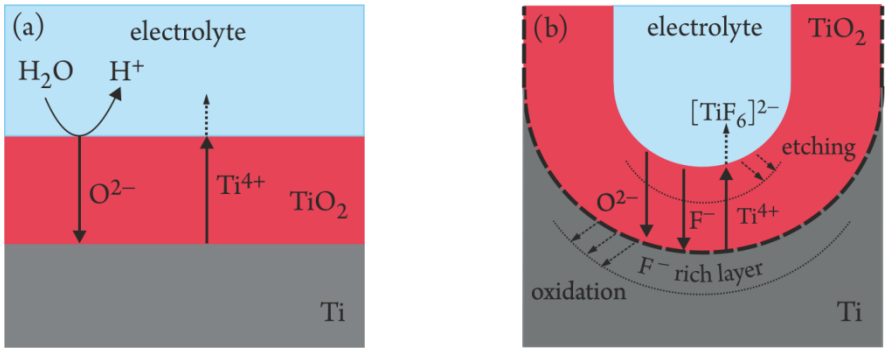

Fig. 4 Schematic drawing of the field-assisted transport processes of the mobile ionic species through the oxide film **(a)** in the absence of fluoride ions and **(b)** in fluoride containing electrolytes. Fast migration of the fluoride ions leads to accumulation at the Ti/TiO_2 interface.

The continuous complexation of the outward migrating Ti^{4+} ions and the associated localized loss of this oxidized titanium species as well as the permanent chemical attack of the formed oxide layer are responsible for the initial nanoscale pore formation on the surface. From now on, progressive growth of these pores occurs due to the faster chemical attack at the pore bottom. Finally, conversion of this porous structure into a nanotubular structure can be observed. At this point, it has to be mentioned that the transformation of the original Ti metal into the oxide is accompanied by a large volume expansion. This change in volume together with electrostrictive forces, generated by the high electric field strength during growth, cause localized stress at the interface of the titanium metal and the oxide. As a result a so-called plastic flow is induced by this compressive stress, which pushes up the oxide and the fluoride-rich layer in such a way that the accumulated fluoride species, originally found at the titanium/TiO_2 interface, builds up now the outer-tube wall of the formed tube, while the oxide layer, initially grown at the TiO_2/electrolyte interface, becomes the inner-tube wall. A compact hexagonal-shaped structure of connected consecutive tubes is obtained. Apart from this tube shape formation, the plastic flow additionally pushes the other inward migrating fluoride ions towards the newly formed cell boundaries leading to a further accumulation of the fluoride species there. Since the formed fluoride compounds, which are located over the entire nanotube length and at the bottom of the tube, are sensitive to chemical etching, separation into individual nanotubes occurs due to the selective dissolution of the fluoride species accumulated along the cell boundaries. The transition of the nanopores into the nanotubular morphology is graphically illustrated in Fig. 5 (a). Henceforth, the length of the individual nanotubes continuously increases, until an equilibrium state between oxide growth and chemical dissolution is reached.

These three stages in the electrochemical formation of nanotubes can also be recognized in the current-time curves recorded during the anodization process (see Fig. 5(b)). Initially, the formation of the compact oxide film with a low conductivity leads to an exponential decay of the current (I). During the next stage, an increase in current can be observed due to the larger reactive area caused by the random formation of pores and their growth (II). In the third stage, the current first decreases as a self-organized, regular nanotube layer forms and finally reaches a stable state as a result of the continuous tube growth (III).

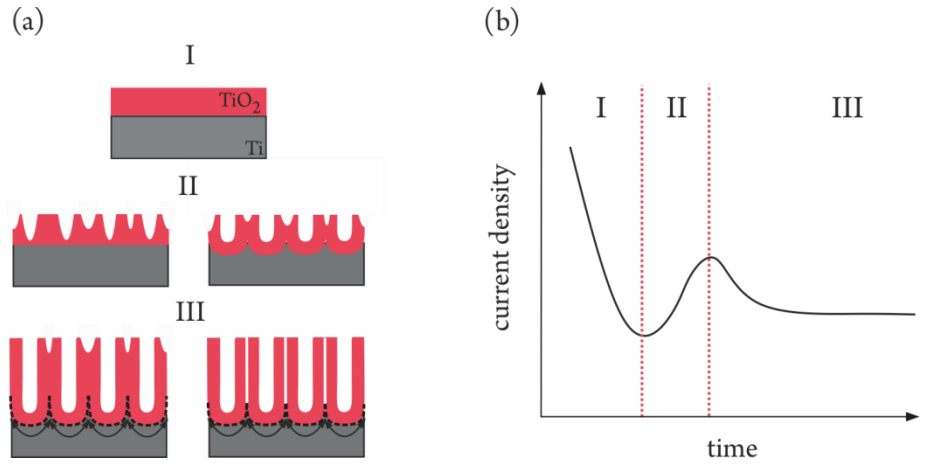

Fig. 5 **(a)** Successive steps in the electrochemical formation of the TiO_2 nanotubular structure (I: high-field aided growth of compact oxide layer; II: pore formation and growth; III: pore to tube transition). **(b)** Characteristic current-time curve recorded during the anodization process.

3.1.2 Control over self-ordering and ideal tube tops

Undesirable features that often go along with the anodization process are not perfectly arranged and ideally self-organized nanotubes as well as the existence of non-ideal tube tops. The degree of ordering of the tubes strongly depends on the purity and the conditions of the metal surface [104, 115], while non-ideal tube tops originate from debris of the initial layer, collapsing nanotubes or the formation of nanograss [103]. The remaining parts of the initial layer may cover the tops of the tubes, thus hindering any transport process into the nanotubes. Since the nanotube top ends are in contact with the fluoride-containing electrolyte for the longest period of time, progressive etching of these parts can be observed resulting in thinning down of the tubular walls. As a consequence, collapsing and bundling of the tube ends occur caused by the capillary effects when drying. Further etching of the top ends of the nanotubes leads in the long

run to disintegration and perforation of the tube walls. The resulting morphology is often described as "nanograss" [103]. One possibility to obtain well-ordered nanotubes with open tube tops is the application of a two-step anodization process. In the first step the nanotubes are conventionally grown on the titanium substrate. Then the formed nanotube layer is removed from the underlying Ti metal resulting in a titanium surface that is completely covered by ordered dimples. These well-organized dimples can act as nucleation sites for the growth of the nanotubes in the subsequent anodization step [117]. Apart from that further approaches [118, 119] have been developed to obtain ideal tube tops.

3.1.3 Control over geometry, morphology and composition

The geometry, morphology and composition of the formed titania nanotubes are strongly influenced by both the anodization chemistry (used electrolyte, fluoride concentration and water content) and the anodization conditions including anodization time, applied potential and temperature. The tube diameter is controlled by the applied voltage and linearly increases with the potential for a given temperature and electrolyte [120]. This is due to the fact that more intense chemical etching at the surface of the oxide layer occurs at higher potentials resulting in larger diameter pores [121]. The anodic potential also has a great effect on the tube length. Since a high-electric field mechanism, showing a growth factor of approx. 2.5 nm / V for anodic oxides, is responsible for the growth of the TiO_2 layer, thicker nanotube layers are obtained at higher potentials [120]. Additionally, high voltages lead to a higher chemical etching rate at the pore bottoms, thus longer nanotubes are produced [121]. At a certain potential, the length is determined by the anodization time [113]. However, the maximum nanotube length is limited, since an equilibrium state between oxide growth and chemical dissolution is achieved at some point being the case in long-lasting anodization processes [103]. Furthermore, length and diameter are strongly affected by the anodizing temperature. With decreasing temperature both the oxide growth rate as well as the electrochemical dissolution rate slow down owing to the decelerated migration rate of the mobile ions leading to shorter tubes with reduced pore diameter [122]. On the contrary, if the temperature gets too high, only no regular and unstable bundles of nanotubes are obtained [113].

One parameter that has a strong influence on the morphology is the concentration of fluoride ions present in the electrolyte. Compact oxide layer formation is observed at low concentrations (< 0.05 wt %), since the amount of F^- ions in the electrolyte is insufficient to initiate chemical etching of the oxide. At a high fluoride content (approx. 1 wt %) the oxidized titanium species immediately reacts with the F^- ions forming the water-soluble $[TiF_6]^{2-}$ complex, hence, oxide formation does not occur. Growth of nanotube layers is only observed for intermediate fluoride concentrations [103].

Differences in morphology, geometry and composition can be recognized, when anodization is carried out in various types of electrolyte. For instance, from aqueous electrolytes short tubes (in the range of a few micrometers) showing an irregular shape with ripples at the tube wall can

be grown. This appearance can be explained by the higher water content in this kind of electrolyte, which leads to a faster electrochemical etching of the nanotubes compared to its growth [123]. In contrast, tubes grown from viscous organic electrolytes, which contain a lower amount of water, generally show smooth tube walls [124]. Additionally, large diameters and long nanotubes can be obtained, as chemical etching is considerably slower in them [125]. The composition of the tube walls is also dependent on the anodizing electrolyte, as the ions present in the electrolyte can be incorporated into the tube structure. Carbon species can be found, when anodization is carried out in organic electrolytes, while small amounts of hydroxides are present, when aqueous electrolytes are used [114].

3.2 Properties of TiO_2 nanotubes

TiO_2 nanotubular structures show a large variety of unique and outstanding properties that enable their use in a wide range of applications. In this chapter, some important properties are briefly addressed; for readers interested in a more detailed overview, the following review articles [103, 104] are recommended.

3.2.1 Crystal structure

TiO_2 occurs in nature in three modifications known as rutile, anatase and brookite [126]. Additionally, three synthetically produced phases (e.g., TiO_2(B)) and some high-pressure forms exist [127]. Among all these polymorphic forms, rutile is shown to be the most stable phase in the bulk, while anatase crystals present the thermodynamically highest stability at the nanoscale. This is due to the lower surface energy of the anatase crystalline phase compared to rutile resulting in a better phase stability in the nanometer range [103]. Furthermore, titania nanotubes synthesized by anodic oxidation typically exhibit an amorphous structure [57]. Conversion into anatase and rutile forms was achieved under certain anodization conditions such as higher voltages or extended times [128-130].

3.2.2 Electrical and optical properties

Generally, amorphous titania nanotube layers show a wide band-gap in the range of 3.2 to 3.5 eV [131], thus, limiting its direct use in photochemical and electronic applications. It is therefore crucial for both, the electrical and the optical properties that additional states, e.g., by the presence of defects, are created in the band-gap either close to the valence band or the conduction band. In particular, generation of Ti^{3+} species is of major importance, as the corresponding states are located near to the conduction band. As a general remark, titania is known to have a tendency for being oxygen defective, a situation that results in a n-type material. A higher bulk state charge carrier density (10^{18}–10^{19} cm^{-3} [132]) compared to conventional

nanoparticles can hence be achieved, which leads to a higher photoresponse and an enhanced conductivity of self-organized titania nanotubes [133].

On the other hand, this higher density of bulk states is also responsible for the slower transport of charge carriers in the titania nanotubes. However, under exposure to UV light, a 30 times higher diffusion path length for electrons can be observed in the tubes due to a lower likelihood of surface recombinations [134]

Another important optical feature that needs to be mentioned is the relatively high refractive index for TiO_2 compared to other materials, which allows creation of photonic (meta-)materials [133, 135].

3.2.3 Reactivity

The high reactivity of titania nanotubes can be related to its highly defined geometry with a relatively large surface area and the presence of a high density of defects that can act as reaction sites [133]. To date, successful adsorption of H_2 [136], CO [137], CO_2 and alkanes [138] on TiO_2 nanotubular layers have been reported. Recently, it has been detected that oxygen can adsorb on crystalline anatase titania nanotubes – a remarkable attribute observed for the first time on non-defective rutile and anatase materials [139]. This is of high interest, as adsorption of O_2 is required for many surface reactions.

An electrochemically interesting and very important feature of titania nanotubes is its ability for the insertion of small cations, such as H^+, Li^+ and Na^+, into the TiO_2 lattice, when an external negative potential is applied. This insertion reaction goes along with the reduction of the Ti^{4+} species to Ti^{3+} according to the following equation [104, 133]:

$$Ti^{IV}O_2 + A^+ + e^- \rightleftharpoons ATi^{III}O_2 \quad (A = Li^+, Na^+, H^+) \tag{3.9}$$

Since this process is highly reversible, this property is exploited for applications in rechargeable battery systems [106] and electrochromic devices [140].

The TiO_2 nanotubular structure also has considerable advantages, when used as a support for noble metal catalysts in electrocatalytic reactions. Apart from providing a high surface area, catalyst aggregation on the surface can be prevented resulting in a higher reactivity rate and more specific reactions. As a result, loading of the usually expensive catalyst can be reduced. Furthermore, oxygen evolution takes place at a high overpotential, thus, faster and more facile catalytic reactions can be observed [133].

3.3 Modification of TiO_2 nanotubes

Modifications of titania nanotubes are sometimes necessary to adapt them for various applications that require specific optical, electrical and chemical properties. The most important modification approaches are (i) heat treatment to a defined crystalline structure, (ii) introduction of an additional electronically active element into the TiO_2 lattice by doping, (iii) filling or surface decoration of the tubes with a second functional material and (iv) covalent attachment of monolayers [133]. In the following, modification by heat treatment and filling will be discussed in more detail. Doping and monolayer attachment are not subject of this thesis and are not covered herein. For more information about these approaches, the reader may consult references [133, 141-143].

3.3.1 Heat treatment

As already mentioned, titania nanotubes formed by anodic oxidation are typically amorphous, but conversion to crystalline anatase or rutile phases can be achieved by using an adequate heat treatment either in a reducing (Ar or N_2) or an oxidizing (air or O_2) atmosphere. Annealing at 450°C completely transforms the originally amorphous material to anatase. This can be explained by the lower surface energy of the anatase crystal compared to rutile, which determines the thermodynamic stability in this temperature range; thus the anatase form occurs [144]. In addition, it is interesting to mention that the onset temperature for anatase formation strongly depends on the annealing gas atmosphere. While small amounts of anatase phase already exist at 250°C for samples annealed in O_2 or air, transition is much slower under reducing conditions [145]. At higher annealing temperatures (> 450°C) rutile starts to form resulting in a complete conversion of the titania nanotubes into the crystalline rutile structure at 900°C [146]. It has been observed that formation of the rutile phase is favored in reducing atmosphere, as a small amount of rutile is already present at temperatures lower than 450°C, when heat treatment was carried out in argon or N_2 [145].

Additionally, annealing can eliminate unwanted species, such as fluorides or carbon that are incorporated during the anodization process, from the tube wall [144, 146] and significantly reduces the amount of surface hydroxide groups [147]. Since fluoride species are toxic and corrosive and may create undesired additional states in the band-gap, their removal has a positive impact on several applications [144].

Undesired effects that arise as a result of heat treatment at higher temperatures are the appearance of numerous stress-induced cracks in the nanotube wall and the formation of a thin rutile layer underneath the tubes. This oxide layer originates from the direct thermally activated oxidation of the underlying Ti substrate to rutile during heat treatment under oxidizing conditions. The thickness of this solid layer increases with the annealing temperature and in more oxidizing atmosphere. Both effects are responsible for a slower electron transport reported for annealed tubes and negatively influence the conductivity of the nanotubular layer [148].

Finally, it is worth noting that annealing temperature and time also have an impact on the resulting tube morphology. For extended heat treatments at temperatures higher than 650°C, larger crystallites grow, the porous layer densify and the nanotubes disappear [146].

In conclusion, heat treatment is crucial for an enhanced conductivity and improved optical features. On one hand the crystalline anatase phase is more conductive compared to the amorphous form [149], on the other hand annealing in oxygen-free atmosphere leads to the formation of Ti^{3+} species and thus, to the introduction of additional electronic states near the conduction band [133]. The most commonly used temperature for heat treatment of titania nanotubes when conversion to anatase is desired is from 400 to 450 °C.

3.3.2 Filling of the tubes

The highly ordered vertically alignment of the TiO_2 nanotube layer allows for filling with a second functional material including semiconductors or metals resulting in nanotubes with either enhanced or entirely new properties. For instance, filling of titania nanotubes with Ni oxide results in a higher photoresponse [150], while Fe_3O_4 enables additional magnetic properties [151]. Preparation of Ag/TiO_2 nanocomposites again enhances the photocatalytic activity [152]. Furthermore, TiO_2 nanotubes filled with Sn or Sb are of great interest due to their better electrochemical performance. Among several approaches that have been reported to deposit different materials into the tubes, electrodeposition seems to be a reliable and effective method to prepare such nanocomposites.

4 Diffusion in solid-state matter

4.1 Basics of diffusion [153-156]

Diffusion is defined as the temperature dependent transport of particles (atoms, molecules, ions) against a concentration gradient by thermal motion. In the case of an inhomogeneous distribution of atoms and molecules, statistically more particles move from regions of high concentration to regions of lower concentration resulting in a thermodynamic equilibrium and in an equalization of the concentration – a process, which is driven by an increase in the entropy ΔS. The relation between the flux j_x of the diffusing particles along one dimension (x-direction) in an isotropic medium and the concentration gradient $\partial c/\partial x$ in the same dimension is given by *Fick's first law* and can be written as

$$j_x = -D\frac{\partial c}{\partial x}\,. \tag{4.1}$$

The proportionality constant D is referred to as *diffusion coefficient* or *diffusivity* and has the dimension m^2s^{-1}. The minus sign implies opposite directions of the increasing concentration gradient and the flux of the diffusing particles. If we take three-dimensional particle flux into account, a vector notation is used and Eq. (4.1) can be rewritten as

$$\boldsymbol{j} = -D\nabla c\,, \tag{4.2}$$

where $\boldsymbol{j} = (j_x, j_y, j_z)$ describes the diffusion flux in all three dimensions and the *nabla* symbol $\nabla = (\partial/\partial x, \partial/\partial y, \partial/\partial z)$ signifies the vector differential operator. For isotropic media the diffusion coefficients from Eq. (4.1) and (4.2) can be considered equal, which is the case for solid polycrystalline samples, as no macroscopic crystalline orientation is found in this kind of material, and hence an averaged diffusion coefficient can be measured. On the contrary, in an anisotropic medium, where diffusion occurs directional, D is denoted by a tensor of the second order and Eq. (4.2) is only valid for very slow diffusion processes or time constant concentration gradients.

Taking the assumption that the diffusing particles do not undergo any reactions or exchanges, and thus the number of diffusing species is preserved, the *equation of continuity* applies:

$$\frac{\partial c}{\partial t} = -\nabla \boldsymbol{j} \,. \tag{4.3}$$

The combination of Eq. (4.2) and (4.3) gives *Fick's second law*, also called diffusion equation:

$$\frac{\partial c}{\partial t} = \nabla \cdot (D \nabla c). \tag{4.4}$$

This partial differential equation of second order is non-linear if the diffusion coefficient is dependent on the concentration and usually has to be solved numerically. Indeed, in the case of concentration-independent diffusion, as observed in ideal solutions or in chemically homogenous systems, Eq. (4.4) simplifies to

$$\frac{\partial c}{\partial t} = D \nabla^2 c \equiv D \Delta c \,, \tag{4.5}$$

where $\Delta \equiv \nabla^2 \equiv (\partial^2/\partial x^2 + \partial^2/\partial y^2 + \partial^2/\partial z^2)$ represents the Laplace operator. This linear diffusion equation can be solved analytically, if initial and boundary conditions are formulated. The diffusivity D is determined by recording concentration profiles as a function of position x and time t and by fitting these profiles $c(x, t)$ to the analytical solution. For more detailed information, see the books of Mehrer [153] and Murch [156].

The diffusion coefficient depends on temperature and usually shows Arrhenius behavior according to

$$\mathrm{D} = D_0 \exp\left(-\frac{E_\mathrm{A}}{k_\mathrm{B} T}\right), \tag{4.6}$$

where D_0 denotes the pre-exponential factor, E_A the activation energy, k_B the Boltzmann constant and T the temperature [156].

4.2 Diffusion in solids

Diffusion in solid-state matter significantly differs from that in liquid systems. Let us first consider ion-transport in liquid aprotic electrolytes. Here, the solvated mobile species migrate in the solvent medium back and forth between the electrodes. Due to fast exchange processes between the solvated ions, the solvent molecules and the surroundings, a flat potential energy landscape, as shown in Fig. 6 on the left side, can be assumed for the migration of mobile species in liquid aprotic electrolytes [157]. In contrast, a crystalline solid consists of a well-defined,

distinct arrangement of atoms, which restrict the free migration path of the diffusion particles. Thus, diffusion occurs by hopping of the mobile species from one stable site to an adjacent one through a higher energetic environment (see Fig. 6, right side). The local minima are typically crystallographic sites that the ions can occupy and their distance is defined by the lattice parameter [153].

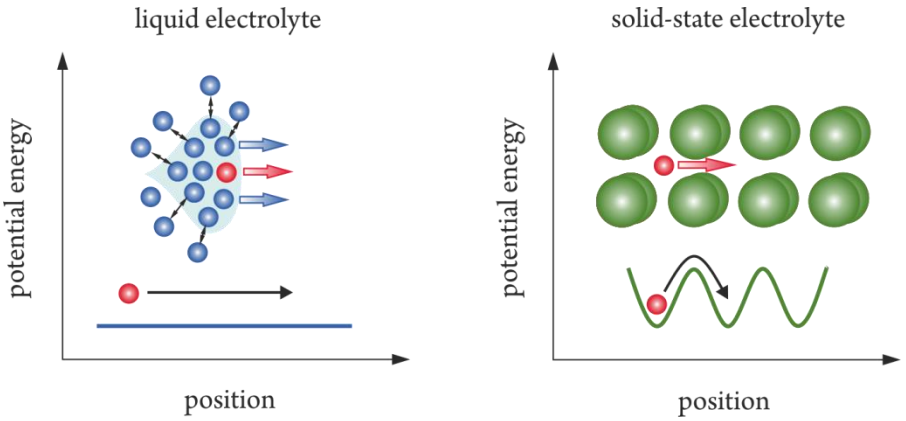

Fig. 6 Potential energy landscape the mobile ion (in red) is exposed to in liquid electrolytes (left side) and solid-state electrolytes (right side) (adopted from references [157, 179]).

The aforementioned ion hopping mechanism can be described by the so-called *random walk theory* [153, 155]. This theory assumes that diffusion is the result of many individual jumps and that these jumps take place completely randomly through the lattice. Correlation effects between the jumps are not considered [153]. The relation between three-dimensional random motion of the diffusing species through the crystal solid and the diffusion coefficient D is given by the Einstein-Smoluchowski equation

$$D = \frac{a^2}{6\tau}, \tag{4.7}$$

where a denotes the jump distance, τ the mean residence time of the diffusing species on a certain site and τ^{-1} the jump rate. This equation shows that the diffusivity can be simply expressed by physical quantities that are able to describe the jump processes in crystalline solids [154].

However, generally correlation effects between individual jumps will be present in solids. This is always the case, when diffusion does not occur via interstitial sites (see chapter 4.4 for more details about diffusion mechanism). Correlated diffusion can be accounted for by the introduction of a correlation factor f and Eq. (4.7) must be rewritten as

$$D = f \cdot \frac{a^2}{6\tau}. \tag{4.8}$$

In summary, for interstitial diffusion (in very dilute interstitial solid solution) we have $f = 1$. Other diffusion mechanisms show correlation factors smaller than unity.

In crystalline solids the ion hopping processes are usually thermally activated and follow Arrhenius behavior according to

$$\tau^{-1} = \tau_0^{-1} \exp\left(-\frac{E_A}{k_B T}\right). \tag{4.9}$$

Here, the pre-factor τ_0^{-1} represents the attempt or vibrational frequency, E_A the activation energy, k_B Boltzmann's constant, and T the absolute temperature. For a better understanding of the physical quantities that describe ion dynamics in solid-state matter, we consider an ion localized in a potential energy landscape as shown in Fig. 7 [153]. Due to lattice vibrations this ion in the potential well oscillates around its equilibrium site according to a harmonic oscillator with an eigenfrequency of $\omega_0 = (k/m)^{1/2}$, where m is the ion mass and k a force constant that considers the potential well curvature. These vibrations typically show a frequency in the range of the Debye frequency (1012 to 1013 Hz) and are usually not strong enough to allow for a jump to the neighboring potential well. The activation energy E_A (also known as migration energy E_m) is given by the energy barrier the ion species has to overcome when hopping from one site to the adjacent one. According to Eq. (4.9) hopping processes are favored by thermal activation. This means, that at a given temperature T, the thermal energy of the vibrating ion is high enough to overcome this energy threshold leading to a successful jump [154].

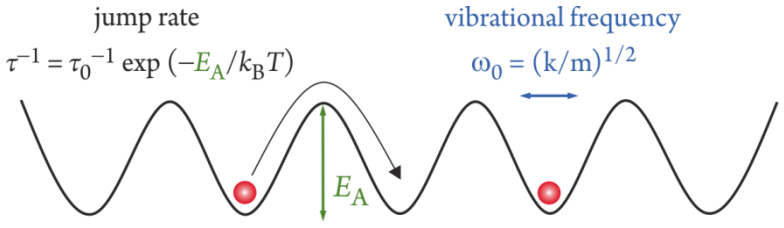

Fig. 7 Mobile ion (in red) localized in a potential energy landscape of a crystal structure. Due to lattice vibrations the ion in the potential well oscillates around its equilibrium state with an attempt frequency ω_0. The activation energy E_A is the energy barrier the mobile species has to overcome, when hopping from one stable site to an adjacent one. Since the hopping process is thermally activated, at a given temperature the thermal energy of the vibrating ion is high enough to overcome this energy threshold.

4.3 Defects and diffusion

As already mentioned, diffusion occurs by hopping of the mobile species from one potential well to an adjacent one. But, apart from the energy barrier to be overcome, this jump is only possible if the neighboring potential well is vacant. These vacancies, either found on regular lattice sites or interstitial sites, are induced by crystallographic defects. The presence of defects is therefore a basic requirement for the migration of mobile ions through the crystal lattice; there is no diffusion without defects. Classically, solid-state defects can be classified according to their dimensionality [158].

Point defects, or zero-dimensional defects, play an important role in diffusion processes, as they can move through the crystal lattice via different mechanism, thus mediating atomic diffusion. Additionally, they are always present in crystalline solids at thermodynamic equilibrium [153]. This means that even "perfect" crystals without atomic imperfections contain point defects at temperatures above 0 K [155]. The reason for this is that defects introduce disorder within a crystal lattice and therefore increase entropy resulting in a lower Gibbs free energy, which is thermodynamically favored (see Fig. 8) [159].

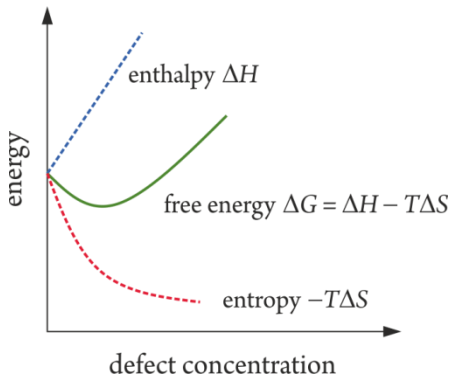

Fig. 8 Dependence of the Gibbs free energy on the defect concentration. Every solid matter has a thermodynamic tendency to acquire defects, as they introduce disorder resulting in a lower entropy and Gibbs free energy – this relationship can be described using the Gibbs–Helmholtz–equation $\Delta G = \Delta H - T\Delta S$.

Point defects are atomic defects and hence only occur at a single atom site, either in form of vacancies or interstitials. Ionic vacancies represent empty sites in the regular crystal lattice, which are usually occupied, while interstitials describe extra atoms or ions at non-regular lattice sites in a crystalline solid [155]. These point defects can be either of an *intrinsic* or an *extrinsic* nature.

Typical intrinsic defects include *Schottky* and *Frenkel disorder*, actually pair defects, both of which preserve charge neutrality in the ionic crystal. Schottky-type defects comprise the formation of an equal number of vacancies at regular lattice sites in both the cation and the anion sub-lattice. Frenkel disorder describes the situation, where cations or anions (much less common) are displaced from regular to interstitial sites leaving behind vacancies [159]. On the contrary, extrinsic defects can be introduced by impurity atoms or dopants, which occupy regular lattice sites, forming substitutional defects, or interstitial sites. In case of heterovalent dopants, additional vacancies are generated in the sublattice of the opposite valency in order to guarantee charge neutrality. Depending on the size of the dopant, contraction or expansion of the crystal lattice can be observed [158].

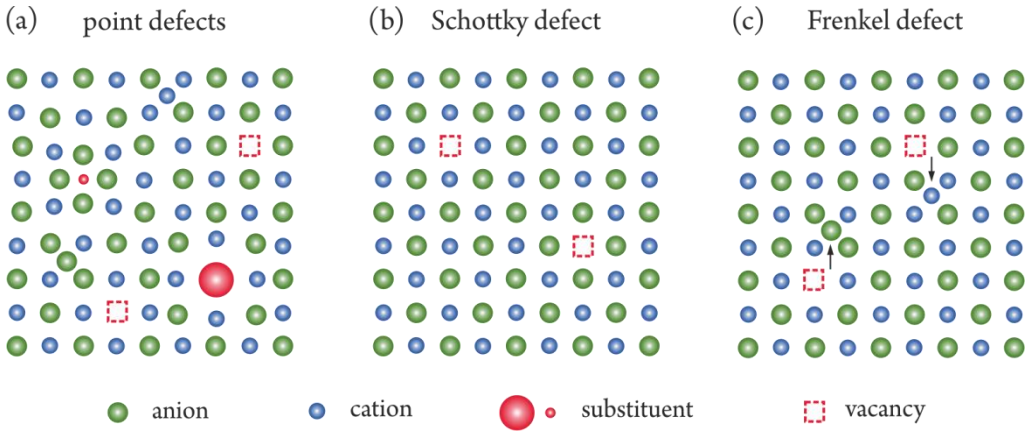

Fig. 9 Schematic representation of point defects in a crystal lattice. **(a)** Intrinsic defects such as cation/anion interstitials and vacancies as well as extrinsic defects in form of substituents are shown. **(b)** Schottky-type and **(c)** Frenkel-type defect. See text for further explanation.

For the sake of completeness, extended defects showing higher dimensionality are briefly described in this paragraph. *One-dimensional defects* extend along a line and are, unlike point defects, non-equilibrium defects. *Dislocations*, either in form of screw or edge dislocations, belong to this class of defects. They can move easily and hence not only affect the deformation properties of a crystal [158], but also significantly influence the diffusional properties, since moving dislocations can annihilate existing interstitials and vacancies, or can create new ones [160]. Examples for *two-dimensional (planar) defects* are *stacking faults* or *grain boundaries*. Stacking faults arise from errors in the periodic stacking of the planes in a crystal, while grain boundaries represent interfaces between grains that show the same phase but differ in orientation [158]. In polycrystalline solids, such grain boundaries provide faster diffusion pathways for the mobile species compared to the bulk material [161]. *Three-dimensional defects* are *volume defects* and include voids/pores and precipitates. The former corresponds to clusters

of vacancies, while the latter are defined as accumulations of impurities, which form inclusions of a foreign phase inside the crystal. In both cases, a great impact on the diffusion properties of a given material can be observed [162].

4.4 Mechanism of diffusion

Migration of the atomic particles through the crystal lattice can be facilitated via various diffusion mechanisms depending on the chemistry and size of the diffusing atom, the host crystal structure and the nature of the present defects. In this section the most common mechanisms of solid-state diffusion are briefly discussed. For more detailed information the reader is referred to references [153-156].

Vacancy mechanism. – Diffusion via vacancies takes place preferentially in metals and alloys. Here, matrix or solute atoms migrate by jumping from their original regular lattice site into an adjacent vacant site resulting in an exchange of their positions as illustrated in Fig. 10 (a). Each diffusing atom thus exchanges places with a series of vacancies - which are from time to time in its immediate vicinity - as it moves through the crystal lattice [153]. Therefore, diffusivity strongly depends on the mobility and the availability of vacant sites [155].

Divacancy mechanism. – Similar to the vacancy mechanism is the divacancy mechanism, where diffusion takes place via vacancy pairs; see Fig. 10 (b). Such bound pairs of vacant sites (divacancies) are formed from simple vacancies (monovacancies) at thermal equilibrium. Both, the monovacancies as well as the divacancies are thermally activated. However, with increasing temperature the concentration of vacancy pairs becomes more significant. This type of diffusion mechanism plays an important role in fcc metals due to the higher mobility of divacancies compared to simple vacant sites in these metals [153, 154].

Interstitial mechanism. – The simplest diffusion mechanism is the interstitial mechanism, which is also often referred to as direct interstitial mechanism. Here, diffusion exclusively occurs via interstitial sites. Since this mechanism is not mediated by defects and thus the diffusing atoms do not have to wait to be adjacent to a vacancy, higher diffusion coefficients compared to other mechanism are observed [153]. Solute atoms, smaller than the host atoms, prefer this type of diffusion. They can be easily incorporated on interstitial sites of the host lattice, forming a solid solution, and migrate through the lattice simply by jumping from one interstice to the neighboring (unoccupied) interstitial position as shown in Fig. 10 (c). These successive jumps are uncorrelated, because the sequence of the jumps is independent of the preceding ones [155]. In bcc and fcc crystal lattices, such interstices are often tetrahedrally or octahedrally coordinated [154].

Interstitialcy mechanism. – If the interstitial atoms and the host atoms are similar in size, a direct jump to the next interstitial site is energetically not favored [153]. The interstitialcy mechanism, also known as indirect interstitial mechanism, involves the simultaneous movement of two atoms. Here, the initial interstitial atom displaces one of the adjacent host atoms from its regular lattice site, which then moves to the next available interstice [156]. Fig. 10 (d) illustrates this type of diffusion mechanism.

Interstitial-substitutional mechanism. – This mechanism is based on the fact that solute atoms are able to occupy both substitutional and interstitial sites in the crystal lattice. Two types can be distinguished: the kick-out mechanism and the dissociative mechanism. In both cases the solute atom at the interstice first diffuses via the aforementioned interstitial mechanism. In the knock-out mechanism this interstitial subsequently displaces a host atom from its regular lattice site according to the interstitialcy mechanism, while it combines with a vacant site in the dissociative mechanism [156]; see Fig. 10 (e).

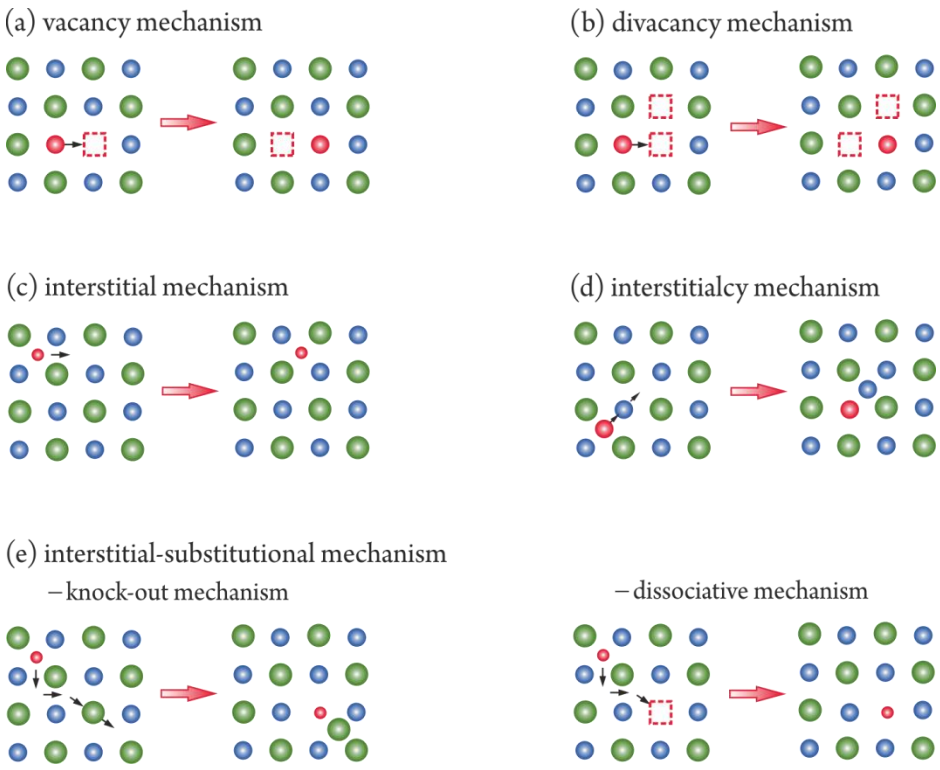

Fig. 10 Schematic representations of the most common diffusion mechanisms in solids (adopted from references [153, 156]).

4.5 Solid electrolytes

Current Li- and Na-ion based technologies mainly use organic liquids as electrolytes [8, 17]. Although these electrolytes offer the benefits of excellent wetting properties of the electrode surfaces and high ionic conductivity, they often suffer from safety issues, such as flammability and leakage, and inadequate thermal and electrochemical stabilities, thus complicating its application in large-scale systems and electric vehicles [18]. All-solid-state batteries (ASSBs) based on solid electrolytes are one option to overcome these safety and stability problems due to diminished flammability, enhanced thermal stability and the wider electrochemical voltage stability window [19]. Furthermore, they are expected to withstand a large number of cycles at full storage capacity, which is indispensable for large-scale stationary energy storage applications [20]. The replacement of liquid organic electrolytes by solid-state electrolytes has even more advantages. For instance, due to their high electrochemical stability, metallic lithium and sodium can be adopted as anode material leading to higher capacity values and an enhanced energy and power density of the battery [163]. High decomposition voltages also allow the use of high voltage positive electrode materials [20]. Additionally, they offer the possibility for the use of new electrode materials, which are not stable in liquid electrolytes. Moreover, no separator is needed in the battery system. Solid-state electrolytes could also facilitate battery miniaturization and the development of a more versatile battery design [18].

A good solid-state electrolyte has to meet various requirements, the most important of which are (i) a high room temperature ionic conductivity ($> 10^{-3}$ S/cm), but negligible electronic conductivity, (ii) a wide electrochemical and thermal stability window, (iii) no reactivity with other components, (iv) good interfacial compatibility and (v) good mechanical properties. Low cost, simple fabrication and environmental friendliness should also be considered for practical applications [21, 22]. In the past decade, organic polymer electrolytes as well as inorganic glassy and ceramic solid electrolyte materials have been extensively studied [18, 21, 22, 164, 165]. Among them, inorganic crystalline materials have attracted the most attention and promise to be a good choice as solid electrolytes in all-solid-state alkali-ion batteries [21]. Such ionic conductors are built up of mobile ions as well as nonmetal and metal ions that form the polyhedra skeleton of the crystal structure [157].

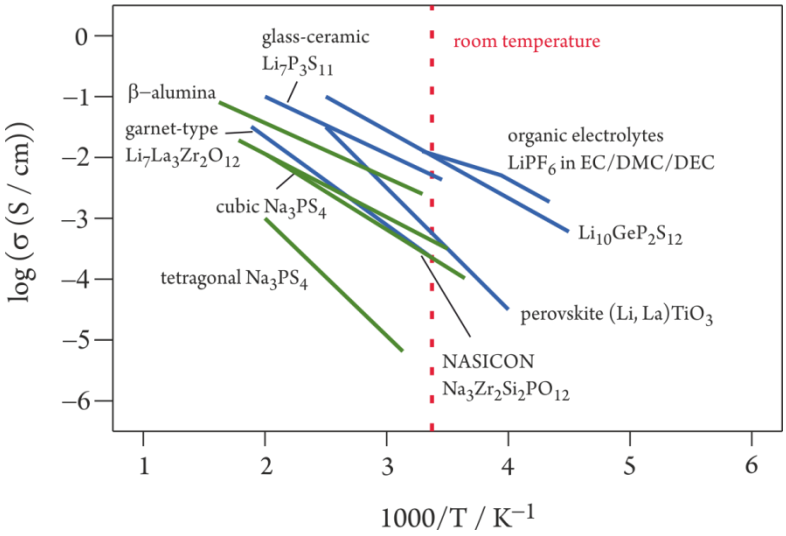

Fig. 11 Ion conductivities as a function of the temperature for a selection of solid electrolytes for lithium (in blue) and sodium (in green) systems (adopted from references [21, 23, 165, 170]).

Fig. 11 shows the ion conductivities as a function of the temperature for a selection of solid electrolytes for lithium and sodium systems. Regarding the lithium-ion conductors research has mainly focused on oxide-based and sulfide-based materials. The oxidic solid-state electrolytes can be classified, according to their structural family, into garnets (such as $Li_7La_3Zr_2O_{12}$ [166]), perovskites (for example, $La_{0.5}Li_{0.5}TiO_3$ [167]), LISICON (lithium super ionic conductor – e.g., $Li_{14}ZnGe_4O_{16}$ [168]) and NASICON-like structures (sodium super ionic conductors – for example, LATP, $Li_{1.5}Al_xTi_{2-x}(PO_4)_3$ [169]) [21]. All these conductors can exhibit ionic conductivities in the range of 10^{-5} to 10^{-3} S/cm at room temperature [22], which is lower than those of currently used organic liquid electrolytes [170] (usually in the order of 10^{-2} S/cm at ambient temperature [171]). However, these materials are characterized by their excellent chemical, mechanical and electrochemical stability. Abundant starting materials, ease of preparation and low cost are also attractive. But, at the same time, poor interfacial compatibility and high grain boundary resistance limit their performance [21]. It should also be noticed that oxide-based solid electrolytes containing titanium in its structure, such as LLTO, are not suitable for lithium batteries due to the easy reduction of Ti by metallic lithium [167].

Sulfide-type compounds, which make use of the better polarization ability and larger size of the sulfur anion, are found to generally show higher ionic conductivities than oxidic electrolytes [172]. The most promising candidates are argyrodites and some structures of the thio-LISICON family. The lithium argyrodite compounds of the general formula Li_6PS_5X (X = Cl, Br, I) are a relatively newly discovered class of fast Li-ion conductors, which can achieve ionic conductivities

in the order of 7×10^{-3} S/cm [173]. They have attracted additional attention due to their exceptional wide electrochemical stability window (0 – 7 V *vs.* Li^+) [174]. Compared with LISICON, in the thio-LISICON family $Li_xM_{1-y}M'_yS_4$ (M = Ge, Si and M' = Ga, Zn, Al, Sb, P), which usually crystallizes in the γ-Li_3PO_4-type structure, the anion backbone consisting of oxygen atoms is replaced by sulfur atoms [175]. The $Li_{3.25}Ge_{0.25}P_{0.75}S_4$ solid electrolyte, for example, shows room temperature ionic conductivities in the order of 2.2×10^{-3} S/cm [176]. Recently, the highest Li-ion conductivity to date (about 1.2×10^{-2} S/cm at room temperature) was reported for the $Li_{10}GeP_2S_{12}$ LISICON-like conductor, which is comparable to that of commercial liquid organic electrolytes [177]. Substitution of Ge by Si or Sn in this structure also yields high ionic conductivity values [178, 179]. These thio-LISICON based solid electrolytes show good mechanical properties, a stable electrochemical window between 0 and 4 V *vs.* Li and electric insulation. Additionally, glass-ceramics (crystallized glass) of the binary Li_2S-P_2S_5 system [180-182], such as $Li_7P_3S_{11}$ [183] and Li_3PS_4 [184], have also attracted particular attention due to their high ionic conductivities combined with a high electrochemical stability window, which is ascribed to the absence of Si and Ge, two strong network formers, in the structure [175, 185]. For the $Li_7P_3S_{11}$ glass-ceramic a lithium ion conductivity of 3.2×10^{-3} S/cm was first reported [181], but over the years the ionic conductivity was continuously improved reaching values of up to 1.2×10^{-2} S/cm, when the glass-ceramic is densified by optimized heat treatment [186]. The lithium thiophosphate, Li_3PS_4, shows thio-LISICON framework structure, where the sulfide ions are hexagonally close-packed and the PS_4 tetrahedra are isolated from each other. Three temperature dependent modifications, namely α, β and γ phase, of this structure are known. The corresponding lithium-ion conductivity depends on the arrangement of the PS_4 tetrahedra, since they affect the position of the lithium ions in the framework and thus the preferred diffusion mechanism [187]. For more information about lithium diffusion in this type of material the reader is referred to the manuscript with the title "Nuclear spin relaxation in nanocrystalline β-Li_3PS_4 reveals low-dimensional Li diffusion in an isotropic matrix", which can be found in the Results and Discussion part.

Generally speaking, impressive ionic conductivity, acceptable electrochemical stability window, good mechanical properties and negligible grain boundary resistance make sulfide-based materials promising candidates for solid-state electrolytes. However, they suffer from instability in contact with metallic lithium and oxide cathodes and are very sensitive to moisture, which represent significant difficulties of further research. For a more extensive overview of ceramic solid-electrolytes, the reader is referred to the following review articles [21, 22, 157, 170].

Among the possible candidates as solid electrolytes for all-solid-state sodium-ion batteries, Na β''-alumina should be mentioned, which has already been commercialized in high-temperature sodium-sulfur batteries. This fast sodium ion conductor has a layered structure and provides two-dimensional Na-ion diffusion [188]. NASICON phases of the general formula $Na_{1+x}Zr_2Si_xP_{3-x}O_{12}$ ($0 < x < 3$) [91, 189] are another type of attractive fast Na-ion conductors due to their high room temperature ionic conductivities and their stability against moisture and

air. It was found that NASICON phases, which contain 3 – 3.5 mol sodium per formula show the highest ionic conductivity and that substitution of Zr by Sc can further enhance the conductivity. As a result, the highest conductivity value of 6.9×10^{-4} S/cm at ambient temperature was observed for the compound $Na_{3+0.4}Sc_2Si_{0.4}P_{3-0.4}O_{12}$ [190]. Despite their considerable sodium-ion conducting properties, their required high-temperature processing to reduce grain boundary resistance and the presence of voids limit their practical application [188]. Additionally, some thiophosphate materials, which are promising solid-state electrolytes for lithium systems, have also been successfully synthesized as Na-ion conductors. Indeed, the high-temperature cubic phase of Na_3PS_4 shows a room temperature ionic conductivity in the order of 2×10^{-4} S/cm. Stabilization of the cubic phase, since also a low conductivity tetragonal phase of Na_3PS_4 exists, and reduction of the grain boundaries are necessary prerequisites to achieve this high conductivity value [191]. This glass-ceramic electrolyte has already been tested in all solid-state sodium batteries operating at ambient temperatures [192]. Recently, high ionic conductivity (4×10^{-4} S/cm) has also been reported for the $Na_{10}SnP_2S_{12}$ electrolyte. Furthermore, it was predicted by DFT calculations that substitution of Sn by Si or Ge should result in even higher conductivities. Compared to the sulfide-based lithium-ion conductors, which tend to react with metallic lithium resulting in a decomposition of the electrolyte, these sulfidic sodium-ion conductors are much more stable due to the lower reductive potential of Na [193].

In conclusion, the solid electrolytes reported so far for lithium as well as sodium systems are not able to meet all the requirements mentioned above. Especially, their low room temperature ionic conductivities and poor stabilities limit the commercial applications of ASSBs. Thus, much effort is spend on the optimization and design of inorganic solid electrolytes with enhanced ionic conductivity and higher stability, which will be subject in the following chapter.

4.6 Design principles of inorganic crystalline solid-state electrolytes

Generally, such crystalline solids, which are considered as potential solid-state electrolytes, consist of mobile ions (in our case Li^+ or Na^+) as well as spatially arranged immobile ions (metals or nonmetals). The immobile ions typically form polyhedra, which are either ordered into isolated polyhedral units or are interlinked via corners, edges or faces, thereby creating the skeleton of the crystal structure [157]. The mobile ions usually occupy octahedral or tetrahedral sites within the structure [194]. While the spatial arrangement of the immobile ions has great effects on the dimensionality and the migration path of the mobile ions, the interaction between the immobile framework and the mobile species strongly influences the mobility of the Li- or Na-ions [170]. As already mentioned in chapter 4.2., diffusion in crystalline solids occurs by hopping of the mobile species from one stable crystallographic site to an adjacent one through a higher energetic environment. This energetic barrier (activation energy, E_A), which represents a bottleneck the mobile ions have to pass through along their minimum energy diffusion pathway, has an influence on the ionic conductivity and mobility, where low activation energies result in high ionic conductivity and mobility [157].

The ion conductivity σ of a given material is determined by the product of density n_i, the charge q_i and the mobility μ_i of the charge carriers:

$$\sigma = \sum n_i q_i \mu_i \,. \tag{4.10}$$

Assuming that the ions do not interact, the mobility μ_i can be related to the diffusion coefficient D by the Nernst-Einstein equation

$$\mu = \frac{qD}{k_B T} \,, \tag{4.11}$$

where T represents the temperature and k_B the Boltzmann constant. Thus, the ionic conductivity can be rewritten as

$$\sigma = \frac{nq^2 D}{k_B T} \tag{4.12}$$

The ionic conductivity usually shows Arrhenius behavior and can also be expressed as

$$\sigma = \sigma_0 \exp\left(-\frac{E_A}{k_B T}\right) \tag{4.13}$$

with E_A representing the activation energy and σ_0 the pre-exponential factor.

To acquire fast ion conduction, the following criteria should be fulfilled, when designing suitable solid electrolytes: (i) enough defects in form of vacancies or interstitials should be available for the mobile species to occupy; (ii) the activation energy should be low enough to ensure easy hopping between neighboring available sites; (iii) connection of these available sites is necessary to provide the mobile ions with a continuous diffusion pathway [21]. In addition, the diffusion mechanism present also influences the ionic conductivity [170].

Let us first consider the influence of defect concentration and distribution on the ionic transport. Since mobile ions migrate via interstitials or vacancies through the crystal lattice, particularly these point defects (see chapter 4.3. diffusion and defects) play an important role in diffusion processes and thus directly affect the ionic conductivity. They can occur in solid electrolytes under different conditions. First of all, partial occupation of ion sites can lead to the formation of many vacancies in the crystalline solid. For instance, in β-Li_3PS_4, the inequivalent lithium ion sites 4b and 4c are 68 % and 32 % occupied, respectively [170]. Second, aliovalent substitution, which creates both interstitials and vacancies, can also increase the mobility and concentration of mobile species in the solid electrolyte. However, it should be noted, that the substitution level is limited, since a higher concentration of substitution results again in a decrease of the ionic conductivity. This can be attributed to interactions between the mobile ions or to increases in the activation energy caused by strong distortions of the lattice at high substitution concentrations [157].

The next two aspects, low activation energy and continuous diffusion pathways for the mobile species, are strongly correlated with the spatial arrangement of the immobile ions. To allow for fast ion transport the energy barriers between the available sites should be low and these sites should possess equivalent energies with large channels connecting them. This feature was found, for example, in the superionic lithium-ion conductor $Li_{10}GeP_2S_{12}$, which shows the highest ionic conductivity at room temperature reported to date. The structure of LGPS reveals a bcc-like anion framework with predominantly tetrahedrally coordinated Li, P and Ge cations. The most stable site for Li is therefore a tetrahedral site. In this lattice, the Li ions preferentially migrate along interconnected face-sharing tetrahedral sites, which are energetically equivalent with a low energy barrier of 0.15 eV. To summarize, a network of face-sharing tetrahedra is required for optimal lithium ion diffusion, since migration through connected tetrahedral-tetrahedral sharing faces enlarges the bottleneck size for diffusion resulting in smaller activation energies [194].

Another possibility to increase the bottleneck size for ion diffusion is to increase the lattice volume by cation substitution. It was found that isovalent substitution within a given structural family with cations of a larger size leads to enhanced ionic conductivities and reduced activation energies [157]. Recently, a new approach to lower the energy barrier has been proposed. In contrast to the aforementioned concept, where a decrease in activation energy can be achieved by lowering of the transition state either through a network of face-shared tetrahedra or opening of diffusion channels, increasing the energy (destabilization) of the stable states can also result in lower energy barriers. Both concepts to lower the energy barrier are graphically illustrated in Fig.

12. Destabilization of the initial and final state can be observed in materials with a frustrated energy landscape as in the case of $LiTi_2(PS_4)_3$ (LTPS). In the crystal structure of LTPS no regular tetrahedral or octahedral sites for lithium to occupy are found along the diffusion pathway. Instead all available sites for Li within the crystalline Ti-P-S framework are highly distorted and are hence, energetically unfavorable Li sites. This results in a relatively flat energy landscape with small energy barriers and numerous diffusion paths. LTPS exhibits the highest diffusion coefficient at room temperature (around 1.2×10^{-11} m^2/s) ever reported, one order of magnitude higher than that of LGPS. The ionic conductivity of 6.1×10^{-2} S/cm is competitive to the LGPS material. For more information about the frustrated energy landscape concept relating to the $LiTi_2(PS_4)_3$ compound, the reader is referred to the introduction on LTPS, which can be found in chapter 6 Results and discussion.

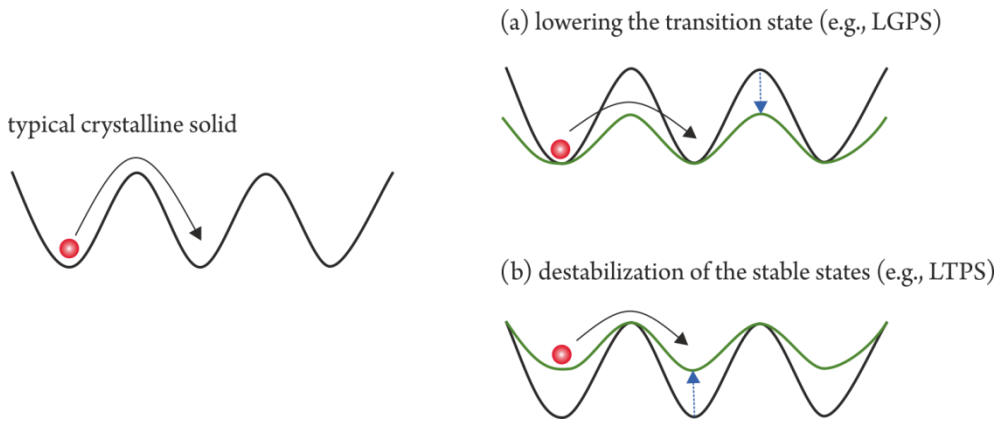

Fig. 12 *Left:* Typical potential energy landscape the mobile species is exposed to in a crystalline solid. *Right:* The energy barrier can be lowered either by lowering the transition state or by destabilizing of the stable states.

5 Experimental techniques

5.1 Cyclic voltammetry

Cyclic voltammetry (CV) is a convenient and versatile electroanalytical method for initial electrochemical studies of electroactive species. It allows the identification of redox potentials and provides qualitative information about the kinetics and thermodynamics of redox reactions. This method is also proven to be useful for the analysis of adsorption processes or coupled electrochemical reactions [195].

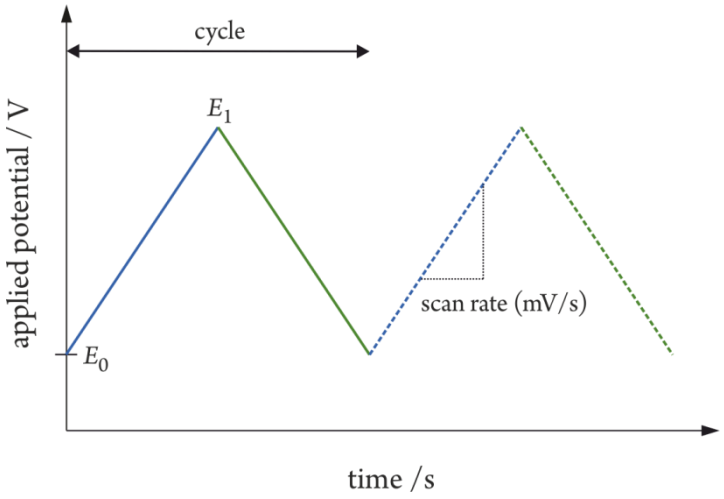

Fig. 13 Potential-time profile for a cyclic voltammetry experiment. E_0 and E_1 are switching potentials.

Generally, in a CV experiment, the potential of the working electrode is varied linearly with time with a given scan rate (in mV/s) between two potential limits E_0 and E_1, also known as switching potentials or vertex potentials (see Fig. 13) [196]. A full potential cycle is obtained, when the voltage applied is scanned from E_0 to E_1 and then swept back to the value of E_0. This cycle can be repeated several times [195]. Both scan rate and potential limits can be easily varied after each full cycle. As a result, the current response at the working electrode is recorded and plotted versus the applied potential to give a cyclic voltammogram as shown in Fig. 14 (a) [197].

It can be seen that the recorded current values pass through a maximum during scanning of the potential. The current response depends on the diffusive mass transport to/from the surface of the electrode and the kinetics of electron-transfer reaction [196]. As the voltage applied approaches the potential at which the electrode reaction takes place, the current starts to increase due to reduction or oxidation of the electroactive species. As the voltage sweep continues, at some point, the reactants supply at the electrode surface cannot be sustained by the mass transport mechanism (*i.e.* diffusion in unstirred solutions) resulting in a decrease of the electrochemical reaction and hence, in a decay of the current values. In the case of a reversible redox couple, a corresponding peak can be observed, when the scan is reversed. The investigated potential range should be wide enough that most of the electrode reactions are encompassed [28]. Parameters of interest of such an *i*–*E* curve are the location of the electrode potential at which the current peak occurs (E_p) and the magnitude of the peak (I_p) [195].

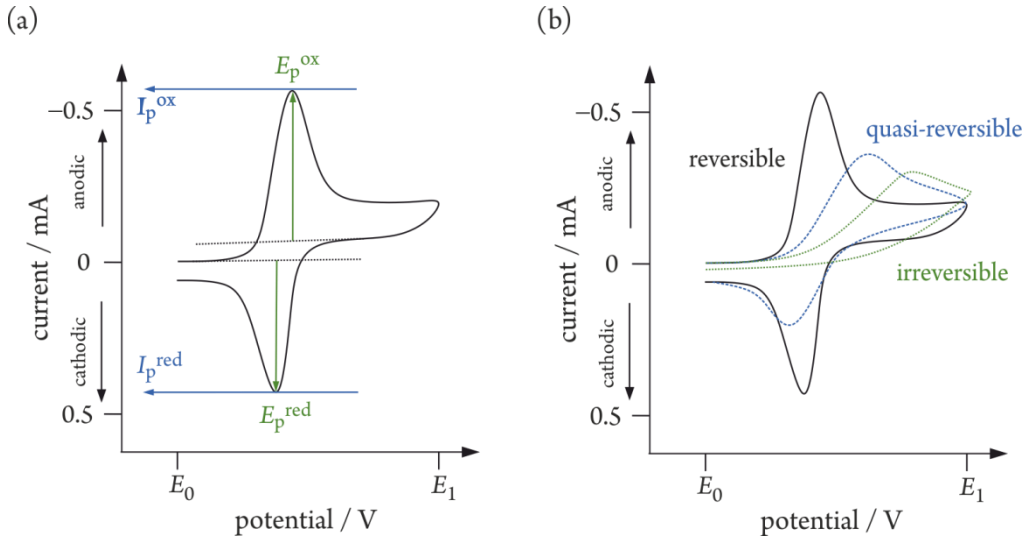

Fig. 14 **(a)** Resulting cyclic voltammogram showing the most important parameters E_p (peak position) and I_p (peak height) of the reduction and oxidation process, respectively. **(b)** Characteristic cyclic voltammograms of a reversible (diffusion-controlled), quasi-reversible (dependent on the kinetic and mass transport) and irreversible (kinetically inhibited) redox process.

Depending on the rate of the heterogenous electron-transfer reaction, different voltammetric profiles are obtained. Fig. 14 (b) illustrates cyclic voltammograms for reversible, quasi-reversible and irreversible redox processes. In the case of electrochemically reversible behavior, the electron exchange kinetics are so fast that the diffusion-controlled mass transport is the rate-limiting step even at relatively small overpotentials. Usually, a reversible reaction exhibits almost symmetrical current peaks with $I_p^{ox}/I_p^{red} = 1$ and a relatively small separation of the peak

potentials, which ideally should be $\Delta E_p = (E_p^{ox} - E_p^{red}) = 0.059/n$. The value of ΔE_p does not depend on the applied scan rate meaning that the peak potential does not shift with varying sweep rate. Indeed, the peak height I_p increases with the square root of the scan rate as described by the Randles-Sevcik equation:

$$I_p = \pm 0.446nFAC(nFDv/RT)^{1/2}, \tag{5.1}$$

where n denotes the number of exchanged electrons, F the Faradaic constant, A the electrode surface, C the concentration, D the diffusion coefficient, v the scan rate, R the gas constant and T the temperature.

In a quasi-reversible system the rate of the mass transport is comparable to that of the electron-transfer reaction. Here, the peak potentials are located further apart and a shift in the electrode potential peak is observed with increasing scan rate. This is due to the fact that higher scan rates also lead to an increase in the rate of the mass transport. Thus, an overpotential is required to maintain the rate of the electron-transfer reaction. Compared to a reversible redox-couple the current peaks are reduced in magnitude, but the peak height still increases with the sweeping rate.

Electrochemically irreversible behavior occurs, when the electron transfer is very slow compared to the mass transport. In the majority of cases, no current peak is observed in the reversed scan direction. Again, as in the quasi-reversible case, the potential of this single current peak is dependent on the scan rate [28, 195].

5.2 Galvanostatic cycling with potential limitation

Galvanostatic cycling with potential limitation (GCPL) is a reliable method for studying the electrochemical behavior of an electrode material during the insertion/extraction process. It allows the estimation of specific capacity values of electroactive materials as well as their initial and subsequent irreversible capacities and helps to evaluate the cycling stability. Useful information can also be obtained about over-potentials at various kinetic rates by observing the occurring polarization effects during charging and discharging [198]. In this technique, a constant (anodic or cathodic) current is applied to the working electrode within pre-set potential range limits and its voltage response is recorded as a function of time [199]. The measured electrode potential gradually varies with time as the reactant to product concentration ratio changes due to the electrode reaction [198]. The applied current can either be expressed as current per mass of electroactive material in mA/g or by using the C-rate convention (see below). Depending on whether a negative or positive current is imposed, reduction or oxidation of the electrode material takes place. Upon reaching the pre-defined potential limits, the current switches from reducing to oxidizing current or vice-versa. This charge-discharge cycle can be repeated for several times (see Fig. 15).

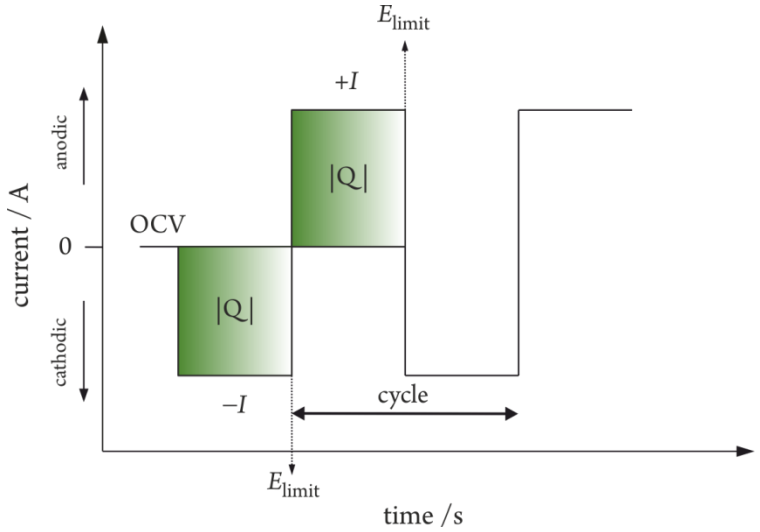

Fig. 15 Current plotted as a function of time for a typical galvanostatic cycling experiment with potential limitations.

The charge Q, which is transferred during the charge or discharge process is given by the product of the current I (in A) and the time t (in h) [29]. The capacity, defined as the maximum amount of energy stored in a fully discharged electrode material, can be calculated from the

transferred charge at a given cycling rate. It is often expressed in terms of mAh/g as specific capacity or mAh/cm^2 as areal capacity for thin film electrodes. Usually, the specific capacity values are measured at different current rates and plotted versus the cycle number to evaluate the rate capability. The estimated capacities typically decrease with increasing charging/discharging rate. Characteristic voltage profiles can be obtained, when the potential response is plotted as a function of the specific capacity, *cf.* Fig. 16 [198].

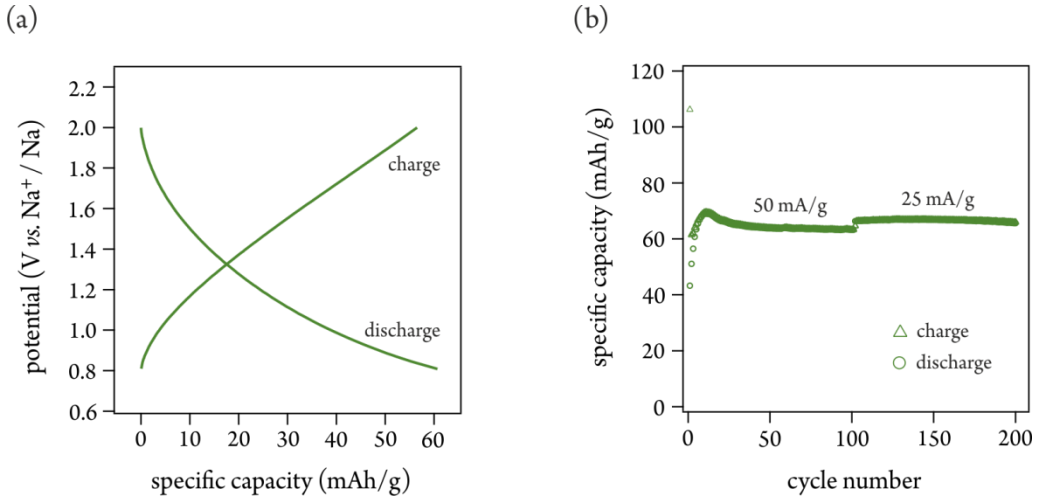

Fig. 16 **(a)** Galvanostatic charge/discharge curve corresponding to the insertion of sodium in TiO_2 nanotubes that were obtained by anodization at 30 V for 2 hours. **(b)** Specific sodium storage capacity obtained at two different current rates within the 0.8 – 2 V potential limits plotted as a function of the cycle number for the same titania nanotubes (30 V, 2 h).

Another important parameter that needs to be mentioned is the so-called C–rate. It describes the charging or discharging current relative to its capacity and has the dimension A (amps). A 1 C-rate means that the battery is fully charged or discharged in one hour. For example, to charge a battery with a capacity of 20 Ah in one hour, a current of 20 A must be applied. Higher C-rates result in higher currents and hence, in shorter charge/discharge times [29].

5.3 Impedance spectroscopy

Impedance spectroscopy is a sensitive, versatile and powerful method for the study of ion dynamics in solid-state matters. It allows the determination of some important parameters such as the impedance (Z), the dielectric permittivity (ε) and the ionic conductivity (σ) at different temperatures as a function of the frequency. These data also provide useful information about activation energies, long- as well as short-range ion transport mechanisms and the contribution of grain boundary or bulk diffusion to the overall conductivity.

In an impedance measurement, the investigated sample material in form of a cylindrical pressed pellet is placed between two identical electrodes. An alternating voltage signal over a wide frequency range is then applied to this system under investigation and the current response is recorded, *cf.* Fig. 17 (a) for an experimental set-up. With modern impedance spectrometers, frequencies in the range of a few mHz up to several GHz are accessible. The following section should provide an insight into the basic principles of this method. For a more detailed description of impedance spectroscopy, the reader is referred to the books of Lvovich [200] and Barsoukov [201].

Basic concept of impedance

To measure the electrochemical impedance of a cell, a sinusoidal alternating voltage V with a frequency $\upsilon = \omega/2\pi$ and an amplitude V_0 is applied. This time-dependent voltage signal $V(t)$ has the general form:

$$V(\mathrm{t}) = V_0 \sin(\omega t)\,. \tag{5.2}$$

Since, typically, a small voltage amplitude is used, a linear response of the system is obtained resulting in an output current signal $I(t)$ that is also sinusoidal with the same frequency, but phase shifted (φ) with a different amplitude (I_0):

$$I(\mathrm{t}) = I_0 \sin(\omega t + \varphi)\,. \tag{5.3}$$

Fig. 17 (b) represents the sinusoidal voltage input V and the resulting current output I as a function of the time [200].

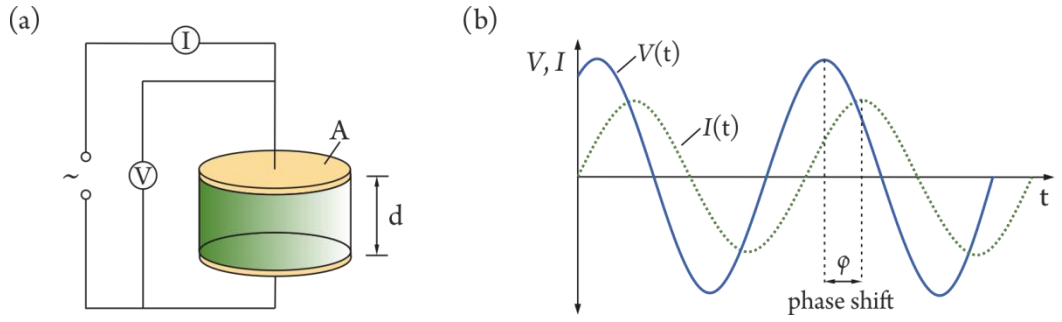

Fig. 17 **(a)** Principle of a complex impedance measurement. The material in form of a cylindrical pressed pellet with an area A and a thickness d is placed between two identical electrodes. An alternating voltage signal is applied and the current response recorded. **(b)** Sinusoidal voltage input V and current output I signal shown as a function of time.

In analogy to the resistance $R = V/I$, the impedance can also be expressed as ratio between voltage signal $V(t)$ and current response $I(t)$ according to Ohm's law, thus giving

$$Z = \frac{V(t)}{I(t)} = \frac{V_0 \sin(\omega t)}{I_0 \sin(\omega t + \varphi)} = |Z| \frac{\sin(\omega t)}{\sin(\omega t + \varphi)} \tag{5.4}$$

with $|Z|$ being the absolute value of $Z_0 = V_0/I_0$. By using Euler's formula $\exp(i\varphi) = \cos\varphi + i\sin\varphi$, it is possible to represent the impedance as a complex function. For this purpose, both quantities $V(t)$ and $I(t)$ have to be expressed in the complex domain. Eq. (5.2) and Eq. (5.3) are therefore rewritten as:

$$V^*(t) = V_0 \exp(i\omega t) \tag{5.5}$$

$$I^*(t) = I_0 \exp(i\omega t - i\varphi)\,. \tag{5.6}$$

The complex impedance is then given by

$$Z^* = \frac{V^*(t)}{I^*(t)} = |Z^*| \exp(i\varphi) = |Z^*| (\cos\varphi + i\sin\varphi) = Z' + iZ'', \tag{5.7}$$

where $Z'' = |Z^*| \cos(\varphi)$ denotes the real part and $Z'' = |Z^*| \sin(\varphi)$ the imaginary part [200]. The impedance can be considered as a vector quantity and can therefore be plotted in the complex plane using polar $(|Z|, \varphi)$ and rectangular (Z', Z'') coordinates as indicated in Fig. 18. From this figure it is evident that $|Z| = [(Z')^2 + (Z'')^2]^{1/2}$ represents the length of the vector, while the phase angle $\varphi = \arctan(Z''/Z')$ at a specific radial frequency ω is determined by the ratio of the imaginary and real impedance terms [201].

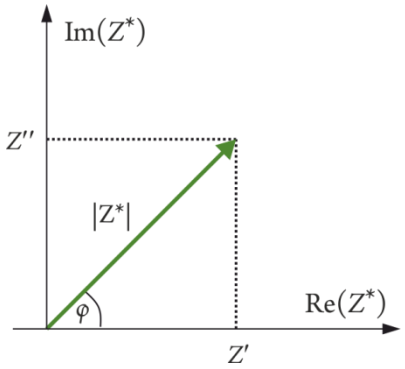

Fig. 18 Complex plane plot, where the impedance Z^* is plotted as a vector in the plane using polar $(|Z|, \varphi)$ and rectangular (Z', Z'') coordinates.

Other important complex quantities related to impedance, are the so-called admittance Y^*, the modulus function M^* and the dielectric permittivity ε^*. The admittance corresponds to the reciprocal value of the impedance and can be expressed as:

$$Y^* = |Y^*| \exp(-i\varphi) = |Y^*| (\cos(\varphi) - i\sin(\varphi)) = Y' + iY''. \tag{5.8}$$

The modulus function and the dielectric permittivity are defined as

$$M^* = M' + iM'' = i\omega C_0 Z^* \tag{5.9}$$

and

$$\varepsilon^* = \varepsilon' - i\varepsilon'' = M^{*-1} = \frac{Y^*}{i\omega C_0} \tag{5.10}$$

with $C_0 = \varepsilon_0 A/d$, where C_0 denotes the capacitance of the cell without a sample, ε_0 the vacuum permittivity (8.85×10^{-12} F/m), A the electrode area and d the distance between the two electrodes [201]. Further details on these three functions, also known as immittances, can be found in references [201, 202].

Talking about diffusion, one of the most important quantities derived from impedance spectroscopy is the conductivity. The complex conductivity σ is defined as the inverse of the specific complex impedance $Z_s^* = Z^* \cdot A/d$, which depends on the geometry of the measured sample, thus giving

$$\sigma^* = \frac{1}{Z_s^*} = Y^* \cdot \frac{d}{A} \tag{5.11}$$

and consists of a real part σ' and an imaginary part σ''

$$\sigma = \sigma' + i\sigma''. \tag{5.12}$$

Interpretation of the data

In most cases it is not possible to represent the electrochemical processes and phenomena that take place in an investigated system by a simple ideal capacitor or resistor. As seen from Eq. (5.7) the impedance consists of a real and an imaginary part, where the real impedance term describes the ability to resist an electrical current flow, while the imaginary impedance compound demonstrates the ability to store electrical energy. Thus, electrical equivalent circuits combining both capacitive and resistive elements provide a good way to approximate the experimental impedance data [200]. These electrical circuits usually consist of ideal capacitors, resistors, sometimes inductances and various other circuit elements, which are connected either in series or in parallel. In such an idealized model concept, a resistor, for example, could describe the conductive path either along grain boundaries or within the bulk material, while a capacitor could represent a space charge polarization region across a grain boundary or adsorption and desorption processes at the electrode surface [201].

A common graphical representation of the complex impedance data is the so-called Nyquist plot, where the negative imaginary impedance part is plotted versus the real impedance part. As illustrated in Fig. 19 the resulting graph is semi-circular in shape. It is important to note, that each point on this plot corresponds to the impedance at a certain frequency and that the value of the frequency increases from the right to the left side. This semicircle can be modeled by a simple circuit consisting of a capacitor connected in parallel to a resistor as shown in the inset of Fig. 19. In the high-frequency range the impedance shows completely capacitive behavior, while it becomes completely resistive at low frequency approaching the value of R, which is equal to the diameter of the semicircle in the Nyquist plot [200]. The RC element is often associated with the time constant τ and can be expressed as

$$\tau = RC. \tag{5.13}$$

Since the value for the time constant is usually very small in impedance measurements, the condition

$$\omega_{max}\tau = 1 \tag{5.14}$$

is satisfied at the highest applied angular frequency ω_{max}. The combination of Eq. (5.13) and (5.14) then results in

$$\omega_{max}RC = 1. \tag{5.15}$$

Using this relation the capacitance C of the corresponding underlying process can be determined. Both parameters, ω_{max} and R, can be estimated from the Nyquist plot. While ω_{max} can be calculated from the frequency at the top of the semicircle with $\omega_{max} = \nu 2\pi$, R results from the intersection of the semicircle with the x-axis [201]. Generally, grain boundary diffusion exhibits higher capacitance values than diffusion in the bulk as described by West *et al.* [203].
If different diffusion processes are present, multiple arcs can show up in the Nyquist plot as indicated by dotted lines in Fig. 19. The use of ion blocking electrodes, which inhibit the transfer of the ions into the external circuit, usually results in an inclined line in the low-frequency range of the Nyquist plot [200].

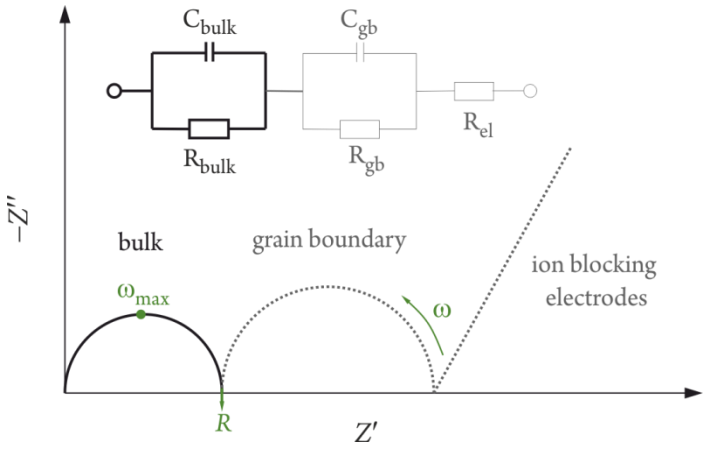

Fig. 19 Nyquist plot and corresponding equivalent circuit. See text for further details.

As already discussed in detail in chapter 4, diffusion in a crystalline solid occurs by hopping of the mobile ions between adjacent stable sites. Information about this ionic motion can be obtained from conductivity measurements, since the time-dependent hopping characteristics of the mobile ions are directly related to the frequency-dependent properties of the ionic conductivity. In Fig. 20 (a) and (b) the real parts of the ionic conductivity σ' and the dielectric permittivity ε' measured at different temperatures are plotted as a function of the applied

frequency ν using a double logarithmic scale. These isotherms can be subdivided into three regimes as outlined below [204].

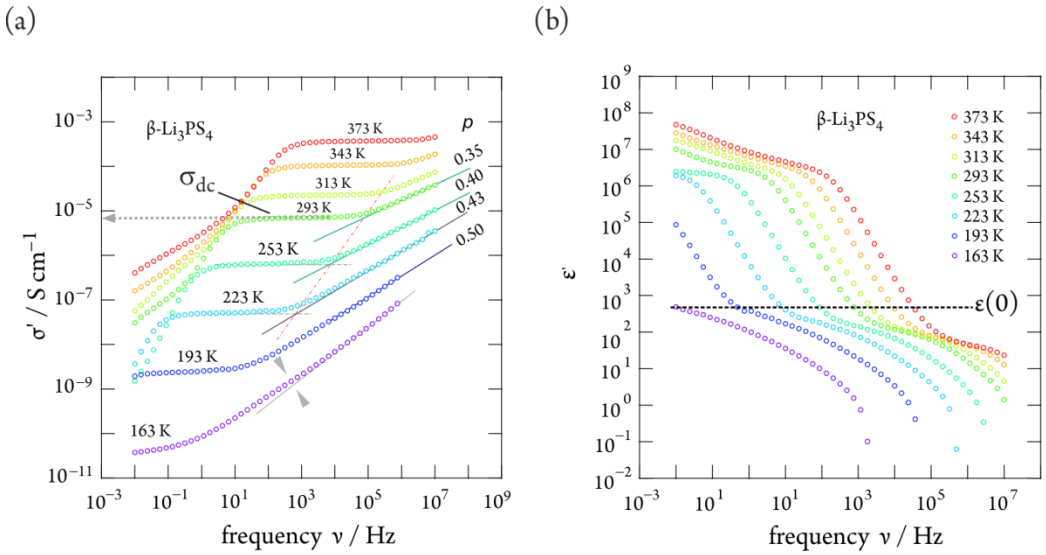

Fig. 20 Selected **(a)** conductivity and **(b)** permittivity spectra of β–Li_3PS_4 exemplifying the characteristic regimes found nearly universally in impedance spectroscopy. Data are taken from the manuscript "Nuclear spin relaxation in nanocrystalline β–Li_3PS_4 reveals low-dimensional Li diffusion in an isotropic matrix". (See p. 183).

At lower frequencies and higher temperatures polarization effects appear due to the use of ion-blocking electrodes. This phenomenon, also known as electrode polarization, is caused by the accumulation of ions at the interface of the electrode. The resulting space charge hampers further ion transport to the electrode and leads to a drop off of the conductivity. In contrast, the dielectric permittivity sharply increases owing to this large bulk polarization. At higher frequencies the conductivity isotherms merge into distinct, frequency independent plateaus, the so-called dc-conductivity plateaus with $\sigma_{dc} = \sigma'(0)$, which reflect the long-range ion diffusion across the material [204]. These distinct plateaus are shifted to higher frequencies with increasing temperature. Their temperature dependence usually shows Arrhenius behavior according to $\sigma_{dc}T \propto (-E_A/k_BT)$ with T the temperature, k_B the Boltzmann's constant and E_A the activation energy. Thus, a logarithmic plot of the product of the σ_{dc} values, read off from the dc plateaus, and the temperature versus the reciprocal of the temperature allows the determination of the average activation energy describing the long-range ion transport. Sometimes a second plateau can show up towards higher frequencies, if different ion transport processes (such as grain boundary and bulk diffusion) are present. The permittivity isotherms feature a shoulder at frequencies similar to those of the σ_{dc} plateaus reflecting dipole moment changes, which occur

during the hopping process of the ions [204]. From this shoulder ε' can be determined that allows the estimation of the electrical capacitance C of the material using the equation of a parallel-plate capacitor, $C = \varepsilon'\varepsilon_0(A/d)$ with ε_0 the vacuum permittivity (8.85×10^{-12} F/m), A the electrode area and d the distance between the two electrodes [200]. In the high-frequency range the dc conductivity plateaus pass into a dispersive regime. There, the conductivity increase with the frequency according to Jonscher's power law $\sigma' = \sigma_{dc} + A\nu^p$, where the exponent p defines the slope of the conductivity values in the dispersive part. The magnitude of this exponent provides information about the dimensionality of the underlying diffusion process and approaches the value of 1 with decreasing temperature [205]. By contrast, the dielectric permittivity further decreases, since the matrix atoms are elastically polarized in this frequency range [204]. The origin of this dispersive region is due to the non-ideal behavior of crystalline solids leading to correlation effects that contribute to the frequency dependence of σ' [206].

The ionic dc-conductivity σ_{dc} obtained from impedance measurements can be related to the diffusion coefficient using the Nernst-Einstein equation

$$D^{\sigma} = \frac{\sigma_{dc} \cdot k_B T}{n \cdot q^2}, \tag{5.16}$$

where q denotes the ion charge, n the charge density, T the temperature and k_B the Boltzmann's constant. D^{σ} represents the charge diffusion coefficient [153].

5.4 Nuclear magnetic resonance (NMR) spectroscopy

Solid-state nuclear magnetic resonance spectroscopy, especially NMR spin-lattice relaxometry (SLR) is a versatile and powerful method for the investigation of ion dynamic properties in solids on different length-scales. It provides information about both, short-range/local and long-range ion transport and helps to understand the relationship between dynamic parameters and local structures. Besides the determination of some relevant diffusion-induced parameters, such as jump rates (τ^{-1}) and activation energies (E_A), it is also possible to draw conclusions regarding the diffusion pathways (dimensionality) through the crystal lattice [23].

In short, this technique is based on the interaction of an atomic nucleus with a magnetic field. In the following section, the theoretical basics of NMR are briefly explained using the classical vector model. Furthermore, the spin-lattice relaxometry technique is presented in more detail and the extraction of the most relevant parameters from these measurements is outlined. For more detailed information on the fundamentals of solid-state NMR and the different techniques, I would recommend the books of M. Levitt [207], H. Friebolin [208] and J. Keeler [209].

5.4.1 Basics of NMR

The physical phenomenon of nuclear magnetic resonance can be observed for nuclei that possess a non-zero nuclear spin angular momentum and hence a magnetic dipolar moment [209]. The spin angular momentum, also often referred to as nuclear spin, is an intrinsic property of the atomic nucleus itself, like its charge or mass, and can be considered as the quantum-mechanical analogue to the classical angular momentum [207]. It is a vector quantity described by a direction and a magnitude and takes the inner rotational motion of the spherical nucleus about an axis into account [209]. For reasons of clearness vector quantities are indicated by bold letters in the following discussion. Like other atomic quantities, the *nuclear spin angular momentum* $\boldsymbol{I}$ is quantized and the absolute value of $\boldsymbol{I}$ is given by

$$|\boldsymbol{I}| = \sqrt{I(I+1)}\hbar\,, \tag{5.17}$$

where I represents the *spin quantum number*, which takes integer or half-integer values $I = 0, 1/2, 1, 3/2, 2, \ldots$ and $\hbar$ is the reduced Plank's constant with $\hbar = h/2\pi$ [207, 208].

Closely linked to this spin angular momentum $\boldsymbol{I}$ is the magnetic moment $\boldsymbol{\mu}$, which can be calculated from the product of the proportionality factor γ and $\boldsymbol{I}$:

$$\boldsymbol{\mu} = \gamma \cdot \boldsymbol{I}\,. \tag{5.18}$$

γ is the so-called *gyromagnetic ratio* and its value varies by each atomic species and may have either sign. Nuclides with a large γ show high detection sensitivity, while those with a small value

of γ are not easy to detect. From Eq. (5.17) and (5.18) it is clear that nuclei with $I = 0$ do not possess a nuclear magnetic moment and can therefore not be observed by NMR spectroscopy [208].

When an atomic nucleus with $I \neq 0$ is placed in an external magnetic field $\boldsymbol{B}_0$ (as we do for NMR measurements), interaction between this applied field and the nuclear magnetic moment $\boldsymbol{\mu}$ occurs. While the magnetic moments are randomly oriented in equilibrium, they now start to align in the direction of $\boldsymbol{B}_0$. As a result, $\boldsymbol{\mu}$ rotates around the magnetic field on a cone [209]. The frequency of this precession, also known as Larmor frequency is proportional to the magnetic field strength $\boldsymbol{B}_0$:

$$\boldsymbol{\omega}_0 = -\gamma \cdot \boldsymbol{B}_0 \,. \tag{5.19}$$

Nuclei with a positive value of γ precess clockwise around the magnetic field, while for nuclei with a negative gyromagnetic value the direction of the precession is anticlockwise [207].

Assuming that the orientation of the static magnetic field is along the z-axis, the component I_z of the nuclear spin angular momentum $\boldsymbol{I}$ can be described by

$$I_z = m_I \hbar \tag{5.20}$$

with m_I representing the magnetic quantum number, which can take values $m_I = I, I-1, \ldots..-I$. Now Eq. (5.18) can be rewritten as:

$$\mu_z = \gamma m_I \hbar \tag{5.21}$$

Quantum mechanics tell us that the magnetic quantum number m can have $(2I + 1)$ different values. Consequently, $(2I + 1)$ possible orientations for I_z and μ_z exist [208]. If no external field is applied, these nuclear states are degenerated, meaning they are of equal energy. But, in the presence of $\boldsymbol{B}_0$ splitting of these nuclear levels occurs resulting in slightly different energy for each sublevel. This effect of energy separation is known as *Zeeman splitting* [207]. The energy states (Zeeman levels) that the magnetic moments can take in the applied field can be expressed as

$$E_{Z,m} = -\mu_z \cdot B_0 = -\gamma m_I \hbar B_0 \,. \tag{5.22}$$

Here, the negative sign indicates that the energy is lowest, when the magnetic dipoles are aligned parallel to the field (positive m-values). These energy states are spaced equally and the energy difference ΔE between two adjacent levels can be calculated as

$$\Delta E = \hbar |\gamma| B_0 \,. \tag{5.23}$$

Let us consider, for example, an atomic nucleus with $I = 3/2$ such as ^{7}Li. There are four different values of m (+3/2, +1/2, −1/2 and −3/2) resulting in four possible orientations of I_z. Accordingly, an equal number of equidistant energy states can be found in the magnetic field as schematically illustrated in Fig. 21 [208].

At thermal equilibrium the occupation probability of these energy levels follows a Boltzmann distribution and depends on the temperature. The population N_m of an energy state with a certain spin quantum number m can therefore be expressed as

$$N_m = \frac{1}{Z} \exp\left(-\frac{E_{Z,m}}{k_B T}\right) \tag{5.24}$$

with $Z=\Sigma_{m'} \exp(-E_{Z,m'}/k_B T)$. By irradiating the nuclei with an electromagnetic wave of appropriate frequency ω, transition from one energy level to another can take place. However, according to the selection rule $\Delta m = \pm 1$, transitions are only allowed between adjacent energy states. Thus, the relative population $N_{m(2)}/N_{m(1)}$ of these two energy levels which allow transition depend on their energy difference and is given by

$$\frac{N_{m(2)}}{N_{m(1)}} = \exp\left(\frac{E_{Z,m(1)} - E_{Z,m(2)}}{k_B T}\right) = \exp\left(\frac{-\gamma \hbar \boldsymbol{B}_0}{k_B T}\right). \tag{5.25}$$

The occupation of these two energy states is almost the same. Only a small excess is present in the lower energy level [208, 209]. The required energy $\Delta E = \hbar\omega$ to observe transition, can be derived from Eq. (5.17) and (5.23). The resonance condition follows as

$$\Delta E = \hbar|\gamma|B_0 = \hbar\omega_0 = h\omega \tag{5.26}$$

It can be seen that transition only takes place when the frequency ω of the irradiated electromagnetic wave matches the Larmor frequency ω_0 [208].

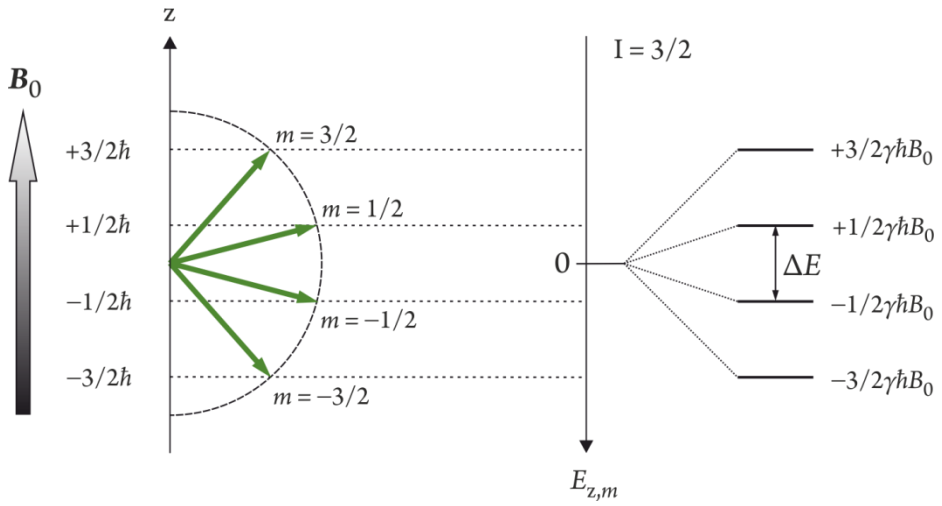

Fig. 21 Zeeman splitting for an atomic nucleus with $I = 3/2$ such as ^{7}Li, when placed in an external static magnetic field $\boldsymbol{B}_0$. Four different values of the spin quantum number m and thus four possible orientations for I_z can be found. Accordingly, an equal number of equidistant energy levels show up. Adapted from reference [208].

As already mentioned above, in the absence of an external applied field, the magnetic dipolar moments of the atomic nuclei are randomly oriented, since all orientations are of equal energy. When the sample is now placed in a static magnetic field, there is an energetic advantage for the magnetic dipoles to be aligned parallel to the applied field. As a result the NMR sample as a whole becomes magnetized and a macroscopic net magnetization in the direction of the magnetic field is obtained. This macroscopic magnetization $\boldsymbol{M}$ is measured during an NMR experiment and can be described as the sum over all individual magnetic moments $\boldsymbol{\mu}$ in a sample with the volume V.

$$\mathbf{M} = \frac{1}{\mathrm{V}} \sum_{\mathrm{i}=1}^{\mathrm{N}} \boldsymbol{\mu}_{\mathrm{i}} \tag{5.27}$$

At thermal equilibrium, where $\boldsymbol{M} = \boldsymbol{M}_0$, the magnetization vector is composed of the z-components of the magnetic dipoles $\boldsymbol{\mu}_i$ so that $M_z = M_0$ and $M_x = M_y = 0$. According to the classical representation the magnetization $\boldsymbol{M}_0$ precess around the field $\boldsymbol{B}_0$ in the z-direction as shown in Fig. 22 [209].

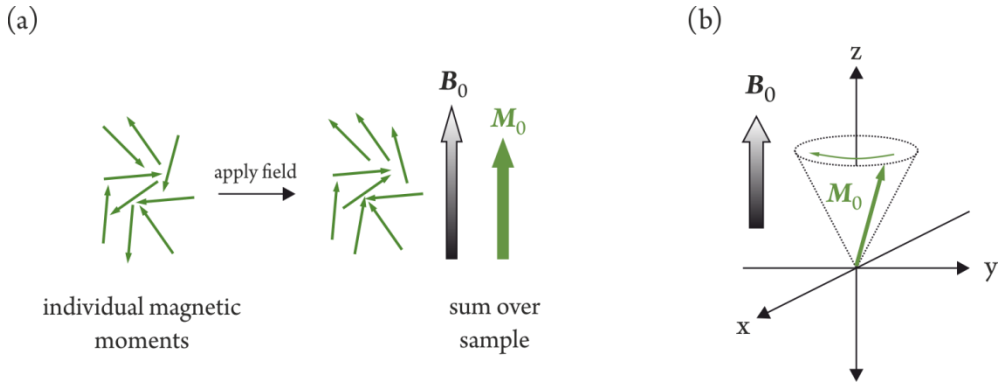

Fig. 22 **(a)** In the absence of an external magnetic field, the individual magnetic moments are randomly oriented. When the sample is now placed in a static magnetic field $\boldsymbol{B}_0$ the dipoles start to align along this field. As a consequence, a macroscopic net magnetization $\boldsymbol{M}_0$ directed along the magnetic field is obtained. **(b)** Precession of $\boldsymbol{M}_0$ around the field $\boldsymbol{B}_0$ at thermal equilibrium. (Adopted from reference [205]).

This equilibrium net magnetization can be perturbed by applying a radiofrequency (RF) pulse to the sample, which is usually generated by a small RF coil placed perpendicular to the static magnetic field $\boldsymbol{B}_0$. The resulting magnetic field $\boldsymbol{B}_1$ of the RF pulse along the x-direction oscillates linearly with the angular frequency ω and can be expressed as the sum of two counter-rotating fields, one of which rotates clockwise, the other one anticlockwise around the z-axis. However, only the field component, that rotates in the same direction as the precessing magnetization can interact with the magnetic dipoles. For further discussion, only this resonant contribution is considered and called $\boldsymbol{B}_1$. To simplify the description, how the applied field affects the magnetization $\boldsymbol{M}_0$, we change from the stationary (laboratory frame) x, y, z to a *rotating coordinate system* (rotating frame) x', y', z that rotates around the static magnetic field $\boldsymbol{B}_0$ in the same direction and with the same frequency as $\boldsymbol{B}_1$. As a consequence, $\boldsymbol{B}_1$ appears to be stationary on the rotating x'-axis [208, 209].
If the resonance condition $\omega = \omega_0$ is now fulfilled, the magnetization vector $\boldsymbol{M}_0$ is rotated from its equilibrium position in the y', z-plane by an angle θ. This so-called pulse or flip angle is given by

$$\theta = \omega_1 \tau_p = \gamma \boldsymbol{B}_1 \tau_p \tag{5.28}$$

with ω_1 denoting the precession frequency of the magnetization vector in the y', z-plane and τ_p the pulse length. Thus, an increase in the duration of the applied pulse leads to an increase of the angle through which the magnetization vector has been rotated [208, 209].

Most of the pulse techniques used are based on pulse angles of 90° = $\pi/2$ and 180° = π. In the case of a $\pi/2$ on-resonance pulse, the macroscopic net magnetization is rotated to the y'-axis, thus $M = M_{y'}$ and $M_z = 0$. On the contrary, after a 180° pulse, the initial magnetization is inverted and ends up along the $-z$-direction. Fig. 23 graphically illustrates the direction of the magnetization vector after a 90° and 180° pulse. Since the receiver coil, the same coil that generates the RF pulse, can be found in the x, y-plane, the transverse magnetization $M_{y'}$ plays an important role for the detection of an NMR signal. This transverse component induces an oscillating electric current in the electromagnetic coil, which can be amplified and then recorded to give the free induction decay (FID) [209]. From Fig. 23 it is obvious that this signal reaches its maximum value immediately after a 90° ($\pi/2$) pulse, whereas no signal can be detected for a 180° (π) pulse [208].

The rotation of the magnetization vector $\boldsymbol{M}_0$ from its equilibrium position as a result of the applied RF pulse also involves a manipulation of the population of the two energy states that allow transition. While both energy levels are equally populated following a 90°-pulse, a 180° on-resonance pulse leads to an inversion of the occupation [208].

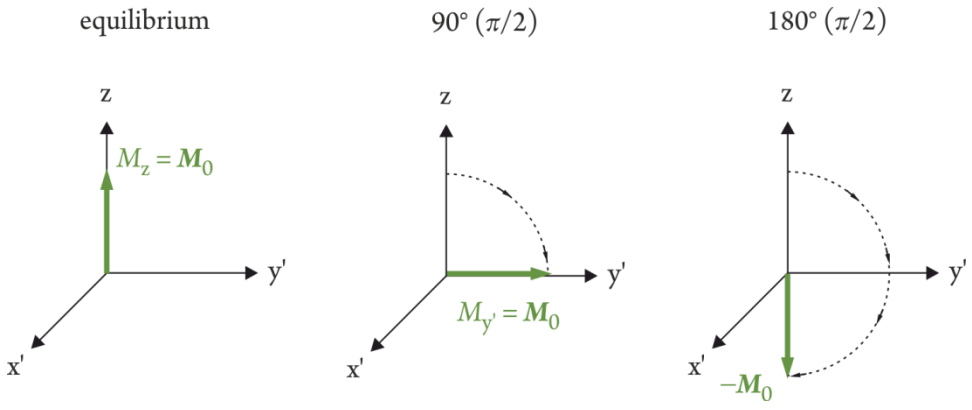

Fig. 23 Direction of the magnetization vector at thermal equilibrium and after a 90° ($\pi/2$) and 180° (π) on-resonance pulse, respectively. The radiofrequency (RF) pulse, which is used to perturb the equilibrium net magnetization, is generated by a small RF coil perpendicular to the static magnetic field $\mathbf{B}_0$. Thus, the resulting magnetic field $\mathbf{B}_1$ is directed along the x'-axis.

5.4.2 Relaxation

As already mentioned in the previous section, the population ratio of the energy states and thus the equilibrium magnetization can be manipulated by an appropriate radiofrequency-pulse. After switching off this additional RF field the system will immediately return to its equilibrium state by processes known as *relaxation* with the longitudinal magnetization M_z approaching its initial value $\boldsymbol{M}_0$, while the transverse magnetization $M_{x'}$ or $M_{y'}$ decays toward zero. Two different types of relaxation processes can be distinguished: the *spin-lattice* or *longitudinal relaxation*, which occurs with the time constant T_1 and the *spin-spin relaxation*, also known as *transverse relaxation*, characterized by the time constant T_2. The variation of the magnetization components $M_{x'}$, $M_{y'}$ and M_z with time during relaxation can be described by the Bloch equations

$$\frac{\mathrm{d}M_z}{\mathrm{d}t} = -\frac{M_z - M_0}{T_1} \tag{5.29}$$

$$\frac{\mathrm{d}M_{x'}}{\mathrm{d}t} = -\frac{M_{x'}}{T_2} \quad \text{and} \quad \frac{\mathrm{d}M_{y'}}{\mathrm{d}t} = -\frac{M_{y'}}{T_2} \tag{5.30}$$

From these differential equations it is obvious that the time constant T_1 denotes relaxation in the direction of the static magnetic field $\boldsymbol{B}_0$, while T_2 describes relaxation of the transverse magnetization components in the $x'y'$-plane [208]. The reciprocal values of the time constants $R_1 = 1/T_1$ and $R_2 = 1/T_2$ represent the rate constants, which determine the rates at which the equilibrium state is approached [209]. Since the spin-lattice relaxation process forms the basis for the pulse experiment used to characterize the materials described in the present work, it will be treated in more detail in the following discussion.

Spin-lattice relaxation (SLR) always involves energy transfer from the spin system to the surrounding lattice leading to the restoration of the Boltzmann equilibrium. The energy absorbed during the RF-pulse is released by a depopulation of the higher energy states. These nuclear spin transitions are mediated by fluctuating magnetic fields of an appropriate frequency caused by ionic or molecular motion [208]. As a result, the longitudinal component M_z of the magnetization vector regrows to its thermal equilibrium value $\boldsymbol{M}_0$. The recovery of M_z as a function of time can be expressed as:

$$M_z(t) = \boldsymbol{M}_0 \left(1 - \exp\left(-\frac{t}{T_1}\right)\right) \tag{5.31}$$

Thus, the greater the value of T_1 (or of the rate constant), the faster the magnetization along the z-axis approaches its equilibrium position [209]. Fig. 24 shows the temporal evolution of the

longitudinal component M_z following a 90° on-resonance pulse. $M_z(t)$ is initially zero, but recovers exponentially to its thermal equilibrium value $\boldsymbol{M}_0$.

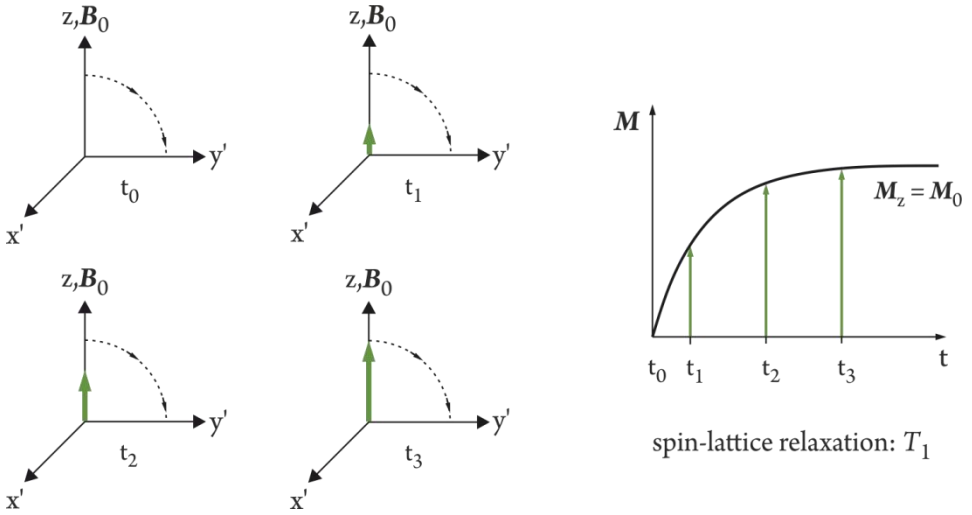

Fig. 24 Temporal evolution of the longitudinal magnetization component M_z after a 90° pulse. M_z is initially zero, but regrows exponentially to its thermal equilibrium value $\mathbf{M}_0$ according to Eq. (5.31).

Another important time constant apart from T_1 and T_2 that needs to be mentioned is $T_{1\rho}$, the so-called *spin-lattice relaxation time constant in the rotating frame*. However, this notation is unfortunate, since this relaxation time is more related to the spin-spin lattice time constant T_2, which describes the decay of the transverse magnetization component $M_{y'}$ in the static magnetic field $\boldsymbol{B}_0$. Additionally, no energy transfer to the lattice is required for $T_{1\rho}$. The $T_{1\rho}$ process is based on spin locking and allows the investigation of slow molecular dynamics, since transitions between smaller Zeeman levels can be measured [207]. Let us start with a 90° pulse that rotates the magnetization vector M_z to the y'-axis in the rotating coordinate system. Normally, after switching off the RF-pulse, the spin system relaxes according to the time constants T_1 and T_2. But, if immediately after the 90° pulse, a RF field is applied along the y'-direction, the transverse magnetization vector $M_{y'}$ becomes locked along the y'-axis [208]. The strength of this magnetic field $B_{1y'}$ is rather low (in the range of some mT) and thus gives rise to a much smaller Zeeman splitting compared to that of the external magnetic field $\boldsymbol{B}_0$. After turning-off the spin-lock field, the spin system relaxes towards the new equilibrium state by transitions between the Zeeman levels defined by the spin-locking field $B_{1y'}$, which shows a much lower y'-magnetization [210]. Consequently, the magnetization component $M_{y'}$ decays exponentially towards zero with the

time constant $T_{1\rho}$ [207], but with a much smaller equilibrium amplitude [23]. The spin-lock process is schematically illustrated in Fig. 25.

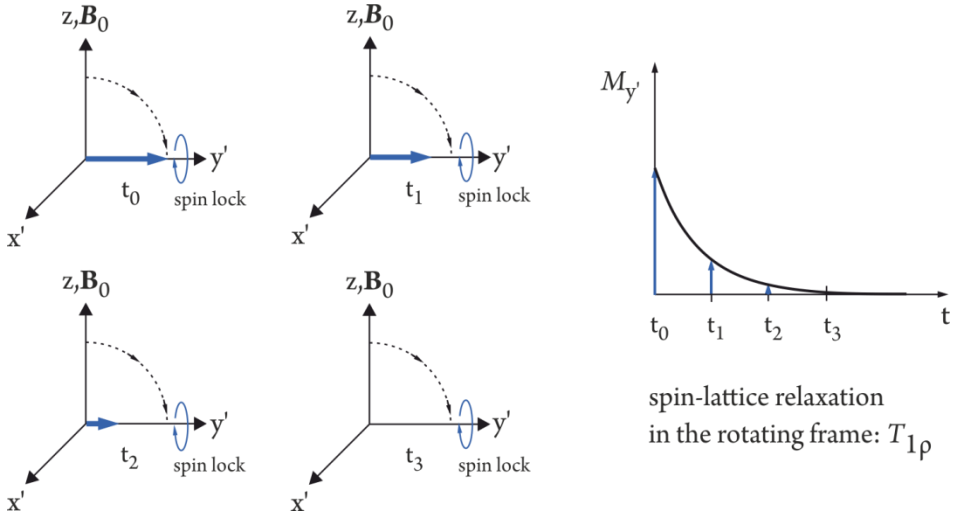

Fig. 25 Evolution of the transversal magnetization component $M_{y'}$ after applying a spin-lock field $B_{1y'}$ and the corresponding FID. The component $M_{y'}$ decays exponentially towards zero with the time constant $T_{1\rho}$.

Techniques to measure R_1 and $R_{1\rho}$

The spin-lattice relaxation rate R_1 can be estimated by using the saturation recovery experiment, whose pulse sequence [n x 90° – t_d – 90° – FID] is graphically depicted in Fig. 26 (a). Here, the initial n closely spaced 90° pulses destroy the longitudinal equilibrium magnetization ($M_z = \boldsymbol{M}_0$) so that M_z gets zero at $t = 0$. After a variable relaxation delay time t = t_d, a single 90° pulse is applied to probe the subsequent recovery of $M_z(t)$, which is then monitored as a function of t_d. The rate constant R_1 is obtained by parameterizing the magnetic transient $M_z(t_d)$ with stretched exponentials [211].

The rotating- frame NMR rate constant $R_{1\rho}$ is determined by the following pulse sequence (see Fig. 26 (b)), which makes use of the spin-lock technique: immediately after the 90° RF-pulse, the magnetization vector $\boldsymbol{M}$ pointing along the y'-direction is locked by a rather low magnetic $B_{1y'}$ field [211]. The decay of the transverse magnetization $M_{\rho y'}$ is then monitored as a function of the variable locking pulse length t_{lock}. No additional detection pulse is required as in the case of R_1, since the residual transverse magnetization component $M_{y'}$, which shows up after the applied spin-lock pulse, directly give the FID [210].

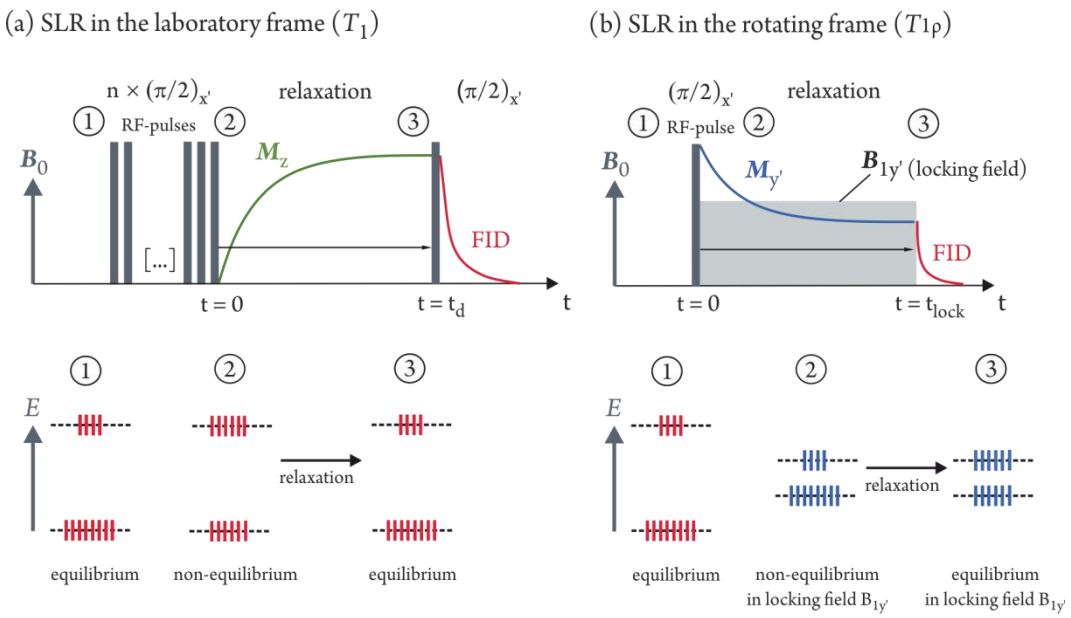

Fig. 26 **(a)** Saturation recovery pulse sequence used to estimate the spin-lattice relaxation rate R_1. **(b)** Spin-lock pulse sequence for the determination of the rotating-frame NMR rate constant $R_{1\rho}$. The lower part of this figure graphically illustrates the population of the Zeeman levels in the course of the NMR experiment.

Data interpretation

As discussed above, magnetic fluctuations of internal fields caused by ionic motions are responsible for the relaxation process, since they can induce Zeeman transitions, if their frequency contribution is in the order of the Larmor frequency. These temporal fluctuations can be described using an autocorrelation function. For random diffusive motion in three-dimensions, they can be well characterized with the so-called BPP-model proposed by Bloembergen, Purcell and Pound [212], which takes the assumption, that the corresponding correlation function $G(t)$ is single exponential and decays with the correlation time τ_c according to:

$$G(t) = G(0) \exp -\frac{|t|}{\tau_c}. \tag{5.32}$$

The correlation time specifies the mean period of time between transition inducing fluctuations and is hence, directly related to the mean residence time τ of a diffusing particle between two successive hops [23]. Its temperature dependence shows Arrhenius behavior and can be described by

$$\tau_c^{-1} = \tau_{c0}^{-1} \exp\left(-\frac{E_A}{k_B T}\right), \tag{5.33}$$

where its reciprocal value τ_c^{-1} represents the correlation rate, which equals the jump rate τ^{-1} governing the hopping process. τ_{c0}^{-1} denotes the pre-exponential factor, E_A the activation energy the diffusing species has to overcome and k_B the Boltzmann constant [210].

Fourier transformation of the exponential time-dependent correlation function $G(t)$ of Eq. (5.32) yields the Lorentzian-shaped spectral density function $J(\omega)$, which is direct proportional to the spin-lattice relaxation rate R_1

$$\frac{1}{T_1} = R_1 \propto J(\omega) = G(0)\frac{2\tau_c}{1+(\omega\tau_c)^2}. \tag{5.34}$$

It is worth noting that the spectral density $J(\omega)$ is dependent on the correlation time τ_c, which in turn is reliant on the temperature. Most importantly, relaxation can occur, when $J(\omega)$ has contributions at the resonant frequency ω_0 (usually in the MHz regime) [23]. Eq. (5.34) can therefore be rewritten as

$$\frac{1}{T_1} = R_1 \propto J(\omega_0) = G(0)\frac{2\tau_c}{1+(\omega_0\tau_c)^2}. \tag{5.35}$$

Accordingly, for a specified Larmor frequency ω_0, the diffusion-induced relaxation constant R_1 initially increases with the temperature then passes through a maximum value at a definite temperature T_{max} and finally decreases again at even higher temperatures. As a result, a symmetric diffusion-induced relaxation rate peak with two distinct flanks on either side of the peak maximum can be observed as graphically illustrated in Fig. 27 (a), where the logarithm of R_1 is plotted versus the inverse temperature. At the rate peak maximum ($T = T_{max}$) the correlation rate equals the Larmor frequency ω_0 according to

$$\omega_0\tau_c \approx 1. \tag{5.36}$$

Due to the relation $\tau_c^{-1} = \tau^{-1}$, it is possible to determine the jump rate from this maximum condition. At lower temperatures ($T < T_{max}$), in the so-called low-temperature limit, we can observe the following proportionality:

$$R_1 \propto \tau_c^{-1}\omega_0^{-2} \text{ for } \omega_0\tau_c \gg 1. \tag{5.37}$$

In this regime the SLR rates exhibit a quadratic frequency dependence, which is also indicated in Fig. 27 (b), where the relaxation rate peaks are demonstrated for three different frequencies $\omega_0(\mathrm{I}) > \omega_0(\mathrm{II}) > \omega_0(\mathrm{III})$. It can be seen that the peak maximum is shifted to higher rates and lower temperatures with lower Larmor frequencies ω_0. This LT-flank is sensitive to short-range diffusion and thus provides information about local diffusive motion. At higher temperatures ($T > T_{\mathrm{max}}$), in the high-temperature limit, the SLR rates become independent of the resonance frequency given by

$$R_1 \propto \tau_c \text{ for } \omega_0\tau_c \ll 1\,. \tag{5.38}$$

This HT-flank is characteristic for long-range ion dynamics in the observed material. From the slope of this LT- and HT-flank, it is possible to determine the activation energy E_A of the diffusion process [213].

It can be noted that spin-lattice relaxation measurements allows the determination of jump processes in the order of the resonance frequency $\omega_0 = 10^9\ \mathrm{s}^{-1}$. On the contrary, slower diffusion processes can be probed with the help of the spin-lock technique, where the relaxation rates $R_{1\rho}$ are sensitive to ionic jump rates in the range of the locking field $\omega_1 = 10^5\ \mathrm{s}^{-1}$ [210]. The corresponding relaxation rate peaks show the same behavior as in the case of the laboratory frame described above with the maximum condition being fulfilled at $\omega_0\tau_c = 0.5$ (see Fig. 27). Due to the lower applied locking frequency ω_1 compared to ω_0, the rate peak maxima are shifted towards lower temperatures [213].

However, quite often, experimental data shows deviations from the ideal uncorrelated BPP behavior and asymmetric SLR rate peaks showing a smaller slope of the LT-flank compared to the HT-flank are observed. This is the case in structurally disordered materials, *e.g.* glasses, where the mobile ions are exposed to a heterogenous potential landscape. Here, ion dynamics can no longer be assumed as purely isotropic and random. Defect-rich regions, for example, can lead to a decrease of the energy barrier the diffusing particles have to overcome. As a result, short-range diffusion is preferred and lower activation energies in the low-temperature limit are obtained than predicted by BPP-type relaxation. Additionally, correlation effects in structurally ordered systems can also cause asymmetric rate peaks [154]. Irrespective of the origin, the aforementioned deviations from uncorrelated diffusion can be taken into account by the introduction of a correlation parameter β according to

$$J(\omega) = G(0)\,\frac{2\tau_c}{1+(\omega\tau_c)^{\beta}}\,. \tag{5.39}$$

In the case of ideal BPP-type behavior the exponent β equals 2, whereas for correlated ion dynamics $1 < \beta < -2$ is found. Concerning both temperature limits, we can now observe the following proportionality:

$$R_1 \propto \tau_c \text{ for } \omega_0\tau_c \ll 1 \tag{5.40}$$

$$R_1 \propto \tau_c^{1-\beta}\omega_0^{-\beta} \text{ for } \omega_0\tau_c \gg 1\,. \tag{5.41}$$

It can be seen that only the low-temperature flank is affected by correlated diffusion, whose slope is reduced by β. This goes hand in hand with a decrease of the activation energy on the LT side given by:

$$E_A^{LT} = (\beta - 1)\, E_A^{HT} \tag{5.42}$$

Structurally confined ionic motions as seen, for example, in layer-structured or channel-type materials can also have an influence on the shape of the relaxation rate peak. But, in contrast to correlated motion, lower-dimensional diffusion processes affect the high-temperature limit of the rate peak. Fig. 27 demonstrates the relaxation rates for a two-dimensional case in comparison to those derived from BPP-type relaxation. While their LT flanks coincide, differences are observed in the limit $\omega_0\tau_c \ll 1$. The relaxation rates of a lower-dimensional diffusion process not only reveal a smaller slope of the high-temperature flank, but also show a dependency on the resonance frequency ω_0. Thus, measuring the relaxation rates R_1 at a constant T in the high-temperature range as a function of ω_0 offers an opportunity to distinguish between a 2D and 3D diffusion process. A suitable model that deals with anisotropy effects arising from structurally confined ionic motion in two dimensions can be found in the work of P. Richards [214].

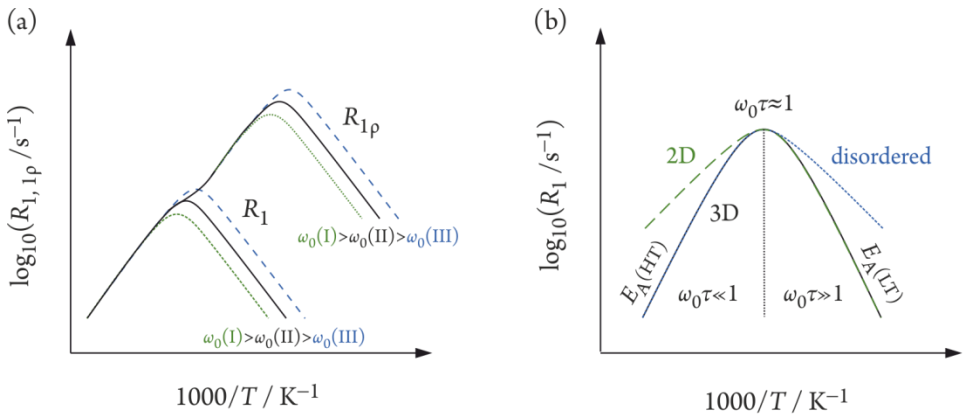

Fig. 27 (a) Schematic representations of the relaxation rates R_1 and $R_{1\rho}$ as a function of the inverse temperature for uncorrelated three-dimensional diffusion. Additionally, the frequency dependence of the rates in the low temperature limit is shown. The rate peak maximum is shifted toward higher temperatures with increasing Larmor frequency. **(b)** R_1 rate peaks observed for 3D diffusion according to the BPP-model (solid line), two-dimensional diffusion (dashed line) and disordered systems (dotted line). In the case of uncorrelated 3D motion a symmetric rate peak is observed. A lower-dimensional diffusion process leads to a smaller slope of the HT-flank, while disordered systems influence the low-T limit. See text for further information. (Taken and adapted from reference [209]).

NMR diffusion coefficient

NMR relaxation gives access to a microscopic self-diffusion coefficient via the maximum conditions $\omega_0\tau_c \approx 1$ and $\omega_0\tau_c \approx 0.5$ for measurements in the laboratory and rotating frame of reference, respectively. Due to the relation $\tau_c^{-1} = \tau^{-1}$, the jump rate at the temperature of the rate peak maximum T_{max} can be deduced. The relationship between the NMR diffusion coefficient and the jump rate is given by the Einstein-Smoluchowski equation

$$D_{NMR} = \frac{a^2}{6\tau} \tag{5.43}$$

with a representing the average jump distance, which can be derived from the crystal lattice parameters. The obtained diffusion coefficient values can be compared with those calculated from conductivity measurements via the following relations

$$D_{tracer} = H_r\, D_{cond.} = f\, D_{NMR}\ , \tag{5.44}$$

where D_{tracer} denotes the *tracer diffusion coefficient*, H_r the Haven ratio and f the correlation factor. Combination of the Eqs. (5.16), (5.43) and (5.44) yields

$$D_{tracer} = \frac{H_r \sigma k_B T}{nq^2} = f\,\frac{a^2}{6\tau}\ , \tag{5.45}$$

which in turn results in

$$\tau^{-1} = (H_r / f)\ \frac{6k_B T}{nq^2 a^2}\cdot\sigma \tag{5.46}$$

directly linking the correlation rate $\tau_c^{-1} = \tau^{-1}$ available from NMR with σ. The ratio (H_r/f) almost equals 1, assuming that $H_r = 1$ and $f = 1$ in the case of uncorrelated motion [23].

6 Results

The results of this doctoral thesis are presented cumulatively in form of articles already published or submitted to peer-reviewed journals (P) and manuscripts (M). They are categorized into three sections relating to common attributes of the investigated materials. Each section provides a brief introduction and additional information not included in the articles and manuscripts. The sections are as follows:

6.1 TiO_2 nanotubes

6.1.1 Preparation of metal-titania nanocomposites by pulsed electrodeposition

- P1: *Electrochemical preparation of tin-titania nanocomposite arrays*
- M1: *Embedding Base Metals in Anodic Titania Nanotubes – A Potential Electrochemical Approach*

6.1.2 Titania nanotubes and Sn/TiO_2 nanocomposites as anode material for sodium-ion and lithium-ion batteries

-P2: *Long-Cycle-Life Na Ion Anodes Based on Amorphous Titania Nanotubes – Interfaces and Diffusion*

-M2: *Electrochemical behavior of highly ordered Sn/TiO_2 nanocomposites for lithium and sodium ion batteries – Sn confinement effects and capacity evolution*

6.2 Ion transport and electrochemical activity of nanostructured ceramics

P3: *Nanostructured Ceramics: Ionic Transport and Electrochemical Activity*

6.3 Solid-state electrolytes

6.3.1 Sulfide-based solid electrolytes

P4: *Nuclear spin relaxation in nanocrystalline β-Li_3PS_4 reveals low-dimensional Li diffusion in an isotropic matrix*

M3: *^{7}Li NMR spin-lattice relaxation measurements of $LiTi_2(PS_4)_3$ (LTPS)*

6.3.2 NASICON electrolytes

P5: *Fast Na ion transport triggered by rapid ion exchange on local length scales*

6.1 TiO_2 nanotubes

The successful preparation of carbon-based nanotubes in the early 90s [215], has triggered intense research interest in nanostructured materials with a one-dimensional (1D) geometry in the form of nanofibers, nanorods, nanotubes and nanowires owing to their combination of shape, size and outstanding chemical and physical properties [97-99]. Today, the synthesis and characterization of 1D nanostructured transition metal oxides is of major importance opening the way towards biomedical, environmental, photochemical and electronic applications [100, 101]. Among them, highly parallel, self-assembled TiO_2 nanotubular layers have attracted the most attention as they can provide a controllable, ordered and defined morphology with a relatively large specific surface area combined with a unique set of properties. The oxide is known to be biocompatible, environmentally friendly, non-toxic, corrosion-resistant, chemical and mechanical stable, photocatalytic active and shows semiconductive behavior [102-104].

Such self-organized TiO_2 nanotubes can be simply formed on a metallic titanium substrate by a conventional electrochemical oxidation (anodization) process, which is usually carried out in a two-electrode cell at constant voltages [103, 104]. It is found that F^- plays a crucial role in the formation of the nanotubular structure, since on the one hand, it can form soluble $[TiF_6]^{2-}$ complexes with the Ti^{4+} species and on the other hand, is sensitive to chemical dissolution [116]. A typical anodization bath consists of ethylene glycol or glycerol containing small amounts of water and NH_4F as fluoride ion source. The use of viscous organic electrolytes allows the fabrication of smooth, long nanotubes keeping the same diameter along the entire tube length [124].

The formation of titania nanotube layers involves two opposing processes: (i) TiO_2 formation and (ii) chemical dissolution of the formed oxide. Thus, optimized electrochemical conditions result in vertically aligned and highly parallel ordered tubes grown from the titanium substrate. In addition, a relation between the dimensions of the titania nanotubes and the anodization conditions exist. A direct connection is given between the lengths and diameters of the tubes and the potential applied. In principle, the higher the applied voltage, the longer the tubes and the larger the tube diameters [104]. For example, for an anodization process carried out at constant voltages between 30 and 60 V, the diameters can be adjusted in the range of 70 to 130 nm. For a given time the lengths varied between 4.5 and 17.3 μm, respectively [57]. At a certain voltage, the tube length is defined by the anodization time [104].

To conclude, this tunable and unique morphology of the TiO_2 nanotubes doubled with the key functional properties mentioned above allow their use in a variety of potential applications such as rechargeable batteries [106], self-cleaning coatings [110], gas sensing [107], electrochromic [112] and biomedical devices [111], photocatalysis [108, 109] and solar cells [105].

6.1.1 Preparation of metal-titania nanocomposites by pulsed electrodeposition

The highly ordered and vertically aligned geometry of the titania nanotubes enables introduction of a second active material such as semiconductors or metals into the inner volume of the tubes forming nanocomposites. This is done either to enhance their functional properties or to create entirely new ones broadening their range of possible applications. For instance, filling with noble metals such as Ag, Au or Pt results in a higher photocatalytic activity of TiO_2 [152], while Fe_3O_4 nanoparticles implement additional magnetic properties [151]. Cu-loaded titania nanotubes have also been reported due their potential use in solar energy conversion [216]. Furthermore, the combination of TiO_2 and ZnO can improve the gas sensitivity of zinc oxide [217]. The preparation of nickel-titania nanocomposite arrays has also attracted much interest for applications in electrochromic devices and catalysts [150]. Finally, encapsulation of Sn or Sb metal into TiO_2 nanotubes can prevent particle agglomeration thus, ensuring better electrochemical performance [218, 219].

To date, several approaches have been reported for embedding different foreign materials into TiO_2 nanotube layers. Among them, pulsed-current electrodeposition seems to be the most reliable and cost-effective method to prepare such metal-titania nanocomposites. This technique allows the accurate control of the deposited metal content inside the tubes and the preparation of fine and uniform deposits. To the best of our knowledge, apart from the report by Liu *et al.* [220] on the loading of Cu, Au, Ag and Pt into anodic titania nanotubular arrays by electrodeposition, no study is available dealing with the filling of TiO_2 nanotubes with any base metals such as Sb, Sn, Zn, In or Ni.

In the following article **P1** we presented the successful embedding of Sn metal into highly ordered titania nanotubes using pulsed-current electrodeposition. We discussed on some relevant electrochemical parameters, the need of high current densities and the underlying deposition mechanism. However, our observations seem to disagree from results that have already been published in the literature. There, the tube bottoms are suggested as the preferred place for metallic tin to nucleate and grow. In contrast we proposed that tin is deposited via an indirect, redox-mediated mechanism and that deposition starts at the tube tops.

Additionally, we tried to fill anodic titania nanotubes with other metals such as Sb, Ni, Cu, Zn and In using the same pulsed electrodeposition procedure as for the tin deposition process. The results are thoroughly summarized in the subsequent manuscript **M1**. While antimony and nickel metal have been successfully embedded into the inner volume of the titania nanotubes, deposition of copper, zinc and indium inside the tubes was not achieved under these conditions.

P1:

Electrochemical preparation of tin-titania nanocomposite arrays

D. Prutsch, M. Wilkening and I. Hanzu

RSC Adv., **6** (2016), 98243.

RSC Advances

COMMUNICATION

View Article Online
View Journal | View Issue

Open Access Article. Published on 10 October 2016. Downloaded on 11/9/2018 7:40:47 PM.
This article is licensed under a Creative Commons Attribution 3.0 Unported Licence.

Cite this: *RSC Adv.*, 2016, **6**, 98243

Electrochemical preparation of tin–titania nanocomposite arrays†

D. Prutsch,[a] M. Wilkening[ab] and I. Hanzu*[ab]

Received 29th July 2016
Accepted 10th October 2016

DOI: 10.1039/c6ra19209b

www.rsc.org/advances

We report the first successful electrodeposition of Sn inside self-organized anodic titania nanotubes. Several relevant electrochemical parameters are identified and mechanistic aspects are briefly discussed. It appears that the role of the substrate is complex, titania acting as a mediator for Sn electrodeposition.

Introduction

Over the last decades, one-dimensional nanostructured materials, such as nanowires, nanofibers, nanorods and nanotubes have attracted significant attention following the combination of size, shape and exciting physical and chemical properties. The synthesis of transition metal oxide nanostructures with controlled dimensions and chemical composition is today of major importance, opening unmatched opportunities towards photochemical, electronic, biomedical and environmental applications. In particular, self-assembled, highly parallel TiO_2 nanotubes fabricated by anodization (*i.e.* electrochemical oxidation) of titanium have attracted significant interest in the past decade.[1] These nanotubular structures, that usually feature a relatively large surface area and a well defined geometry, possess a unique combination of properties such as non-toxicity, good chemical and mechanical stability, high oxidative power, resistance to corrosion, photocatalytic activity, environment-friendliness and even biocompatibility. These outstanding features resulted in a continuously expanding panel of proven applications including self-cleaning coatings,[2] solar cells,[3] gas sensing,[4] switching electrochromic devices,[5] rechargeable batteries,[6] electrocatalysis,[7] photocatalysis[8] and biomedical applications.[9]

Moreover, due to their highly ordered nanotubular structure, TiO_2 nanotubes can serve as an excellent substrate for further loading with a second functional material such as metals (*e.g.*, Ni, Ag, Pt)[10–12] or semiconductors (*e.g.*, CdS, $ZnFe_2O_4$, Cu_2O)[13–15] resulting in tubes with either enhanced or completely new properties. Yang *et al.*[16] found out that filling of the nanotubes with Co–Ag–Pt increases the catalytic activity, while Fe_3O_4 introduces additional magnetic properties.[17] Although, so far, several approaches for the deposition of different materials into titania nanotubes have been reported, electrodeposition is probably the most cost-effective method to fill TiO_2 nanotubes. Liu *et al.*[18] already reported on the electrodeposition of some noble metals (Pt, Au, Ag) as well as Cu into anodic TiO_2 nanotubes. However, to the best of our knowledge, there is hitherto no report available that deals with the electrochemical embedding of any base metals, such as Sn, into the inner volume of the tubes. Nanostructured Sn-based materials were already demonstrated as high-capacity anodes in Li-ion[19,20] and Na-ion batteries.[21,22] Encapsulation of Sn metal is expected to prevent coalescence of Sn nanoparticles, thus ensuring a longer cycle life of the electrode.[23] Also, it is possible to convert the Sn nanostructures into SnO or SnO_2 and obtain materials with applications to solar cells,[24] sensors[25] and catalysis.[26]

Here we report, for the first time, the partial filling of highly ordered TiO_2 nanotubes with Sn metal by electrodeposition using a simple pulsed-current deposition technique. We briefly discuss on some relevant electrochemical parameters, morphology of the deposits as well as on the apparent complexity of Sn electrodeposition onto anodic titania nanotubes.

Results and discussion

As mentioned above, electrodeposition of some noble metals as well as Cu into anodic TiO_2 nanotubes was earlier reported by Liu *et al.*[18] They used a pulsed current electrodeposition approach: each short negative (reduction) current pulse (1 s) was followed by a relatively long rest period (7 s) in order to allow the electrode surface to replenish with aqueous cations by diffusion. So far, only the influences of the pulse length and the rest periods are discussed. The best conditions for electrodeposition are, however,

[a]*Institute for Chemistry and Technology of Materials, Graz University of Technology, Stremayrgasse 9, 8010 Graz, Austria. E-mail: hanzu@tugraz.at*

[b]*Christian Doppler Laboratory for Lithium Batteries, Graz University of Technology, Stremayrgasse 9, 8010 Graz, Austria*

† Electronic supplementary information (ESI) available. See DOI: 10.1039/c6ra19209b

Open Access Article. Published on 10 October 2016. Downloaded on 11/9/2018 7:40:47 PM.
This article is licensed under a Creative Commons Attribution 3.0 Unported Licence.

still unclear. In general, electrodeposition on oxidic substrates is notoriously difficult to conduct[27] because numerous electrochemical parameters, whose values are initially unknown, may significantly influence the deposition process. Thus, in order to shed some light on this essential information and to quickly identify the relevant parameters that lead to filling of the titania nanotubes, the successful silver electrodeposition bath of Liu *et al.* was used as a starting point. Cyclic voltammetry experiments were carried out in a conventional 3-electrode electrochemical configuration with a glassy carbon working electrode. In the second step, the same experiments were done for the Sn-containing electrodeposition bath. The results are shown in Fig. 1.

We noticed that Ag deposit already has a visible dendritic appearance even at relatively low current densities of 3.6 mA cm^{-2} while the Sn looked significantly smoother on the surface of the glassy carbon electrode even at a current density as high as 15.4 mA cm^{-2}. Dendritic electrodeposition of metals occurs when the limiting diffusion current is exceeded, at least locally. As the surface of the electrode is depleted on cation species, inhomogeneous growth occurs. Once nucleated, the dendrites grow very fast as the electric field at their point tips is significantly higher than on the flat surface of the electrode.

Based on the report of Liu *et al.* and on our observations it appears that in order to successfully achieve the electrodeposition of a metal inside the anodic titania nanotubes it is preferable to work at high current densities, *i.e.*, above the limit of dendritic deposition. Since there were visual indications that even at a current density of 15.4 mA cm^{-2} the Sn deposit still had a smoother appearance than Ag we decided to drastically increase the current density for the pulsed electrodeposition of Sn in TiO_2 nanotubes to 1 A cm^{-2} in order to achieve the dendritic electrodeposition regime that seemed necessary. First, a short reduction pulse ($I_{on} = -1$ A cm^{-2}, $t_{on} = 0.5$ s) was applied in order to electrodeposit Sn followed by a rest period of 10 s to restore the tin concentration at the interface.

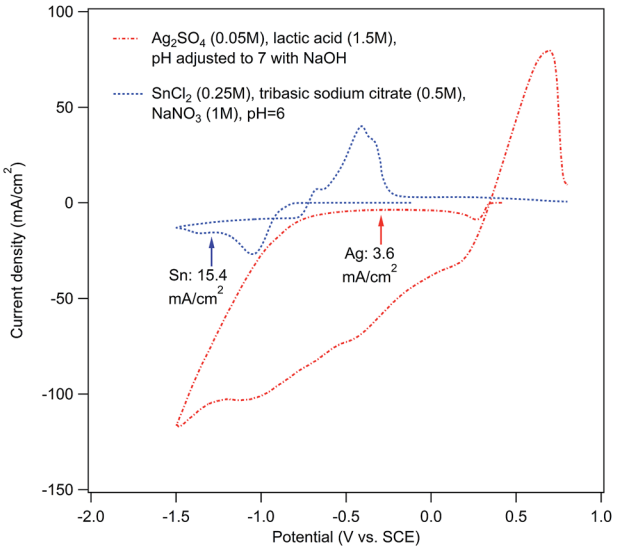

Fig. 1 Cyclic voltammograms of the electrodeposition baths for Ag and Sn at a scan rate of 25 mV s^{-1} between 0.8 V and −1.5 *vs.* SCE.

Fig. 2, left side, shows top-view (a) and cross-section (b) Scanning Electron Microscopy (SEM) images acquired using a Secondary Electrons (SE) detector. The images show the titania nanotube layer on which Sn was electrodeposited after a total of 90 current pulses according to the pulsed electrodeposition procedure described above. On the right side, the same regions are shown, however, imaged with a Back-Scattered Electrons (BSE) detector which delivers SEM micrographs featuring good chemical element contrast. The bright regions correspond to the Sn deposit. It can clearly be seen that Sn has been successfully embedded into the inner volume of the nanotubes. It is also evident that Sn is not found in all the nanotubes which means that electrodeposition does not occur in a homogeneous manner. The presence of metallic Sn was confirmed by X-ray diffraction (see ESI, Fig. S2†).

In Fig. 3 the corresponding potential response is shown. Upon the application of the reduction pulse I_{on}, the potential of titania nanotubes electrode drops to very low values of approximately −9.5 V *vs.* SCE (Saturated Calomel Electrode). Subsequently, a relatively small voltage recovery is recorded over the entire duration of the current pulse (see the inset of Fig. 3). This relative potential variation is consistent with a typical chronopotentiometric response of an electrodeposition process. The enormous potential drop to −9.5 V can be explained by the relatively low electronic conductivity of the initial TiO_2 nanotubes[28] that lead to high ohmic drops. This assumption is supported by the instant potential recovery to approx. −1.5 V *vs.* SCE that occurs just after the reduction current pulse. Afterwards, from −1.5 V, also a relatively fast recovery of the electrode potential was recorded; the potential effectively reaches a stable value after 6 s. Indeed, for the last 4 seconds of the rest period a variation of the electrode potential of less than 25 mV has been found. This fast relaxation behaviour may be explained if we consider the stirring effect generated by the significant hydrogen evolution at the electrode which leave only small concentration gradients in the electrodeposition bath at the end of the current pulse.

If we consider that at the beginning the electronic conductivity of anodic titania nanotubes is low, the preferred place for the nucleation and grow of Sn should be at the bottom of the nanotubes. This expectation is, however, not supported by observation. In fact, the Sn appears to nucleate and grow from the top towards the inner volume of the nanotubes (see ESI, Fig. S1†). This intriguing behaviour is an indication of a fundamentally different electrodeposition mechanism. Indeed, it is known that it is possible to reduce TiO_2 in aqueous media and insert a significant amount of protons in TiO_2 nanotubes.[29,30] The Ti^{3+} centres formed are, however, not stable in aqueous media and Ti^{3+} re-oxidizes completely within minutes back to Ti^{4+}. It is then plausible to assume that the deposition of Sn inside the nanotubes might occur according to the following mechanism. First, the high current pulse reduces TiO_2 to H_xTiO_2. Since the Ti^{3+} state is not stable, it is likely that during the rest period Sn^{2+} is in fact reduced by the re-oxidation of H_xTiO_2, thus, leading to the slow growth of Sn in the nanotubes with the nucleation point at the top of the nanotubes rather than at the bottom. Thus the high current reduction

 This journal is © The Royal Society of Chemistry 2016

Open Access Article. Published on 10 October 2016. Downloaded on 11/9/2018 7:40:47 PM.
This article is licensed under a Creative Commons Attribution 3.0 Unported Licence.

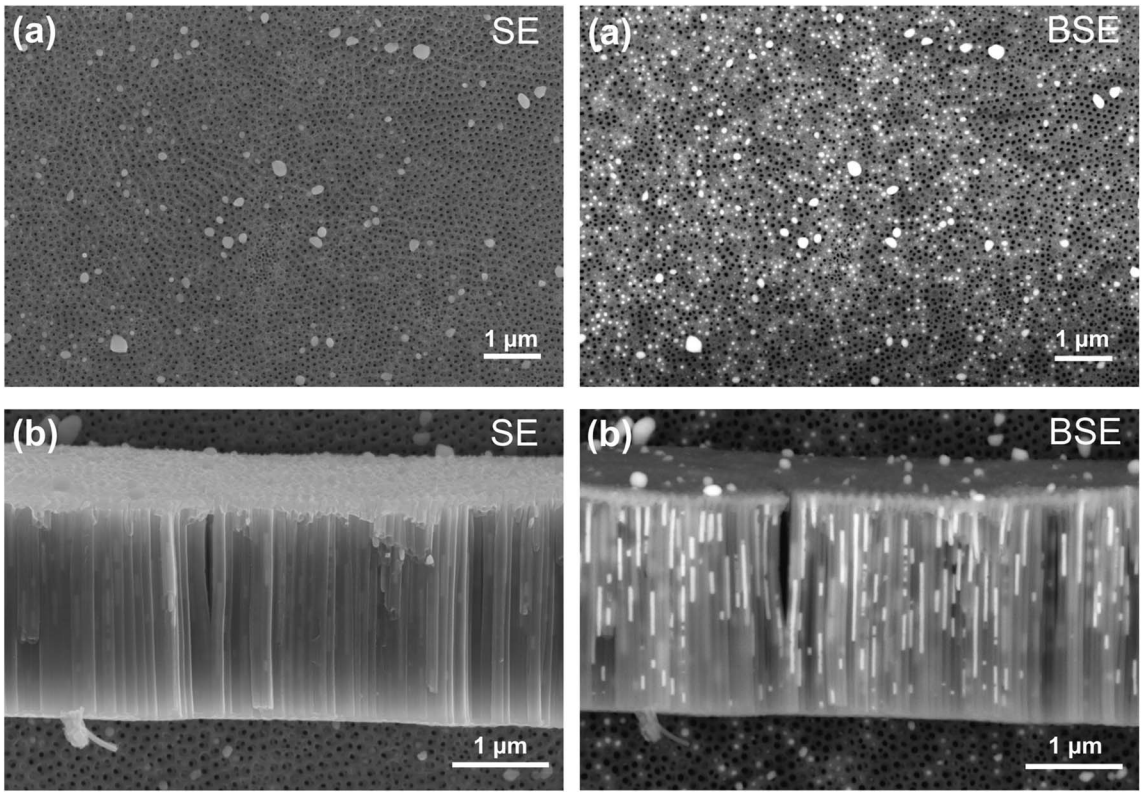

Fig. 2 Left: Secondary Electrons (SE) SEM images in top-view (a) and cross-section (b) of a TiO_2 nanotube layer on which Sn has been deposited using a pulsed electrodeposition technique. Right: The same regions imaged with a Back-Scattered Electrons (BSE) detector showing an improved chemical composition contrast. It is obvious that Sn is indeed embedded inside the nanotubes. See text for further discussion of the deposition mechanism.

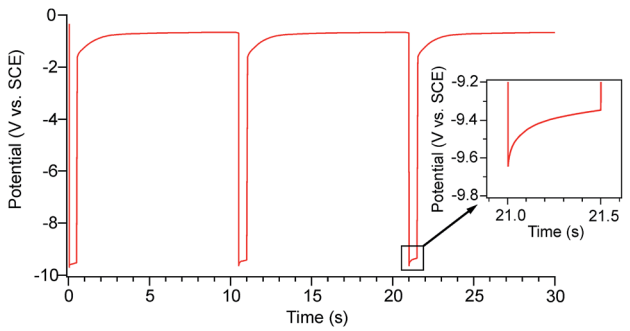

Fig. 3 Chronopotentiometric curves recorded during the pulsed Sn electrodeposition on anodic TiO_2 nanotubes. See text for further explanation.

pulses might not directly lead to the Sn growth inside the nanotubes but to the germination of Sn crystallites. These crystallites may subsequently act as seeds for the relatively slow growing of Sn during the rest periods. Obviously, according to this scenario only the germs that have access to a sufficient Sn^{2+} flux will grow. The germs closer to the open top of the nanotubes will grow while those at the bottom will never develop further. With each reduction pulse the Ti^{3+} reserve is replenished and Sn growth inside the nanotubes continues, at points where Sn^{2+} is available. In the case of electrodeposition, the nucleation of Sn on titania nanotubes substrates is instantaneous,[31] *i.e.* all tin germs form at the beginning upon the application of the current, with only growth of the germs occurring thereafter. Since the rest period during the reduction pulses is relatively long, each reduction pulse will also generate new Sn germs within the nanotube layer. Consequently, there is a direct dependence of the nanotube filling ratio on the number of pulses applied (see ESI, Fig. S1†). This mechanism could explain satisfactorily the wide distribution of the Sn deposits length inside the nanotubes, as is clearly seen in Fig. 2. Hence, the distribution width is a natural consequence of the variable access to aqueous tin species as well as the different moment at which the tin germs form and start growing.

Conclusions

We report, for the first time, the electrodeposition of Sn inside anodic titania nanotubes by using a high-current density pulsed electrodeposition method. While at first sight, it appeared that dendritic electrodeposition is required to embed metals within the inner volume of the nanotubes, the mechanism in the present case seems to be quite different from that of classical electrodeposition. It turned out that the growth of Sn inside the nanotubes is much more complex than expected. We suggest that it occurs through an indirect, redox-mediated mechanism

Open Access Article. Published on 10 October 2016. Downloaded on 11/9/2018 7:40:47 PM.
This article is licensed under a Creative Commons Attribution 3.0 Unported Licence.

in which the titania substrate most likely plays the role of redox mediator. This could in fact constitute a more general route, opening the way for the facile realization of highly regular titania-base metal nanocomposites by easily practicable electrochemical means.

Experimental

The Ag electrodeposition bath reported by Liu *et al.* (containing 0.05 M Ag_2SO_4, 1.5 M lactic acid; the pH was adjusted to 7 with NaOH) was prepared and cyclic voltammetry experiments were carried out in a classical three-electrode configuration with a glassy carbon working electrode, a platinum gauze counter electrode and a Saturated Calomel Electrode (SCE) in a Haber–Luggin capillary that served as a reference electrode. Cyclic voltammograms were recorded between −1.5 V and 0.8 V at scan rates of 25 and 50 mV s^{-1} using a Parstat MC potentiostat running Versa Studio software. The same experiments were done for a Sn deposition solution consisting of $SnCl_2$ (0.25 M), tribasic sodium citrate (0.5 M) and $NaNO_3$ (1 M), whose natural pH = 6. For the preparation of the electrodeposition baths de-ionized water (Millipore) was used. All experiments were carried out at room temperature.

Titanium foils (99.7% purity, 0.25 mm thickness, Sigma Aldrich) cut in small pieces of 12.5 mm × 12.5 mm were ultrasonically cleaned in acetone, isopropanol and methanol for 10 minutes, in this order, followed by rinsing with distilled water and drying with compressed air. A two-electrode electrochemical cell with the titanium substrate as working electrode and a stainless steel counter electrode was used to perform the anodic growth of the TiO_2 nanotubes. In this cell, the sample was pressed against a brass ring in order to ensure a good electrical contact, while leaving a surface area of approx. 0.708 cm^2 of the titanium substrate exposed to the anodization bath. The electrolyte used consisted of 97.6 wt% ethylene glycol, 2 wt% distilled water and 0.4 wt% NH_4F. The electrodes were connected to a precision DC power supply (Agilent E3610A) and anodization was carried out at a constant voltage of 60 V for 1 h. The as-anodized samples were then rinsed with distilled water and dried with compressed air. In order to achieve an ordered and highly-regular tube morphology a second anodization step was applied. For this, the first nanotube layer was removed from the titanium substrate by using an adhesive scotch tape and on the same titanium substrate, after ultrasonically cleaning in acetone, isopropanol and methanol for 10 minutes, subsequent rinsing with distilled water and drying with compressed air, TiO_2 nanotubes were grown under same conditions for 5 minutes. The ordered dimples that cover the titanium substrate after peeling off the nanotube layer are acting here as nucleation sites for the titania nanotube growth in the second step. To form an oxide sealing layer underneath the titania nanotubes the samples were anodized again in a solution of 0.2 M H_3PO_4 in ethylene glycol at 20 V for 10 min in a two electrode system with a stainless steel counter electrode. Finally the as-prepared samples were rinsed with distilled water and dried with compressed air.

Partial filling of the TiO_2 nanotubes was accomplished by using a pulsed galvanostatic method. The electrodeposition experiments were carried out in a classical three-electrode configuration with the nanotube layer on the titanium substrates as working electrode, a platinum gauze as counter electrode and a Saturated Calomel Electrode as reference. The samples were fit in the same electrochemical cell that was already used for the anodization process, so that only the nanotube layer (an area of 0.708 cm^2) on the titanium substrate was exposed to the Sn deposition solution. The electrolyte for the electrodeposition of Sn metal was a mixture of $SnCl_2$ (0.25 M), tribasic sodium citrate (0.5 M) and $NaNO_3$ (1 M), pH 6. All solutions were prepared with de-ionized water (Millipore). For Sn deposition a current pulsing approach with a short pulse of negative current ($I_{on} = -1$ A cm^{-2}, $t_{on} = 0.5$ s), followed by a delay time ($I_{off} = 0$ A cm^{-2}) of $t_{off} = 10$ s was used. Different number of pulses (2, 5, 10, 20 and 90) was applied in order to follow the degree of tube filling. All electrodeposition experiments were performed at room temperature using a multichannel VMP-3 potentiostat equipped with a 20 A current booster kit from Biologic Science Instruments running EC-LAB-software (v.10.34). After Sn deposition the samples were rinsed with Millipore de-ionized water and carefully dried with compressed air. Scanning Electron Microscopy (Zeiss Ultra 55 and Vega Tescan) was employed for the morphological characterization of the filled TiO_2 nanotubes. SEM cross-section images were taken from samples that were scratched just before placing them in the SEM vacuum chamber.

Acknowledgements

Sanja Simic from Austrian Centre for Electron Microscopy and Nanoanalysis (FELMI-ZFE) is kindly acknowledged for the SEM micrographs. We also thank Brigitte Bitschnau from Institute of Physical and Theoretical Chemistry (PTC) for XRD measurements. Financial support by the Austrian Federal Ministry of Science, Research and Economy, and the Austrian National Foundation for Research, Technology and Development is greatly appreciated. Furthermore, we kindly acknowledge the Austrian Research Promotion Agency (FFG) through the RSA-AIMS project, Grant No. 4338751, as well as the Deutsche Forschungsgemeinschaft (DFG) through the Research Unit 1277 (molife), Grant No. WI 3600/4-2 and HA 6996/1-2, for financial support.

References

1 S. Berger, R. Hahn, P. Roy and P. Schmuki, *Phys. Status Solidi B*, 2010, **247**, 2424–2435.
2 R. Wang, K. Hashimoto, A. Fujishima, M. Chikuni, E. Kojima, A. Kitamura, M. Shimohigoshi and T. Watanabe, *Adv. Mater.*, 1998, **10**, 135–138.
3 J. M. Macák, H. Tsuchiya, A. Ghicov and P. Schmuki, *Electrochem. Commun.*, 2005, **7**, 1133–1137.
4 M. Paulose, O. K. Varghese, G. K. Mor, C. A. Grimes and K. G. Ong, *Nanotechnology*, 2006, **17**, 398–402.

 This journal is © The Royal Society of Chemistry 2016

Open Access Article. Published on 10 October 2016. Downloaded on 11/9/2018 7:40:47 PM.
This article is licensed under a Creative Commons Attribution 3.0 Unported Licence.

5 A. Ghicov, H. Tsuchiya, R. Hahn, J. M. Macak, A. G. Muñoz and P. Schmuki, *Electrochem. Commun.*, 2006, **8**, 528–532.
6 D. Prutsch, M. Wilkening and I. Hanzu, *ACS Appl. Mater. Interfaces*, 2015, **7**, 25757–25769.
7 J. M. Macak, F. Schmidt-Stein and P. Schmuki, *Electrochem. Commun.*, 2007, **9**, 1783–1787.
8 A. L. Linsebigler, G. Lu and J. T. Yates, *Chem. Rev.*, 1995, **95**, 735–758.
9 S. H. Oh, R. R. Finones, C. Daraio, L. H. Chen and S. Jin, *Biomaterials*, 2005, **26**, 4938–4943.
10 Y. Zhang, Y. Yang, P. Xiao, X. Zhang, L. Lu and L. Li, *Mater. Lett.*, 2009, **63**, 2429–2431.
11 K. Xie, L. Sun, C. Wang, Y. Lai, M. Wang, H. Chen and C. Lin, *Electrochim. Acta*, 2010, **55**, 7211–7218.
12 Y.-Y. Song, Z.-D. Gao and P. Schmuki, *Electrochem. Commun.*, 2011, **13**, 290–293.
13 Y.-Y. Song, Q.-L. Zhuang, C.-Y. Li, H.-F. Liu, J. Cao and Z.-D. Gao, *Electrochem. Commun.*, 2012, **16**, 44–48.
14 Y. Hou, X.-Y. Li, Q.-D. Zhao, X. Quan and G.-H. Chen, *Adv. Funct. Mater.*, 2010, **20**, 2165–2174.
15 S. Zhang, S. Zhang, F. Peng, H. Zhang, H. Liu and H. Zhao, *Electrochem. Commun.*, 2011, **13**, 861–864.
16 L. Yang, D. He, Q. Cai and C. A. Grimes, *J. Phys. Chem. C*, 2007, **111**, 8214–8217.
17 N. K. Shrestha, J. M. Macak, F. Schmidt-Stein, R. Hahn, C. T. Mierke, B. Fabry and P. Schmuki, *Angew. Chem., Int. Ed.*, 2009, **48**, 969–972.
18 N. Liu, K. Lee and P. Schmuki, *Angew. Chem., Int. Ed.*, 2013, **52**, 12381–12384.
19 Y. M. Lin, R. K. Nagarale, K. C. Klavetter, A. Heller and C. B. Mullins, *J. Mater. Chem.*, 2012, **22**, 11134–11139.
20 Y. H. Xu, Q. Liu, Y. J. Zhu, Y. H. Liu, A. Langrock, M. R. Zachariah and C. S. Wang, *Nano Lett.*, 2013, **13**, 470–474.
21 D. H. Nam, T. H. Kim, K. S. Hong and H. S. Kwon, *ACS Nano*, 2014, **8**, 11824–11835.
22 H. L. Zhu, Z. Jia, Y. C. Chen, N. Weadock, J. Y. Wan, O. Vaaland, X. G. Han, T. Li and L. B. Hu, *Nano Lett.*, 2013, **13**, 3093–3100.
23 C. Wu, J. Maier and Y. Yu, *Adv. Funct. Mater.*, 2015, **25**, 3488–3496.
24 S. S. Bhande, G. A. Taur, A. V. Shaikh, O. S. Joo, M. M. Sung, R. S. Mane, A. V. Ghule and S. H. Han, *Mater. Lett.*, 2012, **79**, 29–31.
25 S. Das and V. Jayaraman, *Prog. Mater. Sci.*, 2014, **66**, 112–255.
26 Z. Y. Zhou, N. Tian, J. T. Li, I. Broadwell and S. G. Sun, *Chem. Soc. Rev.*, 2011, **40**, 4167–4185.
27 T. Djenizian, I. Hanzu, M. Eyraud and L. Santinacci, *C. R. Chim.*, 2008, **11**, 995–1003.
28 I. Hanzu, T. Djenizian and P. Knauth, *J. Phys. Chem. C*, 2011, **115**, 5989–5996.
29 I. Hanzu, T. Djenizian and P. Knauth, *Wide Bandgap Semiconductor Materials and Devices 12*, 2011, vol. 35, pp. 21–31.
30 I. Hanzu, V. Hornebecq, T. Djenizian and P. Knauth, *C. R. Chim.*, 2013, **16**, 96–102.
31 I. Hanzu, T. Djenizian, G. F. Ortiz and P. Knauth, *J. Phys. Chem. C*, 2009, **113**, 20568–20575.

M1

Embedding Base Metals in Anodic Titania Nanotubes – A Potential Electrochemical Approach

D. Tapler, M. Wilkening and I. Hanzu

under preparation

Embedding Base Metals in Anodic Titania Nanotubes – A Rational Electrochemical Approach

D. Tapler, M. Wilkening, I. Hanzu

Institute of Chemistry and Technology of Materials, Graz University of Technology, Stremayrgasse 9, 8010 Graz, Austria

Abstract. Filling of self-organized TiO_2 nanotubes with the base metals Sb and Ni was successfully achieved by a pulsed-current electrodeposition approach. The morphology and composition of the metal-titania nanocomposites were investigated by scanning electron microscopy and energy-dispersive X-ray spectroscopy. It was found that an optimized composition of the deposition bath and the used pulse program is necessary for the successful embedding of these metals into the inner volume of the tubes.

Introduction

Self-organized TiO_2 nanotubular structures formed on titanium are opening today the path towards important technological applications. These nanotube layers, that commonly feature a controllable, defined geometry with a relatively high surface area, show a variety of unique properties such as high mechanical strength, good chemical stability, high corrosion resistance, wide band-gap semiconducting behavior, photocatalytic activity along with environmental-friendliness and non-toxicity [1-3]. These extraordinary features enable their versatile use in a wide range of applications including solar cells [4], rechargeable batteries [5], gas sensing [6], catalysis [7], self-cleaning coatings [8] and even biomedical [9] and electrochemical devices [10]. To further broaden their applications range, the introduction of a second functional material such as semiconductors or metals into the inner volume of the TiO_2 nanotubes is an effective way to enhance their properties or endow then with entirely new ones. For instance, filling of titania nanotubes with Ni oxide results in a higher photoresponse [11], while Fe_3O_4 enables additional magnetic properties [12]. Preparation of Ag/TiO_2 nanocomposites further enhances the photocatalytic activity [13]. Also, TiO_2 nanotubes filled with Sn or Sb are of great interest due to their better electrochemical performance [14,15]. Electrodeposition is a highly reliable and most cost-effective method to prepare such metal-titania nanocomposites. This technique allows the accurate control of the deposited metal content inside the tubes and the preparation of fine and uniform deposits [16, 17]. To the best of our knowledge, apart from the report by Liu *et al.* [18] on the loading of Cu, Au, Ag and Pt into anodic titania nanotubular arrays by electrodeposition, no study is available dealing with the filling of TiO_2 nanotubes with any base metals such as Sb, Sn, Zn, In or Ni.

In this paper, we report on the successful filling of titania nanotubes with metallic Sb and Ni by pulsed-current electrodeposition. The attempts made to embed Zn, In or Cu into the inner volume of the tubes by electrodeposition is also discussed.

Experimental

Self-organized TiO_2 nanotube arrays were formed on titanium substrates by a two-step anodization process. Prior to anodization, the titanium foils (0.25 mm thick, purity: 99.7%, Sigma Aldrich) were cut in square pieces of 12.5 mm x 12.5 mm and degreased by ultrasonic cleaning in acetone, isopropanol and methanol successively, for 10 minutes in each solvent. Subsequently, these substrates were thoroughly rinsed with deionized water and quickly dried in a compressed air stream. For the anodization processes, a two-electrode cell with the cleaned titanium foil as working electrode and a stainless steel plate as counter electrode was used. The electrolytic bath consisted of 0.4 wt % ammonium fluoride, 2 wt % deionized water and 97.6 wt % ethylene glycol. The first anodization step was carried out at 60 V for 1 hour. The as-prepared samples were then carefully rinsed with deionized water and quickly dried with compressed air. To perform the second anodization step the titania nanotubes were peeled off from the underlying titanium foil with an adhesive scotch tape and the same titanium foil was anodized again for 5 minutes at 60 V under the same conditions, after ultrasonically cleaning of the titanium substrate in acetone, isopropanol and methanol for 10 minutes, rinsing with deionized water and drying in a compressed air stream. To seal any defects at the tube bottoms, an oxide layer is formed by anodizing the samples again in a 0.2 M H_3PO_4/ethylene glycol electrolyte at 20 V for 10 minutes using the same experimental set-up. Finally the as-prepared TiO_2 nanotube samples were rinsed with deionized water dried in a compressed air stream. All anodization experiments were performed by using a precision DC power supply (E3610A) from Agilent and at room temperature.

Filling of the titania nanotubes with different metals (Sb, Ni, Cu, Zn and In) was performed by using a pulsed-current deposition technique. For all electrodeposition experiments the same cell was used as for the anodization process, however operated in a three-electrode configuration having the TiO_2/Ti substrate as working electrode, a Pt gauze as counter electrode, and a commercial (Schott) saturated calomel electrode (SCE) as reference electrode. The composition of the electrolytes used for the electrodeposition of the different metals is summarized in a table at the end of the experimental part. All deposition solutions were prepared with Millipore water and stirred for at least 1 hour before carrying out the electrochemical deposition process. No electrodeposition bath de-aeration step was carried out. The used pulse program consisted of short negative current pulses (t_{on} = 0.5 s, I_{on} = –1 A/cm^2) followed by long rest periods (t_{off} = 10 s, I_{off} = 0 A/cm^2). A total number of 90 pulses were applied. All electrodeposition experiments were carried out at room temperature with a multichannel VMP-3 potentiostat connected to a 20 A current booster from Biologic Science Instruments (EC-LAB-software). After electrochemical deposition the samples were immediately rinsed with Millipore water and dried in a compressed air stream. The morphology and the composition of the as-prepared nanocomposites were characterized by scanning electron microscopy (SEM) and energy dispersive X-ray spectroscopy (EDS) using a Zeiss Ultra 55 microscope. To obtain cross-section images the samples were deliberately scratched with a sharp steel needle prior to SEM characterization.

Electrodeposited metal	Composition of deposition solution
Sb	$SbCl_3$ (0.1 M), citric acid (0.5 M)
	Sb_2O_3 (0.1 M), citric acid (0.5 M) (pH = 6, adjusted with 5 M KOH)
	Sb_2O_3 (0.1 M), citric acid (1 M) (pH = 6, adjusted with 5 M KOH)
Ni	$NiSO_4 \cdot 6\,H_2O$ (1 M), $NiCl_2$ (0.2 M), H_3BO_3 (0.5 M)
	$NiCl_2$ (0.1 M), citric acid (0.5 M)
Cu	$CuSO_4$ (0.4 M), lactic acid (3 M) (pH = 7, adjusted with 5 M KOH)
Zn	$ZnCl_2$ (0.25 M), H_3BO_3 (0.5 M)
	$ZnSO_4 \cdot 7\,H_2O$ (0.6 M), $(NH_4)_2SO_4$ (0.1 M)
In	$InCl_3$ (0.1 M), citric acid (0.5 M)

Results and discussion

Electrodeposition of Sn metal alone into anodic TiO_2 nanotubes has already been reported in one of our previous works [1]. We used a pulsed-current deposition approach, which consists of a short negative reduction pulse ($I_{on} = -1A/cm^2$, $t_{on} = 0.5$ s) in order to electrodeposit tin followed by a long rest period of 10 s to allow restoration of the Sn concentration at the interface. A total number of 90 current pulses were applied. Here, the same pulsed electrodeposition procedure was used to fill titania nanotubes with other metals such as Sb, Ni, Cu, Zn and In.

Fig. 1 shows Scanning Electron Microscopy (SEM) images in cross-section (a) and top-view (b) of the titania nanotube layer prepared by anodization before loading with a metal. It can be seen that compact, highly ordered and vertically aligned nanotube arrays are formed. The average tube diameter is found to be ~75 nm and the layer thickness is about 2.783 μm.

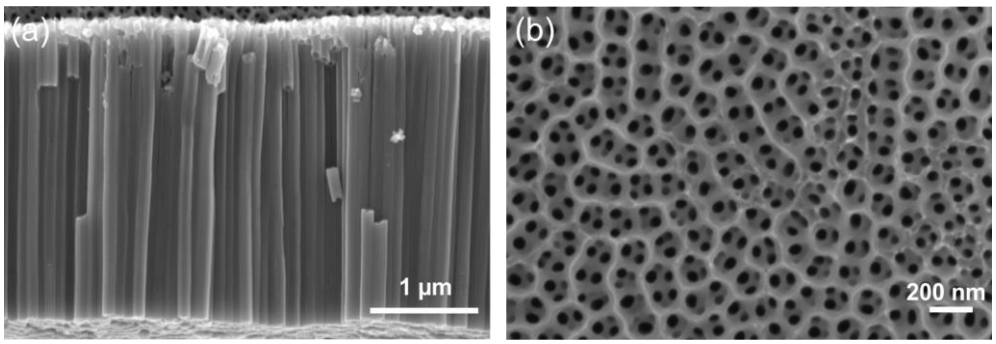

Fig. 1 SEM images in cross-section (**a**) and top-view (**b**) of self-organized TiO_2 nanotubes prepared by a two-step anodization process.

At first, we will consider the results obtained from Sb electrodeposition. Fig. 2 represents SEM cross-section images acquired with a Secondary Electrons (SE) detector, left side, and Back-Scattered Electrons (BSE) detector on the right side. SEM micrographs recorded in BSE mode have the advantage to feature good chemical element contrast. The images show the TiO_2 nanotubular layer, on which antimony was electrodeposited from the deposition bath consisting of 0.1 M $SbCl_3$ and 0.5 M citric acid using the pulse parameters described above. From the BSE images it is evident that Sb has been embedded inside the nanotubes finding most of the deposited Sb metal close to the top of the titania nanotubes. This observation is in good agreement with our suggested electrodeposition mechanism that the growth of the metal particles is redox-mediated with the nucleation point found at the top part of the tubes. It can also clearly be seen that Sb is not present in all of the nanotubes, which indicates that nucleation and growth occurs in an inhomogeneous manner. In addition, a thick layer consisting of agglomerated large-sized Sb particles has been deposited on the surface of the TiO_2 nanotubular array.

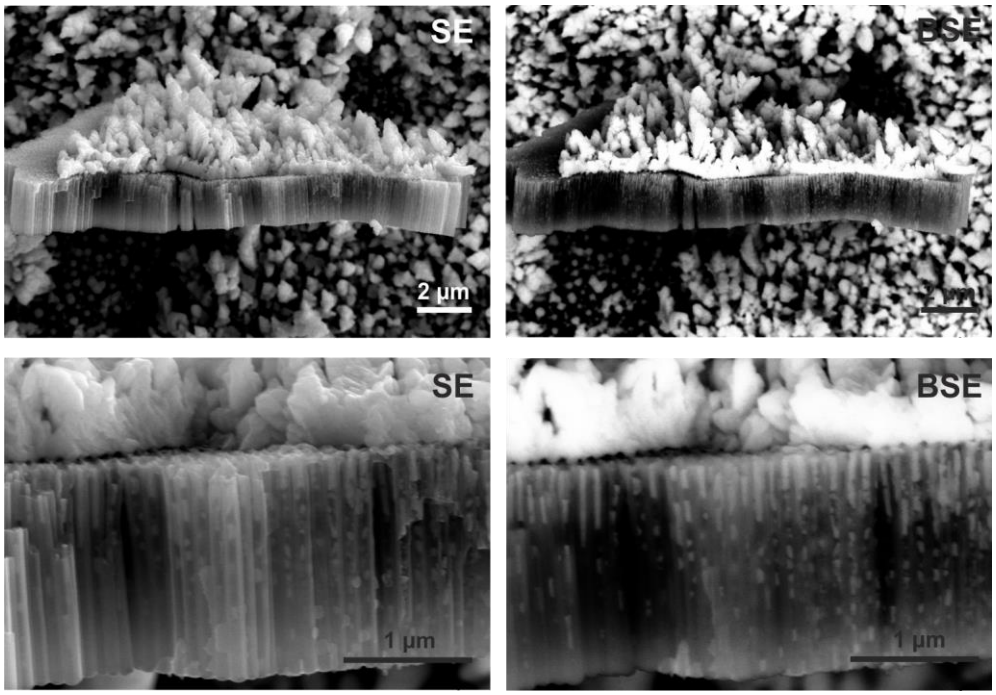

Fig. 2 *Left:* Secondary Electrons (SE) SEM images in cross-section of a titania nanotubular layer on which Sb has been electrodeposited from a solution consisting of 0.1 M $SbCl_3$ and 0.5 M citric acid using a pulsed-current deposition technique. *Right:* The same cross-sectional SEM images acquired in Back-Scattered Electrons (BSE) mode featuring improved chemical contrast. The bright regions correspond to the antimony deposit.

To confirm the presence of antimony in the inner volume of the nanotubes, EDX analysis is performed. The corresponding EDX spectrum is illustrated in Fig. 3.

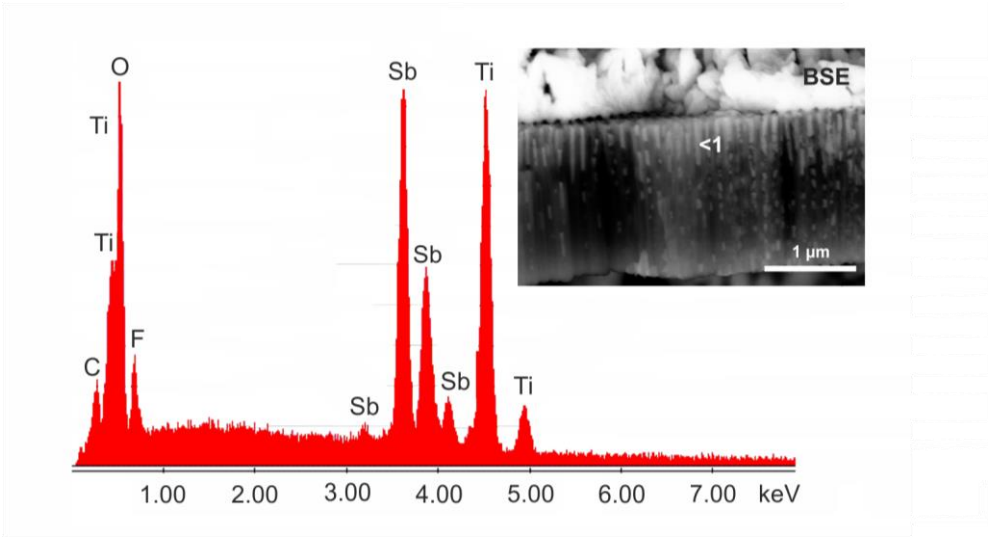

Fig. 3 EDX spectrum recorded from region 1 of the titania nanotubes on which Sb has been electrodeposited. This spectrum confirms the presence of antimony inside the tubes (inset shows corresponding SEM image in BSE mode indicating region 1).

Sb was also electrodeposited under the same conditions from solutions based on Sb_2O_3 as Sb^{3+} source and citric acid. Fig. 4 shows cross-sectional SEM images in BSE mode of the TiO_2 nanotube layers prepared from deposition baths containing 0.1 M Sb_2O_3 and 0.5 M citric acid (left side) and 0.1 M Sb_2O_3 and 1 M citric acid (right side), respectively. The pH of both solutions is raised to 6 by subsequent addition of 5 M KOH, since slightly acidic conditions inhibit oxide precipitation during deposition. From these SEM micrographs it is apparent that Sb can be deposited into the inner volume of the titania nanotubes in both cases. However, a larger amount of antimony as well as a wider distribution of the Sb deposits length inside the anodic TiO_2 tubes is obtained at lower concentrations of the complexing agent. This might be due to the fact that the availability of free Sb^{3+} ions decreases, the more citric acid is added. Additionally, large agglomerates of deposited Sb particles are observed on the surface of the titania nanotube layer. The insets of Fig. 4 (b) and (d) show representative EDX spectra of the deposit inside the tube and confirm the presence of antimony in the Sb/TiO_2 nanocomposite array.

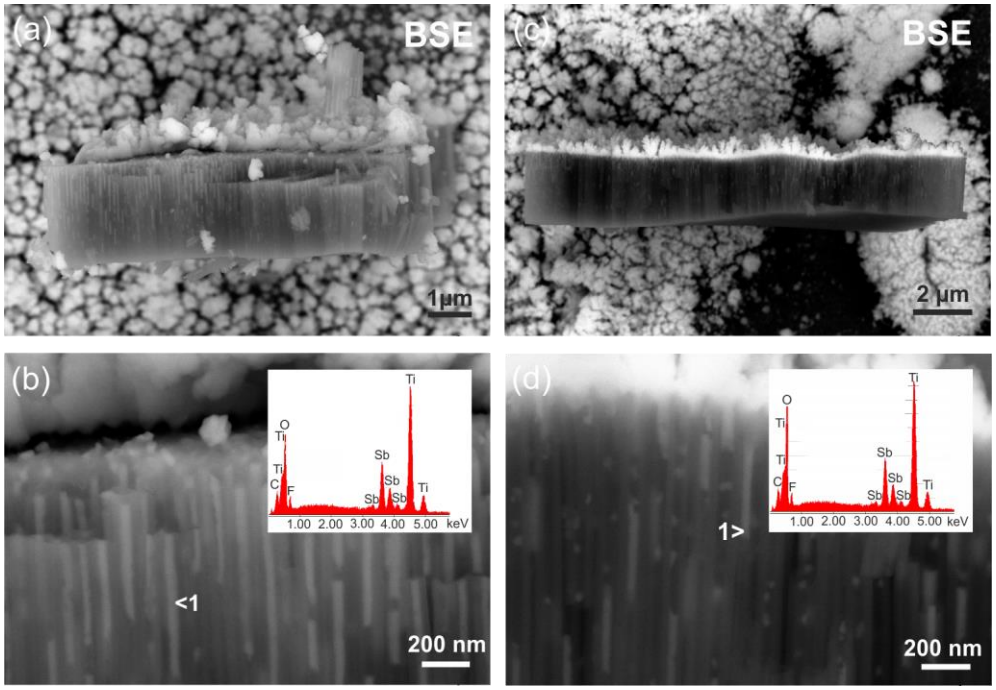

Fig. 4 Cross-sectional SEM images acquired with a BSE detector of titania nanotubes prepared from deposition baths consisting of 0.1 M Sb_2O_3 and 0.5 M citric acid (left side) and 0.1 M Sb_2O_3 and 1 M citric acid (right side). The insets in **(b)** and **(d)** show the corresponding EDX spectrum recorded from region 1.

Electrodeposition of Ni metal inside anodic titania nanotubes has also been investigated. Here, a Watts electrodeposition bath containing 1 M $NiSO_4 \cdot 6\ H_2O$, 0.2 M $NiCl_2$ and 0.5 M boric acid was used as deposition bath and pulsed electrodeposition was carried out at a constant current of $-1A/cm^2$ with a current on-time and off-time of 0.5 and 10 s, respectively. It should be noted that directly after the deposition process the surface of the Ni/TiO_2 nanocomposite substrate exhibited a metallic luster. Fig. 5, left side, illustrates cross-sectional SEM images acquired in SE mode of the as-deposited sample. The same regions are shown on the right side, however imaged with a BSE detector. It can clearly be seen that the titania nanotubes have been successfully filled with large amounts of nickel. Interestingly, in contrast to electrodeposited Sb, the Ni deposits are distributed along the entire tube length and are found in most of the nanotubes.

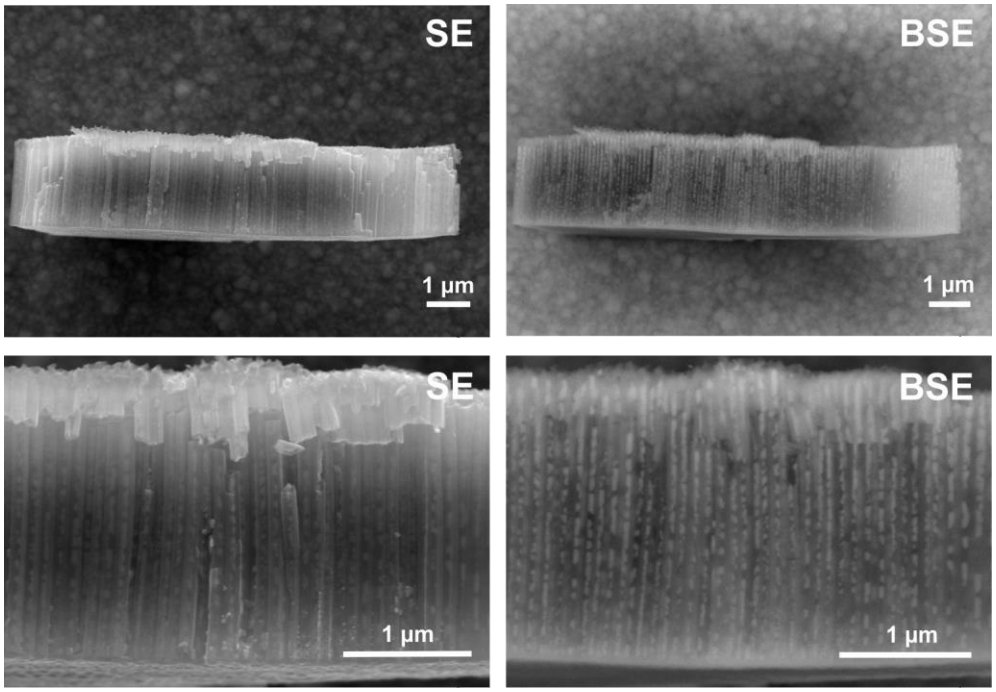

Fig. 5 *Left*: Secondary Electrons SEM images in cross-section view of titania nanotubes after Ni has been successfully deposited from a Watts electrolyte consisting of 1 M $NiSO_4 \cdot 6H_2O$, 0.2 M $NiCl_2$ and 0.5 M boric acid. *Right:* The same regions imaged with a BSE detector. Large amounts of Ni deposits can be found inside the tubes along the entire tube length.

SEM micrographs in top-view, as displayed in Fig. 6, confirm that nickel is indeed deposited into the inner volume of the TiO_2 nanotubes. In addition, a thick Ni layer is deposited on the surface of the titania nanotubes, which is responsible for the metallic luster of the sample after the deposition process. This layer can be peeled off and the surface after removing is illustrated in Fig. 6 (b). EDX analysis reveals the presence of nickel inside the tubes (see Fig. 7).

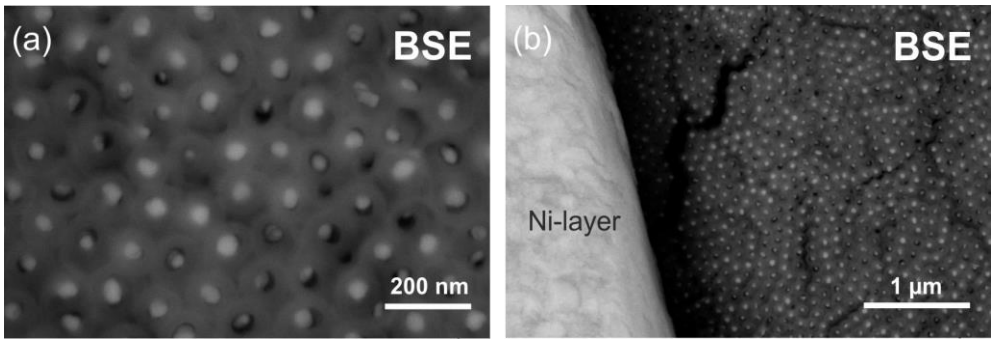

Fig. 6 **(a)** Top-view of the titania nanotube layer after Ni electrodeposition. It is evident that nickel is successfully embedded inside the tubes. **(b)** SEM image in top-view showing remnants of the Ni layer and the tube surface after removing of the layer.

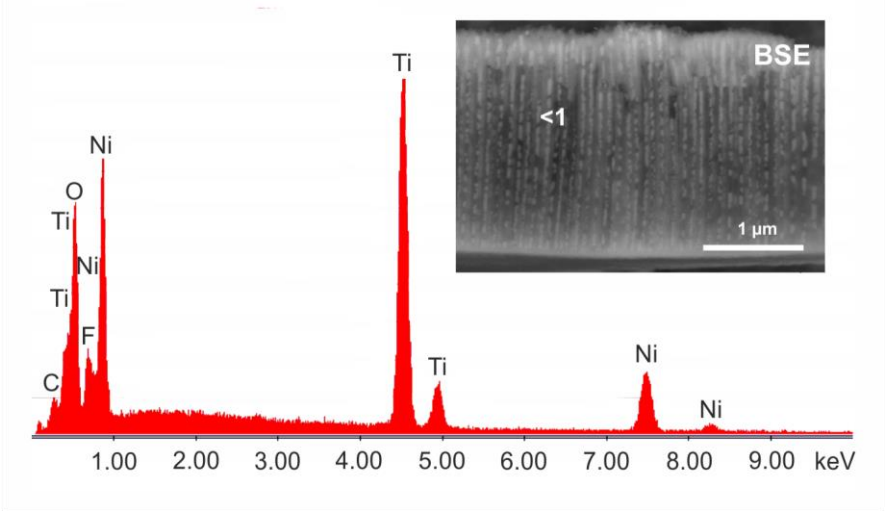

Fig. 7 Representative EDX spectrum obtained from region 1 (see inset) of the Ni/TiO_2 nanocomposite array, which confirms that Ni is present inside the titania nanotubes.

Additionally, we tried to deposit nickel from a solution containing 0.1 M $NiCl_2$ and 0.5 M citric acid using the same pulsed-current electrodeposition procedure described above. However, under these conditions filling of the titania nanotubes with Ni was not successful, as obvious from Fig. 8.

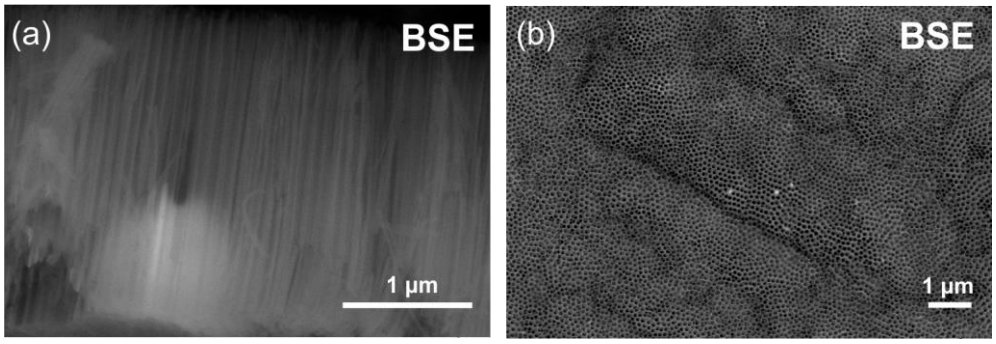

Fig. 8 Back-Scattered Electrons SEM images in **(a)** cross-section and **(b)** top-view of a nanotube layer on which nickel has been deposited from an electrolyte bath consisting of 0.1 M $NiCl_2$ and 0.5 M citric acid. No Ni deposits can be found inside the tubes.

Furthermore, we employed the same pulsed-current electrodeposition procedure described at the beginning to deposit Cu from an electrolyte bath consisting of 0.4 M $CuSO_4$ and 3 M lactic acid (pH to 7 by addition of 3 M NaOH). Fig. 9 presents scanning electron micrographs of the titania nanotube layer after copper electrodeposited. Small Cu particles can be observed on top of the nanotubular array, but not inside the tubes (see Fig. 9 (a)). The top-view image in Fig. 9 (b) corroborates that copper deposits are loaded on the surface and do not enter the tubes. But, from the cross-sectional images at higher magnification (see Fig. 9 (b) and (d)) it is evident, that fine grains of copper are deposited on the outside of the tube walls. The EDX spectrum, shown in the inset of Fig. 9 (d) confirms this observation.

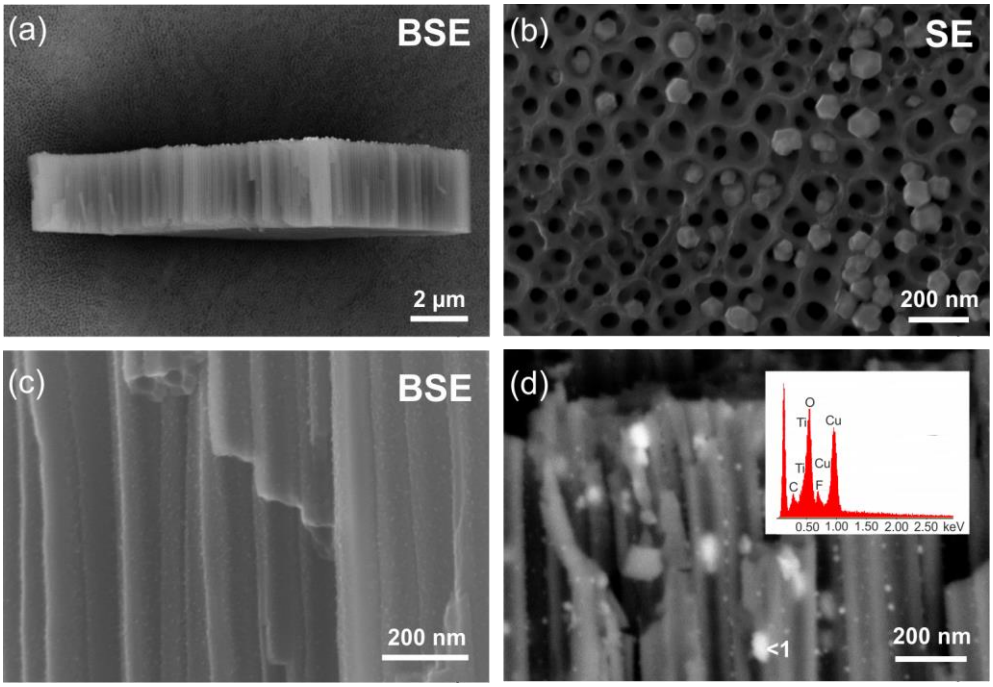

Fig. 9 SEM images in **(a)** cross-section and **(b)** top-view of the titania nanotube layer after electrodeposition of copper from a solution consisting of 0.4 M $CuSO_4$ and 3 M lactic acid (pH to 7 by addition of 3 M NaOH). **(c)** Secondary Electrons SEM image in cross-section at higher magnification. Fine grains of copper can be found on the outer tube wall. **(d)** Magnified BSE SEM micrograph of the Cu/TiO_2 sample. Inset shows the corresponding EDX spectrum recorded from region 1.

For the electrodeposition of Zn we used two different deposition baths: the first one consisted of 0.25 M $ZnCl_2$ as Zn^{2+} source and 0.5 M H_3BO_3, the second one was a sulfate-based bath containing 0.6 M $ZnSO_4 \cdot 7 H_2O$ and 0.1 M$(NH_4)_2SO_4$. Fig. 10 presents SEM images in BSE mode of the titania nanotubes after Zn has been deposited from the solution consisting of $ZnCl_2$ and boric acid. Clearly, zinc can be found in some of the tubes, as seen in the top-view image in Fig. 10 (a). But, the cross-sectional image in Fig. 10 (b) indicates that Zn is only deposited at the top of the nanotubes close to the surface. The EDX spectrum recorded from the top part of the TiO_2 layer confirms the presence of Zn in this region (see Fig. 11).

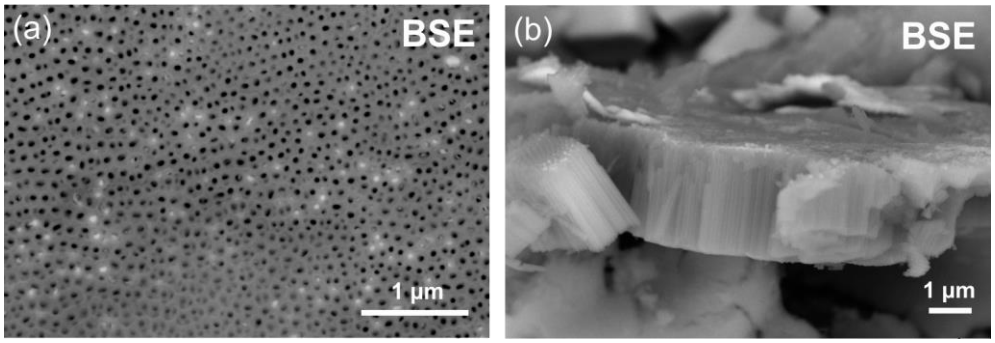

Fig. 10 SEM micrographs acquired with a BSE detector in top-view **(a)** and cross-section **(b)** of the titania nanotube layer on which Zn has been deposited from a solution consisting of 0.25 M $ZnCl_2$ and 0.5 M H_3BO_3. Zinc can only be found in some tubes at the top close to the surface.

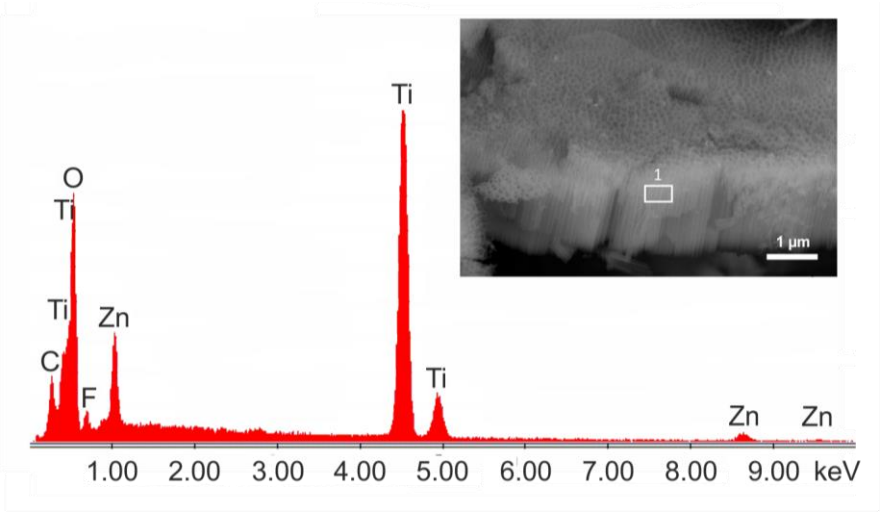

Fig. 11 Corresponding EDX spectrum recorded from the top part of the titania nanotube layer (region 1).

Pulsed electrodeposition of Zn from the sulfate-based bath just leads to the formation of a thick, compact zinc layer on the surface of the titania nanotubular array. No filling of the nanotubes is obtained under these conditions (see Fig. 12).

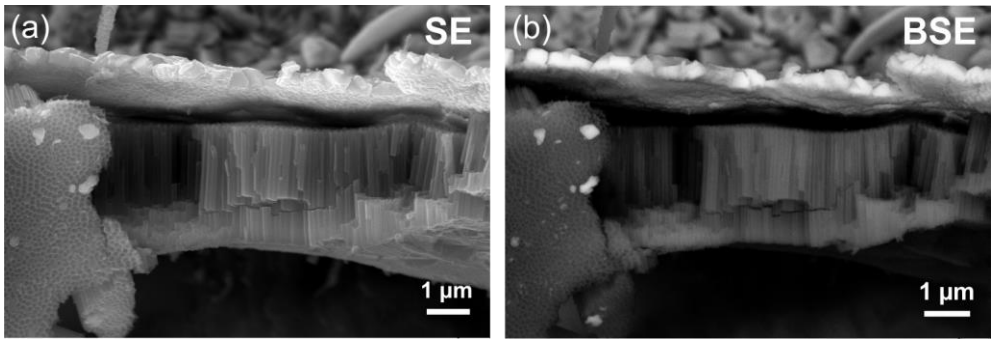

Fig. 12 **(a)** Secondary Electrons SEM image in cross-section after pulsed electrodeposition of Zn from a sulfate-based bath containing 0.6 M $ZnSO_4 \cdot 7\ H_2O$ and 0.1 M $(NH_4)_2SO_4$. **(b)** The same region imaged with a BSE detector. It is evident that electrodeposition of Zn under these conditions leads to the formation of a compact zinc layer on the surface of the tubes.

Finally, we will consider the results obtained from the electrodeposition of indium metal. Fig. 13 presents SEM micrographs in SE and BSE mode of the titania nanotubes after indium electrodeposited from a deposition bath mixture consisting of 0.1 M $InCl_3$ and 0.5 M citric acid. It can clearly be seen that large In particles are formed during the electrodeposition process, which destroy the nanotubular structure. The inset of Fig. 13 (d) shows a representative EDX spectrum of the In deposit between the nanotubes.

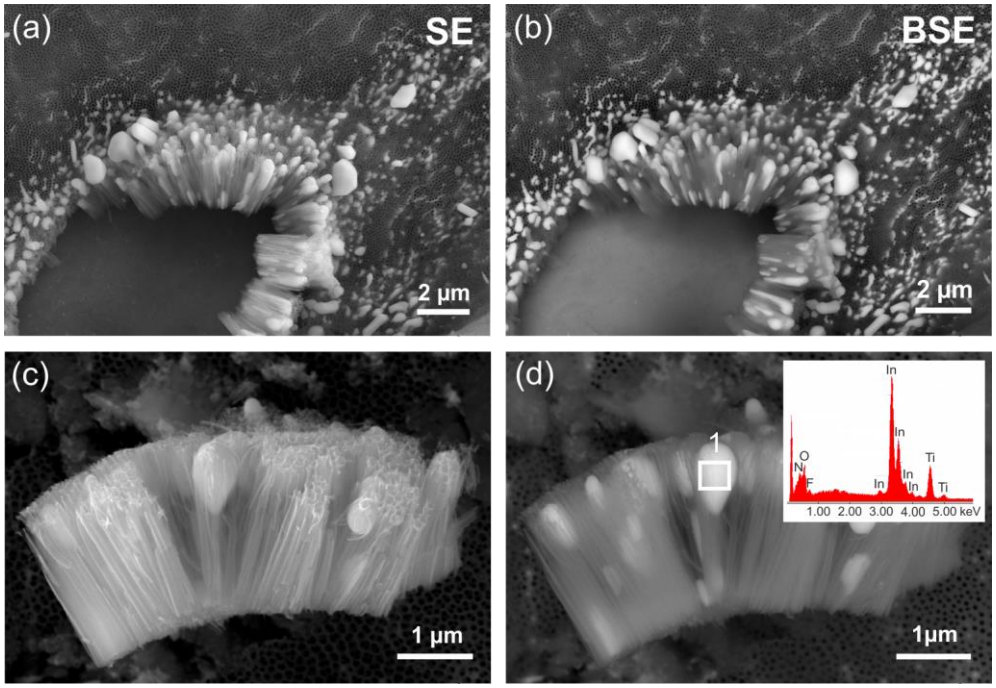

Fig. 13 *Left:* SEM images acquired with a SE detector of a titania nanotube sample on which indium has been deposited. *Right:* The same regions recorded in BSE mode. It can clearly be seen that large In particles are formed during electrodeposition, which leads to a destruction of the nanotubular structure. Inset in **(d)** shows the corresponding EDX spectrum recorded from region 1.

Conclusion

In summary, we have demonstrated that pulsed-current electrodeposition is a versatile and effective method to fabricate various metal/ TiO_2 nanocomposites. The used pulsed deposition procedure (I_{on} = −1A/cm^2, t_{on} = 0.5 s, t_{off} = 10 s) and the optimized composition of the deposition baths resulted in a successful filling of the titania nanotube layers with Sb and Ni metal. Deposition of Cu, Zn and In inside the tubes was not achieved under these conditions. Thus, further optimization of the pulse program and the bath composition is necessary for a successful encapsulation of these metals into the inner volume of the tubes.

Acknowledgement. Financial support by the Austrian Federal Ministry for Digital and Economic Affairs and the National Foundation for Research, Technology and Development is gratefully acknowledged. We also thank the Deutsche Forschungsgemeinschaft (FOR1277, WI 3600 2-1, 4-1; SPP 1415 WI 3600 5-2) for financial support.

References:

1. D.V. Bavykin, J.M. Friedrich and F.C. Walsh, *Adv. Mater.*, **18** (2006) 2807-2824.
2. P. Roy, S. Berger and P. Schmuki, *Angew. Chem. Int. Ed.*, **50** (2011) 2904-1939.
3. J. M. Macák, H. Tsuchiya, A. Ghicov, K. Yasuda, R. Hahn, S. Bauer and P. Schmuki, *Curr. Opin. Solid State Mater. Sci.*, **11** (2007) 3-18.
4. J.M. Macák, H. Tsuchiya, A. Ghicov and P. Schmuki, *Electrochem. Commun.*, **7** (2005) 1133-1137.
5. H. Xiong, M.D. Slater, M. Balasubramanian, C.S. Johnson and T. Rajh, *J. Phys. Chem. Lett.*, **2** (2011) 2560-2565.
6. M. Paulose, O.K. Varghese, G.K. Mor, C.A. Grimes and K.G. Ong, *Nanotechnology*, **17** (2006) 398.
7. J.M. Macák, F. Schmidt-Stein and P.Schmuki, *Electrochem. Commun.*, **9** (2007) 1783-1787.
8. A.L. Linsebigler, G. Lu and J.T. Yates, *Chem. Rev.*, **95** (1995) 735-758.
9. R. Wang, K. Hashimoto, A. Fujishima, M. Chikuni, E. Kojima, A. Kitamura, M. Shimohigoshi and T. Watanabe, *Adv. Mater.*, **10** (1998) 135.138.
10. S.-H. Oh, R.R. Finones, C. Daraio, L.-H. Chen and S. Jin, *Biomaterials*, **36** (2005) 4938-4943.
11. N.K. Shrestha, M. Yang, Y.-C. Nah, I. Paramasivam and P. Schmuki, *Electrochem. Commun.*, **12** (2010) 254-257
12. N.K. Shrestha, J. M. Macák, F. Schmidt-Stein, R. Hahn, C.T. Mierke, B. Fabry and P. Schmuki, *Angew. Chem Int. Ed.*, **48** (2009) 254-257-
13. I. Paramasivam, J.M. Macák, A. Ghicov and P. Schmuki, *Chem. Phys. Lett.*, **445** (2007) 233-237.
14. Z. Wei, H. Mao, T. Huang and A. Yu, *J. Power Sources*, **223** (2013) 50-55.
15. X. Jiao, T. Zeng, P. Ji, Q. Peng, B. Shang and X. Hu, *J. Alloys Compd.*, **739** (2018) 1-8
16. D. Prutsch, M. Wilkening and I. Hanzu, *RSC Adv.*, **6** (2016) 98243-98247.
17. M.S. Chandrasekar and M. Pushpavanam, *Electrochim. Acta*, **53** (2008) 3313.
18. N. Liu, K. Lee and P. Schmuki, *Angew. Chem. Int. Ed.*, **52** (2013) 12381-12384.

6.1.2 Titania nanotubes and Sn/TiO_2 nanocomposites as anode material for sodium-ion and lithium-ion batteries

Self-organized TiO_2 nanotubes have also attracted particular attention in the battery research field [106]. Their ability to reversibly insert small cations, such as Li^+ or Na^+, into its lattice combined with their large specific surface area and relatively short ion diffusion lengths transform them into powerful negative electrode materials for Li-ion and Na-ion batteries [104, 133]. Titania nanotube layers prepared by anodic oxidation of a metallic titanium substrate provide an additional advantage: the direct growth of TiO_2 nanotubes on the current collector eliminates the need for conductive agents and binders. This simplifies the fabrication process and improves the stability of the battery [221, 222]. Such approaches can be highly relevant in the field of microbatteries.

While the electrochemical reactions of anodic titania nanotubular layers with Li^+ have already been studied in more detail [223], the particularities of the Na^+ insertion reaction into nanostructured TiO_2 are a more recent achievement. Thus, in the following article **P2**, we investigated several titania nanotubes samples, which differed in lengths and diameters according to the anodizing conditions, with respect to their Na^+ storage behavior. Electrochemical characterization of the Na half-cells using common techniques such as galvanostatic cycling and cyclic voltammetry allowed us to disclose the underlying storage mechanism. In contrast to lithium insertion into TiO_2, where most of the stored Li^+ ions can be found in the bulk regions, sodium storage preferentially occurs on the surface of the titania nanotube walls. The determined low values of the diffusion coefficient support the proposed interfacial storage mechanism. In addition it was noticed that these materials can withstand a large number of cycles without significant loss of capacity.

Sn-based alloy materials were already considered as promising anode material owing to their high theoretical Li and Na storage capability. In particular, complete lithiation of Sn into $Li_{4.4}Sn$ results in theoretical specific capacity values of 993 mAh/g [27], while Sn and Na can form $Na_{15}Sn_4$ alloy with a capacity of approximately 847 mAh/g [68]. However, these materials suffer from huge volume expansion/contraction during cycling and from particle aggregation leading to severe fracturing and mechanical disintegration of the negative electrode [25]. Encapsulation of metallic Sn into ordered titania nanotubes provides an opportunity to avoid coalescence of tin nanoparticles and to compensate changes in volume during alloying/de-alloying. In doing so, the advantages of both materials, the high capacity of tin and the structural stability of the titania nanotubular layers, can be combined.

In manuscript **M2** the results of the electrochemical study on Sn/TiO_2 nanocomposites as negative electrode material for Li-ion and Na-ion batteries are summarized. Although embedding tin metal into the inner volume of the titania nanotubes does not lead to higher capacity values, a better cycling stability compared to a pure Sn electrode was observed.

P2:

Long-Cycle-Life Na Ion Anodes Based on Amorphous Titania Nanotubes – Interfaces and Diffusion

D. Prutsch, M. Wilkening and I. Hanzu

ACS Appl. Mater. Interfaces, **7** (2015), 25757.

ACS APPLIED MATERIALS & INTERFACES

Research Article

www.acsami.org

Long-Cycle-Life Na-Ion Anodes Based on Amorphous Titania Nanotubes—Interfaces and Diffusion

Denise Prutsch, Martin Wilkening, and Ilie Hanzu*

Institute of Chemistry and Technology of Materials, Graz University of Technology, Stremayrgasse 9, 8010 Graz, Austria
ALISTORE-ERI European Research Institute, 33 rue Saint Leu, 80039 Amiens, France

ABSTRACT: Amorphous self-assembled titania nanotube layers are fabricated by anodization in ethylene glycol based baths. The nanotubes having diameters between 70−130 nm and lengths between 4.5−17 μm are assembled in Na-ion test cells. Their sodium insertion properties and electrochemical behavior with respect to sodium insertion is studied by galvanostatic cycling with potential limitation and cyclic voltammetry. It is found that these materials are very resilient to cycling, some being able to withstand more than 300 cycles without significant loss of capacity. The mechanism of electrochemical storage of Na^+ in the investigated titania nanotubes is found to present significant particularities and differences from a classical insertion reaction. It appears that the interfacial region between titania and the liquid electrolyte is hosting the majority of Na^+ ions and that this interfacial layer has a pseudocapacitive behavior. Also, for the first time, the chemical diffusion coefficients of Na^+ into the amorphous titania nanotubes is determined at various electrode potentials. The low values of diffusion coefficients, ranging between 4×10^{-20} to 1×10^{-21} cm^2/s, support the interfacial Na^+ storage mechanism.

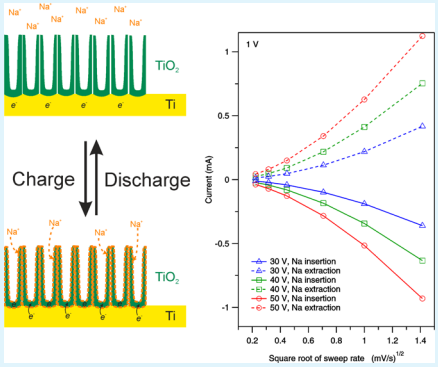

KEYWORDS: *TiO_2 nanotubes, Na-ion batteries, interfaces, faradaic adsorption, diffusion*

1. INTRODUCTION

Apart from the already well-established Li-ion technology, an emergent area of interest in advanced electrochemical energy storage is constituted by the sodium ion (Na-ion) technology.[1−3] In principle, instead of using Li ions in the ionic internal circuit of the battery, these systems make use of Na ions. It is interesting to notice that this field was studied early in the 1980s,[4] long before the commercialization of Li-ion technology and that the field was almost abandoned following the commercial success of Li-ion systems. There is renewed interest in Na-ion systems for various economical and political reasons, such as very low cost and very good availability of sodium in comparison to lithium, sodium resources are evenly distributed with respect to economically viable lithium containing minerals etc. Although Na-ion batteries based on insertion chemistry are, in general, expected to have lower specific capacity and energy than Li-ion systems, it is plausible that Na-ion technology may be a solution of choice for medium- and large-scale application, such as household batteries, designed to secure and buffer the power supply from local renewable sources (e.g., photovoltaics) or even grid-relevant batteries. It is obvious that a low cost as well as an extended cycle-life would represent very valuable assets. However, sodium chemistry in Na-ion galvanic cells is, more often than not, different from lithium. Many particularities are poorly understood and require consistent further study as it is only seldom possible to directly translate the knowledge accumulated in the last two decades for lithium, to the sodium systems.

Historically, the first compounds that were shown to reversibly intercalate sodium ions belong to the category of metal oxide bronzes,[5] that are nonstoichiometric ternary oxides containing an alkali metal and at least one transition metal that may take at least two stable oxidation states. Various sodium bronze phases containing Co[6,7] and Mn[8] were early demonstrated to be electrochemically active with respect to Na insertion reaction. Since then, these materials have been significantly improved[9] and a large variety of other new compounds emerged, such as transition metal fluorides,[10] phosphates[11] and fluorophosphates,[12,13] olivines,[14] NASICON framework compounds,[15] etc. It has to be noted that all these materials will undergo a reaction with sodium ions at high potential vs Na^+/Na reference redox couple, a property that makes them suitable as positive electrode (cathode) materials.

On the other hand, there is a relatively limited choice of suitable compounds operating at low Na^+ insertion potentials and thus able to serve as negative electrode (anode) active materials. It would appear that research on anode materials is lagging behind the development of cathode materials. On short, only hard carbon materials,[16−18] few titanium containing phases,[19−23] as well as some Sn−Sb/C intermetallic nanocomposites,[24−28] Sn−Cu alloys[29] and nanostructured Ge[30] were hitherto reported to present significant sodium storage capacities at low potentials. Many of these materials have less

Received: August 13, 2015
Accepted: October 29, 2015
Published: October 30, 2015

ACS Publications © 2015 American Chemical Society

DOI: 10.1021/acsami.5b07508
ACS Appl. Mater. Interfaces 2015, 7, 25757−25769

than optimum cycle-life. The surface passive films (solid electrolyte interphase, SEI) occurring on Na-ion anodes tend to be unstable and are unfortunately poorly understood, in spite of some encouraging recent developments.[31,32] Thus, research efforts aimed toward synthesis, fabrication, and development of new materials would be fully justified and required in order to achieve high-quality, long-lasting negative electrodes.

From the very beginning, it has been noted that the use of metallic sodium is considered impractical in a real cell. Sodium has a low melting point of 97.7 °C, which is much lower than the melting point of lithium (180.5 °C), a higher reactivity with air, moisture, organic compounds, etc., and a pronounced tendency to form dendrites during Na plating when the cell is recharged. In fact, the use of metallic sodium in a galvanic cell is expected to be even more troubling than lithium, an old issue that has not been satisfactorily solved yet, in spite of at least three decades of research efforts. Thus, high performance host materials that are able to reversibly insert Na^+ at low potentials are sorely needed.

Some time ago, carbonaceous materials mainly consisting of various nongraphitic phases, also known as hard carbons, were shown to present useful sodium storage capacities[33] and reasonable cycling behavior. However, much of their reversible capacity occurs close to 0 V vs Na^+/Na.[17] Such low operating potentials may easily lead to highly undesired, finely divided, metallic Na plating on the electrode upon the slightest electrode overcharge. Needless to say that such a situation would compromise the safety of any electrochemical system and, therefore, materials with slightly higher insertion potentials would be desirable.

Although the existence and synthesis of sodium titanium bronzes was proven decades ago,[34,35] the use of titanium-based materials for negative electrodes in Na-ion batteries was only recently demonstrated. The sodium titanate phase $Na_2Ti_3O_7$ was shown to have one of the lowest sodium insertion potential for an oxide material,[36] approximately 0.3 V vs Na^+/Na, just above the electrochemical potential of hard carbons, a characteristic that would ensure reasonable built-in safety of an eventual Na-ion device. Another interesting material is titania which has relatively re-emerged as a possible negative electrode material for Li-ion batteries[37−39] showing high and very high rate capability and good cycling behavior. Titania is associated with low environmental costs and excellent availability. Although some initial reports showed that anatase titania cannot reversibly insert sodium,[40] very recently, nanostructured TiO_2 was in fact demonstrated to be able to serve as a host material for sodium ions.[41] It appears that a carefully controlled (nano)crystalline structure and morphology of these materials, as well as a careful selection of electrolyte formulation, ensure the good cycling behavior of nanostructured anatase.

In this paper, we present an electrochemical study of sodium insertion into self-assembled amorphous titania nanotubes prepared by electrochemical oxidation (anodization) in nonaqueous electrolytes based on ethylene glycol. The highly parallel titania nanotubular arrays were tested using common electrochemical techniques in the absence of any other additives such as conductive agents or binders. Galvanostatic cycling was carried out routinely for 200 cycles or more. The results offer a valuable insight into the characteristics, behavior, and storage mechanisms of this interesting and relatively new class of materials that broaden the choice of negative Na-ion active materials.

2. EXPERIMENTAL SECTION

2.1. Synthesis of TiO_2 Nanotubes. Titanium foils (99.7%, 0.25 mm thick, Sigma-Aldrich) were cut in small square pieces (12.5 by 12.5 mm). These substrates were ultrasonically cleaned in acetone, isopropanol and methanol, in this order, for 10 min, in each of the above-mentioned solvents. Subsequently, these samples were rinsed with distilled water and quickly dried with compressed air. For anodization, an electrochemical cell in a two-electrode configuration with the titanium foil as working electrode and a stainless steel plate as counter electrode was used. In this cell, the sample was pressed against a brass ring to ensure a good electrical contact, while leaving a surface area of 0.708 cm^2 of the titanium substrate exposed to the anodization bath, which consisted of 0.4 wt % NH_4F, 2 wt % distilled water, and 97.6 wt % ethylene glycol. For the experiments, the cell was connected to a precision DC power supply (Agilent E3610A) and anodization was carried out at several constant voltages (30, 40, 50, and 60 V) and for various time intervals (30 min, 1 and 2 h). Finally, the as-anodized samples were ultrasonically cleaned in distilled water for 15 s and dried with compressed air. All experiments were done at room temperature at approximately 23 (±1)°C.

2.2. Electrochemical Characterization. Na half-cells were assembled in pouch-type cells (Dai Nippon Printing Co., Ltd.) using sodium metal (ACS reagent, Sigma-Aldrich) as counter and reference electrode and two sheets of a nonwoven material as separator (Freudenberg FS 2190). The cells were assembled with the aforementioned titania films (9.5 mm in diameter) supported on a Ti foil 12.5 by 12.5 mm as the working electrode and a Na foil, 14 by 14 mm, approximately 2 mm thick, as the counter electrode. A smaller piece of sodium,was used as a reference electrode of the first kind. The electrolyte consisted of a solution of 1 M $NaClO_4$ in propylene carbonate. Galvanostatic charge/discharge cycling of the sodium half-cells was carried out at constant current rates of 50 mA/g and 25 mA/g in the potential ranges of 0.8−2 V and 0.1−2 V vs Na^+/Na, respectively. Cyclic voltammograms were recorded between 0.1 and 2 V at different scan rates (0.05, 0.1, 0.2, 0.5, 1, 2, 5, and 10 mV/s). Both galvanostatic cycling as well as cyclic voltammetry experiments were performed at room temperature using a multichannel MPG-2 potentiostat from Biologic Science Instruments running EC-LAB VIO-34 software. Cycled electrodes used for analysis were removed from the cells and cleaned by thoroughly rinsing with propylene carbonate (anhydrous, 99.7%, Sigma-Aldrich) and dimethyl carbonate (anhydrous, ≥ 99%, Sigma-Aldrich). All assembling and disassembling operations of the cells were carried out in a glovebox under an argon atmosphere with O_2 and H_2O vapor concentrations lower than 1 ppm.

2.3. Composition and Morphological Characterization. Scanning electron microscopy (INCA X-act Penta FET Precision TESCAN) was employed for the morphological characterization of the pristine TiO_2 nanotubes. To obtain the composition and the morphology of the cycled samples, we used a scanning electron microscope equipped with an EDX-detector (ZEISS Ultra 55). SEM cross-section images were taken from samples that were intentionally scratched just before placing them into the SEM vacuum chamber.

3. RESULTS

SEM (scanning electron microscope) pictures of the pristine samples are presented in Figure 1. It can be noticed that the nanotubes have various diameters and lengths that are directly determined by the anodization conditions. The dependence of the tube diameter on the voltage applied has already been established in the literature.[42] Thus, in our case, the smallest tube diameter, of approximately 70 nm, is observed when anodization is done at 30 V, 100 nm at 40 V, 120 nm at 50 V, and 130 nm at 60 V. The lengths of the nanotubes increase with the anodization time, the voltage and etching rate.[42] It was found that after anodization at 30 V for 2 h the nanotubes length was approximately 4.5 μm, at 40 V after 2 h the tubes were approximately 8 μm long, at 50 V after 1 h the tubes were

DOI: 10.1021/acsami.5b07508
ACS Appl. Mater. Interfaces 2015, 7, 25757−25769

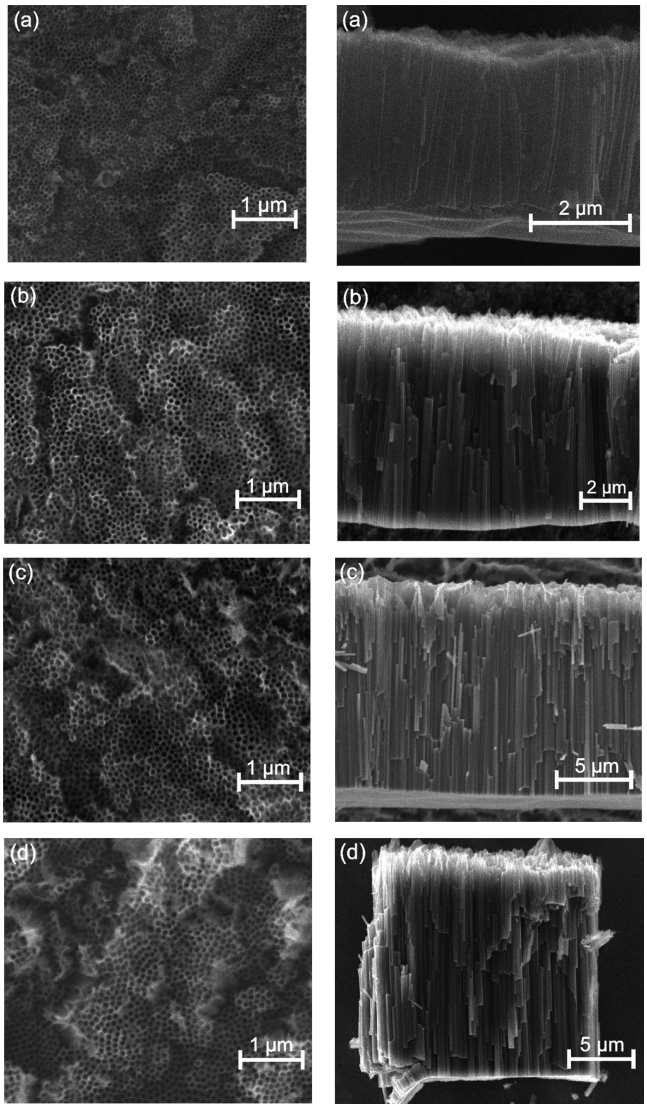

Figure 1. SEM pictures of anodized samples at (a) 30 V for 2 h, (b) 40 V for 2 h, (c) 50 V for 2 h, (d) 60 V for 1 h. Left, top-view, right, cross-section. All samples present the highly parallel nanotubular morphology. The pore diameter is determined by the anodization voltage while the length of the nanotubes is determined by the anodization time, the voltage, and the etching rate.

9.1 μm long, whereas at 60 V after 1 h, the tube length was 17.3 μm.

Galvanostatic cycling with potential limitation was used to investigate the electrochemical Na^+ storage capacity of the nanotubular layers presented in Figure 1. For all these experiments the vacuum-dried nanotube layers were assembled in pouch cells using a Na metal foil as the counter electrode and a small piece of metallic sodium as reference electrode. The electrolyte used was 1 M $NaClO_4$ dissolved in anhydrous propylene carbonate (PC). Two lower cutoff voltage limits were used: 0.8 and 0.1 V, both measured vs Na^+/Na reference. The upper voltage limit was always 2 V vs Na^+/Na reference. The results of the galvanostatic cycling experiments carried out between 0.8 and 2 V vs Na^+/Na are shown in Figure 2.

One of the most remarkable features of these highly parallel titania nanotubes is their ability to withstand a large number of cycles without significant loss of capacity, as illustrated in Figure 2. The majority of the investigated samples present a so-called

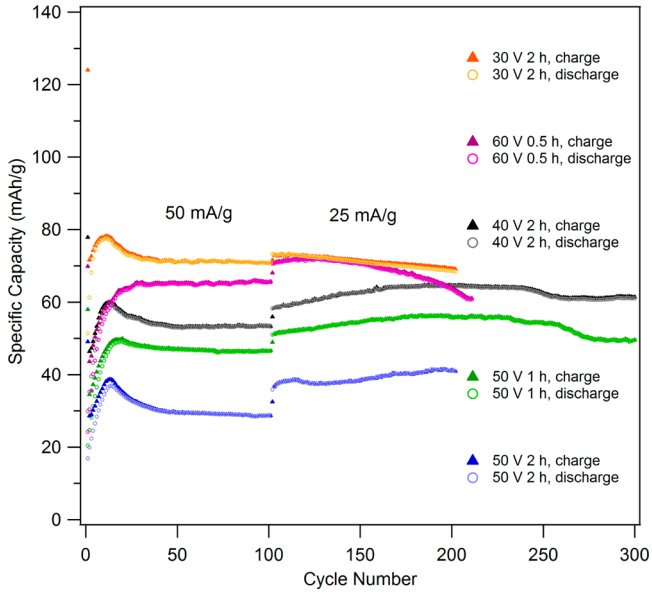

Figure 2. Galvanostatic cycling vs Na of various titania nanotube layers fabricated in different anodization conditions. The samples were cycled between 0.8 and 2 V vs Na^+/Na at two different rates: 50 mA/g during the first 100 cycles followed by 25 mA/g for the following cycles. The stable value of reversible capacity, reached after several tens of cycles, is strongly dependent on the dimension of the nanotubes.

capacity enhancement behavior occurring in the first cycles, a fact that has recently been reported in the literature.[22] It can be noticed in Figure 2 that the capacity increases over the first 10–20 cycles from a relatively low initial value. The specific capacity passes then through a maximum value, finally followed by the stabilization of the capacity at slightly lower values for the next 200 cycles. Furthermore, some self-improvement of the reversible capacity can be also noticed for most of the samples prepared at anodization voltages of 40, 50, and 60 V, when the cycling rate is halved to 25 mA/g, after the nanotubes were cycled at 50 mA/g during the first 100 cycles. It can easily be noticed that the values of the specific capacities are strongly dependent on the dimension of the nanotubes, which are, at their turn, obviously dictated by the anodization conditions. A summary of the recorded capacities at several selected points during cycling is given in Table 1.

To evaluate the behavior of these materials also at low potentials, we extended the lower potential limit used for galvanostatic cycling from 0.8 to 0.1 V and the sample was cycled between 0.1–2 V. These measurements were done after the samples were already cycled between 0.8–2 V. The results of the galvanostatic cycling of titania nanotubes between 0.1 and 2 V vs Na^+/Na are shown in Figure 3. It is obvious that the situation changes dramatically when the lower potential limit used for galvanostatic cycling is extended to 0.1 V. In spite of a somewhat higher initial capacity, all the samples present a continuous decay of capacity with cycling. Whereas the difference between charge and discharge was barely visible when the potential was limited to 0.8 V, lowering the cycling limit to 0.1 V leads to high irreversibility and continuous capacity fading over the entire duration of the cycling, as clearly illustrated in Figure 3.

To understand the behavior of these titania nanotubes with respect to the Na^+ insertion reaction, cycling voltammetry experiments were performed at various scan rates between 0.1 and 2 V vs Na^+/Na reference. These results, presented in

DOI: 10.1021/acsami.5b07508
ACS Appl. Mater. Interfaces 2015, 7, 25757–25769

Table 1. Overview of the Reversible Na^+ Storage Capacity (mAh/g) of Anodic Titania Nanotubes

		cycling rate						
		50 mA/g					25 mA/g	
sample	V limit	1st cycle	5th	max @ cycle no.	50th	100th	150th	200th
30 V 2 h	0.8	51	74	78@11	71	71	71	68
40 V 2 h	0.8	30	46	60@13	53	53	63	64
50 V 2 h	0.8	17	26	36@14	29	29	39	41
50 V 1 h	0.8	21	34	49@19	47	47	55	56
60 V 0.5 h	0.8	24	44	no max	65	65	70	64
40 V 2 h	0.1	152	150	154@2	120	96	54	40
50 V 2 h	0.1	141	143	146@2	106	67	51	37
50 V 1 h	0.1	135	131	138@2	84	60	50	40

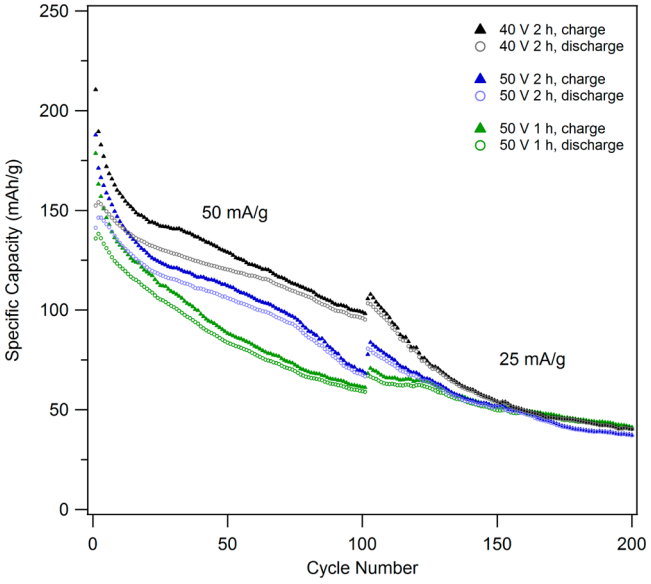

Figure 3. Galvanostatic cycling vs Na of various titania nanotubes prepared in different anodization conditions. The samples were cycled between 0.1 and 2 V vs Na^+/Na after previous cycling between 0.8 and 2 V for 200 to 300 times. The same cycling rates were used: 50 mA/g for the first 100 cycles followed by 25 mA/g for the following cycles. The samples present significant capacity fading over cycling when the potential limit is lowered to 0.1 V.

Figure 4, correspond to a sample anodized at 50 V for 2 h. Very similar behaviors were recorded for samples anodized at 30 and 40 V for 2 h. It can be seen that titania nanotubes do not present any discernible reduction or oxidation peaks associated with the reversible insertion of Na^+ into TiO_2 and the electrochemical reaction takes place over a very large potential domain. This may be understood if we consider that these materials do not undergo a phase transition during the electrochemical reaction with Na^+, a situation that has previously been reported for Li^+ insertion in amorphous titania nanotubes.[43] Indeed, in the case of a single phase mechanism, the electrochemical potential of the titania nanotubes varies continuously with the sodium content (vide infra Section 4.1.).

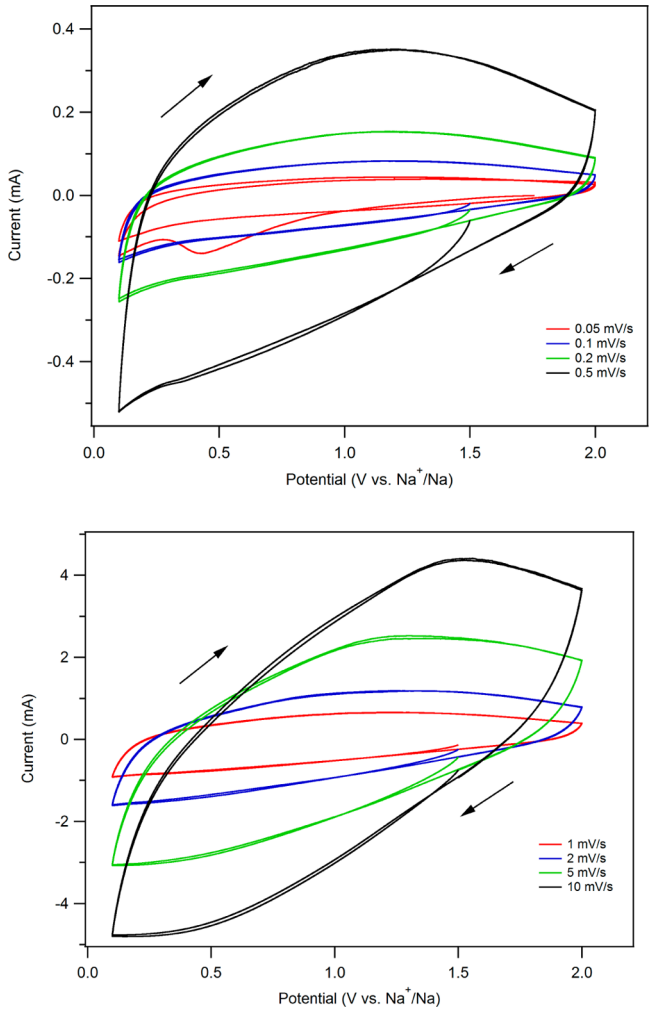

Figure 4. Cyclic voltammetry of an amorphous titania nanotube layer fabricated by anodization at 50 V for 2 h at various sweep rates ranging successively from 0.05 mV/s to 10 mV/s. The experiment was carried out in a solution of 1 M $NaClO_4$ in PC (propylene carbonate) in a three-electrode cell configuration. The working electrode was the titania nanotube while the counter and the reference electrodes were made of metallic sodium. With the exception of the broad irreversible reduction peak at approximately 0.4 V in the first cycle (at 0.05 mV/s), no other peaks are observed pointing to an insertion mechanism that occurs without a phase transition.

Some small changes in the voltammogram slope during the cathodic scan in the regions close to 0.1 V vs Na^+/Na may indicate the onset of some processes having slightly different kinetics that could not be clearly identified. The only clear peak, centered at approximately 0.4 V vs Na^+/Na, although still very broad, can be observed only in the first scan done at a sweep rate of 0.05 mV/s. This irreversible peak, not observed on subsequent cycles, has its likely origin in impurities such as water, ethylene glycol or other anodization compounds that could not be removed after the anodization process. Afterward, all the processes involved show a relatively good reversibility, irrespective of the sweep rate. Indeed, a good overlap is observed for the two cycles carried out at each sweep rate, the only exception being the very first scan as shown before (see above).

Although at slow sweep rates the cathodic part of the cyclic voltammogram is not matched by a symmetrical anodic part, at fast sweep rates it can be noticed that the symmetry of the

DOI: 10.1021/acsami.5b07508
ACS Appl. Mater. Interfaces 2015, 7, 25757−25769

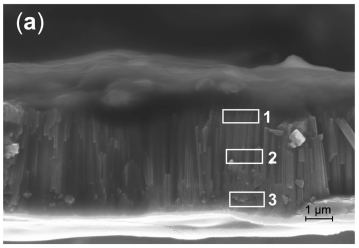

	elements (at%)				
	O	F	Na	Cl	Ti
position 1	62.30	4.41	18.76	0.56	13.97
position 2	55.94	6.26	17.02	0.19	20.59
position 3	53.21	7.06	14.08	-	25.65
surface	61.07	1.75	30.29	0.95	5.93

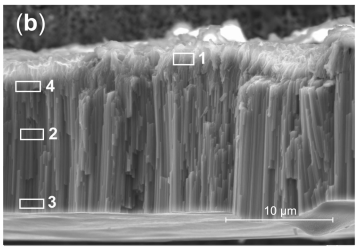

	elements (at%)				
	O	F	Na	Cl	Ti
position 1	61.08	5.07	24.94	-	8.90
position 2	55.75	7.04	16.14	-	21.07
position 3	57.71	7.12	13.44	-	21.72
position 4	63.06	5.19	18.58	-	13.17
surface	57.92	4.87	23.44	-	13.77

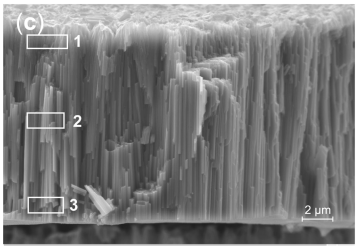

	elements (at%)				
	O	F	Na	Cl	Ti
position 1	61.64	4.24	20.83	-	13.30
position 2	60.88	7.26	15.43	-	16.43
position 3	61.06	8.91	13.42	-	16.62
surface	60.86	4.71	22.08	-	12.36

Figure 5. Cross-section SEM images of nanotube layers anodized at (a) 30 V for 2 h, (b) 40 V for 2 h, and (c) 60 V for 30 min after galvanostatic cycling. In all these pictures, the TiO_2 nanotubes are oriented with their open end at the top of the SEM micrographs. The numbered rectangles indicate the areas from which EDX spectra were recorded. The results of the EDX analyses are given in the tables on the right side. Chlorine was used to check if the washing of the nanotubes with propylene carbonate (PC) was complete, because the electrolyte was 1 M $NaClO_4$ in PC.

cathodic sweep with respect to the anodic sweep increases until, at a sweep rate of 10 mV/s, the cyclic voltammetry curve is, to a much larger extent, symmetrical. This behavior points to a change in mechanism at fast sweep rates above 2 mV/s. Indeed, it may be possible that electrochemical insertion followed by (slow) Na^+ diffusion into the nanotube walls is dominating at slow sweep rates, whereas pseudocapacitive behavior is more prominent at fast sweep rates.

After galvanostatic cycling experiments carried out for a total of 400 cycles, the cells were stopped in the charged state, i.e., in a reduced state, with the nanotubes at their highest sodium content. The cells were then opened and the morphology of the samples was analyzed again by SEM, while EDX (energy-dispersive X-ray spectroscopy) was used to establish their composition. The results are presented in Figure 5. It can be noticed that, in spite of the prolonged cycling to which all the samples were submitted to, the integrity of the films and their nanotubular structure is fully retained with no visible signs of damage. Another feature is represented by the layer found on top of the nanotubes after cycling. Although present in all samples, this layer is clearly visible on top of the nanotube layer prepared at 30 V for 2 h. This layer is rich in sodium and oxygen while the titanium content is low. Taking into account the low potential limit to which these layers were cycled, it is possible that these layers are in fact made of decomposition products from the electrolyte that form at the nanotubular electrode during cycling, in an analogous way to the well-known SEI (solid electrolyte interphase) that occurs in Li-ion batteries. However, the Na-based film observed here does not appear to have the self-limiting properties of a passivation film. Instead, a continuous capacity decay is observed whenever the nanotube samples are exposed to low potentials, i.e., by cycling down to 0.1 V.

Another interesting feature is the sodium distribution within the nanotubular layer. It can be noticed that the sodium content is decreasing from the top to the bottom of the nanotube layer. This is even more remarkable when considering that all the samples were at rest for 7−10 days before cell opening and preparation for the SEM observation. The fact that the sodium concentration is not equilibrated after a relatively long time points toward a slow Na^+ diffusion process in the titania nanotube film.

4. DISCUSSION

4.1. Galvanostatic Cycling and Crystallinity. It has to be noted from the very beginning that no potential plateau was

DOI: 10.1021/acsami.5b07508
ACS Appl. Mater. Interfaces 2015, 7, 25757−25769

observed for any of the studied samples during galvanostatic cycling. Instead, a continuous and rather featureless variation of the electrode potential is recorded, as clearly illustrated on the example shown in Figure 6. The absence of a definite plateau

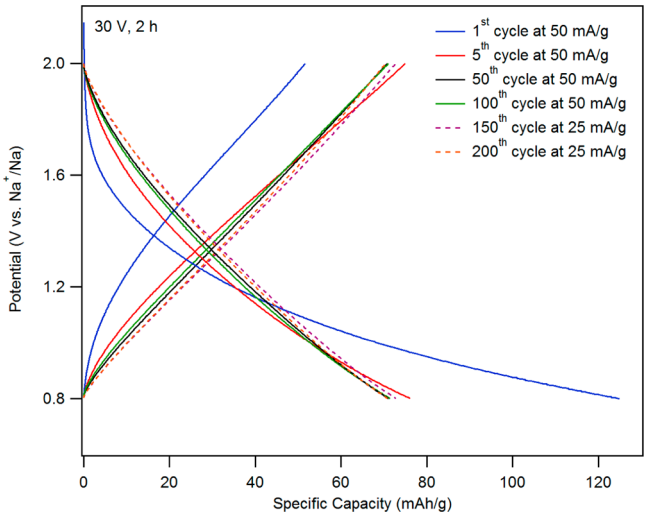

Figure 6. Typical charge/discharge curves corresponding to the electrochemical insertion of sodium ions into anodic amorphous titania nanotubes recorded at selected instances during the cycling of these materials. The graph presented here corresponds to a sample that has been fabricated by anodization at 30 V for 2 h. There are no voltage plateaus that can be positively identified, pointing to a single-phase storage mechanism.

on the potential-capacity profile acquired during galvanostatic cycling is an indication that the electrochemical insertion of Na^+ occurs without phase change. The transition between charged and discharged states involves a state analogous to a solid solution, in which the stoichiometry of the chemical compound varies continuously. Consequently, as a function of the phase composition, its electrochemical potential will show a continuous, sloped variation without any discernible plateaus or shoulders. Also, while sodium ions are inserted and diffuse into the titania structure, electrons are injected in the conduction band of titania. The nanotubes become thus a degenerated semiconductor and their electrical conductivity will increase. From a chemical point of view this translates into having some Ti^{4+} ions reduced to Ti^{3+} ions. The above-described behavior is similar to the insertion of H^+ into γ-MnO_2; Mn^{3+}/Mn^{4+} are effectively forming a solid solution.[44]

A common feature of all the anodic titania nanotubes studied here is their amorphous structure. Repeated X-ray diffraction experiments do not indicate the presence of any long-range crystalline ordering in any of the studied samples. These materials produced by relatively short duration anodization procedures are amorphous after preparation and they preserve their amorphous structure when stored at room temperature. To investigate the effect of crystallinity/amorphicity upon the cycling behavior of titania nanotubes, we annealed some samples at 350 °C for 2 h under argon. After thermal treatment, it is possible to clearly identify the reflections corresponding to anatase (Figure 7b). The Na^+ insertion behavior of this crystalline sample is very different from the amorphous, low temperature anodic titania as it can be seen in Figure 7a. The striking feature is represented by the very low capacity recorded for the annealed sample in comparison to the amorphous ones.

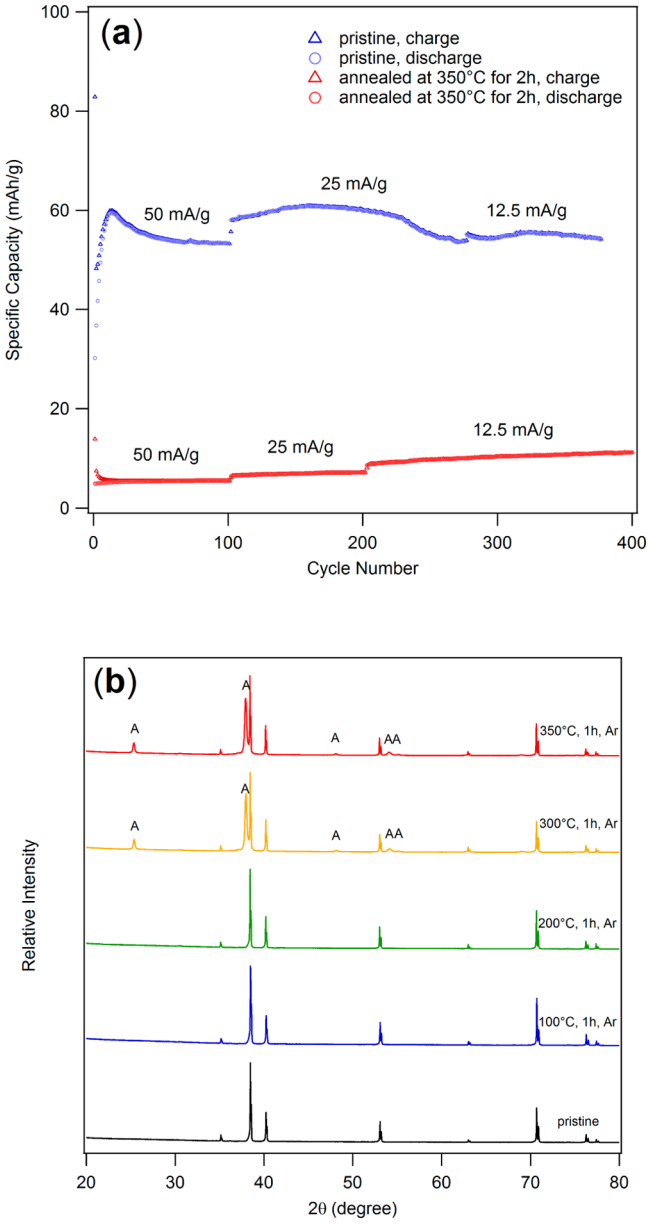

Figure 7. (a) Galvanostatic cycling between 0.8−2 V vs Na^+/Na of a sample annealed in Ar at 350 °C for 2 h compared with an as-prepared pristine sample. The capacity of the annealed sample, that shows the reflections of anatase phase, is much lower than the pristine sample. (b) X-ray diffraction patterns of one titania nanotube sample incrementally annealed at the listed temperatures. The anatase reflections are marked with "A", the unmarked reflections correspond to the titanium substrate.

Although the morphology of the nanotube layers is preserved after annealing, they do not appear to be able to insert an appreciable quantity of Na^+ when they contain a significant amount of anatase phase. The reason for the capacity reduction when the nanotubes are converted into anatase is not properly understood today and it appears that the behavior of crystalline anodic nanotubes with respect to the electrochemical reaction with sodium is very complex. It was shown in a very recent report[45] that anatase exhibits lower capacity than amorphous nanotubes, in a manner similar to our observations. However, the same authors report that a mixture of anatase and rutile nanotubes or a mixture of rutile and a sodium titanate phase

DOI: 10.1021/acsami.5b07508
ACS Appl. Mater. Interfaces 2015, 7, 25757−25769

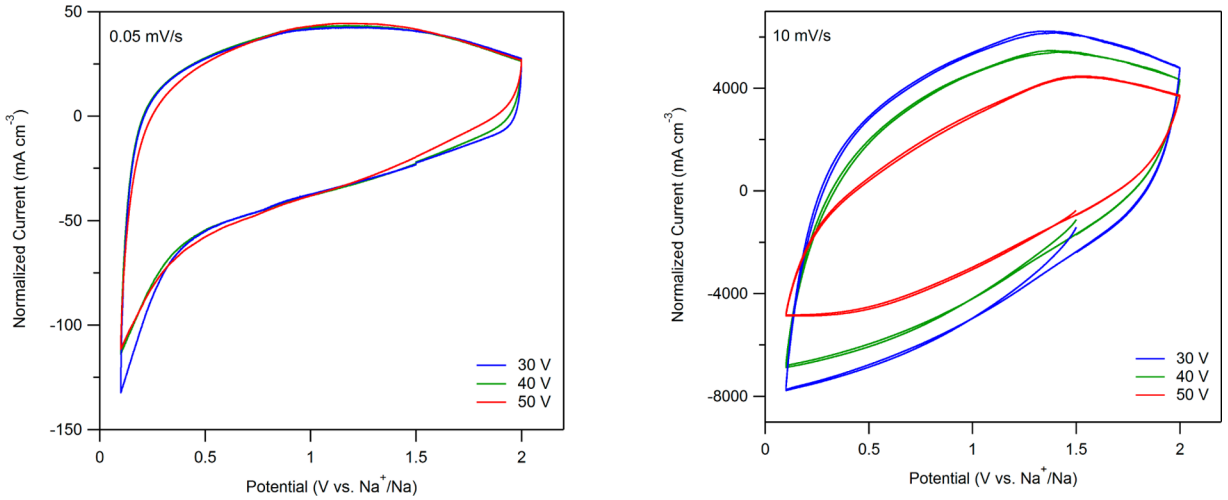

Figure 8. Cyclic voltammetry data normalized to the geometric volume of the titania nanotube film for the slowest (0.05 mV/s) and the fastest (10 mV/s) sweep rates used. While at slow sweep rates the ohmic drops can be neglected and the samples behave in identical manner, at relatively fast sweep rates the ohmic drops in the nanotubular electrodes are significant.

may actually lead to an increase of capacity. The reasons for these capacity variations are hitherto not fully understood. It can also be noticed that the capacity tends to increase slowly but steadily during the extended galvanostatic cycling of this crystalline sample, a situation that has also been recently reported in the literature.[41] One possible explanation would be to consider that at least some regions of the sample undergo a slow reconversion to an amorphous structure during the reversible Na^+ insertion reaction. Because Na^+ insertion into anodic titania nanotubes can clearly be observed to proceed at higher capacities when carried out on amorphous samples, it may be plausible that when Na^+ insertion is carried out on crystalline anatase titania, amorphous domains may develop and this may lead to higher capacities. This steady increase in capacity is in good agreement with some very recent reports where an increase in capacity during Na^+ insertion into nanostructured anatase occurs slowly during cyclic voltammetry experiments.[41]

4.2. Surface Storage vs Bulk Storage. A closer look at the cycling voltammetry data acquired at different sweep rates provides an insight into the behavior of anodic titania nanotubes at micro- and nanoscale level. Figure 8 shows the cyclic voltammetry data that has been normed to the geometric volume of the sample. This volume was simply calculated by multiplying the anodized area, i.e., 0.708 cm^2 for all the samples, with the thickness of the films determined from SEM cross-sections.

On the one hand, it can be noticed that, regardless of the anodization conditions, all the samples have an identical behavior at slow sweep rates. The recorded values of the volume-normed current overlap almost perfectly; this overlap was recorded up to a sweep rate of 2 mV/s. This behavior is a strong indication that, regardless of the anodization conditions, the amount of electroactive surface per unit of volume is identical for all the samples and that there is no qualitative difference in the electrochemical properties of the samples anodized at 30, 40, or 50 V. Because the length of the nanotubes and their diameters are different, it is very likely that all the available inner and outer surfaces are well-soaked in the electrolyte and that the wetting of the nanotubes is not influenced by the physical dimensions of the nanotubes. Thus, because nanotubes having different dimensions yield identical current response, it is very plausible that the entire inner surface is in fact electroactive and that, from an electrochemical point of view, all three samples studied appear to have very similar surface properties. It has to be noted at this point that by the electroactive surface area we understand the total surface area contained in the nanotube layer, mainly the inner and outer nanotube surfaces, that is in ionic contact with electrolyte. Given the observed morphology of the samples, composed of high-aspect-ratio nanotubes, the electroactive surface is clearly expected to be significantly higher than the anodized area, which was deliberately and accurately kept constant for all experiments.

The lack of a current dependence on the length of the nanotubes means that ohmic drops in the titania nanotube films are small and that their influence upon the current response can be neglected in cyclic voltammetry experiments that are carried out at sufficiently low sweep rates, i.e. not exceeding 2 mV/s. Consequently, there is an even electrical potential distribution over the entire electrochemically active surface of the samples, irrespective of the particular conditions used for preparation and the dimensions of the nanotubes. In these conditions, it is possible to effectively control externally, through the potentiostat, the potential on the electroactive surface of the electrodes and accurately record its electrochemical response. Because the ohmic drops are negligible in the anodic titania layer, the potential of the electroactive surface follows accurately the applied potential.

On the other hand, for sweep rates higher than 2 mV/s (i.e., 5 and 10 mV/s) the situation changes. At these relatively fast sweep rates, the ohmic drops influence significantly the current response. At 5 and 10 mV/s, the longer the nanotubes, the lower are the recorded currents, respectively, due to, in this case, non-negligible ohmic drops. The potential is probably not evenly distributed along the nanotubes and, very likely, there will be a difference in potential between the top of the nanotubular layer and the bottom. Thus, although the longer nanotubes would certainly have a much higher total unfolded area than the short tubes and they are as well soaked in electrolyte (see above), not all the area in contact with electrolyte is in fact electroactive and on significant regions no

DOI: 10.1021/acsami.5b07508
ACS Appl. Mater. Interfaces 2015, 7, 25757−25769

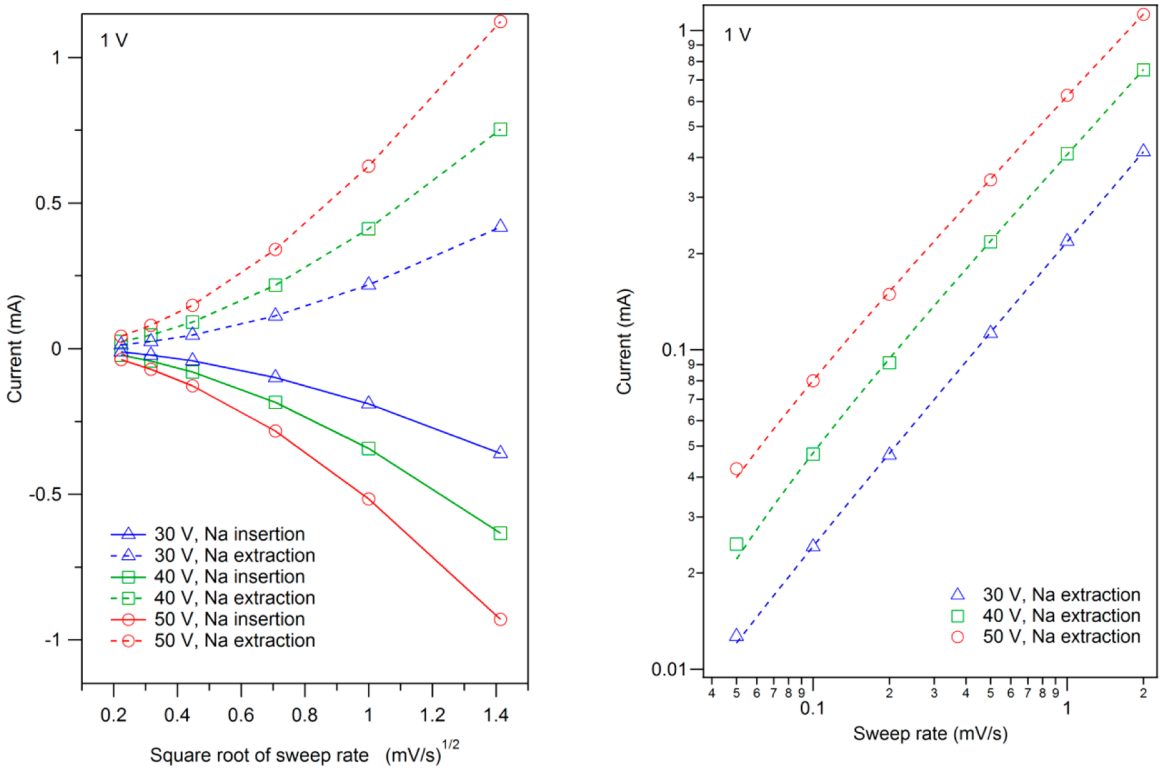

Figure 9. Left: Current values read at a potential of 1 V vs Na^+/Na reference plotted with respect to square root of the sweep rate for the anodic and cathodic scans. There are significant and systematic deviations from the linear behavior that would be expected for electrochemical processes that are limited by mass transport (diffusion) phenomena. Right: Log−Log plot of the anodic current values (Na extraction) at 1 V vs the sweep rate. The dotted lines on the right graph are the fits according to the power law from eq 2.

electrochemical reaction may take place at fast sweep rates. This situation is clearly illustrated in Figure 8, where it can be seen that at 10 mV/s, the lowest volume-normed currents are recorded for the longest tubes (50 V 2 h, 14.2 μm long) while the shortest tubes (30 V 2 h, 4.5 μm long) exhibit the highest current values since the ohmic drops on the shortest tubes are expected to be the lowest. Therefore, for subsequent analysis, only the cyclic voltammetry data acquired at sweep rates between 0.05 and 2 mV/s were used.

The very broad current response recorded for all the samples during cyclic voltammetry experiments points toward non-Nernstian electrochemical reactions that may be best described by quasi-reversible or irreversible kinetics for which the mass transport phenomena represent the rate limiting step, mass transport being several orders of magnitude slower than the electrochemical charge transfer. If the reaction rate of an electrochemical reaction is limited by diffusion phenomena, then the recorded current in a cyclic voltammetry experiment should present a linear dependence on the square root of the sweep rate. The actual relation is given by a modified form of the Randless−Sevcik equation deduced for non-Nernstian, irreversible kinetics, reactions[46]

$$i = 0.4958nFACD^{1/2}\left(\frac{\alpha nF}{RT}\right)^{1/2}v^{1/2} \quad (1)$$

were i represents the peak current in amps, n represents the number of electrons exchanged in the electrochemical reaction, in this case 1, F is the Faraday constant (96485 C mol^{-1}), A is the inner total electroactive area of the porous electrode in cm^2, C is the concentration of electroactive redox centers in the insertion electrode, i.e. in the present case the concentration of Ti centers in TiO_2 lattice in mol cm^{-3}, D is the chemical diffusion coefficient of inserted species (Na^+) into the host lattice in cm^2 s^{-1}, α is the transfer coefficient of the electrochemical insertion reaction and can usually be taken as 0.5, and v is the sweep rate in V s^{-1}. R is the ideal gas constant (in J mol^{-1} K^{-1}) and T is the absolute temperature (K).

However, a plot of the recorded currents with respect to the square root of the sweep rate is far from being linear as illustrated in Figure 9. No matter at what potential the current was read, for both cathodic and anodic scans there are significant and systematic deviations from linearity.

The direction in which this deviation from linearity occurs has an important significance. It is obvious from Figure 9 that the deviation is positive, i.e., the recorded current increases faster than the expected linear behavior when plotted vs the square root of the sweep rate. This behavior could be explained by the so-called capacitive effects that appear to play a significant role in the sodium storage mechanism. In a first approximation, the faster-than-linear increase of the current with respect to the square root of the sweep rate would stem in the surface, or near surface storage of sodium ions without significant diffusion of Na^+ ions into the titania. To preserve the electroneutrality of the surface that is now loaded with Na^+ ions, we reduced the Ti^{4+} ions in the vicinity of the surface to Ti^{3+}. This situation can also be described in reverse: the tetravalent titanium centers are reduced electrochemically to trivalent titanium ions and the Na^+ ions that are consequently bound on the surface would compensate the negative charge that has been injected in the conduction band of titania. The spatially separated negative charges (electrons on Ti centers) and positive charges (Na^+) on the surface form the virtual

DOI: 10.1021/acsami.5b07508
ACS Appl. Mater. Interfaces 2015, 7, 25757−25769

armatures of a capacitor, this configuration resembling the double electrical layer that is ubiquitous at any electronic conductor/electrolyte interface. This Na^+ surface storage phenomenon, which is not limited by sodium diffusion into titania, leads to higher recorded currents than what would be normally expected from a solely (solid state) diffusion limited process. Although Na^+ diffusion into titania is probably not affected by the sweep rate, the charging and discharging rates of these surface films are strongly dependent on the sweep rate. The higher the sweep rate, the higher the deviation from linearity, as can be seen in Figure 9. Nevertheless, the current will eventually be limited by Na^+ mass transport (diffusion) in the liquid state at very fast sweep rates. However, because diffusion in the solid state can safely be assumed many order of magnitudes slower than diffusion in the liquid state, at the relatively slow sweep rates used in our experiments, we estimate this contribution is insignificant and can be neglected.

The surface storage mechanism discussed above, was previously showed to be important to Li^+ storage in anatase titania.[47] However, it was also shown that this is not the only storage mechanism; Li^+ diffusion also occurs and accounts for a significant amount of the capacity.

The current response as a function of the sweep rate was found to follow the same relatively simple power law proposed by Lindström et al.,[47] used before in the case of Li^+ insertion into anatase

$$i = av^b \tag{2}$$

where a and b are adjustable parameters and v is the sweep rate. The b parameter was used by several authors to distinguish between faradaic (diffusion limited insertion) and nonfaradaic (pseudocapacitive) processes, the latter being not limited by diffusion in the solid state. Thus, exponent b values close to 1 are ascribed to a current response dominated by capacitive effects, whereas values close to 0.5 are the signature of a diffusion limited electrochemical reaction. For b = 0.5, the above power law is essentially identical to eq 1.

The b-values corresponding to Na^+ electrochemical reaction with the amorphous titania nanotubes were determined by fitting to eq 2 the cyclic voltammetry currents read at selected potentials. An example of such a fit for one potential value is illustrated in Figure 9 (right), whereas the values of the b exponent over a large potential domain for the three samples studied are shown in Figure 10.

It was found that the exponent b mostly takes values between 0.85−0.92 during the cathodic scan and that they remain relatively constant between 1.5 and 0.1 V vs Na^+/Na. This is a strong indication that the majority of the recorded current during the reduction process is in fact pseudocapacitive with the majority of Na^+ ions stored on the surface. Because b values never reach 1 during the cathodic scan, it is very likely that there is also some Na^+ insertion and diffusion into titania, although in a proportionally smaller amount.

The situation changes significantly when the scanning is reversed and Na^+ is extracted from the electrode during the anodic scan. Although at the end of the cathodic scan the b values are still close to 0.9, when the Na^+ flux is reversed at the beginning of the anodic scan, the b values are much lower. It would appear that electrochemical reaction of amorphous titania nanotubes with sodium ions is mostly governed by pseudocapacitive effects, whereas on the other hand Na^+ extraction is, at least at the beginning, limited by diffusion. This striking asymmetry of the b-values between the anodic and

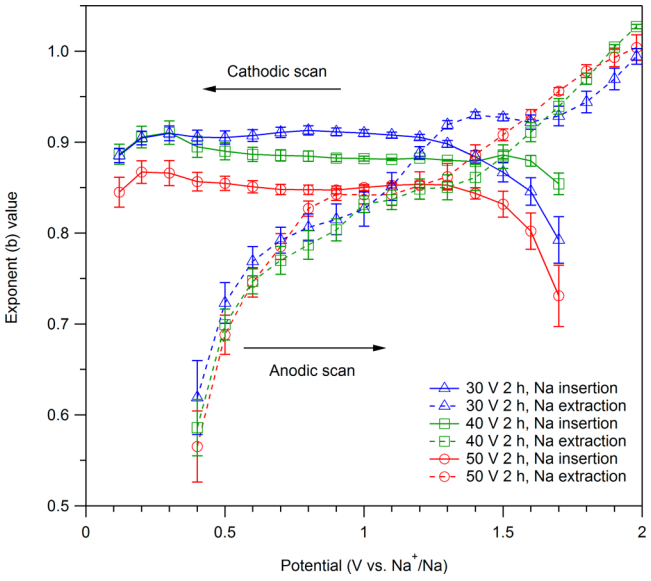

Figure 10. Exponent (b) values obtained by fitting the current vs sweep rate curves at various potentials during anodic and cathodic scans with the power law from eq 2. There is a clearly visible asymmetry between the anodic and cathodic processes.

the cathodic process could be understood if we consider that the Na^+ reaction mechanism at the electrode is composed of two main processes: a relatively fast Na^+ electroadsorption that occurs by the reduction of the interfacial Ti^{4+} centers to Ti^{3+} followed by a relatively slow Na^+ diffusion into the titania. It is possible that electroadsorption kinetics are faster than the desorption kinetics during the anodic scan leading to some hysteresis between adsorption and desorption. This is consistent with a quasireversible kinetics model of the Na^+ insertion reaction.

There might also be thermodynamic factors. Indeed, if we consider that the Na^+ ions are strongly electroadsorbed on the surface at the end of the cathodic scan, releasing the Na^+ ions could be thermodynamically unfavorable in the isothermal conditions of the experiment. The desorption of Na^+ might actually imply breaking some, possibly stronger, bonds between Na^+ and the substrate, followed by the formation of weaker bonds between Na^+ and the solvent. Thus, the desorption process might be thermodynamically unfavorable. For either thermodynamic or kinetic reasons, when the current is reversed, the Na^+ flux does not reverse immediately from the surface source but from the bulk source that is obviously limited by (slow) solid-state diffusion. Hence the asymmetry in actual mechanism that appears visible in the b value plot. Although the bulk source is depleted during the anodic scan, an increasing number of sodium ions are released from the electroadsorbed layer, as hinted by an increase in b values.

We can conclude that the storage of sodium ionic species on the surface of titania nanotubes appears as a complex process that is clearly dependent on the direction of the Na^+ flux. We have to take note that this is very different from what is commonly understood by a capacitance because of its asymmetrical behavior in charge with respect to discharge. In spite of this mechanism being referred to as pseudocapacitance, we found this very term to be misleading, its meaning being, more often than not, overlooked and only rarely explained. Although a capacitor would exhibit symmetrical charge and discharge behavior, these electroadsorbed layers present

DOI: 10.1021/acsami.5b07508
ACS Appl. Mater. Interfaces 2015, 7, 25757−25769

particularities that introduce significant deviations from a capacitor model, by far more significant than the usual model of the double-layer capacitance. Also, in our opinion, the usual classification into faradaic and nonfaradaic processes based on the value of the exponent b from eq 2 is rather inaccurate because it is very likely that, in a simple approximation, both processes occur at the electrode, either concomitantly or consecutively.

From a fundamental point of view, it is worth mentioning that the definition and understanding of faradaic and nonfaradaic processes at insertion electrodes is in many aspects different from classical aqueous electrochemistry where the electrochemical charge transfer takes place through the double electrical layer at the electrode surface. In the case of insertion electrodes, it becomes far more difficult to identify where is the locus of the electron charge transfer. It is certain that in a usual insertion electrode, only ions are transported through the electrochemical interface, whereas electron charge transfer through the electrode/electrolyte interface is undesired. A nonfaradaic current, for instance, the charging and discharging of the double electrical layer, does not change the chemical composition of any constituents of the system. By definition, none of the compounds and phases present in the system could undergo reduction or oxidation caused by a nonfaradaic process. However, during a pseudocapacitive process, such as interfacial Na^+ storage on titania, the redox centers (Ti^{4+}) are reduced and a configuration analogous to a Ti^{4+}/Ti^{3+} solid solution develops within the titania nanotubes (see above). Thus, in our opinion, it is incorrect to understand and refer to pseudocapacitive storage as nonfaradaic. Pseudocapacitive storage is in fact by all means a faradaic process that is coupled with an ion adsorption/chemisorption step and does not (necessarily) present a solid state diffusion step. Therefore, from b value analysis one cannot distinguish between faradaic and nonfaradaic currents. Either at values close to $b = 1$ or at $b = 0.5$ the Na^+ reaction with titania is faradaic. Instead, b values could be used, with caution, to distinguish between interfacial storage and bulk storage. The term pseudocapacitance, already embraced by many authors, can be misleading and might trick the reader into considering pseudocapacitive storage as a nonfaradaic process. We believe that "faradaic adsorption" or "faradaic interfacial storage" might be clearer, more precise, and more meaningful words, which should therefore be preferred over the term "pseudocapacitance".

4.3. Faradaic Adsorption (Pseudocapacitance) and Diffusion into Amorphous Titania Nanotubes. Although a diffusion limited current would only show a linear dependence on the square root of the sweep rate a capacitive current should be directly proportional to the sweep rate and the value of the pseudocapacitance. Thus, the absolute value of a capacitive current i_{cap} is given by the expression[47]

$$|i_{cap}| = Ac_p v \tag{3}$$

where A is the electroactive surface area, c_p is the value of the pseudocapacitance and v is the sweep rate. This would enable us to estimate the diffusion current (i_{diff}) by subtracting the capacitive contributions from the experimentally recorded current (i_{exp}) using the following expression

$$i_{diff} = i_{exp} - Ac_p v \tag{4}$$

Because i_{diff} should have a linear dependence on the square root of the sweep rate (see eq 1), this condition can be used to estimate the value of the capacitance. The value of c_p that leads to a linear plot i_{diff} vs square root of v (the sweep rate) represents the value of the pseudocapacitance. Thanks to the highly regular structure of the titania nanotube layers, the surface can be relatively well estimated from the geometric dimensions of the nanotubes determined from SEM micrographs, assuming the nanotubes are cylindrical and that both the outer and inner surface is electroactive. Thus, it was found that 1 cm^2 of anodized area corresponds to an estimated surface of 330 cm^2 for the sample anodized at 30 V for 2 h, 464 cm^2 for 40 V 2 h, and 715 cm^2 for the sample anodized at 50 V for 2 h. The determined capacitance values according to the above-discussed procedure are shown in Figure 11.

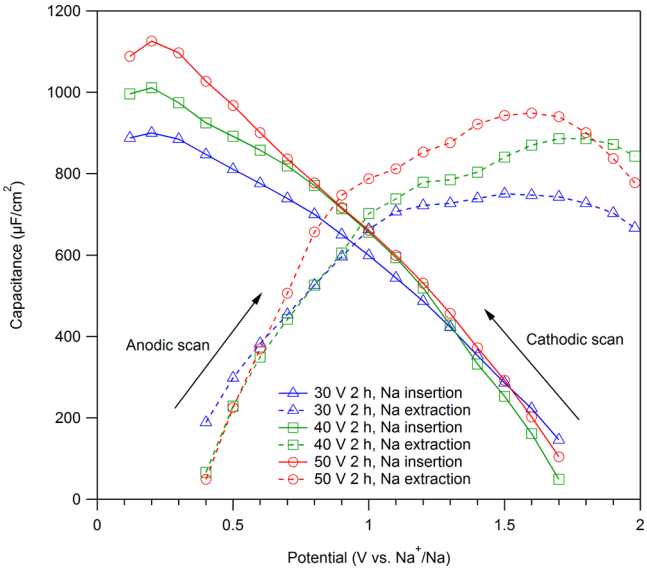

Figure 11. Pseudocapacitance values corresponding to the interfacial storage of Na^+ ions on three different anodic nanotube layers. The surface used for calculation was the estimated developed inner surface of the electrode which is much larger than the anodized area.

As a cross-check, b values were determined from the plots of pseudocapacitance adjusted currents (i_{diff}) vs the sweep rate according to eq 2. This always gave b values close to 0.5 ($\pm$0.03), proving that the subtraction method is able to distinguish between diffusion and pseudocapacitive currents.

As shown in Figure 11, during the sodium insertion (cathodic scan), the pseudocapacitance increases continuously, whereas the potential is decreased indicating that the quantity of Na^+ stored on the surface region of titania nanotubes is also increasing. It can also be noticed that all three samples have similar behavior and the variations of the pseudocapacitance values match relatively well for all the studied samples, pointing one more time to very similar mechanisms of sodium storage. The behavior appears more complex during the anodic scan. When the scan is reversed and electrochemical sodium extraction takes place, the pseudocapacitance increases again from relatively low values, reaches a somewhat constant value, and starts decreasing again toward the end of the anodic scan.

To understand these variations, one should keep in mind that the values of the pseudocapacitance were determined according to eq 4 and that the experimental current is the sum of the (solid state) diffusion current and the pseudocapacitive current. Thus, we model the current response by two in-parallel Na^+ "sinks" or "sources", depending whether the sodium insertion or the sodium extraction takes place, respectively. It is very

DOI: 10.1021/acsami.5b07508
ACS Appl. Mater. Interfaces 2015, 7, 25757−25769

likely that these diffusion (bulk) and surface storage processes do not occur in the same time but in a relative consecutive manner. On the one hand, the Na^+ ionic radius of 1.02 Å, that is significantly larger than the ionic radius of Li^+ (0.76 Å), would probably render the insertion and diffusion of Na^+ into TiO_2 very slowly. Additionally, this process might occur at relatively low values and could be thermodynamically unfavorable. On the other hand, the faradaic adsorption of Na^+ ions probably presents some hysteresis. Indeed, if we consider that the titania surface is oxygen-terminated then Na^+ ions might adsorb strongly from the beginning and would require some energy for their release.

Thus, during the sodium extraction the sodium flux that is released at low potentials from the interfacial source is low, and the pseudocapacitance values are also relatively low. As seen from the *b* values analysis (see above) it is very likely that a large part of the sodium flux, and thus the current, at low potentials during the anodic scan is from the bulk source. As the potentials increase the pseudocapacitance contribution and values increase until they reach an upper limit and/or a relatively constant level. This somehow constant level could be related to the limited kinetics of sodium desorption from the interface regions that might keep the pseudocapacitive current at near constant levels. As both the interfacial and bulk sources are continuously depleted, at high potentials, the values of the pseudocapacitance begins to decrease again because the sodium flux can no longer be sustained.

As a final observation, one should also note that pseudocapacitance reaches values that are 2 orders of magnitude higher than the capacitance of electrochemical double layer, a property that would make these materials well-suited for supercapacitor applications.

Finally, the chemical diffusion coefficient of Na^+ into the amorphous titania nanotubes as a function of the electrode potential was determined and is shown in Figure 12. These values were obtained by fitting to eq 1 the i_{diff} values obtained with eq 4 assuming a concentration of titanium centers in TiO_2 of 2.4×10^{-2} mol cm^{-3}, which would correspond to only half of the titanium centers being electrochemically active. This is the case of Li^+ insertion in anatase but the number of active titanium redox centers is probably lower for Na^+ insertion. Thus, the chemical diffusion coefficient values should be considered as base values for further ion dynamics studies into these amorphous titania nanotubes. It is interesting to note that Lindström et al.[47] found values of the diffusion coefficient of Li^+ in TiO_2 anatase on the order of 1×10^{-17} cm^2/s, which is by itself a low value for lithium ions. Although Na^+ has only approximately 25% larger ionic radius than Li^+, this is enough to lower the chemical diffusivity of Na^+ into titania by at least 4 orders of magnitude. Nevertheless, our determined value of the Na^+ diffusion coefficient is fully coherent with what was already reported for lithium.

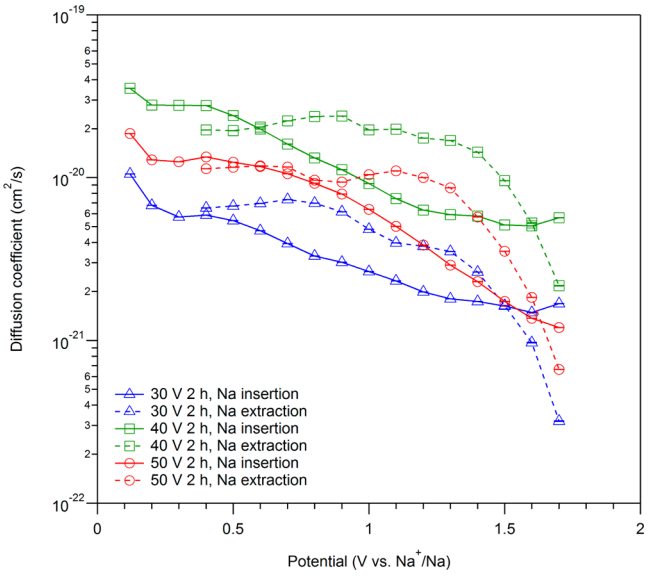

Figure 12. Chemical diffusion coefficient of Na^+ into the walls of amorphous TiO_2 nanotubes determined at room temperature (23 ± 1 °C) according to the eq 1 after subtracting the capacitive contributions for different sample types. The increase of chemical diffusivity during sodium insertion is in line with the recorded behavior of the pseudocapacitance.

5. CONCLUSIONS

The amorphous titania nanotubes investigated in this paper show a very good cycle-life when cycled down to 0.8 V vs Na^+/Na. More than 300 cycles at two different cycling rates were recorded without significant loss of capacity. The electrochemical reaction with sodium ions presents many particularities that are not usually encountered in classical insertion electrodes. From cyclic voltammetry experiments, it was possible to distinguish between two different contributions to the total current response. An important part of the Na^+ ions are stored on the surface or near-surface regions of the walls of the amorphous anodic titania nanotubes, whereas only a smaller fraction is actually able to diffuse in the walls of the titania nanotubes. Although the surface storage mechanism involves a process that shares some similarities with the charging of an electrochemical double electrical layer capacitor, the Na^+ storage via a faradaic adsorption mechanism is clearly a distinct process. The asymmetrical response of the interfacial films in charge with respect to discharge points toward a consecutive operation of bulk diffusion and interfacial storage mechanisms. The determined chemical diffusion coefficient takes low values centered around 1×10^{-20} cm^2/s. The larger size of the Na^+ ions with respect to Li^+ ions, that are known to insert somewhat easier in anatase TiO_2, may explain these relatively low diffusion coefficient values.

The determined values of the faradaic adsorption capacitance, i.e., the pseudocapacitance, are very high. They may reach 2 orders of magnitude higher than the normal values that are characteristic to the usual double electrical layer capacitance, a result that opens the path toward high-performance supercapacitor applications.

AUTHOR INFORMATION

Corresponding Author

*E-mail: hanzu@tugraz.at.

Funding

Denise Prutsch received funding for this research from the Österreichische Forschungsförderungsgesellschaft (FFG) within the frame of the Research Studio Austria (RSA) programe through the project Advance and Innovative Materials for Electrochemical Energy Storage (AIMS) with the FFG Grant 4338751.

Notes

The authors declare no competing financial interest.

DOI: 10.1021/acsami.5b07508
ACS Appl. Mater. Interfaces 2015, 7, 25757−25769

■ ACKNOWLEDGMENTS

Sanja Simic from Austrian Centre for Electron Microscopy and Nanoanalysis (FELMI-ZFE) is kindly aknowledged for the EDX measurements. We also thank Brigitte Bitschnau from Institute of Physical and Theoretical Chemistry (PTC) for XRD measurements. We thank the Research Studio Austria AIMS (FFG, Grant No. 4338751) as well as the Research Unit 1277 (DFG), Grant No. WI 3600/4-2 (Martin Wilkening) and HA 6996/1-2 (Ilie Hanzu), for financial support.

■ REFERENCES

(1) Slater, M. D.; Kim, D.; Lee, E.; Johnson, C. S. Sodium-Ion Batteries. *Adv. Funct. Mater.* **2013**, *23*, 947−958.
(2) Ellis, B. L.; Nazar, L. F. Sodium and Sodium-Ion Energy Storage Batteries. *Curr. Opin. Solid State Mater. Sci.* **2012**, *16*, 168−177.
(3) Palomares, V.; Serras, P.; Villaluenga, I.; Hueso, K. B.; Carretero-Gonzalez, J.; Rojo, T. Na-Ion Batteries, Recent Advances and Present Challenges to Become Low Cost Energy Storage Systems. *Energy Environ. Sci.* **2012**, *5*, 5884−5901.
(4) Delmas, C.; Braconnier, J. J.; Fouassier, C.; Hagenmuller, P. Electrochemical Intercalation of Sodium in Na_xCoO_2 Bronzes. *Solid State Ionics* **1981**, *3*−*4*, 165−169.
(5) Hagg, G. The Spinels and the Cubic Sodium-Tungsten Bronzes as New Examples of Structures with Vacant Lattice Points. *Nature* **1935**, *135*, 874−874.
(6) Fouassier, C.; Matejka, G.; Reau, J.-M.; Hagenmuller, P. Sur de Nouveaux Bronzes Oxygénés de Formule Na_xCoO_2 ($x \leq 1$). Le Système Cobalt-Oxygène-Sodium. *J. Solid State Chem.* **1973**, *6*, 532−537.
(7) Braconnier, J. J.; Delmas, C.; Fouassier, C.; Hagenmuller, P. Electrochemical Behavior of the Phases Na_xCoO_2. *Mater. Res. Bull.* **1980**, *15*, 1797−1804.
(8) Tarascon, J. M.; Hull, G. W. Sodium Intercalation into the Layer Oxides $Na_xMo_2O_4$. *Solid State Ionics* **1986**, *22*, 85−96.
(9) Lu, Z. H.; Dahn, J. R. *In-situ* X-ray Diffraction Study of P2-$Na_{2/3}[Ni_{1/3}Mn_{2/3}]O_2$. *J. Electrochem. Soc.* **2001**, *148*, A1225−A1229.
(10) Kitajou, A.; Komatsu, H.; Chihara, K.; Gocheva, I. D.; Okada, S.; Yamaki, J. Novel Synthesis and Electrochemical Properties of Perovskite-Type $NaFeF_3$ for a Sodium-Ion Battery. *J. Power Sources* **2012**, *198*, 389−392.
(11) Lee, K. T.; Ramesh, T. N.; Nan, F.; Botton, G.; Nazar, L. F. Topochemical Synthesis of Sodium Metal Phosphate Olivines for Sodium-Ion Batteries. *Chem. Mater.* **2011**, *23*, 3593−3600.
(12) Recham, N.; Chotard, J. N.; Dupont, L.; Djellab, K.; Armand, M.; Tarascon, J. M. Ionothermal Synthesis of Sodium-Based Fluorophosphate Cathode Materials. *J. Electrochem. Soc.* **2009**, *156*, A993−A999.
(13) Chihara, K.; Kitajou, A.; Gocheva, I. D.; Okada, S.; Yamaki, J. Cathode Properties of $Na_3M_2(PO_4)_2F_3$ [M = Ti, Fe, V] for Sodium-Ion Batteries. *J. Power Sources* **2013**, *227*, 80−85.
(14) Moreau, P.; Guyomard, D.; Gaubicher, J.; Boucher, F. Structure and Stability of Sodium Intercalated Phases in Olivine $FePO_4$. *Chem. Mater.* **2010**, *22*, 4126−4128.
(15) Plashnitsa, L. S.; Kobayashi, E.; Noguchi, Y.; Okada, S.; Yamaki, J. Performance of NASICON Symmetric Cell with Ionic Liquid Electrolyte. *J. Electrochem. Soc.* **2010**, *157*, A536−A543.
(16) Alcantara, R.; Lavela, P.; Ortiz, G. F.; Tirado, J. L. Carbon Microspheres Obtained from Resorcinol-Formaldehyde as High-Capacity Electrodes for Sodium-Ion Batteries. *Electrochem. Solid-State Lett.* **2005**, *8*, A222−A225.
(17) Komaba, S.; Murata, W.; Ishikawa, T.; Yabuuchi, N.; Ozeki, T.; Nakayama, T.; Ogata, A.; Gotoh, K.; Fujiwara, K. Electrochemical Na Insertion and Solid Electrolyte Interphase for Hard-Carbon Electrodes and Application to Na-Ion Batteries. *Adv. Funct. Mater.* **2011**, *21*, 3859−3867.
(18) Ponrouch, A.; Goni, A. R.; Palacin, M. R. High Capacity Hard Carbon Anodes for Sodium Ion Batteries in Additive Free Electrolyte. *Electrochem. Commun.* **2013**, *27*, 85−88.
(19) Huang, J. P.; Yuan, D. D.; Zhang, H. Z.; Cao, Y. L.; Li, G. R.; Yang, H. X.; Gao, X. P. Electrochemical Sodium Storage of TiO_2(B) Nanotubes for Sodium Ion Batteries. *RSC Adv.* **2013**, *3*, 12593−12597.
(20) Il Park, S.; Gocheva, I.; Okada, S.; Yamaki, J. Electrochemical Properties of $NaTi_2(PO_4)_3$ Anode for Rechargeable Aqueous Sodium-Ion Batteries. *J. Electrochem. Soc.* **2011**, *158*, A1067−A1070.
(21) Gonzalez, J. R.; Alcantara, R.; Ortiz, G. F.; Nacimiento, F.; Tirado, J. L. Controlled Growth and Application in Lithium and Sodium Batteries of High-Aspect-Ratio, Self-Organized Titania Nanotubes. *J. Electrochem. Soc.* **2013**, *160*, A1390−A1398.
(22) Xiong, H.; Slater, M. D.; Balasubramanian, M.; Johnson, C. S.; Rajh, T. Amorphous TiO_2 Nanotube Anode for Rechargeable Sodium Ion Batteries. *J. Phys. Chem. Lett.* **2011**, *2*, 2560−2565.
(23) Xu, Y.; Lotfabad, E. M.; Wang, H. L.; Farbod, B.; Xu, Z. W.; Kohandehghan, A.; Mitlin, D. Nanocrystalline Anatase TiO_2: A New Anode Material for Rechargeable Sodium Ion Batteries. *Chem. Commun.* **2013**, *49*, 8973−8975.
(24) Oh, S. M.; Myung, S. T.; Jang, M. W.; Scrosati, B.; Hassoun, J.; Sun, Y. K. An Advanced Sodium-Ion Rechargeable Battery Based on a Tin-Carbon Anode and a Layered Oxide Framework Cathode. *Phys. Chem. Chem. Phys.* **2013**, *15*, 3827−3833.
(25) Xiao, L. F.; Cao, Y. L.; Xiao, J.; Wang, W.; Kovarik, L.; Nie, Z. M.; Liu, J. High Capacity, Reversible Alloying Reactions in SnSb/C Nanocomposites for Na-Ion Battery Applications. *Chem. Commun.* **2012**, *48*, 3321−3323.
(26) Baggetto, L.; Ganesh, P.; Meisner, R. P.; Unocic, R. R.; Jumas, J. C.; Bridges, C. A.; Veith, G. M. Characterization of Sodium Ion Electrochemical Reaction with Tin Anodes: Experiment and Theory. *J. Power Sources* **2013**, *234*, 48−59.
(27) Wang, Y.; Su, D.; Wang, C.; Wang, G. SnO_2@MWCNT Nanocomposite as a High Capacity Anode Material for Sodium-Ion Batteries. *Electrochem. Commun.* **2013**, *29*, 8−11.
(28) Datta, M. K.; Epur, R.; Saha, P.; Kadakia, K.; Park, S. K.; Kumta, P. N. Tin and Graphite Based Nanocomposites: Potential Anode for Sodium Ion Batteries. *J. Power Sources* **2013**, *225*, 316−322.
(29) Lin, Y. M.; Abel, P. R.; Gupta, A.; Goodenough, J. B.; Heller, A.; Mullins, C. B. Sn-Cu Nanocomposite Anodes for Rechargeable Sodium-Ion Batteries. *ACS Appl. Mater. Interfaces* **2013**, *5*, 8273−8277.
(30) Abel, P. R.; Lin, Y. M.; de Souza, T.; Chou, C. Y.; Gupta, A.; Goodenough, J. B.; Hwang, G. S.; Heller, A.; Mullins, C. B. Nanocolumnar Germanium Thin Films as a High-Rate Sodium-Ion Battery Anode Material. *J. Phys. Chem. C* **2013**, *117*, 18885−18890.
(31) Ponrouch, A.; Dedryvere, R.; Monti, D.; Demet, A. E.; Mba, J. M. A.; Croguennec, L.; Masquelier, C.; Johansson, P.; Palacin, M. R. Towards High Energy Density Sodium Ion Batteries Through Electrolyte Optimization. *Energy Environ. Sci.* **2013**, *6*, 2361−2369.
(32) Ponrouch, A.; Marchante, E.; Courty, M.; Tarascon, J. M.; Palacin, M. R. In Search of an Optimized Electrolyte for Na-Ion Batteries. *Energy Environ. Sci.* **2012**, *5*, 8572−8583.
(33) Alcantara, R.; Jimenez-Mateos, J. M.; Lavela, P.; Tirado, J. L. Carbon Black: A Promising Electrode Material for Sodium-Ion Batteries. *Electrochem. Commun.* **2001**, *3*, 639−642.
(34) Wadsley, A. D.; Andersson, S. Alkali Metal Titanium Oxide Bronzes. *Nature* **1961**, *192*, 551−552.
(35) Andersson, S.; Wadsley, A. D. $Na_xTi_4O_8$, an Alkali Metal Titanium Dioxide Bronze. *Acta Crystallogr.* **1962**, *15*, 201−206.
(36) Senguttuvan, P.; Rousse, G.; Seznec, V.; Tarascon, J. M.; Palacin, M. R. $Na_2Ti_3O_7$: Lowest Voltage Ever Reported Oxide Insertion Electrode for Sodium Ion Batteries. *Chem. Mater.* **2011**, *23*, 4109−4111.
(37) Armstrong, A. R.; Armstrong, G.; Canales, J.; Bruce, P. G. TiO_2-B Nanowires as Negative Electrodes for Rechargeable Lithium Batteries. *J. Power Sources* **2005**, *146*, 501−506.
(38) Lindsay, M. J.; Blackford, M. G.; Attard, D. J.; Luca, V.; Skyllas-Kazacos, M.; Griffith, C. S. Anodic Titania Films as Anode Materials for Lithium Ion Batteries. *Electrochim. Acta* **2007**, *52*, 6401−6411.

DOI: 10.1021/acsami.5b07508
ACS Appl. Mater. Interfaces 2015, 7, 25757−25769

(39) Bruce, P. G.; Scrosati, B.; Tarascon, J. M. Nanomaterials for Rechargeable Lithium Batteries. *Angew. Chem., Int. Ed.* **2008**, *47*, 2930−2946.
(40) Kavan, L.; Kratochvilova, K.; Gratzel, M. Study of Nanocrystalline TiO_2 (Anatase) Electrode in the Accumulation Regime. *J. Electroanal. Chem.* **1995**, *394*, 93−102.
(41) Wu, L. M.; Buchholz, D.; Bresser, D.; Chagas, L. G.; Passerini, S. Anatase TiO_2 Nanoparticles for High Power Sodium-Ion Anodes. *J. Power Sources* **2014**, *251*, 379−385.
(42) Roy, P.; Berger, S.; Schmuki, P. TiO_2 Nanotubes: Synthesis and Applications. *Angew. Chem., Int. Ed.* **2011**, *50*, 2904−2939.
(43) Ortiz, G. F.; Hanzu, I.; Djenizian, T.; Lavela, P.; Tirado, J. L.; Knauth, P. Alternative Li-Ion Battery Electrode Based on Self-Organized Titania Nanotubes. *Chem. Mater.* **2009**, *21*, 63−67.
(44) Mondoloni, C.; Laborde, M.; Rioux, J.; Andoni, E.; Levyclement, C. Rechargeable Alkaline Manganese Dioxide Batteries. 1. *In-situ* X-ray Diffraction Investigation of the H^+/γ-MnO_2 (EMD-Type) Insertion System. *J. Electrochem. Soc.* **1992**, *139*, 954−959.
(45) Cabello, M.; Ortiz, G. F.; López, M. C.; Alcántara, R.; González, J. R.; Tirado, J. L.; Stoyanova, R.; Zhecheva, E. Self-Organized Sodium Titanate/ Titania Nanoforest for the Negative Electrode of Sodium-Ion Microbatteries. *J. Alloys Compd.* **2015**, *646*, 816−826.
(46) Bard, A. J.; Faulkner, L. R. *Electrochemical Methods: Fundamentals and Applications*, 2nd ed.; John Wiley & Sons: New York, 2001; p 226−251.
(47) Lindström, H.; Södergren, S.; Solbrand, A.; Rensmo, H.; Hjelm, J.; Hagfeldt, A.; Lindquist, S. E. Li^+ Ion Insertion in TiO_2 (anatase). 2. Voltammetry on Nanoporous Films. *J. Phys. Chem. B* **1997**, *101*, 7717−7722.

DOI: 10.1021/acsami.5b07508
ACS Appl. Mater. Interfaces 2015, 7, 25757−25769

M2:

Electrochemical behavior of highly ordered Sn/TiO_2 nanocomposites for lithium and sodium ion batteries – Sn confinement effects and capacity evolution

D. Tapler, M. Wilkening and I. Hanzu

under preparation

Electrochemical behavior of highly ordered Sn/TiO_2 nanocomposites for lithium and sodium ion batteries – Sn confinement effects and capacity evolution

D. Tapler, M. Wilkening, I. Hanzu

Institute of Chemistry and Technology of Materials, Graz University of Technology, Stremayrgasse 9, 8010 Graz, Austria

Abstract. Tin-titania nanocomposite arrays prepared by anodization and subsequent pulsed electrodeposition of Sn metal were investigated in terms of their Li^+ and Na^+ storage behavior. Two nanocomposite samples showing a different degree of tube filling with tin were assembled in Li- and Na-ion test cells and electrochemically tested by galvanostatic cycling with potential limitation and cyclic voltammetry. As an anode material for Na-ion batteries they exhibited stable cycle performance delivering volumetric capacity values of 210 and 240 mAh/cm^3 respectively, when cycled at a C-Rate of C/2 in the potential range of 0.1 and 2 V. In the case of lithium storage capability, a gradual decay of capacity was observed during the first few cycles, but it stabilized after 12 cycles and remained at 430 mAh/cm^3 at a C/2 rate. For both test cells it was found that the achievable volumetric capacities decrease with increasing amount of tin embedded in the inner volume of the titania nanotubes and that the capacity decreased with increasing C-rate, but returned back to its initial values at slower cycling rates. In comparison to a pure Sn electrode a better cycling stability is obtained by the Sn/TiO_2 nanocomposites, which is attributed to restrained volume changes during cycling and the prevention of agglomeration of tin particles.

Introduction

To meet the ever-growing demand for rechargeable battery technologies with higher power capability and energy density, high safety, prolonged lifetime and affordable price [1-4], major efforts have been made to enhance already existing systems based on the Li-ion technology [5-6] and to develop alternative energy storage systems such as Na-ion batteries [7-10]. However, neither of these two approaches can be attained without advanced electrode materials. Among possible anode materials, metallic Sn has attracted particular attention due to its high theoretical specific capacity values and low insertion potential. In particular, tin can alloy with lithium and sodium forming Li- and Na-rich intermetallic compounds with theoretical gravimetric capacities of 993 and 846 mAh/g, respectively [11]. Unfortunately, the alloying/de-alloying reaction is accompanied by huge volume changes leading to mechanical disintegration and hence to poor cycle performance of the electrode [12, 13].

TiO_2 nanotubes, on the other hand, undergo small volume expansion and contraction [14] upon insertion/extraction of Li- and Na-ions and can withstand a large number of cycles without significant loss of capacity [15]. However, the resulting specific capacity values are rather low [16]. Thus, tin-titania nanocomposites, more precisely TiO_2 nanotubes filled with Sn particles, might combine the advantages of both materials, the structural stability of the titania nanotubes with the high specific capacity of Sn.

In this study, we prepared Sn/TiO_2 nanocomposite arrays by a pulsed current electrodeposition approach and investigated its electrochemical behavior as anode material in Li- and Na-ion batteries. The nanocomposite samples were tested in the absence of any binders and conductive agents using common techniques such as galvanostatic cycling with potential limitation and cyclic voltammetry.

Experimental

Tin-titania nanocomposite arrays were prepared according to our previous report [17]. In brief, first self-organized TiO_2 nanotubes were grown on titanium substrates by a two-step anodization process, then filling of the tubes with Sn metal was accomplished by means of a pulsed electrodeposition approach. 40 and 90 pulses were applied in order to study the influence of the pulse number on the electrochemical performance. To remove larger Sn particles from the surface of the nanocomposite arrays, the as-prepared samples were immersed in 20% nitric acid for 30 seconds and 1 minute, respectively. Etching for 1 minute was also performed with pristine titania nanotube samples, that were further used as reference pure TiO_2 samples.

The electrochemical performance of the as-prepared Sn/TiO_2 nanocomposite arrays were investigated in pouch-type cells (Dai Nippon Printing Co., Ltd.). Na and Li half-cells were assembled with the nanocomposites, supported on the titanium substrate, as working electrode and lithium (purity: 99.9%, Sigma Aldrich) or sodium metal (ACS reagent, Sigma Aldrich) as both the counter and the reference electrode. A nonwoven material (Freudenberg FS 2190) soaked with 400 µl of the respective Li or Na electrolyte solution was used as separator. The electrolyte for the Na-half cells consisted of 1 M NaFSI (99.7%, Solvionics) in a mixture (4:6 by volume) of ethylene carbonate (anhydrous, 99%, Sigma Aldrich) and diethyl carbonate (anhydrous, ≥ 99%, Sigma Aldrich). For the Li-half cells a commercial electrolyte SelectiLyte^{TM} LP 30 (1/1 wt/wt DMC/EC and 1 M $LiPF_6$) from BASF was used. For comparison Li and Na half-cells were also assembled with pristine and etched titania nanotube samples. Cyclic voltammetry experiments were carried out at scan rates of 0.05, 0.1, 0.2, 0.5 and 1 mV/s in the potential range of 0.1 – 2 V versus Li^+/Li and Na^+/Na, respectively. Charge/discharge cycling in galvanostatic mode was performed in the same potential range at different rates (C/2, 1C, 2C, C/5). The corresponding charge and discharge currents were determined from the practical capacities obtained from the cyclic voltammograms recorded at the lowest scan rate. Generally, all cells were started after a rest period (OCV) of 12 hours to ensure complete wetting of the electrodes. The electrochemical tests were conducted at room temperature with a programmable multichannel potentiostat (MPG-2, Biologic Science Instruments) running EC-LAB software (version: 10.34). For post-mortem analysis the cycled electrodes (lithiated/sodiated and delithiated/desodiated) were removed from the pouch cells and thoroughly cleaned by rinsing with dimethyl carbonate (anhydrous, ≥ 99%, Sigma Aldrich). All assembling and disassembling steps of the pouch cells were performed in an Ar-filled glove box (150B-G, Mbraun) with H_2O and O_2 vapor concentration below 1 ppm.

The morphology and composition of the pristine and cycled samples were analyzed by using a scanning electron microscope (Zeiss Ultra 55) equipped with an EDX-detector. To obtain cross-section images of the nanotubes the samples were scratched with a sharp steel needle before analysis.

Results and Discussion

The preparation of tin-titania nanocomposite arrays has already been reported in one of our previous works and is based on a two-step process [17]. In the first step self-organized titania nanotubes (NTs) are grown from a Ti foil by anodization in a fluoride containing bath, while in the second step deposition of Sn metal into these anodic titania NTs is achieved by a pulsed current electrodeposition approach. To additionally investigate the influence of the Sn content on the electrochemical performance two different samples were prepared by applying a total number of 40 and 90 current pulses, respectively. Fig. 1 shows Scanning Electron Microscopy (SEM) cross-sectional views of titania nanotubes on which Sn has been electrodeposited after 40 and 90 pulses. It can clearly be seen that nucleation and growth of Sn starts at the tube tops and that the deposited tin is then pushed towards the inner volume of the nanotubes with increasing pulse number resulting in a higher Sn content inside the tubes after a total number of 90 current pulses. It is also evident that large amounts of tin in form of particles are deposited on the surface of the nanotube layers. However, the

presence of these large Sn particles on the tube tops can mask the insertion process of Na- or Li-ions into the titania nanotubes and thus need to be removed.

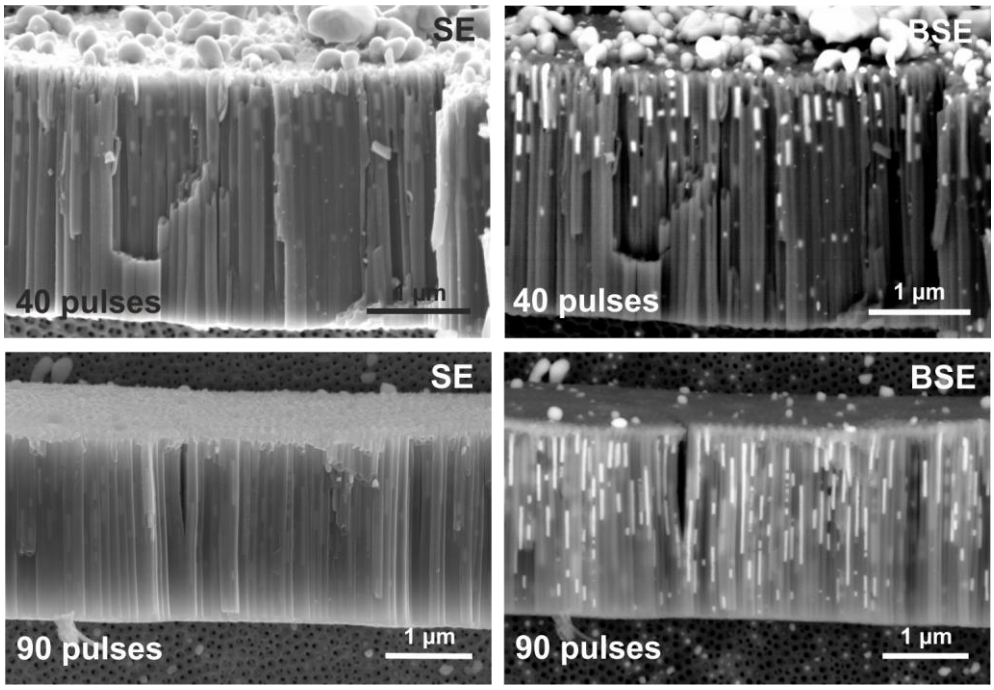

Fig. 1 *Left:* Secondary Electrons (SE) SEM images in cross-section view of titania nanotubes on which tin was deposited with a total number of 40 and 90 pulses, respectively. *Right*: SEM micrographs of the same regions acquired with a Back-Scattered Electrons (BSE) detector, which features chemical element contrast. Metallic Sn deposits are represented by the bright regions.

We noticed that etching of the tin-titania nanocomposite arrays in a 20 % HNO_3 solution for a defined time provides a successful way to clean the surface of the as-prepared nanocomposites. Based on pre-experiments and on our observations it appears that an etching time of 30 s, for the Sn/TiO_2 (40 pulses) sample, and 1 min, for that prepared with 90 current pulses (Sn/TiO_2 (90 pulses)), is appropriate to etch off the large Sn particles from the surface without removing Sn from inside the nanotubes. To ensure that etching in 20 % HNO_3 does not change the morphology and in order to account for any other property change of the nanotube layers, we decided to clean one pristine titania nanotube sample in the same solution for 1 minute. Fig. 2 represents cross-section (a) and top-view (b) SEM images of TiO_2 nanotube layers before and after etching in a 20 % HNO_3 solution for 1 min. It is obvious that the initial nanotubular structure is maintained after the etching process and there are no visible alterations of the nanotubular layer.

In Fig. 3 SEM cross-sectional views of the corresponding tin-titania nanocomposite array samples before (a) and after (b) the etch treatment in HNO_3 are shown. It can clearly be seen that the large Sn particles are successfully removed from the surface of the TiO_2 nanotube layer. In contrast, the tin deposits embedded in the inner volume of the nanotubes are still present.

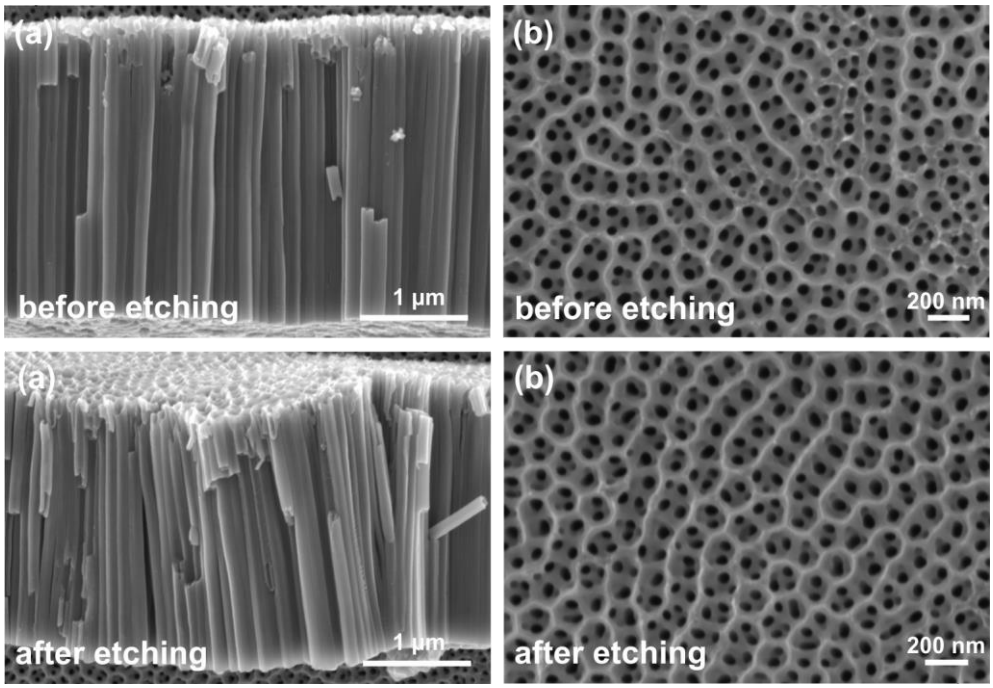

Fig. 2 SEM images in cross-section (**a**) and top-view (**b**) of a TiO_2 nanotube layer before and after etch treatment in 20 % HNO_3 for 1 minute. It can be seen that the nanotubular structure is not attacked by the acid and still retained.

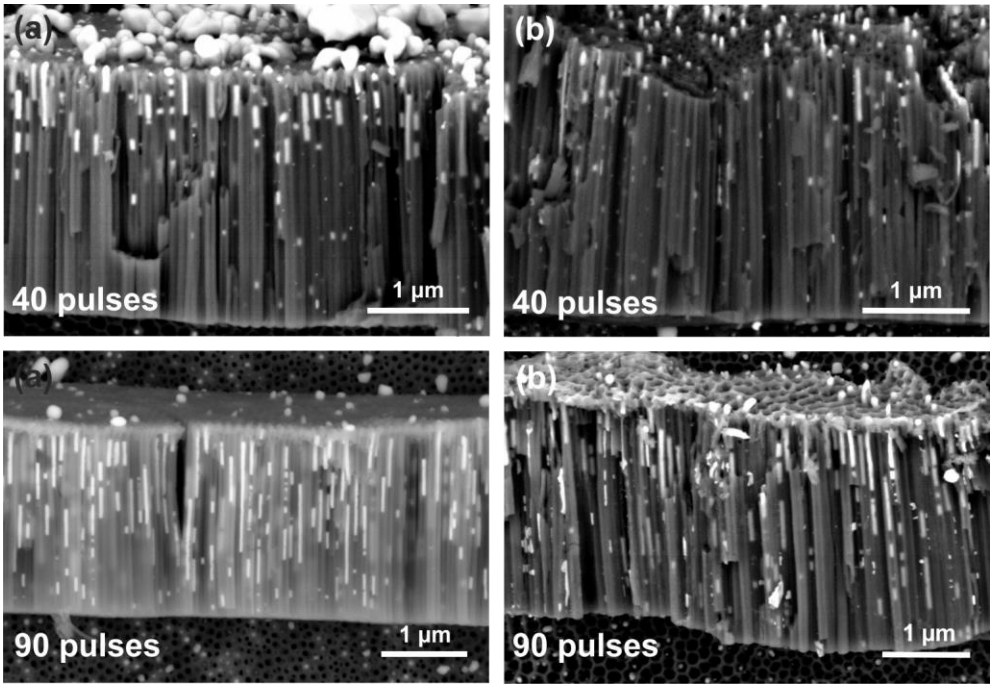

Fig. 3 SEM cross-sectional views of tin-titania nanocomposites before (**a**) and after (**b**) etch treatment in a 20 % solution of HNO_3. The sample prepared with 40 pulses was cleaned for 30 s, the sample on which tin was deposited after 90 pulses was etched for 1 min. It can be noticed, that the large Sn particles are etched off from the top parts of the tubes without removing tin from inside the tubes.

To investigate the electrochemical Li^+ storage ability of the etched and pristine TiO_2 nanotubes and the cleaned 40 and 90 pulses Sn/TiO_2 nanocomposite samples, we used galvanostatic cycling with potential limitation experiments. The insertion of Li in TiO_2 is based on the following reaction

$$xLi^+ + xe^- + TiO_2 \leftrightarrow Li_xTiO_2 \ (0 \leq x \geq 1), \quad (1)$$

while the electrochemical reaction between metallic tin and lithium involves an alloying process according to

$$xLi^+ + xe^- + Sn \leftrightarrow Li_xSn \ (0 \leq x \geq 4.4). \quad (2)$$

For the experiments the vacuum-dried samples were assembled in pouch-type cells with metallic lithium as counter and reference electrode. The electrolyte used consisted of 1 M $LiPF_6$ dissolved in a 1:1 mixture of EC:DMC (LP 30). All Li half-cells were cycled between 0.1 and 2 V vs Li^+/Li reference.

The results of the galvanostatic cycling measurements of the etched and pristine titania nanotubes sample performed at various C-rates are shown in Fig. 4. It can be seen that etching of the TiO_2 nanotube layers has a large influence on the Li^+ storage ability resulting in lower achievable capacities. This can be probably explained by the fact that treatment of TiO_2 in an oxidating reagent leads to the oxidation of any Ti^{3+} that might have been present in the sample. As a consequence, the charge carrier density will decrease and subsequently the electrical conductivity will also decrease probably leading to lower capacities. Although this effect is at this point not completely clear, we can easily imagine that a surface modification of amorphous TiO_2 after treatment with nitric acid could lead to such observations. It is important to note that the results are given in mAh/cm^3, since it is not possible to determine the mass of the active material, which is necessary to calculate the specific capacity.

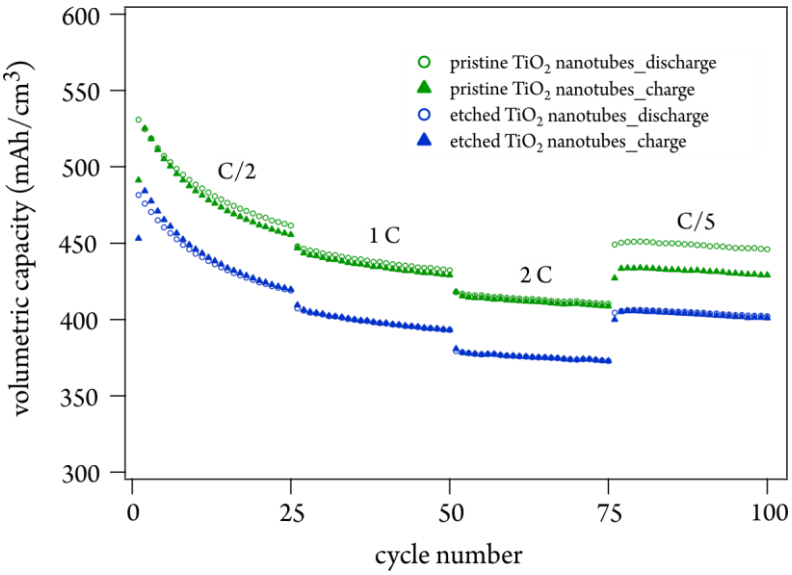

Fig. 4 Galvanostatic cycling *vs.* lithium of the etched and pristine titania nanotubes sample. The Li half-cells were cycled in the potential range from 0.1 to 2 V vs. Li^+/Li reference at different C-rates. Etch treatment of the titania nanotube layers results in lower capacity values.

Fig. 5 compares the cycling performances of the etched pristine titania nanotubes and the Sn/TiO_2 nanocomposite samples (40 and 90 pulses) at different C-rates. Here, the initial volumetric capacity is in the same range for all three samples achieving values in the order of 500 mAh/cm^3 at a charge/discharge rate of C/2. However, the Sn/TiO_2 nanocomposite samples present a gradual decay of capacity within the next cycles at the same C-rate resulting in a remaining capacity after 25 cycles of 365 mAh/cm^3 for the Sn/TiO_2 (40 pulses) and 330 mAh/cm^3 for the Sn/TiO_2 (90 pulses) sample, respectively. The capacity loss observed can be ascribed to some Li^+ being trapped in the Sn/TiO_2 nanocomposite electrode forming "dead" lithium [18] and the formation of a solid electrolyte interphase (SEI) layer, since metallic Sn promotes the decomposition of electrolyte below 1.5 V [19]. In contrast, the etched pristine titania nanotubes sample displayed a better rate capability and a higher Li^+ storage capacity. After a decrease during the first few cycles, capacity stabilizes and remains at 430 mAh/cm^3 after 12 cycles at a C/2 rate. At higher C-rates good cycle stability was achieved in all three cases. Additionally, it can be observed that the reversible capacities decreased with faster cyling rates. But, when returning to slower cycling rates (C/5) the capacities recovered back to its initial values. It is worth noting that even both Sn/TiO_2 nanocomposite samples exhibit capacity values close to those of the etched pristine titania nanotubes at a rate of C/5.

When comparing the Li^+ storage ability of all three samples, it is obvious that the etched pristine TiO_2 nanotubes sample achieved by far the highest capacity values. Interestingly, the results show, besides the fact that the achievable capacities are much lower compared to the pristine sample that the overall capacity decreased with increasing amount of Sn inside the nanotubes. Thus, filling of the titania nanotubes with tin does not have a positive effect in terms of Li^+ storage capability. However, compared to a pure Sn electrode, which usually cycles to death immediately, a better cycling stability can be obtained. This might be due to the fact that the nanotubular structure prevents aggregation of tin particles and restrains volume changes during charging and discharging.

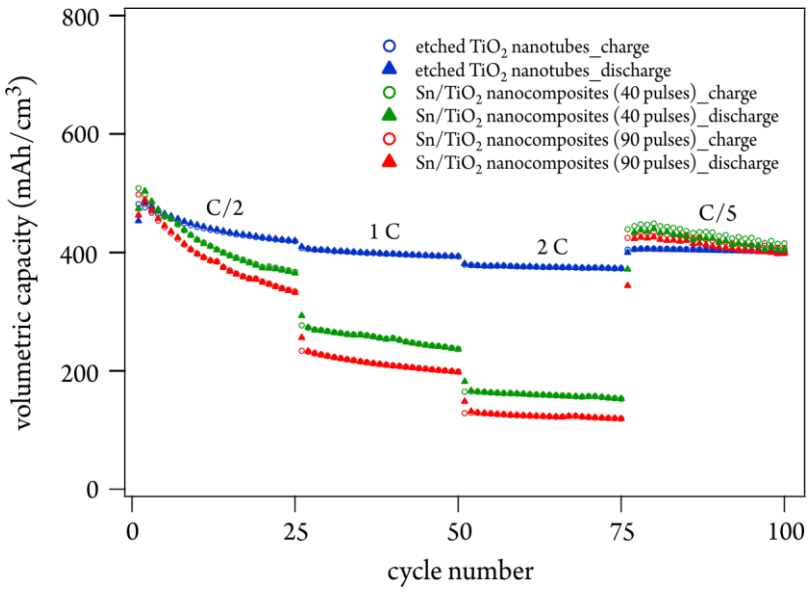

Fig. 5 Cycling performances of the Sn/TiO_2 nanocomposite samples (40 and 90 pulses) and the etched TiO_2 nanotubes at various C-rates. The Li half-cells were cycled between 0.1 and 2 V vs. Li^+/Li reference. It can be seen that the highest capacity values are achieved by the etched titania nanotubes. Interestingly, the overall capacity decreased with increasing amount of Sn inside the tubes.

After galvanostatic cycling experiments the cells were opened and the samples were analyzed again using SEM to explore the influence of the Li^+ insertion/de-insertion process on the morphology. Fig. 6 represents the corresponding post-mortem SEM images. It can be noticed that, in the case of the tin-titania nanocomposite sample prepared with 40 pulses, the nanotubular structure is fully maintained without any sign of damage. Additionally, no progressive tin agglomeration is observed regarding the tin-titania nanocomposites. The nanotubes are still clearly visible in the Sn/TiO_2 nanocomposite (90 pulses) sample. However, a thick layer is found on top of this sample after cycling, which is not present on the surface of the Sn/TiO_2 nanocomposites (40 pulses). As already mentioned above, metallic Sn promotes decomposition of the electrolyte resulting in the formation of a SEI film. This means that layer formation is preferred on the 90 pulses sample due to its higher Sn content. The observed layer might be a possible explanation for the worse cycling performance of the titania nanotubes on which Sn has been deposited after 90 pulses.

To study the morphology of the Sn/TiO_2 nanocomposites at their highest lithium content, i.e., when lithium is inserted, one fresh cell, assembled with the Sn/TiO_2 nanocomposite sample prepared after 90 pulses, is charged to a potential of 0.1 V with a scan rate of 0.5 mV/s and stopped in this state. The results of the corresponding SEM analysis are presented in Fig. 7. Interestingly, the nanotubular structure is not clearly visible at first glance either in Secondary Electron or in Back-Scattered Electron mode. The structure looks somehow amorphous. However, from the cross-section views at higher magnification it is obvious that the nanotubes are still present, albeit covered by a thin layer. In addition to the thick film on the tube tops, also a thin layer forms on the outer tube wall, when Li is inserted. Also noteworthy is that no cracks or destroyed nanotubes are observed, which might be ascribed to the large volume expansion of tin during its electrochemical reaction with lithium. Another important finding is the fact that the SEI layer found on top of the nanotubes is formed during the first charging of the Sn/TiO_2 nanocomposite arrays.

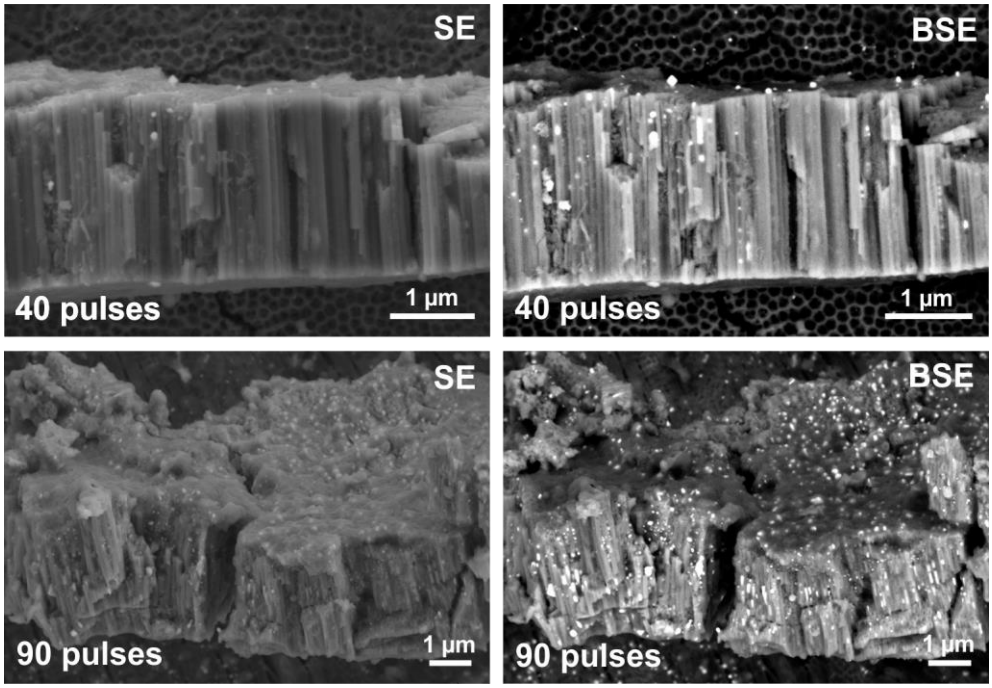

Fig. 6 SEM cross-sectional views in SE and BSE mode of the Sn/TiO_2 nanocomposites after galvanostatic cycling for 100 cycles in the potential range from 0.1 to 2 V vs. Li^+/Li reference at different C-rates. Obviously, the nanotubular structure is fully retained after cycling without any sign of damage. However, a thick layer is present on the tin-titania nanocomposite sample prepared with 90 pulses.

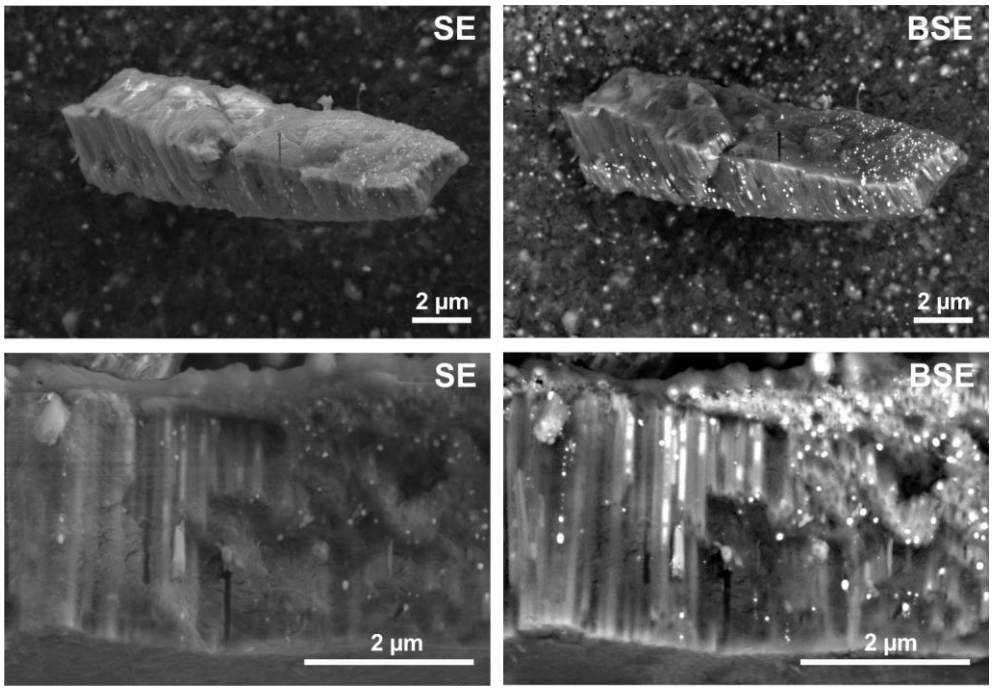

Fig. 7 *Left:* Cross-section SEM images of Sn/TiO_2 nanocomposites (90 pulses) at their highest lithium content. *Right:* Same regions imaged with a BSE detector. For this experiment the Li half-cell is charged to a potential of 0.1 V with a sweep rate of 0.05 mV/s and stopped in this state. From the images at higher magnification it is obvious that the nanotube walls are covered by a thin layer. Layer formation on top of the nanotubes occurs during the first charging.

To evaluate the electrochemical behavior of these Sn/TiO_2 nanocomposites during the Li^+ insertion reaction, cyclic voltammetry (CV) measurements were carried out at scan rates ranging from 0.05 to 1 mV/s between 0.1 and 2 V vs. Li^+/Li reference. Fig. 8 (a) presents the CV curves of the tin-titania nanocomposite sample prepared at 90 pulses for the first two cycles recorded at a scan rate of 0.05 mV/s. In the first cathodic scan, a large increase in reduction current can be observed between 0.6 and 1.6 V, which is not visible in the subsequent cycle. This hump has its origin in the formation of an SEI layer caused by the decomposition of the electrolyte, which is catalyzed by tin particles in this potential range. This observation is in good agreement with our results obtained from SEM analysis. The following three cathodic peaks at 0.6, 0.4 and 0.12 V are related to the electrochemical reaction between metallic tin and lithium forming Li_xSn alloys according to Equ. 2. The distinctive oxidation peaks between 0.6 and 0.8 V in the first reversed scan can then be assigned to the corresponding de-alloying reaction. In addition, a broad anodic peak appears in the range of 1.0 to 1.6 V, which might be attributed to the de-insertion reaction of Li from the TiO_2 nanotubes.

Fig. 8 (b) shows the cyclic voltammograms at higher sweep rates. The distinctive reduction and oxidation peaks assigned to the alloying/de-alloying process are still visible even at higher scan rates. In addition, a good overlap of both cycles recorded at each scan rate can be observed pointing to a relatively good reversibility.

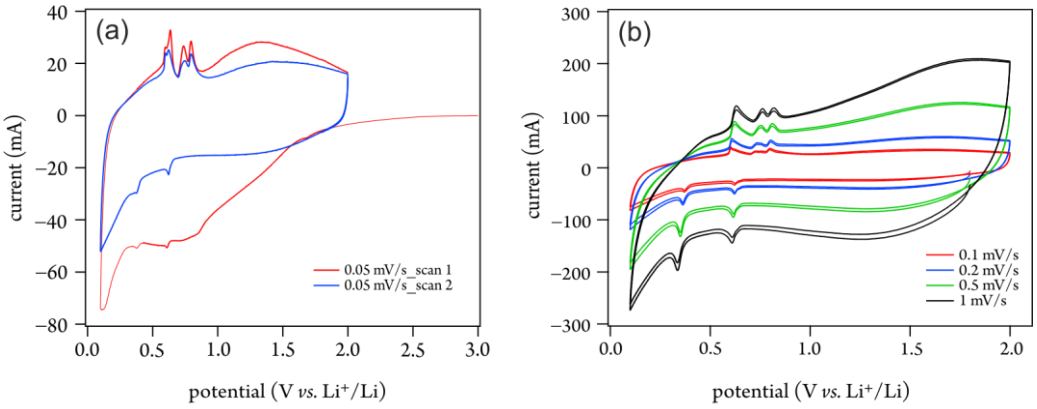

Fig. 8 **(a)** Cyclic voltammetry curves of the first two cycles at a sweep rate of 0.05 mV/s for Sn/TiO_2 nanocomposites prepared with 90 pulses. **(b)** CV curves of the same sample recorded at higher sweep rates. The reductive current in the first cycle is attributed to SEI layer formation. The three cathodic peaks between 0.6 and 0.12 V and the corresponding oxidation peaks between 0.6 and 0.8 V are related to the alloying/de-alloying reaction.

It is also known that tin can form alloys with Na resulting in high capacity values. Furthermore, it has been shown that highly-ordered TiO_2 nanotubes reveal a good cycle performance, when sodium is inserted. Thus, in the present study, we also investigated the electrochemical Na^+ storage ability of the as-prepared Sn/TiO_2 nanocomposite samples. The sodiation of TiO_2 occurs analogous to the Li insertion reaction according to

$$xNa^+ + xe^- + TiO_2 \leftrightarrow Na_xTiO_2 \quad (0 \le x \le 1), \tag{3}$$

while the electrochemical reaction between metallic tin and sodium leads to the formation of several Na_xSn compounds finally obtaining $Na_{3.75}Sn$ ($Na_{15}Sn_4$):

$$xNa^+ + xe^- + Sn \leftrightarrow Na_xSn \quad (3.75 \le x). \tag{4}$$

For the cyclic voltammetry and galvanostatic cycling experiments we assembled Na half-cells using the etched pristine titania nanotubes as well as the Sn/TiO_2 nanocomposites (40 and 90 pulses) as working electrode and metallic Na foil as counter and reference electrode. The electrolyte was a 1 M solution of NaFSI dissolved in a mixture of EC/DEC (4:6). The results of the galvanostatic cycling measurements performed at various C-rates in the potential range from 0.1 to 2 V vs. Na^+/Na reference are shown in Fig. 9. As already noticed in the case of the lithiation process the highest capacity values can be observed for the pristine titania nanotubes. After a continuous decrease during the first few cycles, the capacity finally stabilizes after 15 charge/discharge cycles delivering values of 330 mAh/cm^3 at a C/2 rate. Additionally, only a slight difference in capacity was found at faster cycling rates. Concerning the sodiation of the Sn/TiO_2 nanocomposite samples, self-improvement of the reversible volumetric capacity occurs in the first cycles, which is in contrast to Li-insertion, where a gradual capacity fading is observed during the initial cycles. This kind of capacity enhancement behavior has already been reported in literature [20]. Here, the capacity values of the investigated samples increase over the first 12 cycles, followed by a stabilization of the volumetric capacity even at higher C-rates. The capacity was maintained at 240 mAh/cm^3 for the Sn/TiO_2 nanocomposite sample prepared with 40 pulses and 210 mAh/g for the Sn/TiO_2 nanocomposite (90 pulses) sample at a C-rate of 0.5 (C/2). In analogy to the lithiation process the achievable volumetric capacities decrease with increasing amount of tin embedded in the inner volume of the titania nanotubes. It can also be noticed that the capacity decreased with increasing C-rate, but returned back to its initial values at slower cycling rates.

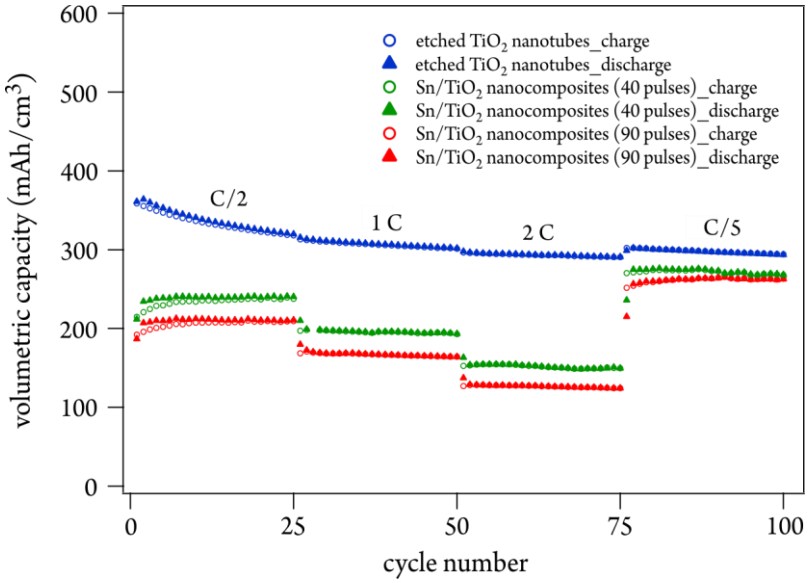

Fig. 9 Galvanostatic cycling *vs.* sodium of the etched titania nanotubes and the Sn/TiO_2 nanocomposites prepared with 40 and 90 pulses. The Na half-cells were cycled in the potential range from 0.1 to 2 V vs. Na^+/Na reference at various C-rates. Regarding the cycling performance of the tin-titania nanocomposites, after some self-improvement of the volumetric capacity, stable values are achieved after ten cycles. The highest overall capacity is observed for the etched titania nanotubes.

Post-mortem SEM analysis, as shown in Fig. 10, documents that the nanotubular structure is retained after cycling in both samples. In addition, no cracks, which might be induced by large volume changes during sodiation/desodiation of Sn, are visible. Another interesting feature is represented by the thick, coarse layer found on the surface of the titania nanotubes. Since this layer is present in both samples, it cannot be ascribed to the catalytic decomposition of the electrolyte caused by metallic tin. It can therefore be concluded that the electrolyte used is not stable within the investigated potential range.

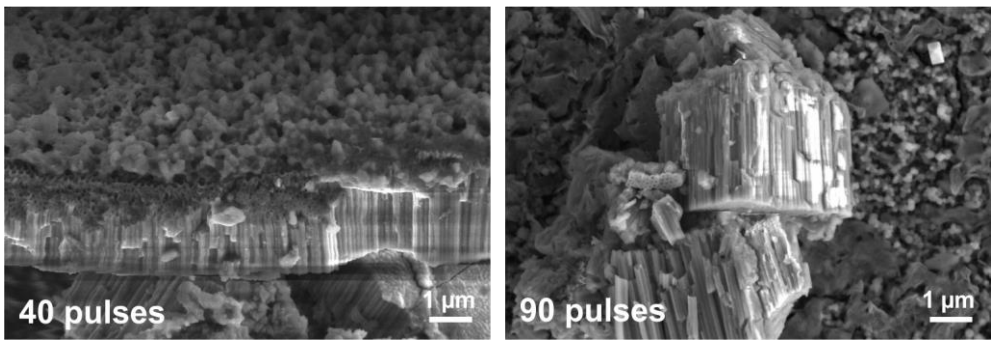

Fig. 10 SEM images of Sn/TiO_2 nanocomposites after galvanostatic cycling for 100 cycles between 0.1 and 2 V at different C-rates. One interesting feature is the thick, coarse layer present on the tube tops.

Fig. 11 illustrates SEM images in cross-sectional views of the Sn/TiO_2 nanocomposite sample (90 pulses) stopped in the reduced state, i.e., in the charged state. Obviously, the top parts of the nanotubes and the outer tube walls are covered with a layer during sodiation (see SEM images at higher magnification). However, the film on the nanotube walls is not observed in the fully cycled sample.

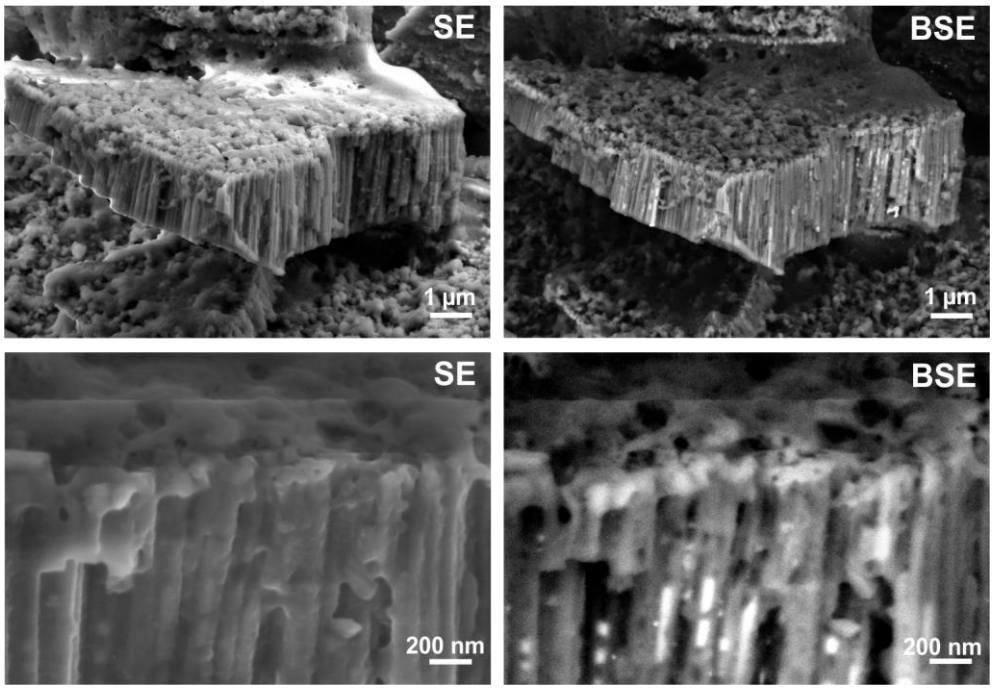

Fig. 11 SEM images in cross-sectional view of tin-titania nanocomposites prepared with 90 pulses, when sodium is inserted. From the images at higher magnification it is obvious that the tubes are covered by a layer during sodiation.

To get more insight into the Na^+ insertion reaction mechanism, cyclic voltammetry measurements were performed at various scan rates in the potential range of 0.1 to 2 V vs. Na^+/Na reference. The results shown in Fig. 12 correspond to the titania nanotubes sample on which Sn has been deposited after 90 pulses. From our previous work we know that the reversible Na-ion insertion into TiO_2 does not show any discernible oxidation or reduction peaks [15]. This means that the three peaks visible between 0.5 and 0.65 V in the anodic scan can be attributed to the electrochemical de-sodiation reaction of the Na_xSn alloys. These three oxidation peaks become blurred at higher scan rates. Considering the cathodic scan no distinctive reduction peaks can be observed. The large discrepancy in the current response between the first and the second cycle might be related to the formation of the SEI layer on top of the nanotubes. It is worth noting that the two cycles of each scan rate almost overlap arguing for good cycle reversibility.

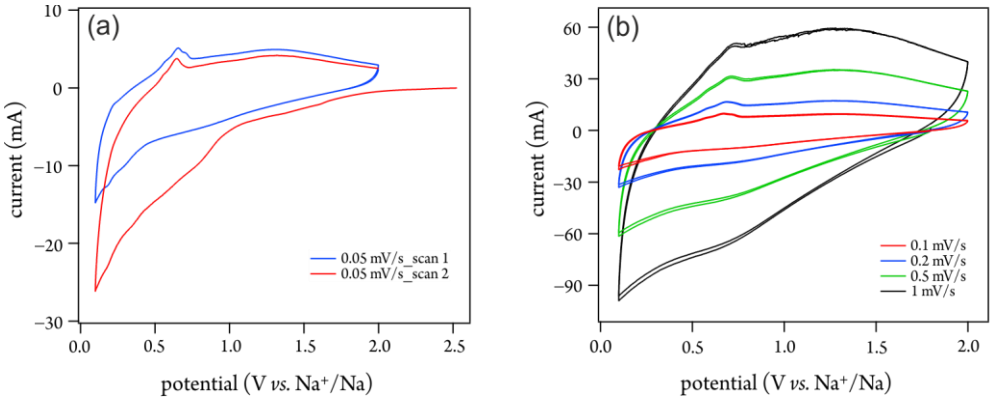

Fig. 12 **(a)** CV curve of the first two cycles at a scan rate of 0.05 mV/s for Sn/TiO_2 nanocomposites (90 pulses). **(b)** Cyclic voltammograms of the same sample recorded at higher scan rates. In the cathodic scan no distinctive peaks can be observed. The three oxidation peaks in the anodic scan are attributed to de-sodiation of Na_xSn.

Conclusion

The electrochemical behavior of Sn/TiO_2 nanocomposites prepared by pulsed current electrodeposition was investigated by means of cyclic voltammetry and galvanostatic cycling experiments. In summary, filling of the titania nanotubes with tin does not have a positive effect in terms of Li^+ and Na^+ storage capability. Lower volumetric capacity values were achieved in contrast to the pristine TiO_2 nanotubes. But, compared to a pure Sn electrode, which usually cycles to death immediately, a better cycling stability can be obtained. This might be due to the fact that the nanotubular structure prevents aggregation of tin particles and restrains volume changes during charging and discharging. We therefore believe that encapsulation of Sn into a stable matrix such as titania nanotubes can help to improve the stability of Sn anodes although in unoptimized conditions this can initially lead to lower capacities.

Acknowledgement. Financial support by the Austrian Federal Ministry for Digital and Economic Affairs and the National Foundation for Research, Technology and Development is gratefully acknowledged. We also thank the Deutsche Forschungsgemeinschaft (FOR1277, WI 3600 2-1, 4-1; SPP 1415 WI 3600 5-2) for financial support.

References

1. Armand, M., Tarascon, J.-M., *Nature*, 2008, **451**, 652.
2. Tarascon, J.-M., Armand, M., *Nature*, 2001, **414**, 359.
3. Whittingham, M.s., *Chemical Review*, 2004, **104**, 4271.
4. Zubi, G., et al., *Renewable and Sustainable Energy Reviews*, 2018, **89**, 292.
5. Palacin, M.R., *Chemical Society Reviews*, 2009, **38** (9), 2565.
6. Nitta, N., et al., *Materials Today*, 2015, **18** (5), 252.
7. Palomares, V., et al., *Energy & Environmental Science*, 2012, **5** (3), 5884.
8. Palomares, V., et al., *Energy & Environmental Science*, 2013, **6** (8), 2312.
9. Ellis, B.L., Nazar, L.F., *Current Opinion in Solid State and Material Science*, 2012, **16** (4), 168.
10. Slater, M.D., et al., *Advanced Functional Materials*, 2013, **23** (8), 947.
11. Huang, B., Pan, Z., Su, X., An, L., *Journal of Power Sources*, 2018, **395**, 41.
12. Wang, J., Raistrick, I.D., Huggins, R.A., *Journal of Electrochemical Society*, 1986, **133**, 457.
13. Li, N.C., Martin, C.R., Scrosati, B., *Electrochemical Solid-State Letters*, 2000, **3**, 316.
14. Wagemaker, M., Kearley, G.J., Well, A.A., Mutka, H., Mulder, F.M., *Journal of American Society*, 2003, **125**, 840.
15. Prutsch, D., Wilkening, M., Hanzu, I., ACS *Applied Material Interfaces*, 2015, **7**, 25757.
16. Bi, Z., et al., *Journal of Power Sources*, 2013, **222**, 461.
17. Prutsch, D., Wilkening, M., Hanzu, I., *RSC Advances*, 2016, **6**, 98243.
18. Rehnlund, D., et al., *Energy Environmental Science*, 2017, **10**, 1350.
19. Beattie, S.D., Hatchard, T., Bonakdarpour, A., Hewitt, K.C., Dahn, J.R., *Journal of Electrochemical Society*, 2003, **150**, A701.
20. Xiong, H., Slater, M.D., Balasubramanian, M., Johnson, C.S., Rajh, T., *Journal of Physical Chemistry Letters*, 2011, **2**, 2560.

6.2 Ion transport and electrochemical activity of nanostructured ceramics

Over the past decades, nanostructured materials have significantly influenced numerous fields in technology and science owing to their beneficial properties. In particular, ceramics with nano-size dimensions have attracted attention for their potential application as sensors [224], adsorbents [225], catalysts [226] or as advanced electrode materials and new electrolytes in batteries [227]. Regarding the electrochemical energy storage sector, the expected advantages that go along with a reduction of the dimension are as follow [25]:

- The smaller particle size leads to a reduction of the diffusion path length for the mobile ions. As a consequence of this, the lithium or sodium diffusivity is improved. This plays an important role for solid electrolytes as well as for active materials, where a higher insertion/extraction rate is achieved.
- The high surface area of nanostructured materials implies a high contact area between electrolyte and active material, leading to an enhanced ion transport across this interface. Additionally, due to the higher surface to volume ratio, more active sites for sodium or lithium storage are present resulting in an increase of capacity.
- Nanostructuring can enable electrochemical activity in materials that are not active in the micrometer range. Rutile, for example, only shows electrochemical activity, when their particle size is in the nanorange.

However, the elementary origin of the superior electrochemical properties of nano-sized ceramics and their ability for ease ion conduction are not completely understood. It is known that the connections of the polehedra and point defects play an important role in facilitating bulk ion transport and jump processes (see 2.3). But also the morphology of the ceramic can determine ion migration over long distances. Depending on the preparation method of nanostructured ceramics, interfaces exhibiting structural disorder as well as amorphous and defect-rich regions can be introduced into the material structure. To understand the connection between microscopic structure and electrochemical performance as well as ion dynamics is necessary for the development of advanced functionalized materials.
In the following review article, **P3**, we studied various nano-sized ceramics in terms of their electrochemical properties and ion transport. Special emphasis is paid on TiO_2 present in amorphous or crystalline nanotube or nanorod form or as mesoporous material. Furthermore, we investigated some nanostructured oxides ($Li_4Ti_5O_{12}$, $LiAlO_2$, Li_2TiO_3, $LiTaO_3$) and peroxides (Li_2O_2) in order to explore the influence of the preparation method on their overall ionic transport.

P3:

Nanostructured Ceramics: Ionic Transport and Electrochemical Activity

D. Prutsch, S. Breuer, M. Uitz, B. Stanje, J. Langer, P. Bottke, S. Lunghammer, P. Posch, V. Pregartner, M. Philipp, A. Dunst, D. Wohlmuth, H. Brandstätter, W. Schmidt, V. Epp, A. Chadwick, I. Hanzu and M. Wilkening

Z. Phys. Chem., **231** (2017), 1361.

Denise Prutsch, Stefan Breuer, Marlena Uitz, Patrick Bottke, Julia Langer, Sarah Lunghammer, Martin Philipp, Patrick Posch, Veronika Pregartner, Bernhard Stanje, Andreas Dunst, Dominik Wohlmuth, Harald Brandstätter, Walter Schmidt, Viktor Epp, Alan Chadwick, Ilie Hanzu* and Martin Wilkening*

Nanostructured Ceramics: Ionic Transport and Electrochemical Activity

A short journey across various families of materials

DOI 10.1515/zpch-2016-0924
Received November 4, 2016; accepted May 23, 2017

Abstract: Ceramics with nm-sized dimensions are widely used in various applications such as batteries, fuel cells or sensors. Their oftentimes superior electrochemical properties as well as their capabilities to easily conduct ions are, however, not completely understood. Depending on the method chosen to prepare the materials, nanostructured ceramics may be equipped with a large area fraction of interfacial regions that exhibit structural disorder. Elucidating the relationship between microscopic disorder and ion dynamics as well as electrochemical performance is necessary to develop new functionalized materials. Here, we highlight some of the very recent studies on ion transport and electrochemical properties of nanostructured ceramics. Emphasis is put on TiO_2 in the form of nanorods, nanotubes or being present as mesoporous material. Further examples deal with

***Corresponding authors: Ilie Hanzu and Martin Wilkening,** Institute for Chemistry and Technology of Materials, and Christian Doppler Laboratory for Lithium Batteries, Graz University of Technology (NAWI Graz), Stremayrgasse 9, A-8010 Graz, Austria; and Leibniz University of Hannover, Institute of Physical Chemistry and Electrochemistry, Callinstraße 3-3a, D-30167 Hannover, Germany, e-mail: hanzu@tugraz.at (I. Hanzu); wilkening@tugraz.at (M. Wilkening)
Denise Prutsch, Stefan Breuer, Marlena Uitz, Patrick Bottke, Julia Langer, Sarah Lunghammer, Martin Philipp, Patrick Posch, Veronika Pregartner, Bernhard Stanje, Andreas Dunst, Dominik Wohlmuth, Harald Brandstätter, Walter Schmidt and Viktor Epp: Institute for Chemistry and Technology of Materials, and Christian Doppler Laboratory for Lithium Batteries, Graz University of Technology (NAWI Graz), Stremayrgasse 9, A-8010 Graz, Austria; and Leibniz University of Hannover, Institute of Physical Chemistry and Electrochemistry, Callinstraße 3-3a, D-30167 Hannover, Germany
Alan Chadwick: School of Physical Sciences, University of Kent, Canterbury, Kent CT2 7NH, UK

Bereitgestellt von | Technische Universität Graz
Angemeldet
Heruntergeladen am | 06.11.18 13:39

nanocrystalline peroxides such as Li_2O_2 or nanostructured oxides (Li_2TiO_3, $LiAlO_2$, $LiTaO_3$, Li_2CO_3 and $Li_2B_4O_7$). These materials served as model systems to explore the influence of ball-milling on overall ionic transport.

Keywords: amorphous materials; conductivity; glasses; lithium ion transport; nanocrystalline oxides; nanotubes; NMR; peroxides; self-diffusion; titania.

1 Introduction and motivation

The mobility of small cations or anions in ionic crystals depend on numerous factors. On the one hand, point defects and polyhedral connections play a decisive part in enabling local jump processes and bulk ion transport. On the other hand, the morphology of the whole ceramic will determine migration of the charge carriers over long, i.e. macroscopic, distances. Disorder can be introduced through many different approaches such as radiation or bombardment techniques. A far more simple approach is to mechanically treat the coarse-grained samples in high-energy mills [1]. Conveniently, high-energy ball milling is carried out at ambient temperature; it allows for the preparation of large quantities. In many cases, if only one component is treated phase pure nanocrystalline materials are obtained with large volume fractions of amorphous regions or at least disordered interfaces [2]. The introduction of point defects and dislocations is, however, also expected for the crystalline cores of the nanocrystallites [3]. So far, many examples have been reported documenting that the ionic conductivity of a poor conductor can significantly be enhanced when transforming the oxides or sulfides into a defect-rich nanocrystalline ceramics [4, 5]. One may regard the excessive generation of defects, greatly exceeding the thermodynamic level, as a possibility to form materials with metastable properties concerning both defect concentrations and non-equilibrium local structures [6–9]. In general, the interfaces in nanostructured ceramics and nano-composites may govern macroscopic properties such as the ionic and electronic conductivity [2, 10–26].

Besides such top-down approaches the direct preparation of nanocrystalline or amorphous ceramic through wet chemical methods or electrochemical techniques is also possible. As an example, the ionic conductivity of sol–gel synthesis of nanocrystalline $LiNbO_3$ is indeed enhanced compared to its single crystalline or microcrystalline form with μm-sized crystallites [4]. Considering, however, the chemically identical samples prepared by heavy ball-milling their ion conductivity is much higher. Obviously, at least in the case of poorly conducting oxides the disordered if not completely amorphous regions are greatly responsible for the

Bereitgestellt von | Technische Universität Graz
Angemeldet
Heruntergeladen am | 06.11.18 13:39

gradual transformation from a poor to a moderate or even highly conducting ion conductor [2, 5, 27–33].

Amorphous regions also immensely influence the electrochemical activity of otherwise poorly active materials. The different modifications of TiO_2 belong to such a class of materials. Only downsizing the crystallite size unlocks the full potential of anatase, rutile or TiO_2-B as anode materials [34–37]. The short diffusion lengths for both ions and electrons transform the transition metal oxide into powerful anode materials showing high rate capabilities and excellent specific charge capacities [34, 35]. This also holds for mesoporous [38, 39] and amorphous TiO_2. In the following we will report on the preparation of amorphous TiO_2 nanotubes via anodic etching [40, 41]. The nanotubes, differing in lengths according to the synthesis conditions, have been investigated with respect to loading with Li and Na ions [42]. Electrochemical investigations using cyclic voltammetry and galvanostatic cycling allowed us to reveal the underlying Na storage mechanism. Li nuclear magnetic resonance (NMR) has been used to evaluate the Li self-diffusion parameters of various electrochemically prepared, mixed-conducting Li_xTiO_2 samples [43–45]. For comparison, Li ion dynamics in mesoporous anatase was studied via spin-lock and stimulated echo NMR [43]. It turned out that Li ion diffusion is unaffected by the phase transformation from anatase to orthorhombic TiO_2 during Li uptake. This result is highly beneficial to enable stable cycling conditions in lithium-ion batteries.

The influence of structural disorder generated through ball milling on ion transport will be discussed for a range of model substances that include nanocrystalline Li_2O_2 [29], Na_2O_2 [46], the ternary oxides $LiAlO_2$ [47], Li_2TiO_3 [27], $LiTaO_3$ [5, 48], Li_2CO_3, as well as the glass former $Li_2B_4O_7$ [28]. Whereas Li ion transport in the materials mentioned above is isotropic, transition metal dichalcogenides such as SnS_2 or TiS_2 crystallize with a layered structure. Chemical lithiation enables the insertion of Li ions into the van der Waals gap between the SnS_2 sheets. The Li ions are expected to diffuse quickly along two dimensions. Preliminary NMR results on Li_xSnS_2 show how the diffusion parameters are altered when the material is exposed to mechanical treatment in ball mills. In contrast to microcrystalline Li_xSnS_2 with its fast but spatially confined 2D diffusion [49], in nanocrystalline Li_xSnS_2 the large number of Li ions in the disordered interfacial regions remarkably influence the NMR response. NMR line shapes point to a two-spin reservoir with fast and slow Li species, see also Ref. [50]. Finally, the effect of high-energy ball-milling on ion transport in $Li_2B_4O_7$ is shown. A significant difference is seen when comparing ionic conductivities of crystalline, nanocrystalline and amorphous $Li_2B_4O_7$. The strategy of introducing structural disorder and stress is useful to transform a poor ion conductor into a moderate one. For very fast ion conductors the situation is, on the other hand, expected to be different.

Bereitgestellt von | Technische Universität Graz
Angemeldet
Heruntergeladen am | 06.11.18 13:39

2 Case studies: from oxides to peroxides and back again

2.1 Electrochemical performance and Li ion transport in various forms of TiO_2

The different modifications of TiO_2 represent promising anode materials that provide hosts to reversibly store small cations such as Li and Na. If present in nanostructured form good rate capabilities and discharge capacities as high as 250 mAh/g were reported [36, 37]. Since such electrochemical properties might be linked also to ion dynamics several NMR studies took up the challenge to quantify Li self-diffusivity via, e.g. relaxometry, stimulated echo spectroscopy or even by 2D exchange spectroscopy [43–45, 51, 52]. In the following some recent studies on amorphous TiO_2 nanotubes, rutile nanorods and mesoporous TiO_2 will be presented that deal with electrochemical properties, mechanisms and ion dynamics in these spatially confined structures.

2.1.1 Amorphous TiO_2 nanotubes: synthesis, ionic diffusivity and the underlying storage mechanisms

The synthesis of anodic titania nanotubes [53–55] follows a top-down approach, self-assembled TiO_2 nanotubes are formed on titanium metal substrates by an anodic electrochemical oxidation process, called anodization. The anodization is usually done in two electrode cells at relatively high voltages, typically ranging from 10 to 200 V. To obtain the required nanotubular morphology, the anodization bath must also contain a Ti^{4+} complexing agent. The most used is F^- with which Ti^{4+} is able to form the soluble $[TiF_6]^{2-}$, see Ref. [56]. The formation of the tubes involves two opposite but balanced processes: (i) the electrochemical formation of TiO_2 and (ii) the chemical etching of the formed oxide by the complexing agent. Under high electric field conditions the anodization results in highly regular layers consisting of parallel TiO_2 nanotubes that grow from the Ti substrate.

Both aqueous-based and organic-based baths have been reported to yield highly regular nanotubular layers. While in aqueous baths the length of the nanotubes is somehow limited to 2–3 μm due to the faster fluoride etching of the electrochemically formed TiO_2, in viscous organic-based baths, e.g. ethylene glycol, it is possible to grow very long nanotubes, sometimes longer than 1 mm [57], while keeping almost the same diameter over the entire length of the nanotubes,

Bereitgestellt von | Technische Universität Graz
Angemeldet
Heruntergeladen am | 06.11.18 13:39

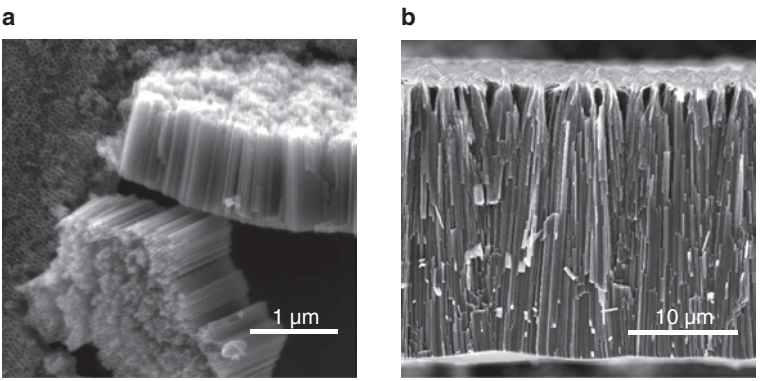

Fig. 1: Scanning electron microscopy (SEM) images illustrating the typical morphology of self-assembled TiO_2 nanotubes fabricated by electrochemical oxidation of Ti metal foil. (a) Top-view and cross-section of a TiO_2 nanotube layer obtained by anodization in an organic electrolyte bath (97.6 wt% ethylene glycol, 2 wt% water, 0.4 wt% NH_4F) at 30 V for 30 min. (b) Cross-section through a TiO_2 nanotube layer fabricated by anodization at 60 V for 1 h 30 min using the same bath composition. While the highly parallel tubular morphology is maintained when the anodization voltage is varied, the rates at which the tubes grow highly depend on the voltage applied.

typically 80–120 nm. Thus, nanotube aspect ratios of $1{:}10^4$ are easily achievable. Since the volume of the produced oxide is larger than the volume of the Ti metal from which it originated, the nanotubes are approximately 1.5 times longer than the corresponding thickness of the Ti layer consumed during anodization [58]. An illustration of some typical anodic TiO_2 nanotubes fabricated in ethylene glycol baths is presented in Figure 1.

Although the relation between the electrochemical conditions and the dimensions and geometry of the anodic titania nanotubes is a relatively complicated topic [58, 59], for a given bath, there is a direct connection between the voltage applied and the tube diameters. In principle, the higher the voltage, the larger the tube diameters are. By this method the diameters can easily be adjusted in practice between 30 and 120 nm.

One of the striking features of anodic TiO_2 is its amorphous structure [59]. In their pristine form, the nanotubes do not present any X-ray reflections in a diffraction experiment as illustrated in Figure 2. In fact, anodic titania is one of the very few known instances in which TiO_2 occurs in its amorphous form. Their unique and tunable morphology doubled by the rare amorphous structure have attracted significant attention; many scientific and technological developments based on titania nanotubes have been brought forward in the last decade [59]. One interesting development is related to the insertion in anodic TiO_2 of ionic

Bereitgestellt von | Technische Universität Graz
Angemeldet
Heruntergeladen am | 06.11.18 13:39

species such as H^+ [60], Li^+ [40] and Na^+ [42] pertaining to the broader field of energy storage and conversion. Whereas earlier NMR studies focused on Li ion diffusion in crystalline nanotubes of TiO_2, mainly TiO_2-B, that were prepared by hydrothermal routes, so far less information is available on Li^+ ion dynamics in amorphous titania nanotubes. Anodic etching allowed the preparation of relatively large quantities and, as mentioned above, according to the exact synthesis conditions both the length and the diameter of the tubes can be controlled. Li is then inserted either electrochemically in half cells with Li metal as anode material or chemically with *n*-BuLi in hexane.

For our first NMR experiments on amorphous TiO_2 rather long tubes (250 µm, see Figures 2a) were synthesized. X-ray powder diffraction confirmed the amorphous structure of the material, Figure 2b, the corresponding pattern for the pristine sample only shows reflections of the Ti metal substrate. Interestingly, the tubes remain amorphous up to 200 °C, at higher temperatures they can be converted into anatase.

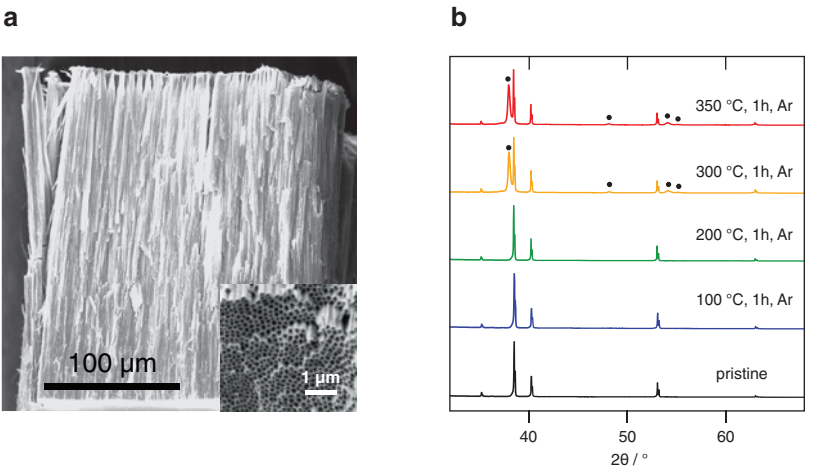

Fig. 2: (a) Cross section SEM micrograph of TiO_2 nanotube layer fabricated by anodization of Ti foil at 60 V for 5 days. The anodization bath consisted of ethylene glycol 97.6 wt%, water 2 wt%, NH_4F 0.4 wt%. The open end of the tubes is at the top of the picture while the closed end is at the bottom of the picture. The nanotubes are approximately 250 µm long and 130 nm in diameter with a wall thickness of 20–30 nm. The inset shows a detailed view of an intentionally broken section revealing the typical morphology of anodic titania nanotubes layers. (b) X-ray diffraction patterns of anodic TiO_2 nanotubes in pristine form and after annealing in Ar atmosphere. Up to 200 °C only the reflections of Ti metal substrate are visible. It is possible to convert the amorphous nanotubes to anatase (•) while keeping the morphology by annealing them in Ar or in air at 300–350 °C.

Bereitgestellt von | Technische Universität Graz
Angemeldet
Heruntergeladen am | 06.11.18 13:39

The typical morphology of the titania nanotube layers is shown in the inset of Figures 2a and 3b. The rather long tubes were used as anode material to prepare Li_xTiO_2 samples with the following compositions $x = 0.5$, $x = 0.75$ and $x = 1.0$.

Variable-temperature ^{7}Li NMR line shape measurements of these tubes revealed that Li ion diffusivity in the amorphous tubes is relatively slow. The rigid lattice line width, which is the line width at sufficiently low T where Li diffusivity has no effect on the NMR line shape, ranged from 12 to 16 kHz according to the amount of Li inserted per formula unit TiO_2. Motional narrowing of the NMR line sets in if Li ion hopping processes reach jump rates that are comparable with the rigid lattice line width. At sufficiently high T these exchange processes start to average homonuclear and heteronuclear dipole–dipole interactions that are responsible for the broadening of the spectra at low T. In the case of Li_xTiO_2 the Li^+–Ti^{3+} interaction leads to further broadening effects. For all compositions motional averaging is seen to take effect on the line shape at temperatures higher than 300 K. This is why so-called spin-alignment echo (SAE) NMR [44, 61–68] proved to be a suitable way to characterize Li ion diffusivity in the tubes prepared (Figure 2a). The method works in the regime where spin–spin-relaxation rates are still unaffected by motional averaging processes [65]. Here, the relatively poor ionic diffusivity as well as the coupling of the Li spins to paramagnetic centers like Ti^{3+} is reflected in a rigid-lattice relaxation time T_{20} of only 6 µs (see Figure 4a). An increase of T_2 is seen at temperatures higher than 330 K. Around this temperature and at $T > 300$ K the SAE NMR decay rates follow Arrhenius behavior with activation energies E_a ranging from 0.3 to 0.5 eV (see Figure 3a). Note that the data points referring to $x = 0.5$ and $x = 1.0$ were vertically shifted by 0.5 orders of magnitude each; the ^{7}Li SAE NMR rates do not significantly depend on composition at low T if rather large values of x are considered. In general, SAE NMR is sensitive to slow Li ion hopping processes ($<10^5$ 1/s) between electrically inequivalent Li sites. Usually the three-pulse sequence introduced by Jeener and Broekaert [61, 69–71] is used to measure a two-time correlation functions S_2 from which the decay rate $1/\tau_{SAE}(T)$ can be deduced.

Interestingly, above 400 K the decay rates from stimulated echo NMR start to decrease again. If T_2 is short enough this behavior can be traced back to averaging processes [61, 72] that occur during the mixing period; such a scenario has quite recently been discussed in detail for fast ion jump processes in Li bearing oxide garnets [73]. In these cases Li exchange processes may become too fast to be collected by SAE NMR. In the present case, however, we have to keep in mind the upper time window of SAE NMR, which is generally restricted by T_2; for comparison with $1/T_2$ the SAE NMR rates $1/\tau_{SAE}$ are jointly plotted with the spin–spin and spin–lattice relaxation rates of $Li_{0.75}TiO_2$ in Figure 4a.

Bereitgestellt von | Technische Universität Graz
Angemeldet
Heruntergeladen am | 06.11.18 13:39

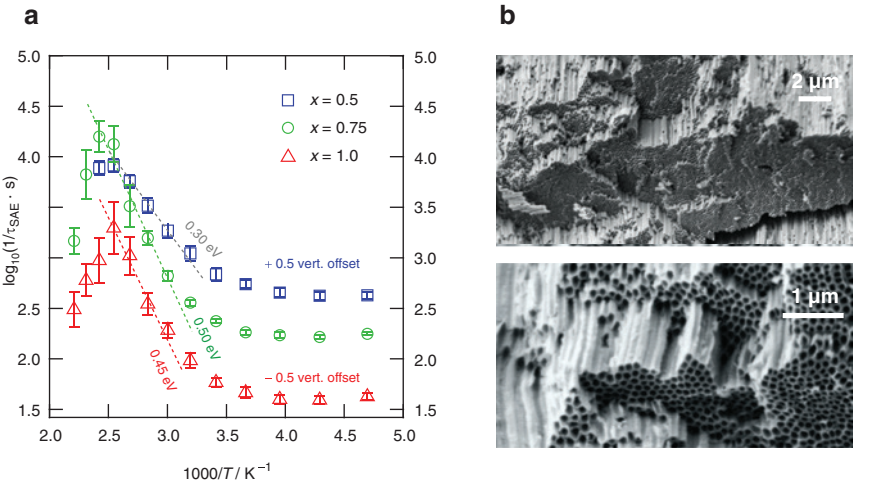

Fig. 3: (a) ^{7}Li NMR spin-alignment echo decay rates (194 MHz) vs. the inverse temperature of various Li_xTiO_2 samples that were prepared electrochemically. To record the rates, two-time correlation functions were measured at constant preparation time (20 µs) but variable mixing-time utilizing the three-pulse sequence by Jeener and Broekaert. (b) SEM images revealing the morphology of the tubes investigated by Li NMR.

Interestingly, for the samples with $x > 0.5$ we observed quite high activation energies by SAE NMR. Values a large as 0.5 eV are in good agreement with those reported for crystalline Li_xTiO_2-B nanowires. Similarly, for mixed-conducting $Li_{1.0}TiO_2$, which was prepared by chemical lithiation, an activation energy of 0.58 eV was obtained (see Figure 4b). While SAE NMR is sensitive to slow Li^+ exchange processes, which in many cases reflect long-range ion transport also accessible by DC conductivity measurements [63], SLR NMR is sensitive to more localized, short-range ion movements [29, 74, 75]. As expected, if the low-T regime of a given $1/T_1(1/T)$ rate peak is considered, much lower activation energies were probed through laboratory-frame ^{7}Li SLR NMR [74, 75]. For $Li_{1.0}TiO_2$ we were able to reach the beginning of the low-T flank of the diffusion-induced $1/T_1(1/T)$ rate peak which resulted in 0.15 eV. Note that this flank was masked in the case of the electrochemically lithiated samples. Presumably, it was hidden by an increased Li–electron contribution to the overall spin–lattice relaxation rate. The electrochemically prepared samples are expected to contain minute amounts of fluorine from anodization. This F content will increase the electronic conductivity of the samples. As a result, coupling of the spins with conduction electrons shortens the overall T_1 relaxation time which narrows the time window of time-domain NMR measurements. In extreme cases the diffusion-induced contributions to the overall spin–lattice relaxation rates are completely masked [45]. In particular, due to the large volume fraction

Bereitgestellt von | Technische Universität Graz
Angemeldet
Heruntergeladen am | 06.11.18 13:39

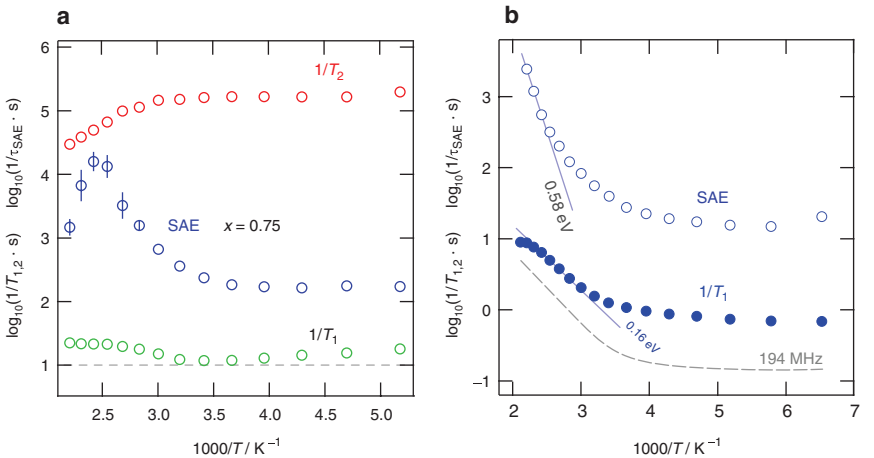

Fig. 4: (a) Temperature dependence of the (i) ^{7}Li SAE NMR decay rates, the (ii) ^{7}Li NMR spin–lattice and the (iii) spin–spin relaxation rates of $Li_{0.75}TiO_2$ (116 MHz). While $1/T_1$ suffers from Li^+–Ti^{3+} interactions as well as the influence of additives such as binders and conductive agents of the electrode resulting in short T_1 times of <1 s, SAE NMR is able to recognize a diffusion-induced increase at $T > 330$ K. The shallow increase of $1/T_1$ at low T can be ascribed to Curie–Weiss behavior. (b) ^{7}Li SAE NMR response of $Li_{1.0}TiO_2$ that was prepared by chemical lithiation of the amorphous titanate nanotubes. As compared to the electrochemically lithiated samples, the absolute, non-diffusive rate $1/T_1$ is lower which allowed us to measure the beginning of a diffusion-induced $1/T_1(1/T)$ rate peak. The curvature seen at high T most likely reflects a local rate maximum which would be in accordance with the low activation energy probed (0.15 eV). At the same temperature (ca. 500 K) SAE NMR points to quite slow Li exchange processes that characterize long-range ion transport with 0.58 eV.

of interfacial regions of nanocrystalline TiO_2 the spin–electron interactions with conductive carbon additives in contact with these surface regions can drastically shorten the T_1 times, which also restricts the applicability of other NMR techniques that are limited by T_1 such as rotating-frame SLR measurements (*vide infra*).

2.1.2 Crystalline TiO_2 nanotubes crystallizing with the anatase structure

As noted above, the amorphous titania nanotubes convert into anatase at elevated T. Alternatively, anatase nanotubes can be prepared following a hydrothermal route. In Figure 5 the high-resolution (HR) transmission electron microscopy (TEM) images of hydrothermally synthesized nanocrystalline TiO_2 tubes are shown. X-ray powder diffraction and ^{7}Li NMR spectroscopy point to a highly crystalline material whose tubes crystallize with the anatase structure (Figure 6). By varying the

Bereitgestellt von | Technische Universität Graz
Angemeldet
Heruntergeladen am | 06.11.18 13:39

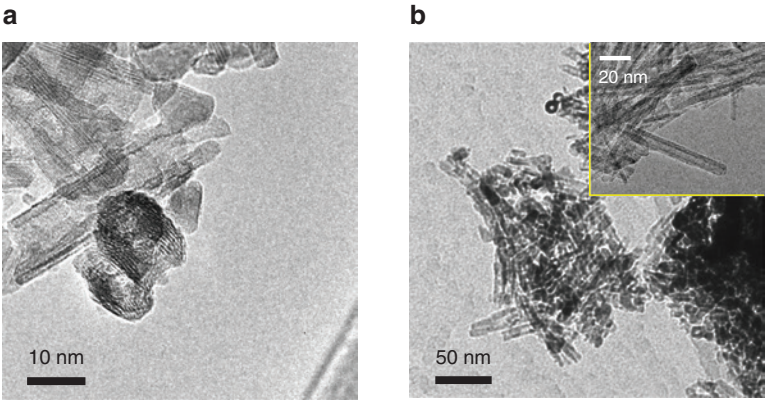

Fig. 5: (a) and (b) HR TEM images of anatase nanotubes prepared hydrothermally. The average length of the tubes is ca. 50 nm. The diameter ranges from 10 to 12 nm. After exchanging the Na^+ ions in the initially formed sodium titanate $Na_{2-x}H_xTi_nO_{2n-1} \cdot yH_2O$ with H^+ the final calcination step yields TiO_2 nanotubes.

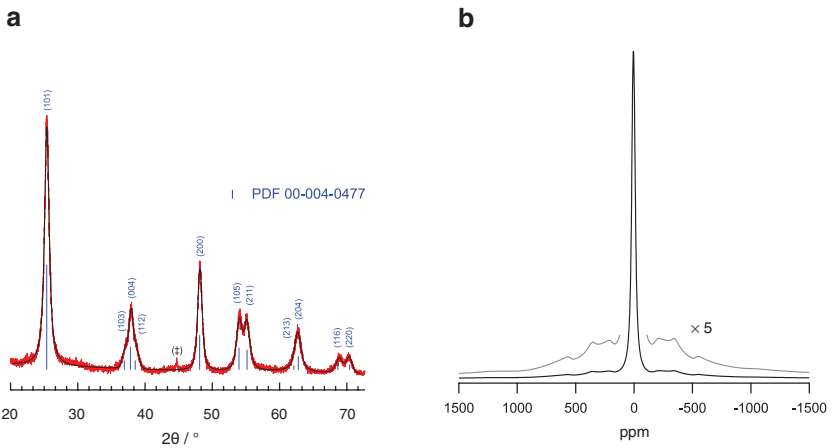

Fig. 6: (a) X-ray powder diffractogram of the nanotubes prepared via hydrothermal synthesis. The Miller indices reflect those of anatase; vertical bars reflect positions and intensities expected for anatase, see the PDF indicated. Strongly broadened reflections reveal a crystalline sample with nm-sized crystallites as could be verified via HR TEM. (b) ^{7}Li NMR spectrum recorded under static conditions (116 MHz). Besides the central transition, the distinct quadrupole powder pattern illustrates the crystallinity of the sample as is also evidenced by the HR TEM images taken.

synthesis conditions, e.g. the synthesis temperature, the molarity of the sodium hydroxide solution, the pH-value during the washing procedure or the temperature while calcination, either anatase or TiO_2-B nanotubes can be obtained. If used

Bereitgestellt von | Technische Universität Graz
Angemeldet
Heruntergeladen am | 06.11.18 13:39

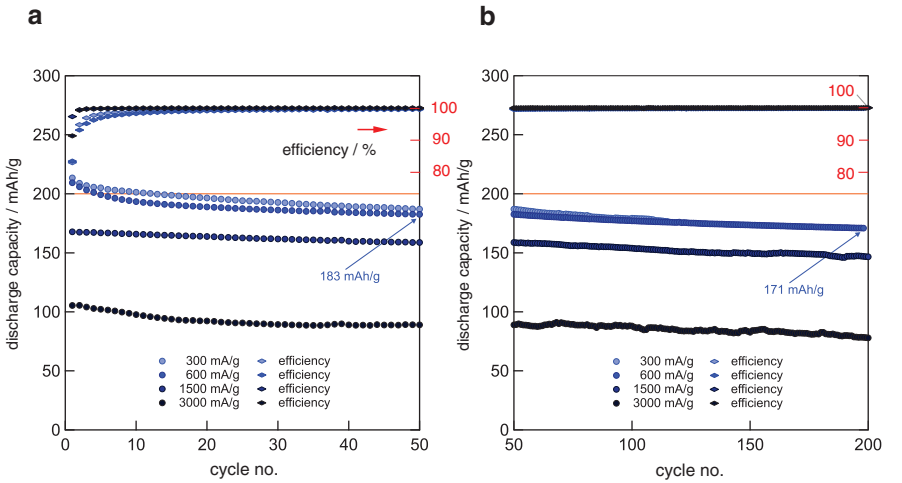

Fig. 7: (a) and (b) Discharge capacities of TiO_2 nanotubes crystallizing with the anatase structure. In (a) the first 50 cycles are shown. The currents indicated correspond to C-rates of 1.5 C (300 mA/g) and 15 C (3000 mA/g), respectively. At 1.5 C capacities in the order of 170 mAh/g are reachable even after 200 full cycles. Coulomb efficiencies are close to 100 %.

as negative electrode material in lithium half cells the anatase tubes show excellent cycling behaviour. At C-rates of 1.5 C a relatively stable discharge capacity of 170 mAh/g is reached (see Figure 7); only a small capacity fade is seen with increasing cycle number. Even after 200 full cycles the Coulomb efficiency is close to 100 %.

To shed light on Li ion dynamics of TiO_2 nanotubes, which were either treated with *n*-BuLi or lithiated electrochemically in Li half cells, we recorded ^{7}Li NMR line shapes and spin–lattice relaxation rates. As an example, in Figure 8 the rates $1/T_1$ and $1/T_{1\rho}$ of $Li_{0.6}TiO_2$ (TiO_2-B) are shown. Li was inserted electrochemically using Swagelok cells; the final electrode contained 15 wt% binder (Kynar Flex 2801) and conducting additives [carbon black 15 wt% (Super P)].

Whereas for $Li_{0.6}TiO_2$ the rate $1/T_1$ only weakly depends on temperature, for the anatase tubes with $x = 0.3$ and $x \approx 0.13$, which were chemically lithiated, $1/T_1$ reveals the shallow flank of a $1/T_1(1/T)$ rate peak that is characterized by ca. 0.15 eV. Most likely, for Li_xTiO_2 such a low activation energy has to be assigned to localized relaxation processes rather than to long-range ion transport. Li ions near the surface regions are expected to be involved in such processes. In all cases and irrespective of the final crystal structure of the titania nanotubes the corresponding spin-lock NMR transients, from which we extracted the rates $1/T_{1\rho}$, obey a rather complex behavior. At sufficiently high x values ($x > 0.1$) we clearly observed a two-step decay behavior.

Bereitgestellt von | Technische Universität Graz
Angemeldet
Heruntergeladen am | 06.11.18 13:39

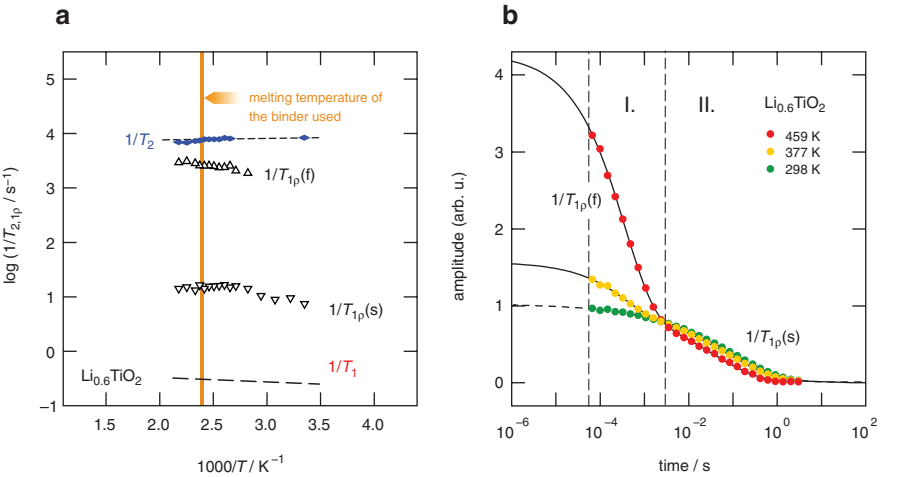

Fig. 8: (a) ^{7}Li NMR spin–spin ($1/T_2$) and spin–lattice relaxation rates ($1/T_{1(\rho)}$) of $Li_{0.6}TiO_2$ (TiO_2-B) nanotubes recorded at a Larmor frequency of 116 MHz. The corresponding spin-lock rates were acquired at a locking frequency of 20 kHz. The dashed line indicates the temperature dependence of the laboratory-frame rates $1/T_1$. Note that the binder used to prepare the electrodes for electrochemical lithiation melts at ca. 415 K, see the vertically drawn line. Above 330 K, for $1/T_{1\rho}$ two rates, marked with (s) and (f), were obtained that significantly differ from each other. The rate $1/T_{1\rho}$(s) could be largely influenced by spin-diffusion effects. The rate $1/T_{1\rho}$(f) might represent a subset of fast Li ions near the interfacial regions of the TiO_2-B nanotubes. (b) Transversal $T_{1\rho}$ magnetization transients (20 kHz) revealing the two sub-transients from which the rates $1/T_{1\rho}$(s) and $1/T_{1\rho}$(f) were extracted. Dashed and solid lines represent fits with a sum of two stretched exponentials. With increasing T the fast decaying contribution emerges (region I.); at 459 K the ratio of the amplitudes of the two signals is 3:1. Thus, the majority of the Li ions, possibly those near the surface regions, has access to a fast spin-lock decay. According to this preliminary explanation, the tail of the overall transients (region II.) should then represent those ions residing in the inner regions of the walls.

This behavior is exemplarily shown for the $Li_{0.6}TiO_2$-B in Figure 8b. Parameterizing the transients with a sum of two (stretched) exponentials results in the rates $1/T_{1\rho}$(s) and $1/T_{1\rho}$(f). The two-step behavior cannot be explained by the spin-properties of the ^{7}Li nucleus as their difference greatly exceeds that usually expected for, e.g. quadrupolar relaxation. While $1/T_{1\rho}$(f) is close to $1/T_2$, independently measured through spin-echo experiments, the rate $1/T_{1\rho}$(s) is in the order of seconds. A significant temperature dependence is obviously masked because of, e.g. Li^{+}–Ti^{3+} interactions, spin-diffusion, surface effects or the presence of a variety of (nm-sized) crystalline regions that differ, e.g. in Li content. The magnitude of $1/T_{1\rho}$(s) and its temperature independence resembles that expected for spin-diffusion that is, e.g. mediated through a spatially homogenous distribution

Bereitgestellt von | Technische Universität Graz
Angemeldet
Heruntergeladen am | 06.11.18 13:39

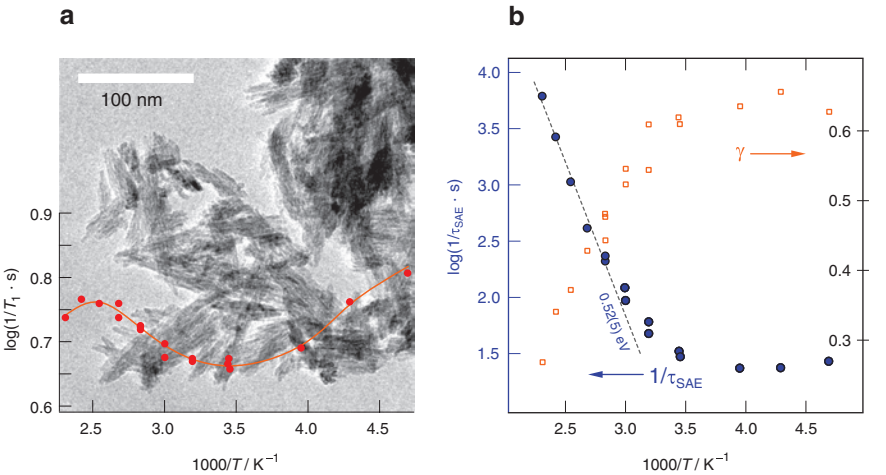

Fig. 9: (a) SEM image of TiO_2 (rutile) nanorods; the needlelike shape of the crystallites is clearly visible. X-ray diffraction confirmed the phase purity of the material. The data points at the bottom of the figure illustrate the temperature dependence of the T_1 relaxation rates measured at a Larmor frequency of 116 MHz. (b) ^{7}Li SAE NMR decay rates of $Li_{0.5}TiO_2$ (rutile); for comparison, the stretching exponents used to parameterize the underlying S_2 decay curves are also shown.

of paramagnetic centers such as Ti^{3+}. The NMR line shapes of all samples investigated point to very slow ion dynamics which is in line with the observations for amorphous titania nanotubes. Additional ^{7}Li SAE NMR measurements are currently running in our labs to shed light on the origins of the two Li sub-ensembles seen in spin-lock NMR.

2.1.3 Li diffusion in rutile nanorods and their electrochemical behaviour

Slow Li ion diffusion was also found for nanostructured rutile whose electrochemical performance in Li-ion cells is comparable to that of the TiO_2 nanotubes investigated. We studied both the cycling behaviour and the Li ion diffusivity of needlelike Li_xTiO_2 crystallizing with the rutile structure. The powder used for the experiments was a commercial one that is characterized by small needles, ca. 40 nm in length and 10 nm in diameter, see Figures 9a and 10a. Earlier ^{7}Li NMR spin–lattice relaxation and SAE measurements (see Figures 9 and 10) were performed on a sample with $x = 0.5$ that was chemically lithiated by treatment in *n*-BuLi dissolved in hexane [76]. SEM images and X-ray powder diffraction of the highly air-sensitive product confirmed that the rutile structure is fully retained

Bereitgestellt von | Technische Universität Graz
Angemeldet
Heruntergeladen am | 06.11.18 13:39

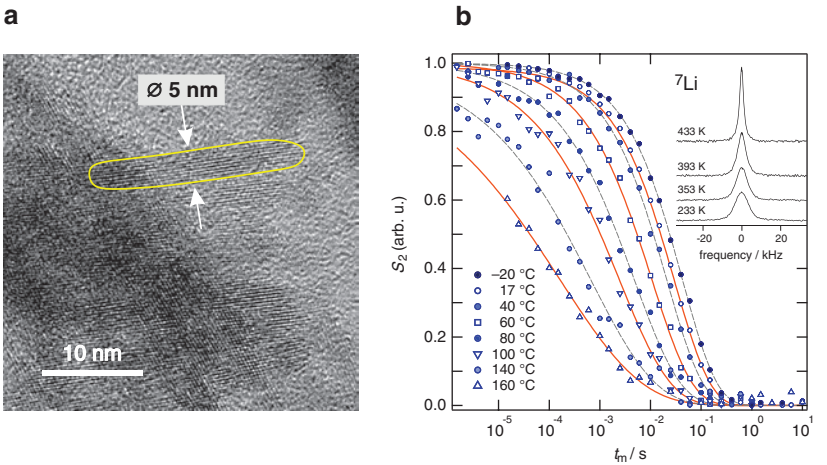

Fig. 10: (a) HR TEM image of the rutile nanorods investigated; a nanorod with a length of ca. 25 nm and a diameter of approximately 5 nm is highlighted. (b) ^{7}Li SAE NMR S_2 decay curves (78 MHz) recorded at a preparation time of 10 µs. The curves were approximated with stretched exponentials; the corresponding stretching factors are shown in Figure 9b; they range from 0.3 to 0.7 clearly representing a non-exponential motional correlation function. Inset: ^{7}Li NMR lines recorded at the temperatures indicated. The lines show a Gaussian shape at low T and transform into a Lorentzian line at elevated T.

during Li insertion. This contrasts with other modifications of TiO_2 for which lithiation is accompanied with a phase transformation. For rutile such transformations are reported for samples with $x > 0.5$.

As in the case of amorphous TiO_2 nanotubes we took advantage of ^{7}Li SAE NMR to characterize Li ion hopping in rutile $Li_{0.5}TiO_2$. Most interestingly, also for nanocrystalline, rutile $Li_{0.5}TiO_2$ the decay rates $1/\tau_{SAE}$ are governed by non-diffusive effects until ca. 310 K. At higher T they discharge into an Arrhenius line that is once again characterized by an activation energy in the order of 0.5 eV. Significant motional line narrowing is recognized at 300–350 K (see inset of Figure 10b), thus at slightly higher temperatures than it was the case for amorphous TiO_2 indicating faster ion dynamics in the structurally disordered samples. Note that for amorphous $Li_{0.5}TiO_2$ the activation energy derived from SAE NMR was only 0.3 eV. As also observed for the amorphous samples, the SAE NMR decay curves S_2 could only be parameterized with stretched exponentials $S_2 \propto \exp(-(t_m/\tau_{SAE})^{\gamma})$, see Figure 10b. The beginning of the diffusion-controlled SAE NMR flank is associated with the beginning of the decrease of the exponent γ ($0 < \gamma \leq 1$) that describes the deviation from single-exponential time behavior $\gamma = 1$. This behavior is generally observed in SAE NMR if materials with a (large) distribution of decay rates are considered.

Bereitgestellt von | Technische Universität Graz
Angemeldet
Heruntergeladen am | 06.11.18 13:39

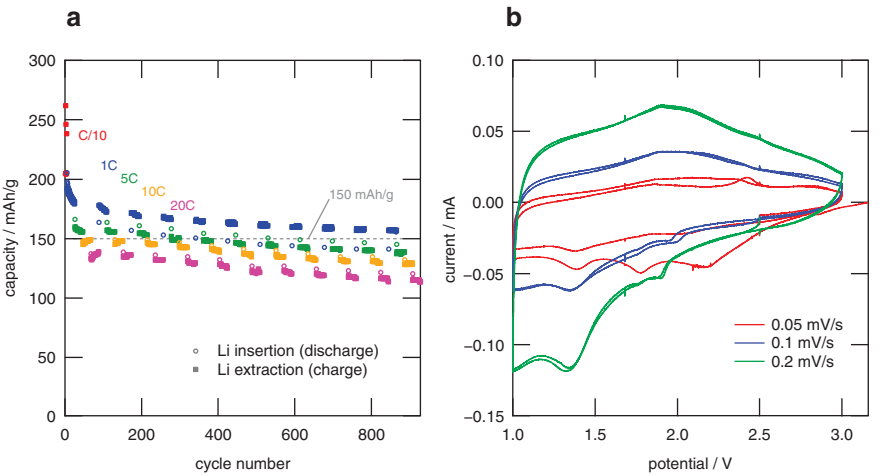

Fig. 11: (a) Discharge/charge capacities of the rutile nanorods if tested in Li half cells at various C-rates ranging from C/10 to 20C. At 1C the capacities are well above 150 mAh/g, thus comparable with those of the anatase nanotubes hydrothermally prepared. (b) Cyclic voltammograms of the Li ion cells equipped with the rutile nanorods.

Despite the moderate to poor ion dynamics in rutile $Li_{0.5}TiO_2$ the nm-sized needles perform exceptionally well in lithium-ion cells; therefore, one might speculate whether surface and interface effects do significantly participate in facile Li storage. To test their electrochemical ability to work as anode material in cells (with Li metal as both counter and reference electrode) we prepared electrodes consisting of nano-$Li_{0.5}TiO_2$, binder (Kynar Flex 2801) and carbon powder (Super C 65); the weight ratio was 75:17:8. The cyclic voltammograms reveal a distribution of various redox processes (Figure 11b), at a scanning rate of 0.05 mV/s three distinct peaks are visible that indicate distinct insertion/de-insertion processes presumably associated with structural changes of the active material if electrochemically lithiated. Galvanostatic cycling at current rates ranging from 0.1 C to 20 C proves a credible rate capability (Figure 11a). For instance, at 1 C the decrease in charge capacity turned out to be marginal; even after 800 cycles the cell delivers a stable discharge capacity of more than 150 mAh/g.

2.1.4 Mesoporous TiO_2 as long-lasting anode material

Mesoporous materials with an ordered 3D pore structure ensure superior storage capacities and facile Li insertion and removal. As mentioned above, these

Bereitgestellt von | Technische Universität Graz
Angemeldet
Heruntergeladen am | 06.11.18 13:39

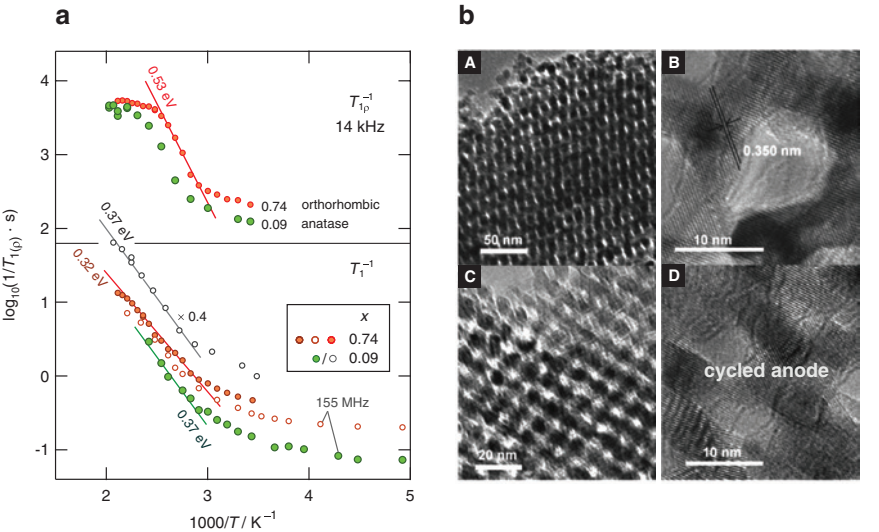

Fig. 12: (a) ^{7}Li NMR spin–lattice relaxation rates of mesoporous Li_xTiO_2 with $x = 0.09$ and $x = 0.74$, see Ref. [43]. The rates were recorded at 78 MHz and 155 MHz. For the sake of clarity, the data of $Li_{0.09}TiO_2$ (78 MHz) were vertically shifted by a factor of 4. In the upper graph of (a) the spin-lock rates are shown that were acquired at a locking frequency of 14 kHz. (b) High-resolution TEM images revealing the pore structure of the material before (A and B) and after cycling (C and D). No significant changes can be seen ensuring a high morphological stability of the mesoporous anode. TEM images taken from Ref. [39], copyright © 2000 by John Wiley Sons, Inc. Reprinted by permission of John Wiley & Sons, Inc.

properties are *inter alia* related to short diffusion lengths of the nm-sized materials [35] as well as, see the discussion above, to the involvement of Li surface storage. Because of the large volume fraction of the interfacial regions this storage mechanism needs to be considered. Recently, excellent cycling behavior of a lithium-ion battery was achieved when mesoporous TiO_2 with a 3D hierarchical pore structure was used as anode material [39]. Even after extensive charging and discharging of the battery, the hierarchical pore structure was preserved throughout clearly illustrating the high stability of the anode, see the HR TEM images in Figure 12b that were taken from Ref. [39].

Initially, the mesoporous TiO_2 crystallizes with tetragonal symmetry. Upon Li insertion the material transforms, however, into an orthorhombic form [39]. Besides kinetic effects also Li diffusion properties are anticipated to govern the insertion and removal rates. To answer the important question if and to which extent Li self-diffusion changes as a function of Li content x in mesoporous Li_xTiO_2, we used ^{7}Li NMR relaxometry and ^{7}Li SAE NMR to probe local activation energies and jump rates [43]. As mentioned above, while ^{7}Li SAE NMR is useful

Bereitgestellt von | Technische Universität Graz
Angemeldet
Heruntergeladen am | 06.11.18 13:39

to probe rather slow Li motions with correlation rates lower than 10^5 Hz, ^{7}Li NMR SLR measurements, in both the laboratory and rotating frame of reference are applicable to detect hopping processes with rates ranging from 10^5 Hz to 10^9 Hz [74, 75, 77]. Owing to the relatively long ^{7}Li NMR SLR rates of the samples in the rigid-lattice regime, we could detect the low-T flanks of the corresponding rate peaks. The key results are shown in Figures 3 and 4.

In Figure 12a ^{7}Li NMR spin–lattice relaxation rates for two compositions x, i.e. two crystal structures, are shown that were recorded at 155 MHz and 78 MHz as well at a locking frequency of 14 kHz. The Arrhenius plot reveals that above 300 K the rates start to be mainly governed by ionic diffusion processes. Below that temperature non-diffusive origins control the rates. As expected, the more Ti^{3+} centers have been generated through the insertion of Li^+/e^- the larger the paramagnetic Li^+–Ti^{3+} spin–spin interaction and the faster the longitudinal recovery in the low-T regime.

In the laboratory frame the diffusion-controlled rates follow Arrhenius behaviour that points to activation energies, E_a, of 0.37 eV ($x = 0.09$) and 0.32 eV ($x = 0.74$), respectively. Both the decrease in E_a and the slight increase in absolute values in the diffusion-induced regime indicate increased Li ion hopping processes in the sample with higher Li content. This view is supported by spin-lock NMR, see the upper part of Figure 12a. At first glance, one would expect a decrease in Li ion diffusivity if x is significantly increased from 0.09 to 0.74. Such a decrease could be the result of large Coulomb interactions at high x values with many interfering Li ions and a restricted number of vacant Li sites. The experimental results, however, point to the opposite direction: the dynamic parameters deduced from NMR turned out to be less influenced by the Li content than expected. If we consider surface effects and the fact that the crystal symmetry reversibly changes from tetragonal to orthorhombic when going from $x = 0.09$–0.74 some solid arguments can be found being able to explain the current NMR response. The orthorhombic structure seems to facilitate Li ion migration which, on the other hand, is highly beneficial for the performance of the anode material that needs to easily accept and conduct Li ions at increased values of x.

The fact that Li bulk diffusivity is seen to increase rather than to decrease with increasing x in mesoporous Li_xTiO_2 is also underpinned by ^{7}Li SAE NMR measurements, Figure 13, see Ref. [43]. Also from the point of view of SAE NMR correlation rates, the gradual transformation into orthorhombic Li_xTiO_2 upon Li insertion, i.e. during charging the anode in a battery with full cell configuration, seems to have a positive effect on Li ion diffusivity (see Figure 12a and b).

By parameterizing the SAE decay curves, exemplarily shown in Figure 13a for $x = 0.09$, we obtain temperature-dependent correlation rates $1/\tau_{SAE}$ that start to be influenced by slow Li exchange processes at temperatures above 250 K. By careful

Bereitgestellt von | Technische Universität Graz
Angemeldet
Heruntergeladen am | 06.11.18 13:39

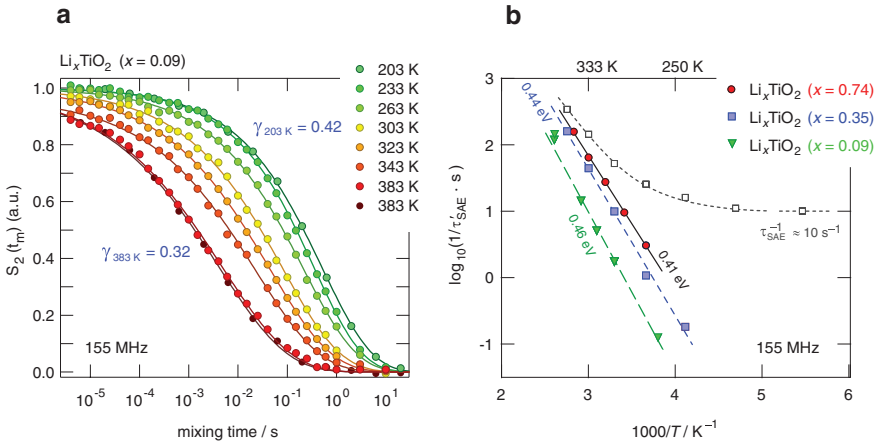

Fig. 13: (a) ^{7}Li NMR two-time (sin–sin) correlation functions recorded at 155 MHz with the Jeener–Broekaert three-pulse sequence to generate stimulated echoes. The amplitude of the echo generated after the reading pulse is plotted as a function of mixing time, t_m, while the preparation time t_p was kept constant (10 μs). The shape of the decay curves do only slightly depend on T; the solid lines show fits with stretched exponentials. For $x = 0.09$ the stretching exponents γ vary from 0.3 to 0.45 indicating correlated motion and/or a relatively wide distribution of motional correlation times. The corresponding decay rates are shown in (b). With increasing x a slight increase rather than a decrease in SAE NMR decay rate is found that corroborates the findings from spin-lock NMR. Figures adapted from Ref. [43].

subtraction of the almost temperature-independent and non-diffusive contributions to the SAE decay from the overall rates we ended up with purely diffusion-controlled rates $1/\tau'_{SAE}$ that follow Arrhenius-type behaviour. The straight lines in Figure 13b represent Arrhenius fits with activation energies of 0.48 eV ($x = 0.09$), 0.44 eV ($x = 0.35$), and 0.41 eV ($x = 0.74$). These values are comparable with those from NMR relaxometry. They are higher than those from SLR NMR in the lab frame since laboratory-frame relaxation is able to gather also short-ranged (local) ion dynamics to which SAE NMR is less sensitive.

On the other hand, SAE NMR, although being able to characterize long-range ion transport, is insensitive to ion jump processes between electrically identic sites that albeit contribute to NMR relaxometry, e.g. in the rotating frame of reference. This fact might explain the higher activation energy seen via spin-lock NMR which obviously also probes ion hopping processes with even larger barriers the ions have to surmount (0.53 eV for the sample with $x = 0.74$). It is, on the other hand, important to mention that the temperature ranges where the two techniques have been applied to measure ion dynamics do not coincide. Above 383 K the SAE decay curves start to be independent of temperature. Thus, at high

Bereitgestellt von | Technische Universität Graz
Angemeldet
Heruntergeladen am | 06.11.18 13:39

temperatures, i.e. in the regime of 'fast' ion dynamics, SAE NMR is unable to produce reliable jump rates and activation energies.

A similar feature can be seen for the spin-lock rates of the sample with $x = 0.74$. At high T, the rates follow an anomalous T behaviour that needs to be investigated in future studies. We suppose that it is related to the, to some extent irreversible, interaction of the active material with binders and carbon additives that are usually added to 'ionically' and electronically activate TiO_2 to prepare a functioning battery anode. Nevertheless, in the T range of battery operation we have seen that at increased values of x the orthorhombic form of mesoporous TiO_2 with its hierarchical pore structure represents a powerful anode material with slightly enhanced Li ion dynamics compared to the initially Li poor TiO_2 with tetragonal symmetry.

2.1.5 Na insertion into amorphous TiO_2 nanotubes: mechanistic details – differences between Li and Na

While the electrochemical reactions of nanostructured TiO_2 with H^+ and Li^+ have been known for a while, the particularities of the electrochemical reaction of Na^+ with anodic titania nanotubes are a more recent achievement. A cyclic voltammetry experiment investigating the Na^+ insertion into amorphous TiO_2 nanotubes (see Figure 14a) does not indicate a definite two-phase insertion mechanism as known for insertion of Li^+ in crystalline forms of titania [42]. A 2-phase mechanism would result in well-defined current peaks in the cyclic voltammogram. The very broad current response, however, hints to a one-phase mechanism that might instead be involved. Another feature is the relatively symmetrical response of the nanotubes with respect to Na^+ electrochemical reaction when the sweep rate is increased, e.g. at 10 mV/s, contrasting with the asymmetric shape of the cyclic voltammogram recorded at relatively slow seep rates of, e.g. 0.5 mV/s.

In Figure 14b the current read at 1 V vs. Na^+/Na has been plotted against the square root of the sweep rate for three different types of amorphous anodic titania nanotubes, see Ref. [42]. Obviously, the nanotubes possess different outer diameters and lengths as follows: after anodization at 30 V for 2 h the nanotubes length was approximately 4.5 μm and 70 nm in diameter, at 40 V after 2 h 8 μm and 100 nm while at 50 V after 1 h the tubes were 9.1 μm long and 120 nm in diameter. For an electrochemical process limited by a mass transport phenomenon a Randles–Ševčík-type plot, as presented in Figure 14b, should be linear. However, even after any ohmic drops were eliminated, there is a clear deviation from this expected linearity. The deviation is always positive, i.e. the current is higher than expected. Moreover, the deviation magnitude increases with sweep rate. This

Bereitgestellt von | Technische Universität Graz
Angemeldet
Heruntergeladen am | 06.11.18 13:39

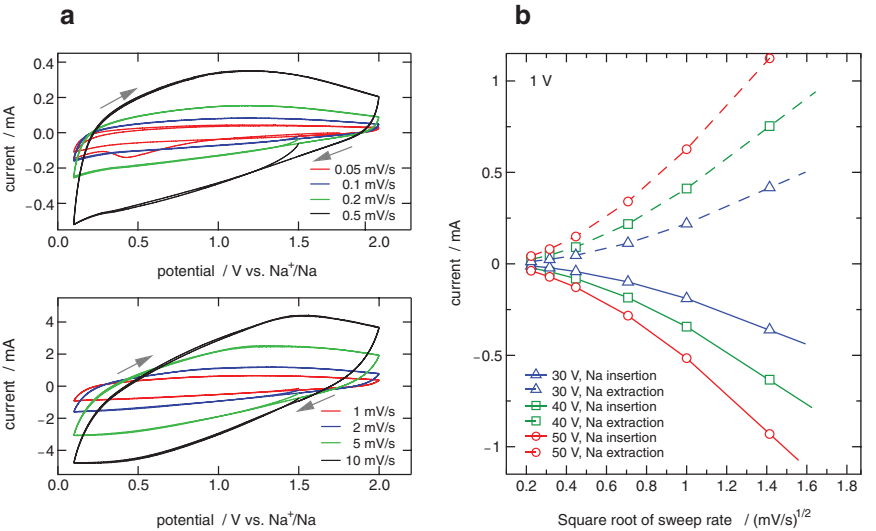

Fig. 14: (a) Cyclic voltammetry response at various sweep rates of an amorphous TiO_2 nanotubes layer fabricated by anodization at 50 V for 2 h. The electrolyte was solution of 1 M $NaClO_4$ in propylene carbonate (PC). The electrochemical response of the sample is consistent with a sodium storage mechanism involving a single phase mechanism. (b) The current values read from a) at a potential of 1 V vs. Na^+/Na plotted with respect to square root of the sweep rate of the anodic and cathodic scans. There are significant and systematic deviations from the linear behaviour that would be expected for electrochemical processes that are limited by mass transport (diffusion) phenomena. Figures adapted from Ref. [42].

observation proves that there is a process, contributing to Na^+ storage, which is faster than solid-state diffusion in the walls of TiO_2 nanotubes. This contributing process is commonly called pseudo-capacitive storage. Although a charge transfer takes place and a Ti^{4+} redox center is reduced to Ti^{3+} during electrochemical reaction with sodium, the corresponding Na^+ ion does not diffuse into the bulk of the amorphous titania material. Instead, it adsorbs onto the titania/electrolyte interface region forming a somehow loose bound with the substrate while still compensating the negative charge of the mobile electron that has been injected into TiO_2 conduction band. This interfacial storage mechanism is obviously not limited by ion diffusion in the solid-state since the Na^+ ions reside on the surface of the material. The only mass transport limitation by diffusion occurs in the liquid state, i.e. chemical diffusion of the sodium species through the liquid electrolyte. Chemical diffusion in the liquid state can, however, safely be considered at least 4–6 orders of magnitude faster than the solid-state diffusion process and, thus, this process is significantly faster than its solid-state counterpart, as is clearly proven by the non-linear relationship observed in Figure 14b.

Bereitgestellt von | Technische Universität Graz
Angemeldet
Heruntergeladen am | 06.11.18 13:39

It is possible to separate the pseudo-capacitive and chemical diffusion process in the solid state by considering that diffusion should present a linear response on a Randles–Ševčík-type plot and that the pseudo-capacitive contribution adds to the diffusion process while being non-linear with respect to the sweep rate. By a relatively simple subtraction technique, detailed elsewhere [42], we found very high values of the pseudo-capacitance as shown in Figure 15a. The pseudo-capacitance is increasing as the potential of the electrode is driven towards more negative values, eventually reaching very high values around 1000 μF/cm^2. Worth mentioning, this value is roughly two orders of magnitude higher than the usual double layer capacitance occurring in the absence of a faradaic process. This opens the path towards the use of anodic titania nanotubes in supercapacitors. While the pseudo-capacitive contribution of the anodic titania is very high, the Na^+ diffusion into the walls of the nanotubes is very slow irrespective of the electrode potential at which it was measured as seen in Figure 15b. The chemical diffusion coefficient values are centered around 10^{-21} cm^2/s which is 4–5 orders of magnitude lower than the corresponding Li^+ diffusion coefficients in anatase TiO_2 [78]. Therefore, there is

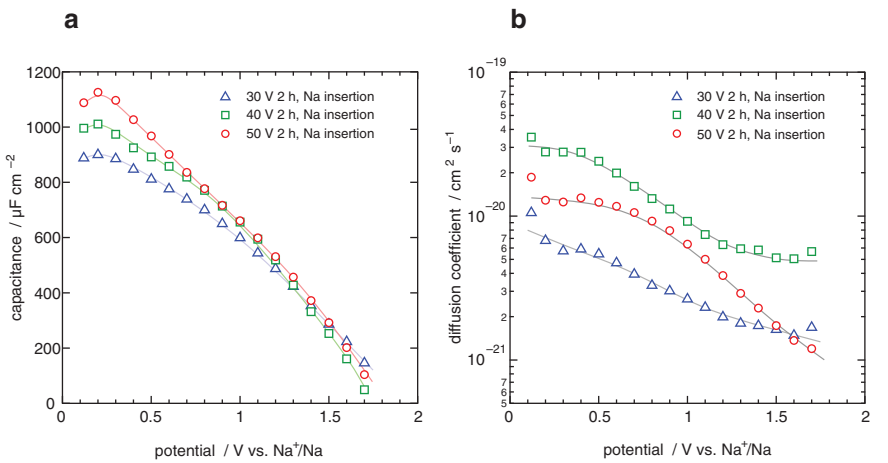

Fig. 15: (a) The pseudo-capacitive Na^+ interfacial storage for TiO_2 nanotubes with respect to the electrode potential. The values of the capacitance are expressed with respect to the surface area of the nanotubes that is much higher than the surface occupied by the nanotubes layer on the Ti substrate. For these samples this surface ratio lies between 450 and 700:1. (b) Chemical diffusion coefficient corresponding to sodium insertion in the walls of the TiO_2 nanotubes; values were determined after subtraction of the pseudo-capacitive contribution. Regardless of the potential of the electrode, diffusion of sodium into TiO_2 turned out to be rather slow process at room temperature. Figures adapted from Ref. [42].

Bereitgestellt von | Technische Universität Graz
Angemeldet
Heruntergeladen am | 06.11.18 13:39

only a small amount of sodium diffusing into the walls of the titania nanotubes, most of the sodium storage capacity originates from the pseudo-capacitive processes. This feature is essentially different from Li^+ insertion in TiO_2, most of the Li^+ is actually stored in the bulk regions of TiO_2 below a certain electrode potential, typically lower than 1.5–1.7 V vs. Li^+/Li.

2.2 Li ion diffusion in layer-structured (nanocrystalline) Li_xSnS_2 with confined Li diffusion pathways

Macroscopic Li diffusion in nanostructured ceramics, such as TiO_2, can be directed if the crystallites assume the shapes of tubes or rods. From the atomic scale point of view the elementary hopping processes have to be characterized in many cases by 3D diffusion unless diffusion of the ions is preferred along a special direction of the crystal structure. Apart from such anisotropic movements in materials offering 3D diffusion there are layer-structured and channel-structured ion conductors with significantly constraint migration pathways [30, 65, 79–84]. Lithium transition metal dichalcogenides represent a typical class of materials that offer 2D diffusion in their van-der-Waals gaps [83]. Of course, besides intralayer diffusion, to a minor extent also interlayer hopping processes across the layers can take place. Considering sulfides, besides, e.g. Li_xTiS_2 [62, 83] and Li_xNbS_2 [81, 85], the Sn-analogue, Li_xSnS_2, constitutes another interesting model system not only to study the influence of dimensionality [49] but also the effect of structural disorder on a spatially confined diffusion process.

In Figure 16a ^7Li NMR spin–lattice relaxation rates of three different Li_xSnS_2 ($x = 0.17$) samples, differing in morphology and mean crystallite size, are shown in an Arrhenius plot. With $x = 0.17$ we ensured that mainly intralayer Li sites, i.e. those between the SnS_2 sheets, have been occupied by the Li ions. The mobile Li ions were chemically introduced into SnS_2 via treatment with *n*-BuLi in hexane. Microcrystalline Li_xSnS_2 served as reference material to reveal the changes in diffusion-induced NMR spin-lock relaxation rates [49]. NMR spin–lattice relaxation in $Li_{0.17}SnS_2$ with µm-sized crystallites turned out to be rather complex. We interpreted the appearance of two diffusion-induced rate peaks as a consequence of a heterogeneous distribution of Li ions in Li_xSnS_2 that can be influenced by annealing [49]. Soft thermal treatment is anticipated to homogenize the sample toward a uniform distribution of intercalants [81]. After thermal annealing the low-*T* peak 1 (see Figure 16b) has significantly been decreased in intensity. We assume that this relaxation peak represents clustered Li ions near the surface-influenced regions having access to fast short-range motions.

Bereitgestellt von | Technische Universität Graz
Angemeldet
Heruntergeladen am | 06.11.18 13:39

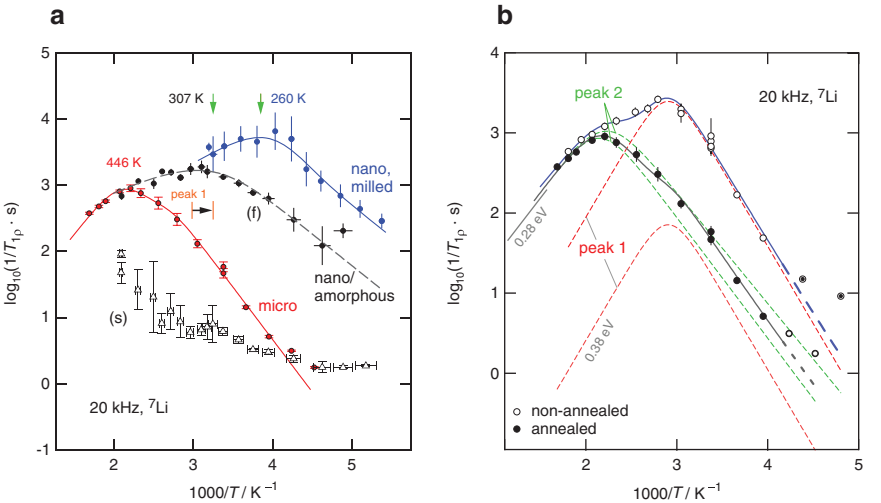

Fig. 16: (a) ^{7}Li NMR spin–lattice relaxation rates of different $Li_{0.17}SnS_2$ samples: a microcrystalline one (see red data points), a nanocrystalline one with a large fraction of amorphous material, and a sample that was prepared mechanochemically from Li_2S and SnS_2 in a planetary mill. The rates were recorded at a locking frequency of 20 kHz. (b) The diffusion-induced NMR locking rates of microcrystalline $Li_{0.17}SnS_2$ before (unfilled symbols) and after annealing the sample (filled symbols). In both cases the data can be best represented by two diffusion-induced rate peaks pointing to two dynamically distinct motional processes. Figure (b) adapted from Ref. [49].

If a nanocrystalline sample is studied that contains large volume fractions of amorphous Li_xSnS_2 the NMR response clearly differs from that found for microcrystalline Li_xSnS_2. At first the corresponding NMR line shapes of the nanocrystalline sample are composed of two contributions with quite different line widths (Figure 17). Thus, we have indeed to deal with a sample consisting of two spin reservoirs largely differing in ion dynamics, see also Ref. [33]. The sharp line resembles that of microcrystalline $Li_{0.17}SnS_2$; most likely, the ions representing this line reflect those in the nanocrystalline grains. The broader line can then be assigned to those in the amorphous regions. The two spin ensembles are also visible in ^{7}Li NMR spin-lock NMR transients which can only be parameterized with a sum of two single transients. The resulting rates are denoted as (fast, f) and (slow, s) in Figure 16a. Worth mentioning, the resulting broad NMR rate peak of the fast diffusing species resembles that obtained for microcrystalline Li_xSnS_2 before annealing. The low-T activation energy is, however, much lower and the

Bereitgestellt von | Technische Universität Graz
Angemeldet
Heruntergeladen am | 06.11.18 13:39

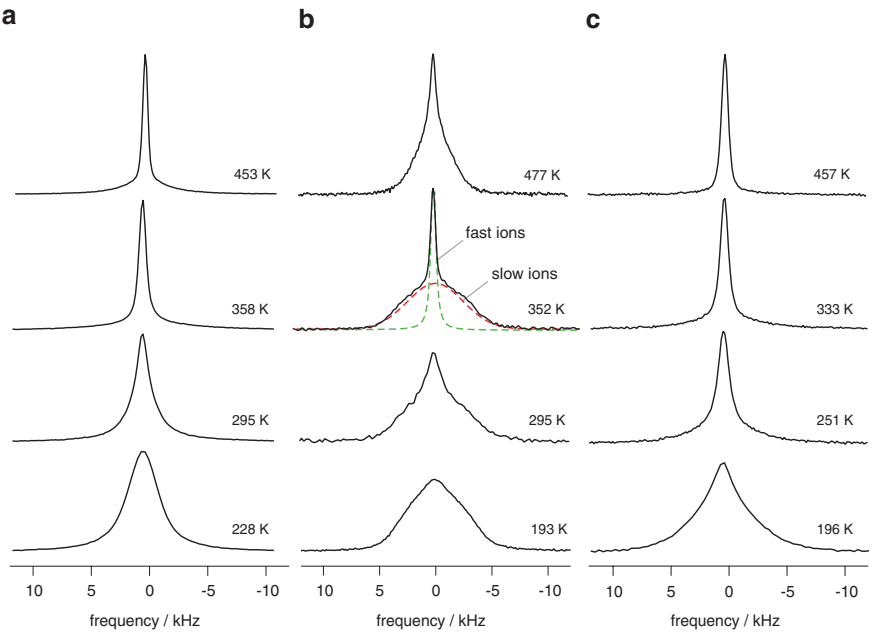

Fig. 17: ^{7}Li NMR line shapes (116 MHz) of (a) microcrystalline, i.e. coarse-grained $Li_{0.17}SnS_2$. (b) NMR spectra of a nanostructured sample with a mean crystallite size in the order of 10–20 nm. This sample contains a large volume fraction of amorphous material which is, in our opinion, represented by the broad, Gaussian-type NMR line (see the dashed lines that were used to deconvolute the overall signal recorded at 352 K). (c) Line shapes of a nanocrystalline sample that was synthesized via a mechanochemical route. Among the three samples it represents the fastest one in regard to Li ion self-diffusivity. This is also confirmed by ^{7}Li spin-lock SLR NMR relaxometry, see Figure 13a.

rate peak is shifted toward lower T as is illustrated by the horizontally drawn arrow in Figure 16a. This observation points to enhanced ion dynamics in the nanostructured form of Li_xSnS_2.

An additional increase in Li ion diffusivity is seen if we consider a sample that has been prepared via mechanochemical reaction of Li_2S and SnS_2 in a planetary mill, see the corresponding ^{7}Li NMR rates in Figure 16a. The shape of the Li NMR spectra do not reveal a pronounced structurally heterogeneous sample as discussed for the nanocrystalline sample before. We suppose that either defects introduced during the synthesize procedure are responsible for fast ionic diffusivity in the bulk or the surface-influenced regions. Heavy formation of amorphous regions, however, seems to slow down Li diffusivity at least in the case of layer-structured materials. Such materials already possess fast diffusion pathways being able to guide the ions also over long distances.

Bereitgestellt von | Technische Universität Graz
Angemeldet
Heruntergeladen am | 06.11.18 13:39

2.3 Enhancing ionic conductivity in poorly conducting ternary oxides and carbonates through structural disorder: $LiAlO_2$, Li_2TiO_3, $LiTaO_3$, $Li_4Ti_5O_{12}$, and Li_2CO_3

Lithium aliuminate is, at least in its γ-modification, known as a very poor ionic conductor if at hand in a coarse-grained or single-crystalline form. The Li ions occupy tetrahedral voids that are connected by corner-sharing. Recently, Wiedemann et al. compared experimental results on Li ion translational dynamics in oriented $LiAlO_2$ single crystals [orientations (100) and (001)] from (i) conductivity spectroscopy, (ii) mass tracer experiments as well as (iii) ^{7}Li NMR measurements. Ion transport turned out to be fully ionic [86]. For short-range Li ion dynamics ^{7}Li NMR relaxation resulted in an activation energy of ca. 0.7 eV, see Ref. [86] for an overview and Ref. [87] for recent measurements on a powder sample. The value of 0.7 eV agrees with that derived from neutron diffraction data that indicated a curved pathway connecting two adjacent Li sites in $LiAlO_2$ [88].

Long-range Li ion transport, on the other hand, has to be described with a higher activation energy [86, 89]. Both secondary ion mass spectrometry (SIMS) and conductivity spectroscopy revealed essentially the same activation energies of ca. 1.20(5) eV and 1.12(1) eV, respectively [86]. From 650 K to 750 K, which was the T range covered by the SIMS experiments, the diffusion coefficient D_{SIMS} equals D_σ meaning that the corresponding Haven ratio is given by $H_\mathrm{R} = 1$ [86]. Note that in Ref. [86] the solid-state diffusion coefficient D_σ was estimated via the Nernst–Einstein equation by assuming that the number density of charge carriers is simply given by the lithium concentration of the oxide. Mechanical loss spectroscopy confirmed these diffusion coefficients and activation energies [89]. Dynamic mechanical analysis, which is sensitive to ultraslow Li ion displacements, points to a Debye-like motional correlation that controls ion dynamics at low temperatures. Recently, activation energies of ca. 1.1 eV have also been found via sin–sin correlation functions probed with the help of ^{7}Li stimulated echo NMR being sensitive to long-range transport, see Ref. [90].

Regarding microcrystalline powder samples a very similar activation energy of ca. 1.14 eV [47] is obtained from conductivity measurements for temperatures below 600 K (see Figure 18a), see also Ref. [86] for an overview. The low conductivities and diffusivities are highly welcome if $LiAlO_2$ is used as, e.g. blanket material in fusion reactors. In such systems diffusion should be strictly prevented. The application of the oxide in electrochemical storage systems, however, requires much better ion diffusivities. For instance, $LiAlO_2$ is considered to act as thin-film electrolyte in all-solid-state batteries prepared with the use of sputtering or other deposition techniques. Furthermore, it has been reported that the oxide can be used as coating for Li_x(Ni, Co, Mn)O_2-based cathodes [91]; Goodenough and

Bereitgestellt von | Technische Universität Graz
Angemeldet
Heruntergeladen am | 06.11.18 13:39

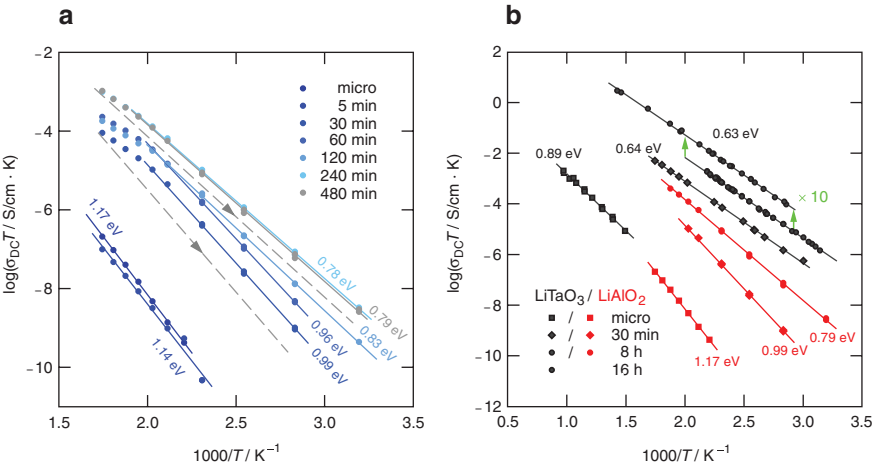

Fig. 18: (a) Ionic conductivities of micro- and nanocrystalline $LiAlO_2$. The latter was obtained by high-energy ball milling the starting material for the milling times indicated. For example, at 450 K the jump in conductivity is five orders of magnitude when going from the microcrystalline material to $LiAlO_2$ that was treated for 480 min in a planetary mill (Fritsch Pulverisette P7). (b) Comparison of the results obtained for nanocrystalline $LiAlO_2$ with those of high-energy ball milled $LiTaO_3$ that was prepared in a shaker mill. Note the data for the 8 h and the 16 h ball milled sample coincide. For better clarity, those of the 16-h-sample were shifted by a factor of 10 upwards. Figures adapted from Ref. [47].

co-workers [92] as well as Cheng et al. [93] have recently shown that during the preparation of the highly-conducting electrolyte $Li_7La_3Zr_2O_{12}$ (LLZO), doped with Al, the LLZO crystallites are often covered by an amorphous layer of $LiAlO_2$. Such a grain-boundary phase can have a negative impact on long-range ion transport in such oxide electrolytes.

Thus, also from an application point of view it seems to be important to study Li ion diffusion parameters in structurally disordered $LiAlO_2$. As is shown in Figure 18a high-energy ball milling significantly influences the DC conductivity of $LiAlO_2$ which can be read off from the frequency independent plateaus of the underlying conductivity isotherms. While overall conductivity has increased by several orders of magnitude, the activation energy decreases from 1.14 eV down to 0.78 eV (Figure 18a), [47]. The same effect is known for nanocrystalline $LiTaO_3$ (see Figure 18b), which has been studied in detail via conductivity spectroscopy and ^{7}Li NMR relaxometry in an earlier work [5].

In order to study the origins that cause the increase in conductivity, XRD, HR TEM and ^{27}Al magic angle spinning (MAS) NMR were employed [47], see also Figures 19 and 20a. In the case of $LiAlO_2$ powder XRD proves nanostructuring of

Bereitgestellt von | Technische Universität Graz
Angemeldet
Heruntergeladen am | 06.11.18 13:39

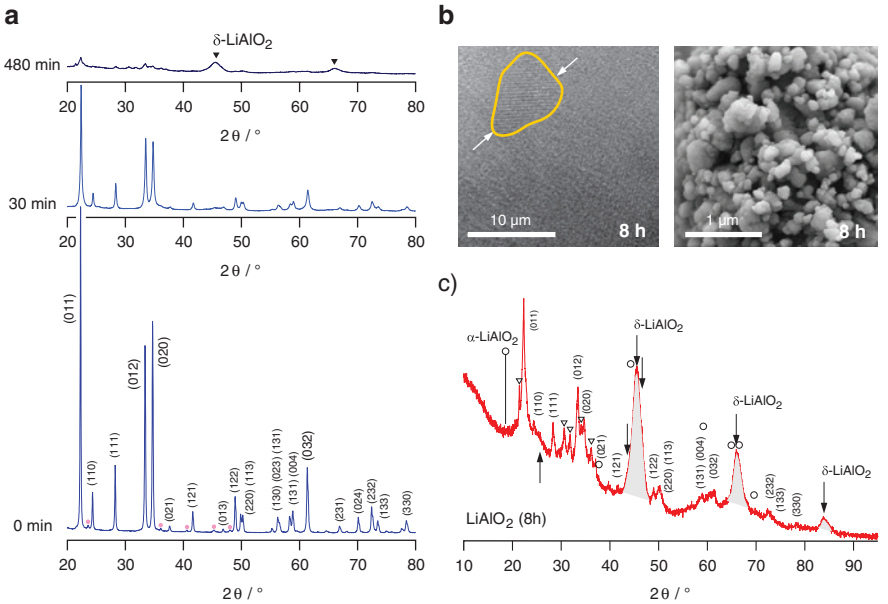

Fig. 19: (a) XRD powder patterns of micro- and nanocrystalline $LiAlO_2$. After 30 min of milling broadening of the reflections is seen but no other phases than the g-form show up. This changes when the milling time is raised to 8 h; the broad intensities at 45° and 67° point to δ-$LiAlO_2$ generated. Simultaneously, significant amounts of amorphous material are formed. (b) HR-TEM image and scanning electron microscopy picture of $LiAlO_2$ (milled for 8 h). (c) Magnification of the XRD pattern shown in (a). As is indicated by XRD, the formation of α-$LiAlO_2$ seems to be negligible. Figures adapted from Ref. [47].

the samples. While after 30 min a nanocrystalline ceramic of γ-$LiAlO_2$ has been obtained, further milling leads to the formation of large amounts of amorphous material and structurally disordered δ-$LiAlO_2$. The δ-form is a high-pressure modification of $LiAlO_2$. This observation was confirmed by ^{27}Al MAS NMR [47]. The more δ-$LiAlO_2$ is formed, the more intense the respective NMR signal at 15 ppm [referenced against $Al(NO_3)$ aqueous solution], which represents those Li ions residing on octahedral sites in the δ-modification. After 8 h of milling, $LiAlO_2$ nanocrystallites are obtained that are embedded in an amorphous matrix of the aluminate (see the HR TEM image shown in Figure 19b). The higher diffusivity in $LiAlO_2$ was also seen in ^7Li NMR line shape measurements [47], see Figure 20b.

Compared to $LiAlO_2$ the enhancement effect observed for $LiTaO_3$ is somewhat stronger. As one might expect because of the similar structure parameters, the behaviour of $LiTaO_3$ resembles that of nanocrystalline $LiNbO_3$. For Li_2TiO_3, on the other hand, the total increase in conductivity is less pronounced. The

Bereitgestellt von | Technische Universität Graz
Angemeldet
Heruntergeladen am | 06.11.18 13:39

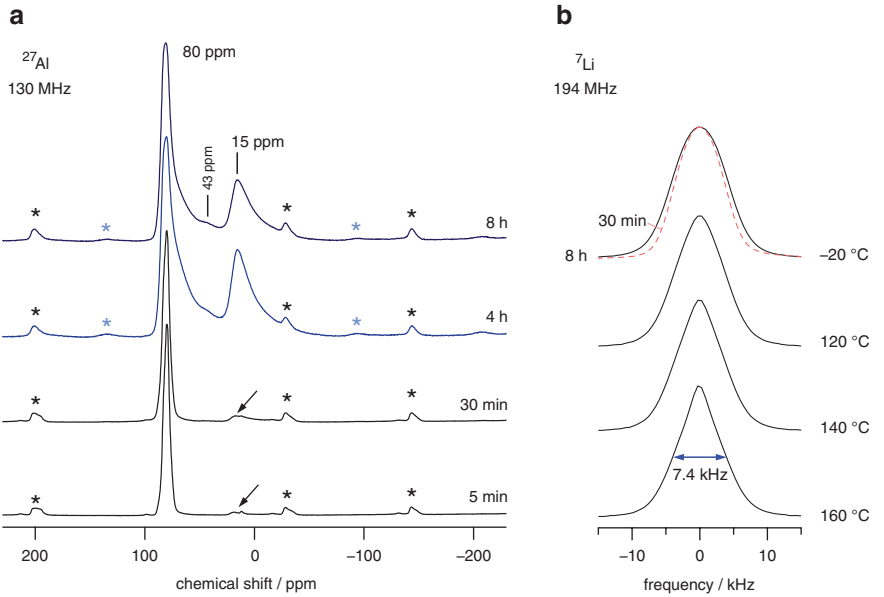

Fig. 20: (a) ^{27}Al MAS spectra of $LiAlO_2$ treated for the milling times indicated; chemical shifts refer to $Al(NO_3)$ 1 M aqueous solution. (b) ^{7}Li NMR line shapes at various temperatures for the sample milled for 8 h (and 30 min, for comparison). Above 140 °C the line shows noticeable narrowing due to Li jump processes with rates of the order of the rigid-lattice line width (see the line recorded at –20 °C). Spectra taken and adapted from Ref. [47].

latter is simply because the conductivity of microcrystalline Li_2TiO_3 is already higher than that of $LiTaO_3$ and $LiAlO_2$. The dashed lines in Figure 21a indicate the conductivities of $LiAlO_2$ and $LiTaO_3$ which were each milled for 8 h in the same planetary mill under the same conditions regarding the vial set and ball-to-powder ratio.

Quite recently, we studied the change in local structure of Li_2TiO_3 and $LiTaO_3$ through (extended) X-ray absorption fine structure (EXAFS) measurements similar to earlier work on $LiNbO_3$ [4]. As an example, in Figure 21b EXAFS data and Fourier transforms are presented for un-milled and mechanically treated Li_2TiO_3. The XAS scans were collected for the appropriate edge (Ti K-edge and Ta L3-edge) at room temperature on beam line B18 at the Diamond Light Source (Oxfordshire). For Li_2TiO_3, ball-milling attenuates the EXAFS and we observed a decrease in the height of the Ti–Ti peak in the Fourier transform. Similar results were also obtained for ball-milled $LiTaO_3$ [5] that was treated in a planetary mill (Figure 22). In Figure 23a and b the conductivities of several samples as well as the corresponding isotherms of a sample milled for 30 min are shown.

Bereitgestellt von | Technische Universität Graz
Angemeldet
Heruntergeladen am | 06.11.18 13:39

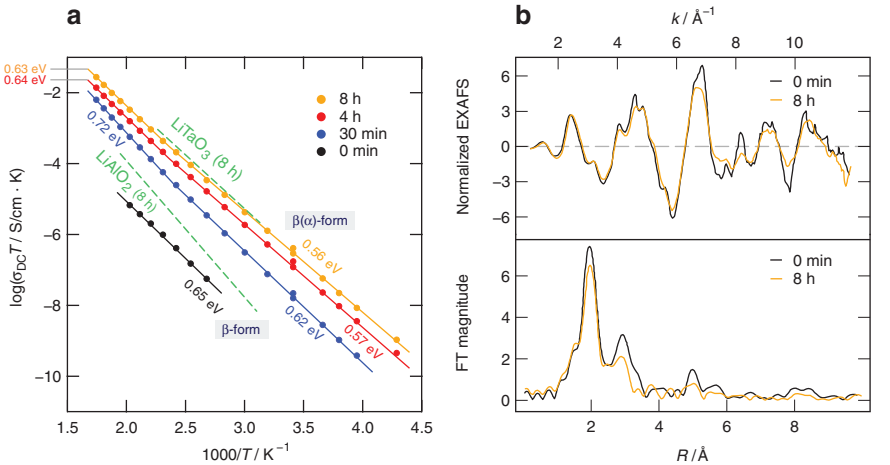

Fig. 21: (a) Arrhenius plot showing the temperature dependence of $\sigma_{DC}T$ of micro- and nanocrystalline β-Li_2TiO_3. Note that, according to X-ray diffraction, after 8 h of milling a mixture of amorphous Li_2TiO_3, the β-form and the α-modification has been formed. The dashed lines indicate conductivities of $LiTaO_3$ and $LiAlO_2$ each milled for 8 h, for comparison. (b) Normalized EXAFS data of the source material and the sample milled for 8 h in a planetary mill; (b) Fourier transforms (FT) of the k^3 weighted normalized EXAFS data shown at the top. The data were analyzed to yield details on the local structure, i.e. bond lengths, *R*, Debye–Waller factors, σ_{DW}. Figures taken from Refs. [27, 48] .

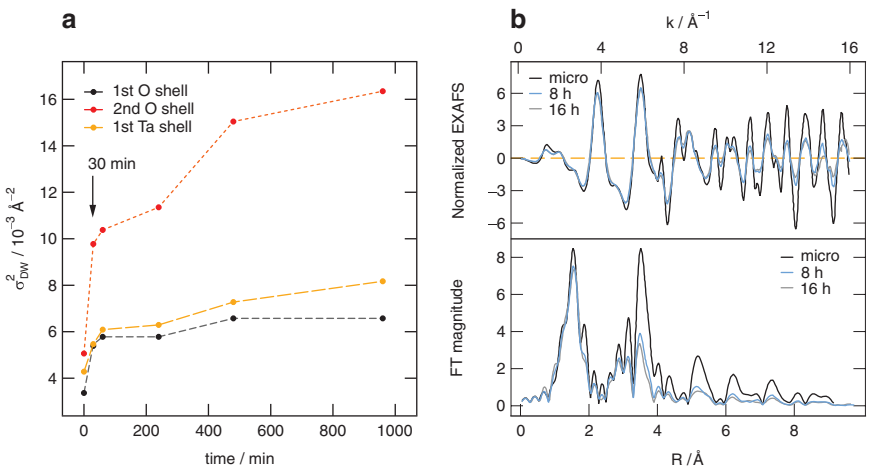

Fig. 22: (a) Change of the Ta L_3-edge EXAFS Debye–Waller factors, plotted as σ^2_{DW}, of nanocrystalline $LiTaO_3$. (b) The Ta L_3-edge EXAFS of $LiTaO_3$, the upper graph shows normalized spectra, the lower one the corresponding Fourier transforms. See Ref. [48] for further details.

Bereitgestellt von | Technische Universität Graz
Angemeldet
Heruntergeladen am | 06.11.18 13:39

For $LiTaO_3$ the decrease in EXAFS is best seen for the Ta–O and Ta–Ta correlations at ca. 2.0 Å and 3.8 Å, respectively (Figure 22b). The effect was analyzed in two ways *viz*. as a change in the Debye–Waller factor σ_{DW} due to (microscopic) disorder and as the effect of amorphous regions introduced during milling. Considering the Debye–Waller factors, shown in the form of σ^2_{DW} vs. milling time, for all the correlations σ^2_{DW} almost doubles after the oxide has been treated for only 30 min (Figure 22a). It can be explained that already after short periods of milling the local structure around the Ta ions is somewhat distorted. With increasing milling the Ta–O Debye–Waller factors show only a gradual change whereas the Ta–Ta correlation, which is significantly larger, continues to increase steeply with increasing mechanical treatment. We assume that at the beginning of the milling process the local Ta–O octahedra are affected while the relative arrangement of the octahedra continues to change with further treatment. Such observation would be expected given that the strong Coulomb interaction between Ta^{5+} and O^{2-} will maintain a relatively rigid local structure.

In an earlier study we used a shaker mill (SPEX 8000) equipped with a single ZrO_2 ball (10 mm in diameter) and a zirconia vial to produce nanocrystalline $LiTaO_3$. After 30 min of milling most of the local electric field gradients in the direct neighborhood of the Li nuclei are still comparable to those in un-milled, coarse-grained $LiTaO_3$. Many hours of milling were needed to destroy the originally well-structured powder pattern. Interestingly, the largest increase in ion conductivity is seen when the sample is milled for 30 min. Obviously, considering ion dynamics in $LiTaO_3$, (local) distortions, point defects, displacements and strain introduced during the first 30 min of milling is sufficient to have a remarkable effect on both short-range as well as long-range ion transport. Interestingly, the previous conductivity studies [5] revealed some subtle dependence of the microstructure on the time of ball-milling. The longer the milling time the more difficult it is to recover crystallinity by thermal annealing. Hence, the additional conductivity enhancement seen for longer milling times is presumably due to the increasing formation of amorphous fractions.

In the case of planetary mills the situation is similar but also entails some differences. For planetary mills, enabling heavy grinding, indeed the generation of amorphous materials is more likely. Although for both types of mills amorphous material is expected to be formed at longer milling times, planetary mills might already produce significant amounts of amorphous material at short milling times. In Figure 23a and b the conductivity results of such samples are shown; they were prepared in planetary mills equipped with up to 140 small milling balls with a diameter of 5 mm only. As can be clearly seen from the Arrhenius plots the ionic conductivity reached an upper limit already after 30 min. Considering the corresponding complex plane plots and capacities of the data, the DC plateaus

Bereitgestellt von | Technische Universität Graz
Angemeldet
Heruntergeladen am | 06.11.18 13:39

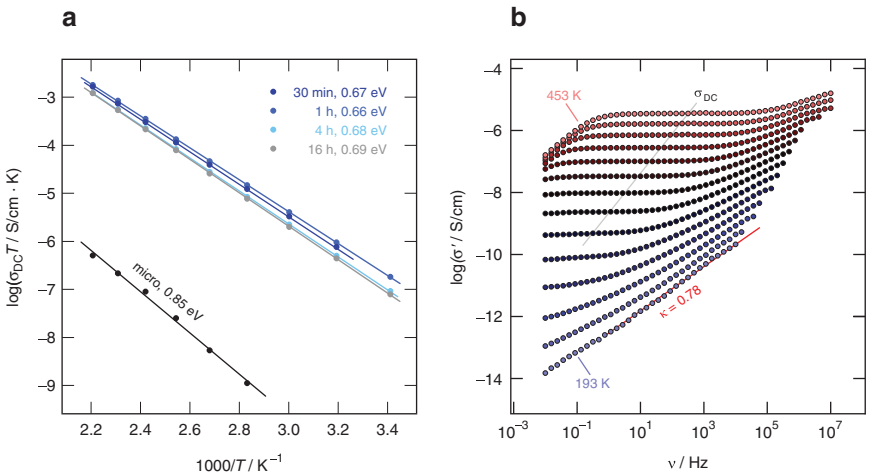

Fig. 23: (a) Temperature dependence of the ionic conductivity of $LiTaO_3$ if treated in a planetary mill for the times indicated. The values for unmilled $LiTaO_3$ are also shown. (b) Conductivity isotherms of $LiTaO_3$ high-energy ball milled for 30 min in a planetary mill. κ denotes the exponent in $\sigma' \propto \nu^{\kappa}$ used to approximate the behaviour in the dispersive regions.

in Figure 23b have to be characterized by capacities typically found for bulk responses that are already affected by the influence of the electrical response of grain boundaries (see Figure 24a).

Milling $LiTaO_3$ for 30 min causes the activation energy to decrease from 0.85 eV to 0.67 eV. Simultaneously, the corresponding pre-factor of the Arrhenius relation increased by 1.5 orders of magnitude. Such an increase might be attributed to free volume generated and structural disorder generated. Longer milling times do not influence the Li ion conductivity further. Once again, after 30 min the extent of structural disorder, i.e. local defects and amorphous material, has already reached a critical level to generate a network of fast migration pathways. We expect the percolating amorphous regions to form such a network. This view is supported by the abrupt change of the corresponding ^{7}Li NMR line shapes observed (Figure 24b). Already after 30 min of milling the ^{7}Li NMR spectrum resembles that of a sample milled for 8 h rather than that of the source material. The samples produced in planetary mills can thus be regarded as heterogeneously disordered materials, i.e. they are composed of (defect-rich) crystalline grains being embedded in an amorphous matrix that ensures fast long-range ion transport.

According to this explanation we alternatively assumed that the attenuation seen in EXAFS of the samples prepared with planetary mills (Figure 22b) stems

Bereitgestellt von | Technische Universität Graz
Angemeldet
Heruntergeladen am | 06.11.18 13:39

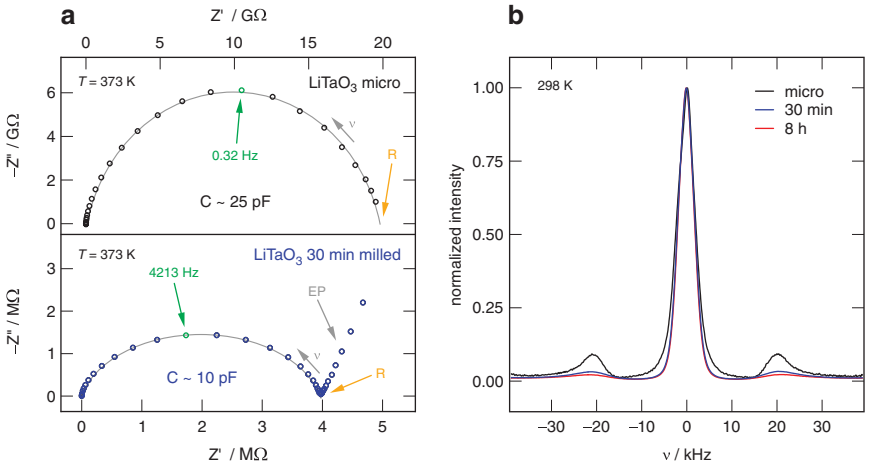

Fig. 24: (a) Nyquist plots of the complex impedance (373 K) of microcrystalline $LiTaO_3$ (upper graph) and nanocrystalline $LiTaO_3$ (milled for 30 min). Note that the two graphs refer to two axes with quite different scale markings which illustrates once more the giant increase in conductivity observed. (b) ^7Li NMR spectra of microcrystalline $LiTaO_3$ and two samples milled for 30 min and 8 h, respectively. Since ^7Li is a spin-3/2 nucleus, the spectrum is composed of a central line flanked by satellite intensities as the nuclear quadrupole moment interacts with electric field gradients in its direct neighborhood. This interaction alters the Zeeman levels in such a way that, according to the orientation of the crystallites with respect to the magnetic field, satellite intensities arise. In the present case, single pulse spectra are shown and the resulting quadrupole powder pattern is, of course, less developed than in the case of echo spectra. Nevertheless, this way the decrease in intensity of the 90° singularities is best seen. For the milled samples only a shallow difference is detected that is in line with the results from conductivity spectroscopy and EXAFS.

only from the amorphous material generated. If we take the Ta–Ta correlation as an indirect (relative) measure for the amount of amorphous $LiTaO_3$ produced, milling for as little as 30 min is estimated to yield already ca. 25 % amorphous material. This parallels the ionic conductivity measurements of the same sample ball-milled for 30 min where the magnitude is four orders higher than that for an un-milled sample (see the data at 360 K). After 8 h of milling, EXAFS suggest that the amount of amorphous $LiTaO_3$ has increased to approximately 60 %. This additional increase has, however, no further effect on the ionic conductivity presented in Figure 23a.

A similar steep increase in conductivity has recently been found for Li_2CO_3, see Figure 25. Lithium carbonate is an important constituent in the passivating interlayer, the so-called solid electrolyte interface (SEI), in liquid-based secondary lithium-ion batteries. During charging and discharging the battery the Li ions

Bereitgestellt von | Technische Universität Graz
Angemeldet
Heruntergeladen am | 06.11.18 13:39

have to surmount this barrier of decomposition products. Thus, the ionic conductivity of its components is key to guarantee powerful cycling and rate capability, particularly if an SEI mainly composed of by Li_2CO_3 is considered. To mimic the presumably amorphous Li_2CO_3 formed inside a battery, we treated microcrystalline Li_2CO_3 to introduce defect structures and to push its conductivity to the upper reachable limit of ion dynamics. As has been seen for $LiAlO_2$, Li_2TiO_3 and $LiTaO_3$, σ_{DC} already increases by several orders of magnitude if treated for short times in planetary mills. The same effect is seen for the carbonate, Figure 25a. The increase in conductivity is accompanied by a decrease of the original activation energy (1 eV) of coarse-grained polycrystalline Li_2CO_3; after 2 h of milling it decreased to 0.66 eV. This value as well as the conductivities obtained almost coincide with those for $LiTaO_3$ that served as an internal benchmark, see the dashed line in Figure 25a.

As compared to the oxides discussed so far, for the titanate $Li_5Ti_4O_{12}$, which is a well-known zero-strain anode material for lithium-ion batteries, the effect of ball milling on Li^+ dynamics is much lower. Although ionic conductivity in microcrystalline $Li_4Ti_5O_{12}$ is poor [94], viz. in the order of 10^{-12} S cm^{-1} at 295 K (ca. 0.76 eV, depending on the defect chemistry and exact morphology [27, 95]), it is, however, by about 1 order of magnitude higher than that of Li_2TiO_3. Milling of $Li_4Ti_5O_{12}$ for

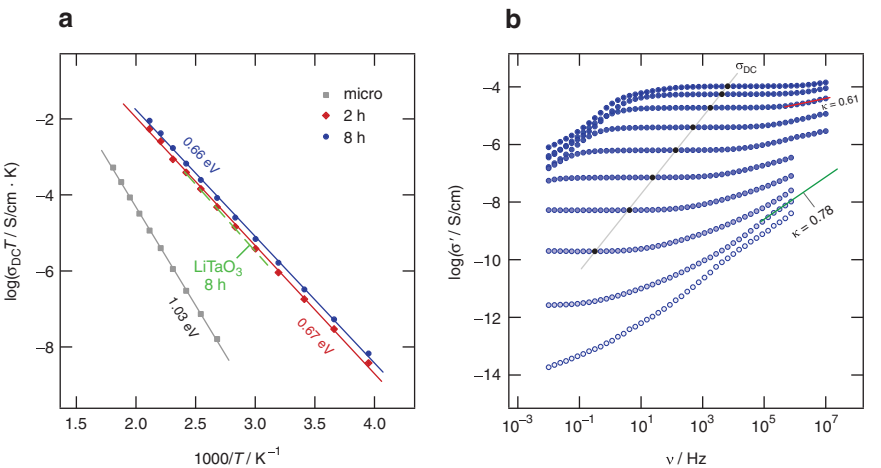

Fig. 25: (a) Change of $\sigma_{DC}T$ of un-milled and milled Li_2CO_3 as a function of the inverse temperature. At 370 K, an increase of σ_{DC} by four orders of magnitude is seen; E_a decreases from ca. 1 eV to 0.66 eV (8 h milling). As a benchmark also the Arrhenius line of nanocrystalline $LiTaO_3$ (8 h, planetary mill) is shown. (b) The corresponding conductivity spectra from which the values σ_{DC} were read off. κ denotes the exponent in $\sigma' \propto \nu^{\kappa}$ used to approximate the behaviour in the dispersive regions.

Bereitgestellt von | Technische Universität Graz
Angemeldet
Heruntergeladen am | 06.11.18 13:39

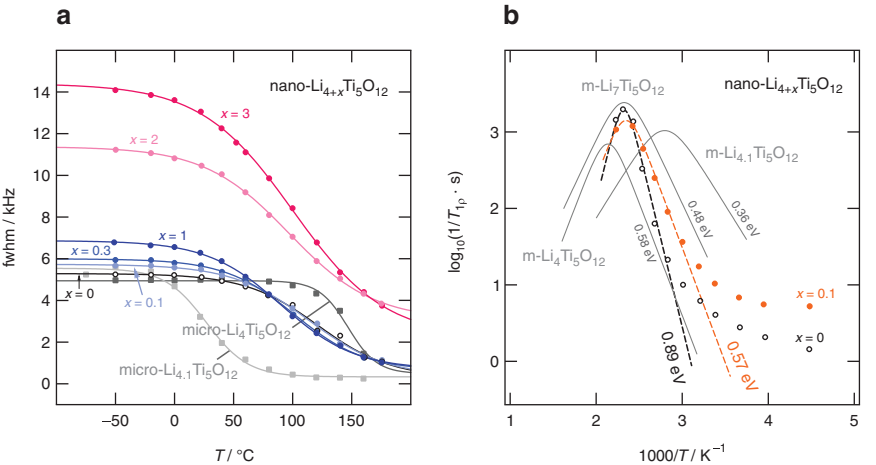

Fig. 26: (a) Li diffusivity in nanocrystalline $Li_{4+x}Ti_5O_{12}$ ($x = 0$, 0.1, 0.3, 1, 2, 3) as seen via ^{7}Li NMR line widths measurements and (b) spin-lock relaxometry carried out a locking frequency of 30 kHz; the samples with $x = 0$ and $x = 0.1$ are shown. Compared to microcrystalline $Li_4Ti_5O_{12}$ the Li diffusivity in the nanocrystalline form ($x = 0$) is slightly enhanced. If nano-$Li_4Ti_5O_{12}$ is, however, treated with *n*-BuLi to form nano-$Li_{4.1}Ti_5O_{12}$ no significant change in Li ion mobility is seen via NMR. This is quite different for the microcrystalline form, for which we observed a steep increase in Li diffusivity when going from $Li_4Ti_5O_{12}$ to $Li_{4.1}Ti_5O_{12}$, see (b). The diffusion-induced relaxation rate peak of microcrystalline $Li_7Ti_5O_{12}$ is shown for comparison.

4 h in a planetary mill causes σ_{DC} to increase by only 0.5 orders of magnitude (330 K). The activation energy is reduced from 0.76 eV to 0.69 eV.

This relatively small effect can also be observed via ^{7}Li NMR relaxometry and complementary line widths measurements. The results shown in Figure 26 refer to nanocrystalline $Li_4Ti_5O_{12}$, which was prepared by high-energy ball milling in ethanol for 3 h. The open symbols in Figure 26a represent the ^{7}Li NMR motional narrowing curve of nanocrystalline $Li_4Ti_5O_{12}$. The curve resembles that of microcrystalline $Li_4Ti_5O_{12}$, which is shown for comparison. The onset of motional narrowing for nano-$Li_4Ti_5O_{12}$ is, however, shifted by 50 K toward lower temperatures revealing (slightly) enhanced ion diffusivity. Most interestingly, if Li is chemically inserted into nanocrystalline $Li_4Ti_5O_{12}$ no drastic change of the motional narrowing (MN) curve is seen if x values of up to 0.3 are considered, Figure 26a. For micro-$Li_4Ti_5O_{12}$ the same treatment in *n*-BuLi causes a significant enhancement of ion mobility – the corresponding MN curve is shifted by almost 150 K toward lower T [96]. The situation for x being larger than 0.3 is more difficult to explain as the increased Li^+–Ti^{3+} interactions additionally broaden the spectra. A significant dependence of Li ion diffusivity on x, as it has been documented for the unmilled form [96, 97], seems to be, however, absent.

Bereitgestellt von | Technische Universität Graz
Angemeldet
Heruntergeladen am | 06.11.18 13:39

The same characteristic for nanocrystalline $Li_4Ti_5O_{12}$ and nano-$Li_{4.1}Ti_5O_{12}$ is seen if we look at the ^{7}Li NMR spin-lock relaxation rates presented in Figure 26b. The corresponding diffusion-induced relaxation rate peaks for $x = 0$ and $x = 0.1$ show up at essentially the same temperature. By coincidence it is what we also found for microcrystalline $Li_7Ti_5O_{12}$. In contrast, the difference for microcrystalline $Li_4Ti_5O_{12}$ and micro-$Li_{4.1}Ti_5O_{12}$ is much larger. Hence, we conclude that in the case of $Li_4Ti_5O_{12}$ the introduction of structural disorder is much less favorable for ionic diffusivity. By comparing the results for micro- and nanocrystalline $Li_4Ti_5O_{12}$ from rotating-frame spin-lock NMR an interesting feature is revealed: although the rate peak of the nanocrystalline sample shifts to lower T, as is expected when comparing the respective MN curves, the low-T flank of nano-$Li_4Ti_5O_{12}$ has to be characterized by a higher activation energy. This feature can only be explained by an enhanced pre-factor of the associated Arrhenius law. If x is increased from $x = 0$ to $x = 0.1$ we witness both a decrease of E_a (from 0.89 eV to 0.57 eV, see Figure 26b) and the associated pre-factor. Without any change of the pre-factor the position of the rate peak should have been changed to be in agreement with a higher mean activation energy.

2.4 Ionic conductivity in nanocrystalline Li_2O_2 and Na_2O_2 – the possible discharge products in Li- and Na-air batteries

Ionic conductivity and diffusivity in peroxides belongs to the white areas of materials science. Li_2O_2 and Na_2O_2 form during discharging a Li metal or Na metal oxygen battery. Elucidating the transport properties of the ionic and electronic charge carriers in these peroxides is of importance in the field of oxygen batteries. Considering the above derived conclusion that ion transport can be, in some cases, greatly enhanced if the poorly conducting oxides were mechanically treated, we tried the same approach to produce phase-pure nanocrystalline Li_2O_2 and Na_2O_2. Thus, we expect that with nanocrystalline, ball-milled Li_2O_2 a material with an upper limit of reachable ion conductivities is at hand. To determine these maximal conductivity parameters might also influence current battery research on metal oxygen systems.

Li_2O_2 crystallizes with the hexagonal space group $P6_3/mmc$ and shows two crystallographically distinct Li sites (Wyckoff positions 2a and 2c). The covalently bonded O_2 dimers are arranged in an alternating ABAB stacking. The trigonal prismatic Li ions in Li_2O_2 are in the same layer as the peroxide anions. The octahedrally coordinated ones reside between the peroxide layers. As revealed by impedance and conductivity spectroscopy Li ion transport in Li_2O_2 is extremely low [29, 98]. In Figure 27a the corresponding overall conductivities of microcrystalline

Bereitgestellt von | Technische Universität Graz
Angemeldet
Heruntergeladen am | 06.11.18 13:39

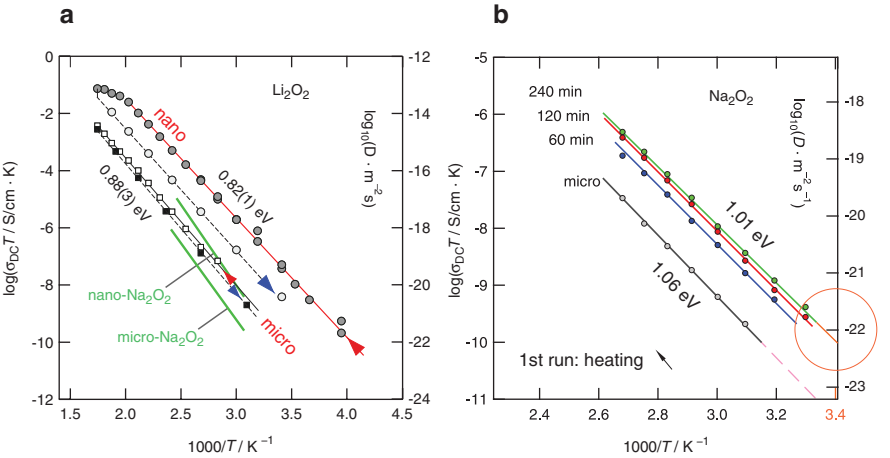

Fig. 27: (a) Arrhenius diagram of the overall conductivities of microcrystalline and nanocrystalline Li_2O_2. The arrows indicate the heating and cooling runs. At high temperatures nanocrystalline Li_2O_2 is exposed to grain growth and healing of defects, thus a decrease in conductivity was seen during cooling. For microcrystalline Li_2O_2 almost no difference was detected. For comparison, the Arrhenius lines of micro- and nanocrystalline Na_2O_2 are also shown. (b) Total Conductivity of micro- and nanocrystalline Na_2O_2 obtained after high-energy ball milling the coarse-grained starting material. The right axes refer to solid-state diffusion coefficients which were obtained by means of the Nernst–Einstein equation using the σ values measured. Figures adapted from Refs. [29, 46].

and nanocrystalline Li_2O_2 are compared with those of isostructural Na_2O_2 [46], see also Figure 27b. While high energy ball milling of Li_2O_2 causes the total conductivity to increase by approximately 2 orders of magnitude, in the case of Na_2O_2 the effect is much less pronounced. For micro-Li_2O_2 we obtained a very low conductivity of 3.4×10^{-13} S/cm at ambient temperature [29]. High-energy ball-milling leads to an increase of σ_{DC} by ca. 2 orders of magnitude reaching 1.1×10^{-10} S/cm; correspondingly, the activation energy decreases from 0.89 eV to 0.82 eV. The electronic contribution to σ, which was measured via polarization experiments, turned out to be in the order of 9×10^{-12} S/cm. This values makes <10 % of the total conductivity. For ball-milled Na_2O_2 at ambient conditions the overall conductivity is in the order of 10^{-13} S/cm. Recent polarization experiments have shown that the partial electronic conductivity ranges between 7.6×10^{-14} S/cm and 1×10^{-13} S/cm. Thus, the total conductivity in the sodium analogue is to a non-negligible extent influenced by electronic charge transport.

The poor ionic conductivity of Li_2O_2 is also represented by ^{7}Li NMR line shape measurements [29]. Interestingly, the ^{7}Li NMR lines of nano-Li_2O_2 undergo a pronounced heterogeneous motional narrowing upon heating the peroxide,

Bereitgestellt von | Technische Universität Graz
Angemeldet
Heruntergeladen am | 06.11.18 13:39

see Figure 28a. The Gaussian shaped NMR line that is seen in the regime of the rigid lattice narrows such that a two-component line shape emerges. The narrow line on top of the broader one represents Li ions being mobile on the time scale defined by the line width at low T, i.e. these ions have access to diffusion processes being characterized by (mean) jump rates in the order of ca. 20 kHz. Most likely, the enhancement in conductivity can be traced back to the generation of a small spin reservoir with mobile Li ions; these are expected to reside in the direct neighborhood of defects generated or near the structurally disordered and defect-rich interfacial regions formed during mechanical treatment.

Through ^{7}Li NMR relaxometry and stimulated echo measurements we could refine the picture presented by conductivity spectroscopy. Interestingly, the diffusion-induced NMR relaxation rates reveal much lower activation energies for Li ion dynamics in Li_2O_2 (0.22–0.24 eV, see Figure 28b). Obviously, the rates probe local or short-range motions rather than long-range ion transport. We may

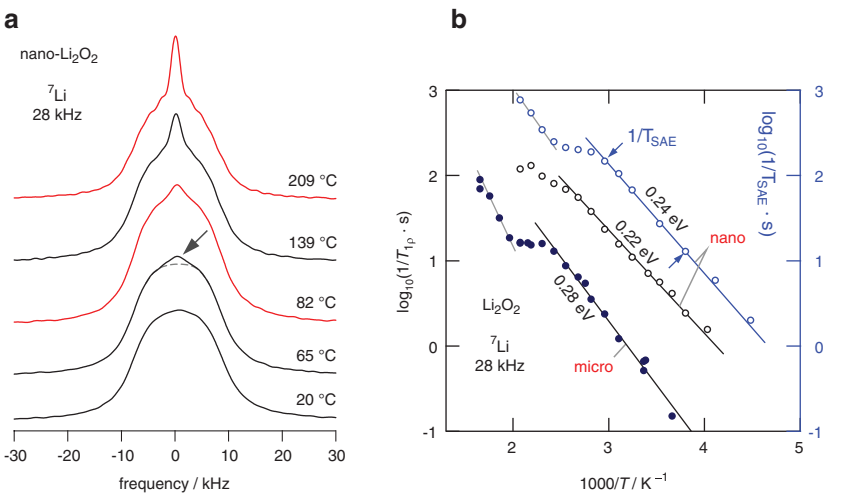

Fig. 28: (a) ^{7}Li NMR line shapes of nanocrystalline Li_2O_2 that was mechanically treated for 3 h in a planetary mill equipped with a milling vial made of ZrO_2. With increasing T a two-component NMR line shape emerges; the narrow line superimposing the broad one reflects relatively mobile ions in nanocrystalline Li_2O_2. (b) ^{7}Li NMR spin–lattice relaxation rates of nanocrystalline Li_2O_2 recorded in the laboratory frame (116 MHz) and in the rotating frame of reference (28 kHz locking frequency). At temperatures lower than ca. 370 K the rates reveal Arrhenius behaviour with a much lower activation energy than detected by conductivity spectroscopy. The same temperature dependence is seen via ^{7}Li SAE NMR if temperatures lower than 330 K are considered (0.24 eV). The discrepancy in E_a clearly points to heterogeneous dynamics with subsets of slow and fast Li ions. The latter predominantly govern the overall NMR rates in this T regime. Figures adapted from Ref. [29].

Bereitgestellt von | Technische Universität Graz
Angemeldet
Heruntergeladen am | 06.11.18 13:39

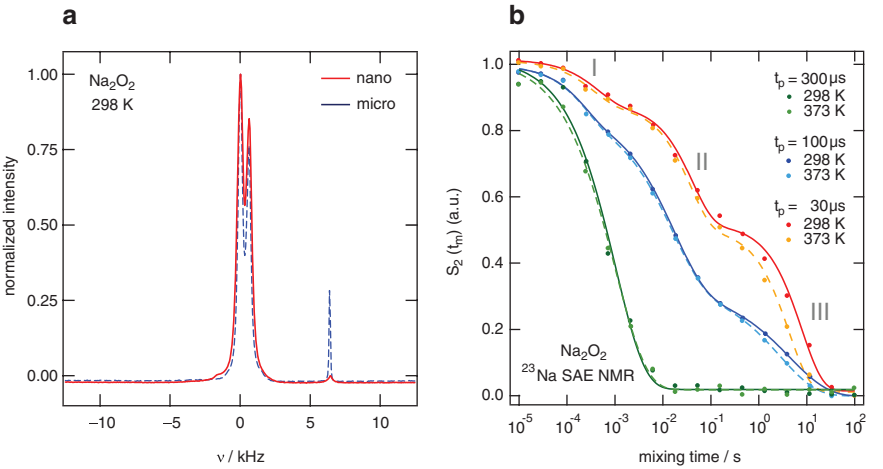

Fig. 29: (a) ^{23}Na MAS spectra of micro- and nanocrystalline Na_2O_2. The spectra were recorded at 132.25 MHz and a spinning speed of 30 kHz. Apart from the two main signals, another line (Na_2O) shows up at higher frequencies. (b) ^{23}Na SAE NMR decay curves of microcrystalline Na_2O_2 recorded at the preparation times and temperatures indicated.

identify the fast subset of Li ions seen in line shape NMR to be responsible for the low E_a values deduced through relaxometry. The same seems to be the case for the ^{7}Li SAE NMR decay rates that are shown in Figure 28b for comparison. At higher T we recognized another thermally activated process that is, in the case of T_1 ^{7}Li NMR relaxation, governed by a higher activation energy of 0.47 eV. A similar increase in decay rates is also seen in SAE NMR (0.41 eV). Most likely, this process is influenced by polaron dynamics; such dynamics were, for example, studied by first-principle calculations by Radin and Siegel who calculated an activation energy of 0.42 eV [99].

In analogy to Li_2O_2 we started to analyze the poor Na ion diffusion in nano- and microcrystalline Na_2O_2, see Figure 27a. High-resolution (MAS) ^{23}Na NMR measurements carried out at 132.25 MHz revealed the two magnetically inequivalent Na sites in Na_2O_2 as expected, see Figure 29a. The spectra shown were recorded at a spinning speed of 30 kHz, no reference was used to measure the chemical shift values; the more intense signal was simply referenced to 0 kHz. Krawietz et al. report chemical shifts of 4.8 and 9.9 ppm [100]. Slow Na ion hopping between the two neighbored sites might be measure bale via 2D exchange NMR or SAE NMR. Preliminary ^{23}Na SAE NMR decay curves of microcrystalline Na_2O_2 are shown in Figure 29b; to the best of our knowledge this is the first time that such curves are reported for ^{23}Na. So far, the SAE technique has been successfully applied to ^{2}H [101, 102], ^{9}Be [71, 103, 104] and the two Li isotopes (^{6}Li and ^{7}Li, [63, 69, 71, 72]).

Bereitgestellt von | Technische Universität Graz
Angemeldet
Heruntergeladen am | 06.11.18 13:39

Extending the technique to the ^{23}Na ($I = 3/2$) nucleus is, however, limited because of the large quadrupole moment of the Na spin that hinders a non-selective excitation. In the present case, the ^{23}Na SAE signal is a mixture of quadrupolar and dipolar contributions.

Although the ^{23}Na SAE S_2 curves recorded at fixed t_p and variable t_m sensitively depend on preparation time, they do not significantly vary with temperature. Hence, Na ion dynamics in microcrystalline Na_2O_2 is by far too poor to be detectable even with NMR methods designed to probe slow ion exchange. The curves recorded at short t_p are clearly composed of three decay steps. While step III reflects the almost T independent T_1 relaxation, step II is most likely driven by spin-diffusion effects. The first decay step seems to be associated with transversal spin–spin relaxation.

2.5 Glass formers: the influence on ball milling on ion transport in crystalline $Li_2B_4O_7$

As has been illustrated above for several oxides, particularly for $LiTaO_3$, $LiAlO_2$ and Li_2CO_3, mechanical treatment can greatly enhance Li ion diffusivity and Li ion transport, respectively. Expectedly the same is true for glass formers such as $Li_2B_4O_7$ that served as another model substance to quantify the effect of high-energy ball milling on DC conductivity [28], in a second step the transport parameters could directly be compared with those of the pure glass that was prepared by quenching a melt of $Li_2B_4O_7$. For coarse-grained polycrystalline $Li_2B_4O_7$ the conductivity isotherms revealed low DC-conductivities and a quite high activation energy of 1.05 eV (see Figure 30). Milling in planetary mills has once again a drastic effect on ion transport. Interestingly, after 8 h of mechanical treatment we reached ionic conductivities that coincide with those of $LiAlO_2$ also milled for 8 h. Increasing the milling time to 16 h results in an additional increase of σ_{DC} by 0.5 orders of magnitude. Comparing a 16-h ball-milled sample and glassy $Li_2B_4O_7$ shows that there is still a large conductivity gap between the two samples, see Figure 30a.

X-ray powder diffraction suggested that the formation of amorphous $Li_2B_4O_7$ is mainly responsible for the increase in ion dynamics. This view is supported by ^{11}B MAS NMR (Figure 31b), cf. Ref. [28]. Concerning ion dynamics, ^7Li NMR line shapes revealed that in addition to the ions in the amorphous regions also those in the crystalline grains nano-$Li_2B_4O_7$ do sense the effect of mechanical treatment; the motional narrowing curve depicted in Figure 30 b unveils the increase in ion dynamics seen in the wake of mechanical treatment. Presumably, defects introduced into the still crystalline grains also drastically influence local hopping

Bereitgestellt von | Technische Universität Graz
Angemeldet
Heruntergeladen am | 06.11.18 13:39

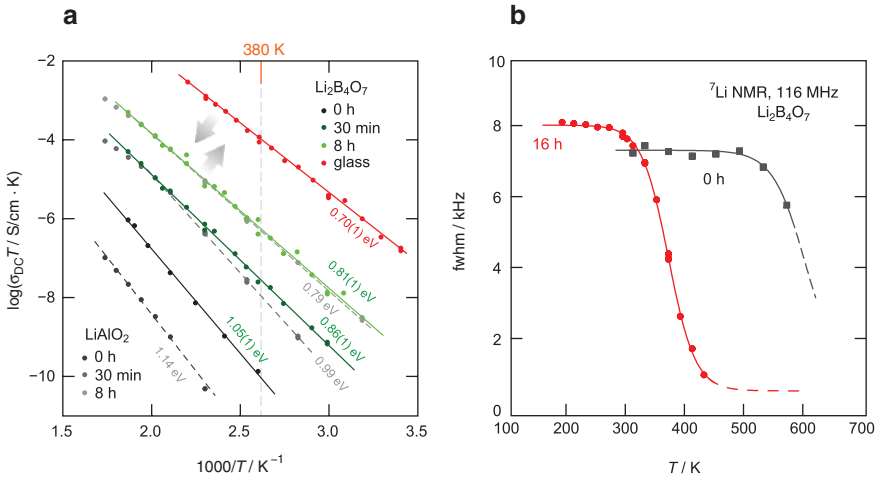

Fig. 30: (a) DC conductivities of nanocrystalline $Li_2B_4O_7$ produced through milling of the microcrystalline source material. For comparison, the results obtained for $LiAlO_2$ are also shown (see dashed lines). The solid lines represent Arrhenius fits, activation energies are indicated. The highest conductivities were obtained for a glassy sample ($E_a = 0.7$ eV). The arrows indicate the change in DC conductivity upon further mechanical treatment of the nanocrystalline material and the glass, respectively. (b) Change of the ^{7}Li NMR (central) line width of nano- and microcrystalline $Li_2B_4O_7$ with temperature. Figures adapted from Ref. [28].

processes. These local ion dynamics are characterized by only 0.3 eV as could be deduced from the low-T flank of the ^{7}Li SLR NMR rate peak (see Figure 31a). For comparison, the flank for micro-$Li_2B_4O_7$ is characterized by 0.5 eV.

$Li_2B_4O_7$ and aluminosilicates easily form glasses if the materials are melted and quenched. Although plenty of studies can be found in literature that deal with ion transport phenomena and diffusion mechanisms in glasses only few report on the change of ion transport parameters if glasses were mechanically treated in shaker or planetary mills. At first glance one would expect no significant influence when an already disordered material is milled. So far only few reports, however, showed that high-energy ball-milling of glassy materials ($LiAlSi_2O_6$ (β-spodumene, [105]), $LiBO_2$ [20, 106]) results in a decrease of the ionic DC conductivity, see also Ref. [107]. The same effect was observed for β-eucryptite [108]. This astonishing decrease was also confirmed by ^{7}Li NMR spectroscopy. For a first interpretation a simple structural model was used to explain the observed trend [105]. This effect is obviously caused by a mechanically induced structural relaxation of the non-equilibrium structure of the glass that was prepared by rapid thermal quenching [105]. Such structural relaxation obviously causes the ionic charge carriers to slow down with respect to those residing in the unmilled

Bereitgestellt von | Technische Universität Graz
Angemeldet
Heruntergeladen am | 06.11.18 13:39

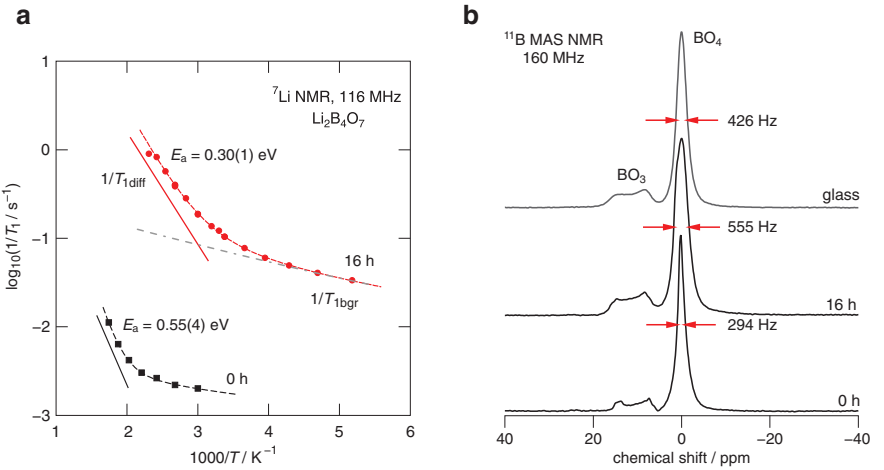

Fig. 31: (a) ^{7}Li NMR SLR rates of micro- and nanocrystalline lithium tetraborate $Li_2B_4O_7$. Unmilled $Li_2B_4O_7$ is characterized by extremely long longitudinal relaxation reaching 500 s at ambient temperature. After mechanical treatment the rate has increased to 5 s. Accordingly, the activation energy decreased from 0.55 eV to ca. 0.3 eV. Milling affected both the non-diffusive relaxation rates, the so-called background relaxation ($1/T_{1\,bgr}$), as well as the diffusion-induced contribution to the overall rate. Besides the introduction of (paramagnetic) impurities, $1/T_{1\,bgr}$ is also expected to be influenced by strictly localized (caged) ion dynamics. (b) ^{11}B MAS NMR spectra of micro- and nanocrystalline $Li_2B_4O_7$. The two resonances reflect the BO_4 and BO_3 units in $Li_2B_4O_7$. Milling causes the lines to broaden; this broadening can be assigned to polyhedra distortions because of mechanical treatment in the planetary mill. After 16 h of milling the line shape resembles that of amorphous $Li_2B_4O_7$. Figures adapted from Ref. [28].

glass matrix. Note that, influenced by the Löwenstein rule, for β-eucryptite, for example, stable and metastable forms with respect to the Al and Si ordering exist in certain temperature ranges. Ball-milling might largely influence local and long-range arrangements of the polyhedra. Hence, the structural arrangement in a quenched glass should not necessarily be identical with that of a milled sample.

3 Summary

Nanostructured materials are of large and ever growing interest due to their beneficial properties. In particular, nanocrystalline ceramics find applications as catalysts, sensors, adsorbents or new electrolytes and advanced electrode materials in electrochemical energy storage. We reviewed recent studies on lithium-ion dynamics and electrochemical activity of various classes of materials.

Bereitgestellt von | Technische Universität Graz
Angemeldet
Heruntergeladen am | 06.11.18 13:39

Nanostructuring is essential for TiO_2 to use the oxide as anode material in lithium-ion as well as sodium-ion batteries. We noticed marked differences in the storage mechanism when amorphous TiO_2 nanotubes are used as active material; the electrochemical reaction with sodium is significantly affected by interfacial effects. Li NMR spectroscopy measurements point to slow Li ion self-diffusivity in the amorphous form. Similarly, poor to moderate ion dynamics also govern ion transport in the other forms of titania such as rutile nanorods or mesoporous TiO_2. In the case of TiO_2-B nanotubes a fast relaxing reservoir of spins is detected that might be ascribed to those ions being located in the surface-influenced regions.

The formation of nanocrystalline ceramics via high-energy ball-milling leads to ion conductors with, in many cases, greatly improved transport properties. By using both NMR and EXAFS we could show that for some of the samples prepared in planetary mills ($LiAlO_2$, $LiTaO_3$, $Li_2B_4O_7$) the formation of amorphous material plays indeed a decisive role in explaining the enhancement seen. For some of the oxides studied an upper limit of σ_{DC} is seen for sufficiently long periods of milling. Besides amorphous structures, the introduction of defects into the bulk regions of the nanocrystallites has also to be considered if samples prepared in shaker mills are to be studied. It turned out that, aside from few exceptions (see, e.g. $Li_4Ti_5O_{12}$, Li_2O_2), ion transport properties can be easily manipulated by tuning the degree of structural disorder. This strategy holds at least for oxides with low conductivities and, of course, depends on the exact crystal structure and bonding situations of the materials as well as their tendencies to form metastable modifications usually showing up at high temperatures or pressures. Fast ion conductors, on the other hand, may suffer rather than benefit from mechanically induced structural disorder.

Acknowledgements: We thank the Deutsche Forschungsgemeinschaft for financial support (FOR 1277, Mobility of Lithium Ions in Solids, sub-projects 7 and 1 (TP 7, TP 1), grant no. WI 3600 4-1(2) and 2-1(2)) over the last 6 years in the Research Unit 'molife'. Moreover, additional financial support by the Austrian Federal Ministry of Science, Research and Economy, and the Austrian National Foundation for Research, Technology and Development (in the frame of the Christian-Doppler-Laboratory of Lithium Batteries: Ageing Effects, Technology and New Materials) is greatly appreciated.

References

1. V. Šepelák, A. Düvel, M. Wilkening, K. D. Becker, P. Heitjans, Chem. Soc. Rev. **42**, 7507 (2013).
2. P. Heitjans, S. Indris, J. Phys. Condens. Matter **15**, R1257 (2003).
3. F. Preishuber-Pflügl, M. Wilkening, Dalton. Trans. **45**, 8675 (2016).

Bereitgestellt von | Technische Universität Graz
Angemeldet
Heruntergeladen am | 06.11.18 13:39

4. P. Heitjans, M. Masoud, A. Feldhoff, M. Wilkening, Faraday Discuss. **134**, 67 (2007).
5. M. Wilkening, V. Epp, A. Feldhoff, P. Heitjans, J. Phys. Chem. C **112**, 9291 (2008).
6. M. Wilkening, A. Düvel, F. Preishuber-Pflügl, K. da Silva, S. Breuer, V. Šepelák, P. Heitjans, Z. Krist.-Cryst. Mater. **32**, 107 (2016).
7. B. Ruprecht, M. Wilkening, S. Steuernagel, P. Heitjans, J. Mater. Chem. **18**, 5412 (2008).
8. B. Ruprecht, M. Wilkening, A. Feldhoff, S. Steuernagel, P. Heitjans, Phys. Chem. Chem. Phys. **11**, 3071 (2009).
9. A. Düvel, B. Ruprecht, P. Heitjans, M. Wilkening, J. Phys. Chem. C **115**, 23784 (2011).
10. A. V. Chadwick, Nature **408**, 925 (2000).
11. A. Chadwick, S. Savin, Solid State Ion. **177**, 3001 (2006).
12. J. Maier, Prog. Solid State Chem. **23**, 171 (1995).
13. J. Maier, Phys. Chem. Chem. Phys. **11**, 3011 (2009).
14. J. Maier, Nat. Mater. **4**, 805 (2005).
15. J. Maier, J. Phys. Chem. Solids **46**, 309 (1985).
16. J. Maier, Chem. Mater. **26**, 348 (2014).
17. J. Maier, Z. Phys. Chem. **217**, 415 (2003).
18. J. Schoonman, Solid State Ion. **157**, 319 (2003).
19. P. Knauth and J. Schoonman (Eds.), Nanocrystalline Metals and Oxides, Kluwer, Boston, MA (2001).
20. P. Heitjans, E. Tobschall, M. Wilkening, Eur. Phys. J. Spec. Top. **161**, 97 (2008).
21. P. Heitjans M. Wilkening, Mater. Res. Bull. **34**, 915 (2009).
22. P. Heitjans, M. Wilkening, Defect Diffus. Forum **283–286**, 705 (2009).
23. P. Knauth, J. Schoonman (Eds.), Nanocomposites – Ionic Conducting Materials and Structural Spectroscopies, Springer, New York (2008).
24. J. M. Laugier, L. Raymond, G. Albinet, P. Knauth, Modell. Simul. Mater. Sci. Eng. **19**, 065001 (2011).
25. P. Knauth, J. M. Debierre, G. Albinet, Solid State Ion. **121**, 101 (1999).
26. P. Knauth, G. Albinet, J. M. Debierre, Ber. Bunsenges. Phys. Chem. **102**, 945 (1998).
27. H. Brandstätter, D. Wohlmuth, P. Bottke, V. Pregartner, M. Wilkening, Z. Phys. Chem. **229**, 1363 (2015).
28. D. Wohlmuth, V. Epp, B. Stanje, A. M. Welsch, H. Behrens, and M. Wilkening, J. Am. Ceram. Soc. **99**, 1687 (2016).
29. A. Dunst, V. Epp, I. Hanzu, S. A. Freunberger, M. Wilkening, Energy. Environ. Sci. **7**, 2739 (2014).
30. V. Epp, M. Wilkening, ChemPhysChem **14**, 3706 (2013).
31. S. Indris, D. Bork, P. Heitjans, J. Mater. Synth. Process. **8**, 245 (2000).
32. S. Indris, P. Heitjans, Mater. Sci. Forum **343–343**, 417 (2000).
33. M. Wilkening, S. Indris, P. Heitjans, Phys. Chem. Chem. Phys. **5**, 2225 (2003).
34. A. S. Arico, P. Bruce, B. Scrosati, J. M. Tarascon, W. Van Schalkwijk, Nat. Mater. **4**, 366 (2005).
35. P. G. Bruce, B. Scrosati, J. M. Tarascon, Angew. Chem. Int. Ed. **47**, 2930 (2008).
36. Z. Liu, Y. G. Andreev, A. R. Armstrong, S. Brutti, Y. Ren, P. G. Bruce, Prog. Nat. Sci.-Mater. **23**, 235 (2013).
37. Y. Ren, Z. Liu, F. Pourpoint, A. R. Armstrong, C. P. Grey, P. G. Bruce, Angew. Chem. Int. Ed. **51**, 2164 (2012).
38. Y. Ren, A. R. Armstrong, F. Jiao, and P. G. Bruce, J. Am. Chem. Soc. **132**, 996 (2010).
39. Y. Ren, L. J. Hardwick, P. G. Bruce, Angew. Chem. Int. Ed. **49**, 2570 (2010).
40. T. Djenizian, I. Hanzu, P. Knauth, J. Mater. Chem. **21**, 9925 (2011).

Bereitgestellt von | Technische Universität Graz
Angemeldet
Heruntergeladen am | 06.11.18 13:39

41. G. F. Ortiz, I. Hanzu, P. Knauth, P. Lavela, J. L. Tirado, T. Djenizian, Electrochim. Acta **54**, 4262 (2009).
42. D. Prutsch, M. Wilkening, I. Hanzu, ACS Appl. Mater. Interfaces **7**, 25757 (2015).
43. P. Bottke, Y. Ren, I. Hanzu, P. G. Bruce, M. Wilkening, Phys. Chem. Chem. Phys. **16**, 1894 (2014).
44. M. Wilkening, J. Heine, C. Lyness, A. R. Armstrong, P. G. Bruce, Phys. Rev. B **80**, 064302 (2009).
45. M. Wilkening, C. Lyness, A. R. Armstrong, P. G. Bruce, J. Phys. Chem. C **113**, 4741 (2009).
46. A. Dunst, M. Sternad, M. Wilkening, Mat. Sci. Engin. B **211**, 85 (2016).
47. D. Wohlmuth, V. Epp, P. Bottke, I. Hanzu, B. Bitschnau, I. Letofsky-Papst, M. Kriechbaum, H. Amenitsch, F. Hofer, M. Wilkening, J. Mater. Chem. A **2**, 20295 (2014).
48. A. V. Chadwick, D. M. Pickup, S. Ramos, G. Cibin, N. Tapia-Ruiz, S. Breuer, D. Wohlmuth, M. Wilkening, Inst. Phys. Conf. Series Mat. Sci. Engin. **169**, 012015 (2017).
49. J. Langer, V. Epp, M. Sternad, M. Wilkening, Solid State Ion. **276**, 56 (2015).
50. M. J. Marczewski, B. Stanje, I. Hanzu, M. Wilkening, P. Johansson, Phys. Chem. Chem. Phys. **16**, 12341 (2014).
51. M. Wagemaker, A. P. M. Kentgens, F. M. Mulder, Nature **418**, 397 (2002).
52. M. Wagemaker, R. van de Krol, A. P. M. Kentgens, A. A. van Well, F. M. Mulder, J. Am. Chem. Soc. **123**, 11454 (2001).
53. V. Zwilling, E. Darque-Ceretti, A. Boutry-Forveille, D. David, M. Y. Perrin, M. Aucouturier, Surf. Interface Anal. **27**, 629 (1999).
54. D. Gong, C. A. Grimes, O. K. Varghese, W. Hu, R. S. Singh, Z. Chen, E. C. Dickey, J. Mater. Res. **16**, 3331 (2001).
55. R. Beranek, H. Hildebrand, P. Schmuki, Electrochem. Solid-State Lett. **6**, B12 (2003).
56. J. J. Kelly, Electrochim. Acta **24**, 1273 (1979).
57. M. Paulose, H. E. Prakasam, O. K. Varghese, L. Peng, K. C. Popat, G. K. Mor, T. A. Desai, C. A. Grimes, J. Phys. Chem. C **111**, 14992 (2007).
58. D. Regonini, C. R. Bowen, A. Jaroenworaluck, R. Stevens, Mat. Sci. Engin. R-Rep. **74**, 377 (2013).
59. D. Kowalski, D. Kim, P. Schmuki, Nano Today **8**, 235 (2013).
60. I. Hanzu, T. Djenizian, P. Knauth, ECS Transact. **35**, 21 (2011).
61. R. Böhmer, K. R. Jeffrey, M. Vogel, Prog. Nucl. Magn. Reson. Spectrosc. **50**, 87 (2007).
62. M. Wilkening, W. Küchler, P. Heitjans, Phys. Rev. Lett. **97**, 065901 (2006).
63. M. Wilkening, P. Heitjans, ChemPhysChem **13**, 53 (2012).
64. M. Wilkening, D. Gebauer, P. Heitjans, J. Phys. Condens. Matter **20**, 022201 (2008).
65. M. Wilkening, P. Heitjans, Phys. Rev. B **77** (2008).
66. M. Wilkening, P. Heitjans, Defect Diffus. Forum **237–240**, 1182 (2005).
67. M. Wilkening, P. Heitjans, J. Phys. Condens. Matter **18**, 9849 (2006).
68. M. Wilkening, A. Kuhn, P. Heitjans, Phys. Rev. B **78**, 054303 (2008).
69. R. Böhmer, T. Jörg, F. Qi, A. Titze, Chem. Phys. Lett. **316**, 419 (2000).
70. F. Qi, G. Diezemann, H. Böhm, J. Lambert, R. Böhmer, J. Magn. Reson. **169**, 225 (2004).
71. F. Qi, T. Jörg, R. Böhmer, Solid State Nucl. Magn. Reson. **22**, 484 (2002).
72. R. Böhmer, F. Qi, Solid State Nucl. Magn. Reson. **31**, 28 (2007).
73. P. Bottke, D. Rettenwander, W. Schmidt, G. Amthauer, M. Wilkening, Chem. Mater. **27**, 6571 (2015).
74. P. Heitjans, A. Schirmer, S. Indris, NMR and β-NMR studies of diffusion in interface-dominated and disordered solids. In: Diffusion in Condensed Matter – Methods, Materials, Models, (Eds. P. Heitjans, J. Kärger) Springer, Berlin (2005), P. 367.

Bereitgestellt von | Technische Universität Graz
Angemeldet
Heruntergeladen am | 06.11.18 13:39

75. V. Epp, M. Wilkening. Handbook of Solid State Batteries, World Scientific, Singapore (2015).
76. J. Heine, M. Wilkening, P. Heitjans, Diff. Fundam. **12**, 95 (2010).
77. A. Kuhn, S. Narayanan, L. Spencer, G. Goward, V. Thangadurai, M. Wilkening, Phys. Rev. B **83**, 094302 (2011).
78. H. Lindstrom, S. Sodergren, A. Solbrand, H. Rensmo, J. Hjelm, A. Hagfeldt, S. E. Lindquist, J. Phys. Chem. B **101**, 7717 (1997).
79. V. Epp, M. Wilkening, Phys. Rev. B **82**, 020301 (2010).
80. S. Nakhal, D. Wiedemann, B. Stanje, O. Dolotko, M. Wilkening, M. Lerch, J. Solid State Chem. **238**, 60 (2016).
81. B. Stanje, V. Epp, S. Nakhal, M. Lerch, M. Wilkening, ACS Appl. Mater. Interface **7**, 4089 (2015).
82. A. F. McDowell, C. F. Mendelsohn, M. S. Conradi, R. C. Bowman, A. J. Maeland, Phys. Rev. B **51**, 6336 (1995).
83. W. Küchler, P. Heitjans, A. Payer, R. Schöllhorn, Solid State Ion. **70**, 434 (1994).
84. M. Uitz, V. Epp, P. Bottke, M. Wilkening, J. Electroceram. in press (2016). DOI: 10.1007/s10832-017-0071-4.
85. V. Epp, S. Nakhal, M. Lerch, M. Wilkening, J. Phys. Condens. Matter **25**, 195402 (2013).
86. D. Wiedemann, S. Nakhal, J. Rahn, E. Witt, M. M. Islam, S. Zander, P. Heitjans, H. Schmidt, T. Bredow, M. Wilkening, M. Lerch, Chem. Mater. **28**, 915 (2016).
87. E. Witt, S. Nakhal, C. V. Chandran, M. Lerch, P. Heitjans, Z. Phys. Chem. **229**, 1327 (2015).
88. D. Wiedemann, S. Indris, M. Meven, B. Pedersen, H. Boysen, R. Uecker, P. Heitjans, M. Lerch, Z. Krist.-Cryst. Mater. **231**, 189 (2016).
89. J. Langer, D. Wohlmuth, A. Kovalcik, V. Epp, F. Stelzer, M. Wilkening, Ann. Phys. **527**, 523 (2015).
90. B. Ruprecht, M. Wilkening, R. Uecker, P. Heitjans, Phys. Chem. Chem. Phys. **14**, 11974 (2012).
91. K. Okada, N. Machida, M. Naito, T. Shigematsu, S. Ito, S. Fujiki, M. Nakano, Y. Aihara, Solid State Ion. **255**, 120 (2014).
92. Y. T. Li, J. T. Han, C. A. Wang, H. Xie, J. B. Goodenough, J. Mater. Chem. **22**, 15357 (2012).
93. L. Cheng, J. S. Park, H. M. Hou, V. Zorba, G. Y. Chen, T. Richardson, J. Cabana, R. Russo, M. Doeff, J. Mater. Chem. A **2**, 172 (2014).
94. M. Wilkening, R. Amade, W. Iwaniak, P. Heitjans, Phys. Chem. Chem. Phys. **9**, 1239 (2007).
95. W. Schmidt, M. Wilkening, Solid State Ion. **287**, 77 (2016).
96. W. Schmidt, P. Bottke, M. Sternad, P. Gollob, V. Hennige, M. Wilkening, Chem. Mater. **27**, 1740 (2015).
97. M. Wilkening, W. Iwaniak, J. Heine, V. Epp, A. Kleinert, M. Behrens, G. Nuspl, W. Bensch, P. Heitjans, Phys. Chem. Chem. Phys. **9**, 6199 (2007).
98. O. Gerbig, R. Merkle, J. Maier, Adv. Mater. **25**, 3129 (2013).
99. M. D. Radin, D. J. Siegel, Energy. Environ. Sci. **6**, 2370 (2013).
100. T. R. Krawietz, D. K. Murray, J. F. Haw, J. Phys. Chem. A **102**, 8779 (1998).
101. M. Lausch, H. W. Spiess, J. Magn. Reson. **54**, 466 (1983).
102. M. Lausch, H. W. Spiess, Chem. Phys. Lett. **71**, 182 (1980).
103. X. P. Tang, R. Busch, W. L. Johnson, Y. Wu, Bulk Metallic Glasses, Mater. Res. Soc. Symp. P **554**, 87 (1999).
104. X. P. Tang, R. Busch, W. L. Johnson, Y. Wu, Phys. Rev. Lett. **81**, 5358 (1998).
105. A. Kuhn, M. Wilkening, P. Heitjans, Solid State Ion. **180**, 302 (2009).
106. A. Kuhn, E. Tobschall, P. Heitjans, Z. Phys. Chem. **223**, 1359 (2009).
107. C. V. Chandran, P. Heitjans, Ann. Rep. NMR Spectrosc. **89**, 1 (2016).
108. P. Bottke, Diploma Thesis, Leibniz University Hannover (2010).

Bereitgestellt von | Technische Universität Graz
Angemeldet
Heruntergeladen am | 06.11.18 13:39

6.3 Solid-state electrolytes

Current Li- and Na-ion based battery systems generally use organic liquids as electrolytes [8, 17]. But, despite their high ionic conductivities and excellent wetting properties, they often suffer from inadequate electrochemical and thermal stabilities as well as safety issues, such as leakage and flammability. The replacement of liquid organic electrolytes by solid-state electrolytes is one option to overcome these safety and stability problems owing to their enhanced thermal stability, diminished flammability and wider electrochemical stability window [19]. In addition, they are resistant to a large number of cycles [20]. For more information about solid electrolytes see chapter 4.5.

A key property solids have to fulfill in order to be considered as suitable solid electrolyte is a high lithium-ion diffusivity (or conductivity) at ambient temperature. Thus, the search for appropriate materials that show fast ion dynamics and vanishing electronic transport has driven the development of ionic conductors to an unprecedented level. In the following manuscripts ion dynamics of two Li-bearing sulfide-based solid electrolytes and one Na-ion conducting material are discussed in more detail. Before each manuscript is presented, a brief introduction containing the most important information on the material is provided.

6.3.1 Sulfide-based solid electrolytes

In addition to oxidic solid-state electrolytes, sulfide-based materials are considered as promising candidates for their use in all-solid-state batteries. Such sulfide-type compounds are preferable to oxides in terms of ionic conduction [228]. This can be explained by the larger size and better polarization ability of the sulfur anion in the framework. More specifically, the larger radius of S^{2-} leads to wider diffusion channels for the mobile ions in the crystal structure, while the higher polarizability weakens the interaction between the mobile species and the immobile skeleton framework resulting in a higher mobility of the lithium ions [229]. In fact, an ionic conductivity in the range of 10^{-3} S/cm was already reported in the early 80s for the LiI–Li_2S–P_2S_5 glass system [230]. Values of up to 1.2×10^{-2} S/cm were found in the thio-LISICON conductor $Li_{10}GeP_2S_{12}$ [177], which is on a par with that of liquid electrolytes.

Another merit of sulfide-based systems in contrast to oxidic solid electrolytes is their negligible grain boundary resistance. The high deformability of sulfide materials allows tight connection and dense packing of the electrolyte particles by conventional cold-pressing and low grain boundary resistances are even obtained in the cold-pressed pellets [191]. Usually, high-temperature sintering is applied to reduce this kind of resistance. The aforementioned mechanical feature is highly advantageous for the construction of solid-state batteries.

However, sulfur-type compounds also represent some difficulties. They react with moisture and are thus not stable at ambient atmosphere and some structures suffer from instability in contact with oxidic cathodes and metallic lithium.

Generally, sulfide-based solid electrolytes can be divided into three groups: glasses, glass-ceramics and ceramics. In the following, the glass-ceramic β-Li_3PS_4 and the crystalline ceramic $LiTi_2(PS_4)_3$ are discussed in more detail. The lithium ion dynamics of these two sulfidic compounds are studied in the manuscripts **P4** and **M3.**

β-Li_3PS_4

Among sulfide-based ionic conductors, the family of thiophosphates is of great interest owing to their high ionic conductivities combined with a high electrochemical stability window [175, 185]. In particular, Li_3PS_4 has attracted attention as it shows superior chemical stability in contact with metallic lithium[184] and a vanishable interfacial resistance when it is used as solid electrolyte in lithium batteries [231]. This compound crystallizes in a thio-LISICON framework structure, where the S^{2-} ions are hexagonally close-packed and the phosphorus cations are allocated to tetrahedral sites. The PS_4 tetrahedra are found in an isolated position to each other. Three temperature dependent modifications of this structure exist, namely α, β and γ-phase. The corresponding lithium-ion conductivity depends on the arrangement of the PS_4 tetrahedra, since they affect the position of the lithium ions in the framework and thus the preferred diffusion mechanism. It is known that the β-modification displays the highest Li diffusivity, especially when prepared in a nanoporous form [184].

In the β-modification of Li_3PS_4 the lithium ions can occupy three different sites 8*d*, 4*b* and 4*c*. While full occupation is found for the 8*d* position, the 4*b* and 4*c* sites are only partially occupied to 70 and 30 %, respectively. PS_4 and LiS_4 tetrahedra combined with LiS_6 octahedra form a three-dimensional skeleton structure. In more detail, in this network the PS_4 tetrahedra are linked with $Li_{4b}S_6$ octahedra via edges. These octahedra on the other hand share edges with each other forming a $(LiS_6)_\infty$ chain in one-dimension. Along this chain the $Li_{8d}S_4$ tetrahedra are connected via corner sharing and between one $Li_{4c}S_4$ tetrahedra and two $Li_{4b}S_6$ octahedra, one tetrahedral interstice can be found [187] (see Fig. 1 in **P4**). Recently, a low-dimension channel-like diffusion pathway has been proposed by Yang et al. to be mainly responsible for the rapid lithium ion dynamics in the β-form of Li_3PS_4.

In the following manuscript **P4**, the glass-ceramic β-Li_3PS_4 was prepared by joint high-energy ball-milling of Li_2S and P_2S_5 and subsequent heat-treatment at 160 °C. We used ^7Li NMR spin-lattice relaxation (SLR) measurements to experimentally test the presence of low-dimensional ionic transport in the β-modification. The diffusion-induced rate peaks obtained by SLR studies do not only provide information on dynamical parameters, but its shape is also affected by dimensionality effects. Especially the high-temperature flank of the rate peak measured as a function of frequency and temperature contains necessary information on the underlying dimensional nature of Li ion transport in the thiophosphate. Our results support the

theoretical considerations of low-dimensional migration processes in β-Li_3PS_4 involving regular and interstitial sites in the structure. The predicted snake-like 1D diffusion pathway occurs in addition to vacancy-mediated Li ion transport in three dimensions, but is energetically much more favorable.

P4:

Nuclear spin relaxation in nanocrystalline β-Li_3PS_4 reveals low-dimensional Li diffusion in an isotropic matrix

D. Prutsch, B. Gadermaier, H. Brandstätter, V. Pregartner, B. Stanje, D. Wohlmuth, V. Epp, D. Rettenwander, I. Hanzu, and H. M. R. Wilkening

Chem. Mater., (2018), in press

CHEMISTRY OF MATERIALS
Cite This: Chem. Mater. XXXX, XXX, XXX−XXX
Article
pubs.acs.org/cm

Nuclear Spin Relaxation in Nanocrystalline β-Li_3PS_4 Reveals Low-Dimensional Li Diffusion in an Isotropic Matrix

Denise Prutsch,[†] Bernhard Gadermaier,[†] Harald Brandstätter,[†] Veronika Pregartner,[†] Bernhard Stanje,[†] Dominik Wohlmuth,[†] Viktor Epp,[†] Daniel Rettenwander,[†] Ilie Hanzu,[†,‡] and H. Martin R. Wilkening*[,†,‡]

[†]Institute for Chemistry and Technology of Materials, and Christian-Doppler-Laboratory for Lithium Batteries, Graz University of Technology (NAWI Graz), Stremayrgasse 9, A-8010 Graz, Austria

[‡]Alistore - European Research Institute, CNRS FR3104, Hub de l'Energie, Rue Baudelocque, 80039 Amiens, France

Supporting Information

ABSTRACT: Lithium-containing thiophosphates represent promising ceramic electrolytes for all-solid-state batteries. The underlying principles that cause high Li^+ diffusivity are, however, still incompletely understood. Here, β-Li_3PS_4 served as a model compound to test the recently presented hypothesis that a channel-like Li^+ diffusion pathway influences ionic transport in its 3D network of the LiS_4, LiS_6, and PS_4 polyhedra. We looked at the temperature dependence of diffusion-induced ^{7}Li nuclear spin−lattice relaxation rates to check whether they reveal any diagnostic differences as compared to the nuclear spin response frequently found for isotropic (3D) diffusion. Indeed, distinct anomalies show up that can be understood if we consider the influence of low-dimensional diffusion. Hence, even for isotropic materials without clearly recognizable 1D or 2D diffusion pathways, such as layered or channel-structured materials, structurally hidden dimensionality effects might help explain high ionic conductivities and refine the design principles currently discussed. In the present case, such rapid pathways assist the ions to move through the crystal structure.

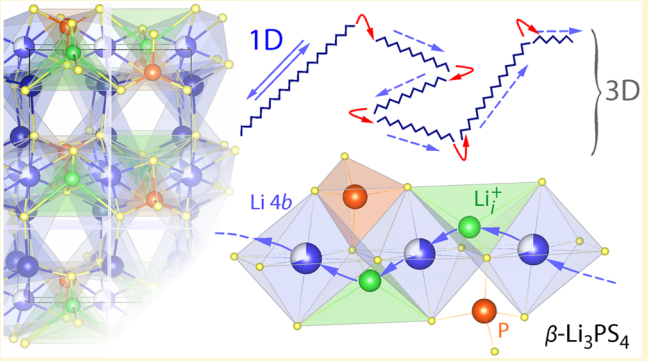

1. INTRODUCTION

Developing devices that can sustainably convert and store energy is one of the key issues of our time.[1] In order to cut our dependency on fossil fuels we need to make efficient use of renewable energy sources such as solar, wind, or tidal. As these are intermittent sources the storage of electrical energy is of utmost importance. Electrochemical energy storage systems represent at least a medium-term solution for this purpose.[1−6] The development of safe and long-lasting systems,[1] being free of environmentally harmful and flammable liquids, has also renewed the interest in ceramic electrolytes with outstanding diffusion properties.[7−12]

As far as lithium-ion conducting materials are considered, over the last couple of years really promising candidates to develop all-solid-state batteries have been presented in the literature.[8,10,13−18] For example, $Li_7La_3Zr_2O_{12}$-type compounds with garnet structure represent the most promising oxide materials.[19−21] In addition, Li-bearing phosphates, such as $Li_{1.5}Al_{0.5}Ti_{1.5}(PO_4)_3$, have been considered to act as powerful electrolytes.[22−25] Argyrodite-type Li_6PS_5X (X = Br, Cl)[16,17,26−28] shows extremely high Li^+ diffusivities and belongs to the large family of thiophosphates (see below). The same holds for $Li_7P_3S_{11}$,[18,29−31] $Li_{10}GeP_2S_{12}$,[14] and its recently studied variant $Li_{9.54}Si_{1.74}P_{1.44}S_{11.7}Cl_{0.3}$.[32] Exploring the principles behind rapid ion dynamics will be an ongoing research topic for years to come.[33] Model substances might be very useful to throw light and to understand at least parts of these general principles. Approaches from theory and experimental techniques, which work at the atomic scale to probe ion dynamics, are both needed to visualize the elementary steps of ion hopping.[34,35]

Considering battery applications as mentioned above, compounds of the family of thiophosphates[36] have attracted large interest to serve as solid electrolytes.[16−18,29,31,37−40] In particular, in 2013 Liu et al. stabilized the β form of Li_3PS_4 at room temperature by taking advantage of a nanoporous morphology.[41] Their study attracted great attention, also from a theoretical point of view,[42−44] as the ionic conductivity of the nanostructured form is reported to be 3 orders of magnitude higher than that of μm-sized, bulk Li_3PS_4.[45] Besides other thiophosphates and sulfides,[36] this high ionic conductivity makes nanostructured β-Li_3PS_4 a promising candidate for all-

Received: June 29, 2018
Revised: October 12, 2018
Published: October 12, 2018

Downloaded via TU GRAZ on November 6, 2018 at 12:36:32 (UTC).
See https://pubs.acs.org/sharingguidelines for options on how to legitimately share published articles.

© XXXX American Chemical Society

DOI: 10.1021/acs.chemmater.8b02753
Chem. Mater. XXXX, XXX, XXX−XXX

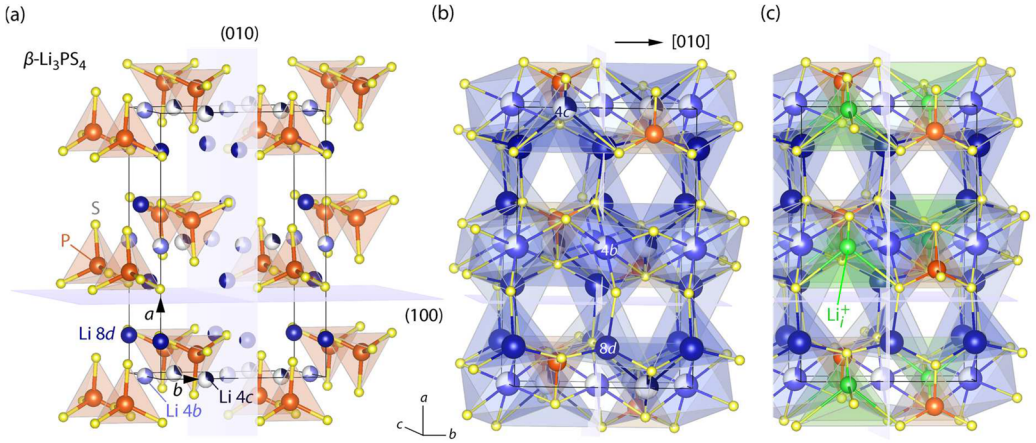

Figure 1. (a) Crystal structure of β-Li_3PS_4 (space group *Pnma*); the PS_4 tetrahedra are shown in orange. Li ions are allowed to occupy several positions labeled 8*d* (fully occupied), 4*b* (partly occupied, 70%) and 4*c* (occupied to only 30%). (b) The 3D network of the PS_4 tetrahedral and LiS_4, LiS_6 octahedra in β-Li_3PS_4. (c) Possible Li interstitial sites (green) located in the channels formed by the 3D skeleton shown in (b). According to Yang et al., interstitial Li ions Li_i at (0.94, 0.25, 0.72) may easily hop along the [010] direction involving the regular but partially occupied 4*b* positions. Li_i is located near the 4*c* site empty in (c). Partial occupation of 4*b* and 4*c*, i.e., Li_i, is expected to result in local structural disorder that is assumed to promote *quasi* 1D Li diffusion along the [010] direction. The corresponding activation energy calculated by Yang et al. is 0.18 eV. Li diffusion in all 3 directions is possible via a vacancy mechanism whose activation energy has been calculated to be 0.40 eV.

solid-state batteries. Relatively little information is, however, known about the underlying length-scale dependent ionic transport properties. Of course, the successful use of thiophosphates as solid electrolytes depends not only on exceptional transport properties but also on electrochemical stability and how it can be achieved. Apart from application-oriented interests, the crystal structures of Li-containing thiophosphates provide a rich playground for curiosity-driven fundamental studies on both Li^+ and Na^+ ionic transport.

Quite recently, Yang et al. studied both defect thermodynamics and Li^+ migration mechanisms in β-Li_3PS_4 and γ-Li_3PS_4 via first-principle calculations.[43] Interestingly, for both the γ and the β modification they report channel-like diffusion pathways. For β-Li_3PS_4, whose crystal structure is shown in Figure 1, the ions are guided along the [010] vector (see Figure 1b,c; also Figure S1 for a comparison of both the crystal structures of the γ and β form as well as their corresponding 1D diffusion pathways). The low-dimensional pathway in the β form of Li_3PS_4, which turned out to be energetically more favorable than other diffusion processes discussed for this modification,[43] attracted our attention. Only a few experimental methods are able to directly support such predictions from theory. Nuclear magnetic resonance (NMR), especially diffusion-induced spin−lattice relaxation (SLR), has been proven useful to differentiate between 3D and low-dimensional (2D or 1D) ionic transport[46−50] or in other words between highly anisotropic and isotropic transport. Most importantly, and in contrast to conductivity spectroscopy needing, for example, single crystals, the method is applicable to *powder* samples.[49,51−53] The underlying spectral density function, to which the NMR SLR rate R_1 is directly proportional, is different for 3D, 2D, and 1D diffusion and information on dimensionality effects can be extracted from relaxation rates measured as a function of both temperature and frequency.[46−50,52]

In recent years a number of layer-structured materials have been studied by NMR to reveal 2D diffusion.[54] In particular, the differentiation between 2D and 1D diffusion is nicely documented by the work of McDowell et al.[55] The use of time-domain NMR to identify, however, 1D diffusion in a crystalline matrix has rarely been documented. Except for the recent study by Blanc and co-workers[56] on Li diffusion in channel-structured $LiMgPO_4$-based phosphates, some investigations of β-eucryptite,[57,58] showing *quasi* 1D diffusion with the influence of interchannel hopping processes, and the work by some of us[59] on $Li_{12}Si_7$, there is, to our knowledge, no study available that clearly reveals hopping processes along 1D pathways through analyzing diffusion-induced, frequency- and temperature-dependent ^{7}Li nuclear spin-relaxation data. Of course, 1D Li^+ diffusion in small channels without vacant lattice sites can easily be blocked resulting in extremely slow, highly correlated dynamics.[60] To probe dimensionality effects in such cases we need NMR measurements at very high temperatures[56] to reach the so-called high-temperature flank of the corresponding diffusion induced relaxation peak. Only this flank contains the necessary information to decide whether diffusion is of low-dimensional nature.[54]

Here, we synthesized polycrystalline β-Li_3PS_4 and employed variable-temperature (and frequency dependent) ^{7}Li NMR (spin-lock) relaxation measurements[61−63] to experimentally test whether NMR provides enough evidence for the channel-like diffusion mechanism proposed. Indeed, an anomalous, so far, rarely observed,[59] nuclear relaxation behavior is seen by both laboratory-frame and rotating-frame SLR NMR. The temperature and frequency dependent observations point to low-dimensional pathways dominating the overall spin relaxation behavior at sufficiently high temperature *T*. Hence, ^{7}Li NMR SLR supports the idea proposed by both Yang et al.[43] and Lim et al.[44] Moreover, our spin-lock NMR rates measured in the low-*T* limit perfectly agree with activation energies from conductivity spectroscopy being sensitive to macroscopic, through-going Li^+ transport in the β-polymorph of Li_3PS_4.

2. EXPERIMENTAL SECTION

A series of samples of β-Li_3PS_4 were prepared by high-energy ball milling combined with a subsequent annealing step. Reagent-grade Li_2S (Alfa Aesar, 99.98%) and P_2S_5 (Alfa Aesar, 99%) in a molar ratio of 3:1 were used as starting materials. The mixture of these microcrystalline source materials was put in a grinding beaker made of ZrO_2 (Fritsch) equipped with 171 ZrO_2 milling balls (5 mm in

DOI: 10.1021/acs.chemmater.8b02753
Chem. Mater. XXXX, XXX, XXX−XXX

diameter). Mechanical treatment was carried out for 36 h at a rotation speed of 500 rpm using a high-energy planetary ball mill (Fritsch, Pulverisette 7). To avoid any contact with moisture and air, the airtight grinding beakers were filled and opened in a glovebox with dry argon atmosphere (concentration of water <0.1 ppm). To initiate crystallization of the milled powder, it was put in a glass tube, which was sealed under vacuum. Annealing temperatures ranged from 433 to 633 K. We kept the sample at elevated T for 17 h, and then it was allowed to slowly cool down to room temperature.

Differential scanning calorimetry (DSC) was performed using a Netzsch STA 409 differential scanning calorimeter coupled with a QMS 403C mass spectrometer. The as-prepared sample was sealed in an Al pan in a dry Ar-filled glovebox and DSC measurements were carried out under a constant He gas flow of 50 mL/min in the temperature range from 293 to 823 K; the heating rate was set to 10 K/min.

XRPD measurements were performed using a Bruker D8 Advance with CuK_α radiation. This was done in order to characterize the synthetic products and to identify all phases present, including determination of the symmetry and unit-cell dimension of the LPS. Data was collected between 15° and 80° 2θ. The pattern was evaluated by performing Rietveld refinement with the program X'Pert HighScore Plus v 3.0 (PANalytical).

Before carrying out conductivity and impedance measurements the samples were cold-pressed to obtain dense pellets by applying a uniaxial force of 10 kN using a cylindrical press set (10 mm in diameter). To ensure good electrical contact, Au electrodes with a thickness of approximately 100 nm were deposited on the pellets with a sputter coater (Leica EM SCD050). The pellets obtained were then put in an airtight cell and impedance measurements were carried out with a Novocontrol Concept 80 broadband analyzer connected to a BDS 1200 cell in combination with an active ZGS cell interface. This setup allows for temperature-variable two-electrode dielectric measurements. The temperature is automatically controlled with an accuracy of at least ±0.1 K by a QUATRO cryo-system (Novocontrol) using either a stream of heated nitrogen gas or a constant flow of cooled nitrogen in the cryostat. Impedances and permittivities were recorded at frequencies ranging from a few μHz up to 20 MHz in a temperature range from 150 to 570 K.

For the NMR measurements, the powder samples were sealed in a NMR glass tube (5 mm in diameter and 3 mm in length) under vacuum to protect them from air or moisture. ^{7}Li NMR spin−lattice relaxation experiments in both the laboratory as well as the rotating frame were performed with a Bruker Avance III spectrometer connected to a precisely shimmed cryo-magnet with a magnetic field of 7 T. This field strength corresponds to a ^{7}Li Larmor frequency of approximately $\omega_0/2\pi$ = 116 MHz. For the measurements at temperatures ranging from 263 to 533 K, a commercial ceramic high-temperature probe head (Bruker Biospin) was used. The $\pi/2$ pulse length was in the range of 2.6 to 4 μs at 200 W. The temperature was controlled and monitored with a Eurotherm unit connected to a type T thermocouple. Low temperature measurements down to 155 K were performed with a cryo probe head (Bruker) cooled with evaporated liquid nitrogen. This probe head allows $\pi/2$ pulse lengths of 4.5 μs at a power level of 90 W. Here, a LakeShore 331 element equipped with two Cernox sensors, one placed in the direct vicinity of the sample and the second one positioned in the cryostat, was used to monitor and control the temperature.

^{7}Li spin−lattice relaxation rates ($R_1 = 1/T_1$) were acquired with the well-known saturation recovery pulse sequence: $10 \times \pi/2 - t_d - \pi/2$ acquisition (acq.).[64,65] This sequence consisted of 10 initial 90° pulses that destroy any longitudinal magnetization M_z; its recovery is then recorded as a function of the relaxation delay t_d. To obtain $M_z(t_d)$ for each delay time, the area under the free induction decays is used. The transients $M_z(t_d)$ were then fitted with stretched exponentials to extract the SLR rates R_1. Stretching factors κ varied from from 0.9 to 1. To record the corresponding rotating frame NMR rates ($R_{1\rho} = 1/T_{1\rho}$) spin-lock measurements, utilizing the pulse sequence $\pi/2 - p_{lock}$ − acq.,[66] were performed at a locking frequency of 20 kHz.[65] The duration t_{lock} of the locking pulse p_{lock} was varied between 22 μs and 300 ms. To ensure full longitudinal relaxation the recycle delay was set to $5 \times T_1$. Again, the magnetization transients $M_\rho(t_{lock})$ were parametrized with stretched exponential functions with the stretching exponent κ_ρ ranging from 0.35 to 0.65 depending on temperature.

3. RESULTS AND DISCUSSION

Before presenting and discussing experimental results we briefly review some structural considerations of the two modifications of Li_3PS_4 with special emphasis on the β form of the thiophosphate. We orientate ourselves toward the very recent study by Yang et al., who studied the Li^+ mobility in Li_3PS_4 via first principle calculations.[43] In their study also the key similarities and differences of the two forms are discussed in detail.

γ-Li_3PS_4 crystallizes with the space group $Pnm2_1$. The sulfide ions are hexagonally closed packed and the PS_4 tetrahedra are connected to the LiS_4 tetrahedra by corner sharing a sulfur anion (the crystal structure is shown in Figure S1). In γ-Li_3PS_4 two crystallographically inequivalent Li sites (4b and 2a) exists. Yang et al. used first-principle calculations to shed light on the diffusion pathway. Importantly, the Li^+ diffusion pathways calculated also included a so-called *direct hopping* transport mechanism involving *interstitial* Li_i^+ sites in γ-Li_3PS_4 located at the fractional coordinates (0.25, 0, 0.68). Indeed, the Li_iS_6 octahedra along the [001] direction form a 3D skeleton structure in which the octahedra are connected by a triangular side plane. Li interstitials are proposed to directly hop along the channel formed (see Figures S1 and S2), the calculated activation energy is 0.16 eV. Hopping along the [100] direction would also lead to 1D diffusion; the activation energy turned out to be, however, much larger, viz., 0.6 eV.[43]

Quite interestingly, a similar situation was also found for the β modification of Li_3PS_4.[43] The migration of Li vacancies results in activation energies of 0.40 eV. Additionally, a channel-like zigzag diffusion pathway involving Li interstitial sites was found which is characterized by only 0.18 eV. Also, Lim et al. report on highly anisotropic Li diffusion with an activation energy of 0.19 eV along the b-axis.[44] This armchair-shaped diffusion pathway is depicted in Figure 2. According to Yang et al.[43] Li ions move from a regular 4b position located at (0, 0, 0.5) to an interstitial Li_i site (0.94, 0.25, 0.72). This site is close to the Li_{4c} position which was, according to experimental studies, reported to be occupied by 30%. Theoretical structure optimization, however, did not find evidence for the occupancy of the 4c void. Instead, the Li ions easily occupy this site as an interstitial one. To migrate along the [010] direction the Li_i ions take advantage of a *knockout* mechanism making use of regularly occupied 4b sites. The resulting snake-like 1D pathway is shown in Figure 2a. Interstitial Li_i ions are tetrahedrally coordinated by sulfur anions; the tetrahedra share common faces with the $Li_{4b}S_6$ octahedra. Thus, the bottleneck to diffuse along the [010] direction is given by the triangular face marked in Figure 2a. Obviously, this polyhedral connection is beneficial for Li hopping processes as the corresponding migration energy E_m turned out to be only 0.08 eV. A very similar geometry for Li diffusion has also been found experimentally for other Li ion conductors. A prominent example is Li_xTiS_2 ($0 < x \leq 1$), which is a pure 2D ionic conductor.[51] In β-Li_3PS_4 the channels formed by the $Li_{4b}S_6$ octahedra and the Li_iS_4 tetrahedra are isolated from each other (Figure 2). Interchannel diffusion, as is shown by calculations,[43] is only possible via a vacancy mechanism, being characterized by 0.4 eV. This pathway also

DOI: 10.1021/acs.chemmater.8b02753
Chem. Mater. XXXX, XXX, XXX−XXX

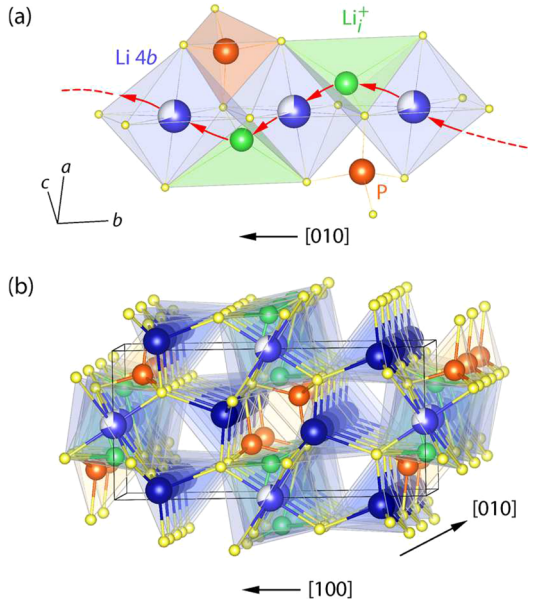

Figure 2. (a) One of the possible, but energetically favored, Li diffusion pathways in β-Li_3PS_4. Knock-off mechanism: Li interstitials are involved when Li ions jump between the 4*b* positions leading to a snake-like pathway. (b) View along the [010] direction to visualize the channel-structure of the diffusion pathway resulting in a zigzag hopping process. See Figure S2 for comparison with the situation in the γ modification.

involves the fully occupied 8*d* sites and would lead, in combination with the channel-like pathway, to 3D ion migration.[44]

To synthesize β-Li_3PS_4 and to test whether we see the channel-like pathway in ^{7}Li nuclear spin relaxation measurements we used a mechanochemical approach to prepare and stabilize the β form of Li_3PS_4 at room temperature. Ordinary high-temperature solid-state synthesis usually yields the γ modification, which transforms into the β form at temperatures larger than 550 K; see the *in situ* X-ray study by Homma et al.[45] As revealed by X-ray diffraction directly carried out after the milling process, an amorphous material with high ionic conductivity is obtained. We systematically annealed this amorphous educt to convert it into nanocrystalline β-Li_3PS_4. In Figure 3 the XRD patterns of the annealed samples are shown. Figure 3a presents the Rietveld refinement of the nanostructured sample that has softly been annealed at 260 °C. Rietveld refinement (R_w = 2.89, goodness of fit: 2.37) points to orthorhombic symmetry (*Pnma*, No. 62; see the entry in the ICSD, no. 35018) and is in line with previous reports.[45] Only a minor amount of an unidentified extra phase is present as indicated by the reflection with low intensity at 2θ = 32.5°. Due to the low signal-to-noise ratio and the interfering background signal, no quantitative structural refinement was carried out. Nevertheless, the unit cell lattice parameter can be calculated precisely without knowing the exact structural factors. The values for *a*, *b*, and *c* are 12.882(2) Å, 8.106(2), and 6.132(1), respectively, in good agreement with results of Homma et al. (*a* = 12.8190(5) Å, *b* = 8.2195(4)Å, *c* = 6.1236(2)).[45] For the sample annealed at 260 °C, which was studied by NMR, the mean crystallite size estimated via broadening of the X-ray reflections is approximately 20 nm.

Ion transport of all samples was investigated by conductivity spectroscopy; see Figure 4 that shows σ_{dc}T vs the inverse temperature in an Arrhenius plot. σ_{dc} refers to the so-called direct current (dc) electrical conductivity that was read off from the corresponding isotherms (see Figure 5), in the low frequency limit. σ_{dc} characterizes the plateaus seen in the conductivity isotherms; at very low frequencies ν electrode polarization effects show up originating from the ion-blocking electrodes used to acquire the spectra. From Figure 4a we can see that, interestingly, the X-ray amorphous mixture of Li_2S and P_2S_5, which was directly obtained after high-energy balling, shows the highest conductivity. To clarify the origin of the high ionic conductivity in this Li_2S:P_2S_5 composite further investigations are needed. Such experiments are out of the scope of the present contribution which focuses on nanocrystalline Li_3PS_4. Most likely, space charge regions and interfacial effects promote Li ion transport in nanostructured Li_2S when in contact with P_2S_5 acting as an ionic insulator. Such effects have been observed earlier for oxide two-phase

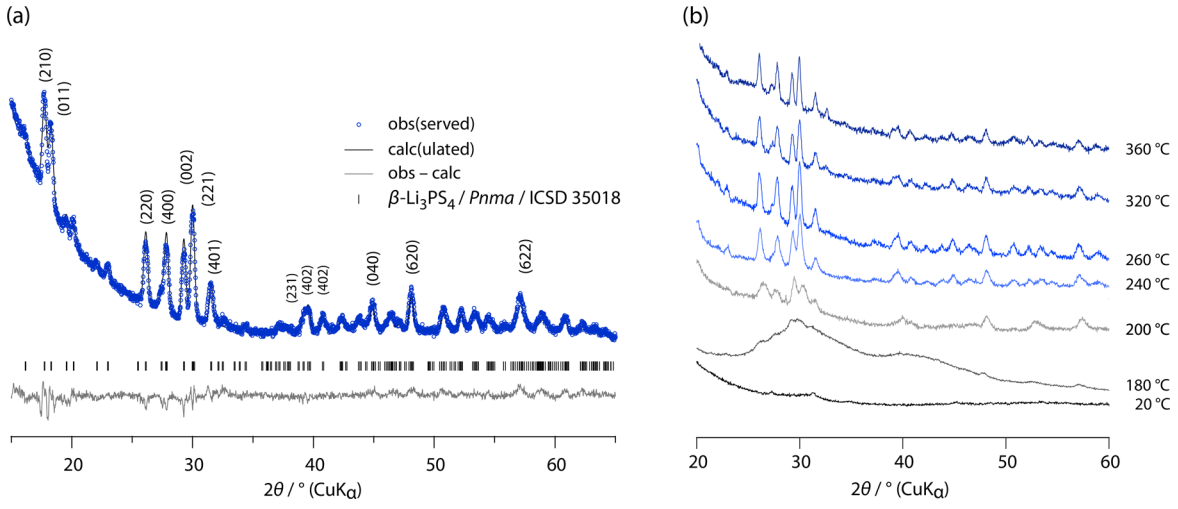

Figure 3. (a) Rietveld analysis and X-ray powder diffraction pattern of nanocrystalline Li_3PS_4 crystallizing with space group *Pnma*. Selected reflections have been indexed. (b) Evolution of nanocrystalline β-Li_3PS_4 with increasing annealing temperature; at the bottom the XRD pattern of the sample directly after milling is shown, which was not annealed. The patterns stacked above refer to the annealed samples with the annealing temperatures indicated. At 180 °C a glassy phase is formed which, above 200 °C, transforms into nanocrystalline β-Li_3PS_4.

DOI: 10.1021/acs.chemmater.8b02753
Chem. Mater. XXXX, XXX, XXX−XXX

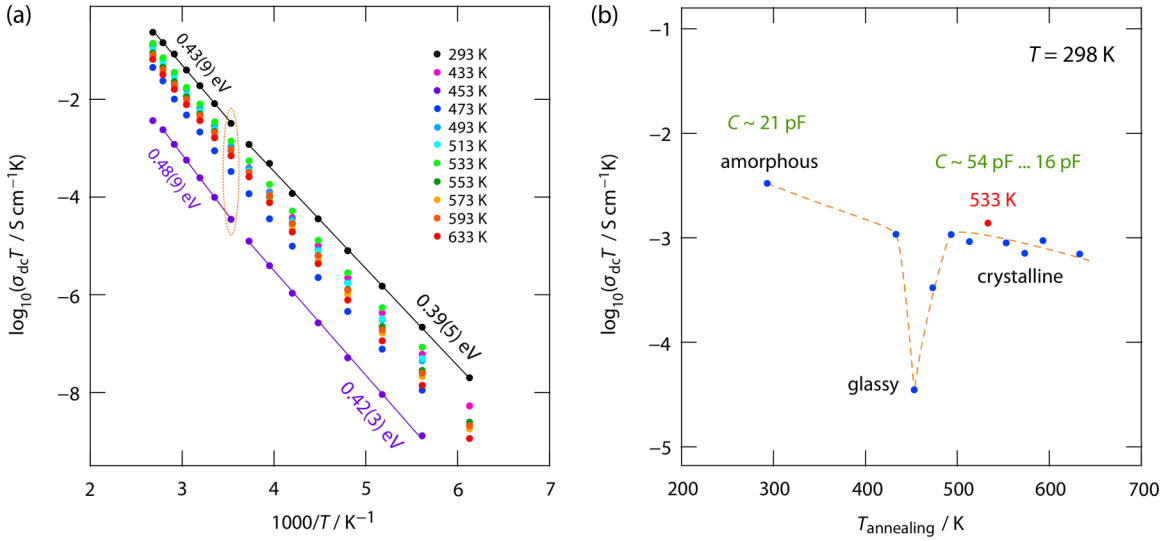

Figure 4. (a) Change of the ionic conductivity of samples with the composition Li_3PS_4 obtained either directly after milling (293 K) or after the annealing step carried out at the temperatures T_a indicated (433 to 633 K). Below 293 K, the activation energy, being independent of the annealing conditions, turned out to be approximately 0.4 eV. Above 293 K the activation energy slightly increases; this behavior is also seen for the sample annealed at 533 K (see Figure 5b). (b) Evolution of the room-temperature ionic conductivity of the samples shown on the right as a function of T_a.

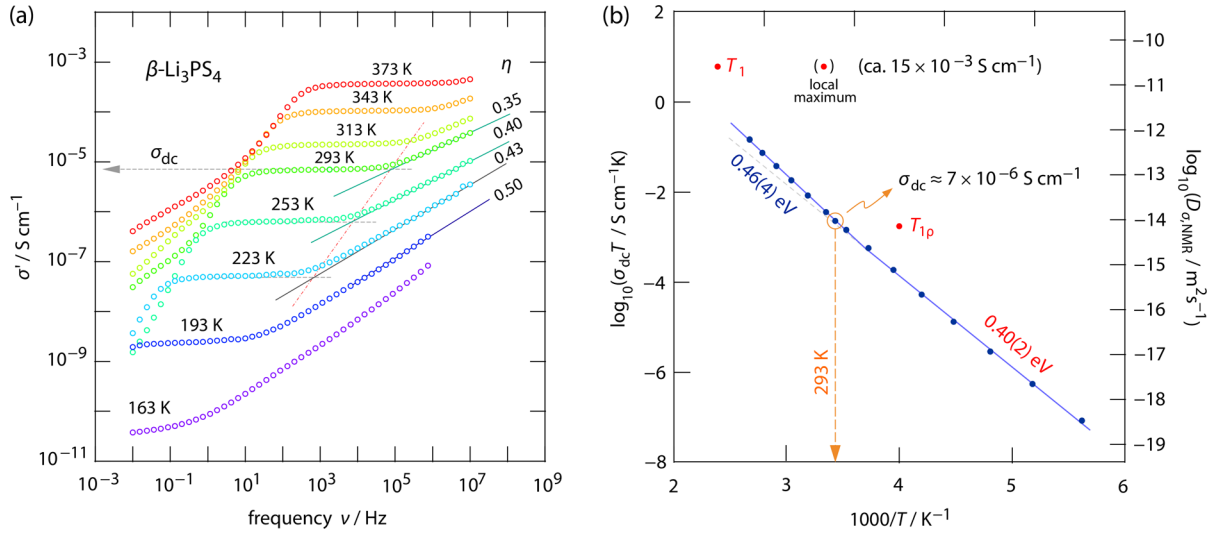

Figure 5. (a) Conductivity isotherms of nanocrystalline β-Li_3PS_4, which has been prepared by high-energy ball milling and subsequent annealing at 533 K. The isotherms can be subdivided into 3 regimes. At low frequencies, electrode polarization dominates the response. This response merges into distinct dc plateaus from which σ_{dc} can easily be determined. In the high-frequency regime the dispersive parts show up, which are characterized by relatively small Jonscher exponents. Values well below 0.6 point to the influence of low-dimensional effects on ion dynamics. Dashed lines mark the crossover from $\sigma_{dc} \neq f(\nu)$ to $\sigma'(\nu)$. (b) Change of σ_{dc}, plotted as $\sigma_{dc}T$, vs the inverse temperature. Below 293 K the activation energy is given by 0.40 eV. Above 293 K it slightly increases reaching a value of 0.46 eV.

nanocomposites such as Li_2O:X_2O_3 (X = Al, B)[67−69] and $LiBH_4$:Al_2O_3.[50]

Annealing the ball milled Li_2S:P_2S_5 sample first leads to a decrease in ionic conductivity. Presumably, a glassy phase is obtained at annealing temperatures as low as 160 °C. The sample prepared in that way is characterized by the lowest conductivity. Increasing the annealing temperature, i.e., initializing crystallization, causes the ionic conductivity to increase by 2 orders of magnitude reaching almost the initial value of the material before heat treatment.

The change in conductivity at 298 K is shown in Figure 5b. Solid lines in Figure 5a show fits with an Arrhenius law. Slightly above ambient temperature, we see a minor change in slope leading to an increase of the activation energy from ca. E_a = 0.40 eV (T < 298 K) to E_a = 0.46 eV (T > 298 K). This feature is similar for all samples; the sample annealed at 533 K has been chosen for our NMR investigation as it revealed the highest conductivity of the samples prepared. Activation energies on the order of 0.4 eV are in good agreement with those obtained from earlier impedance studies on coarse-grained samples presented in the literature.[70] Electrical capacities C of the conductivity response probed here range from 16 to 54 pF, thus pointing to a bulk or an interfacial response that is probed by conductivity spectroscopy. Capacities have been estimated via complex plane representations of the impedance data. Here we obtained depressed semicircles and estimated C according to the condition $\omega_{max}RC$

DOI: 10.1021/acs.chemmater.8b02753
Chem. Mater. XXXX, XXX, XXX−XXX

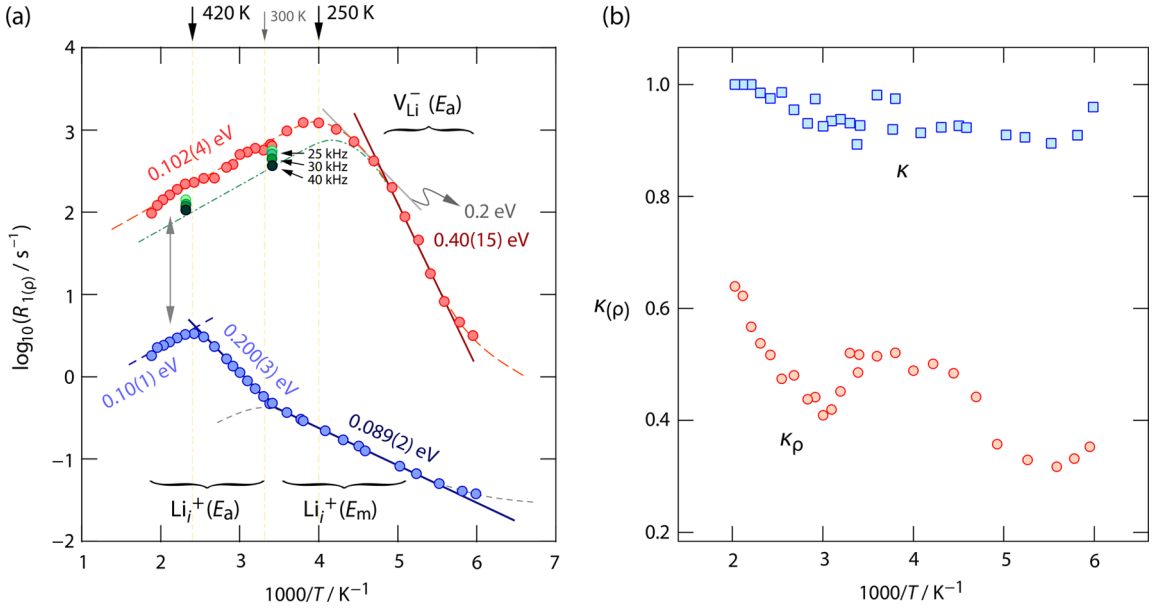

Figure 6. (a) Temperature dependence of the diffusion-induced ^{7}Li NMR spin−lattice relaxation rates of nanocrystalline β-Li_3PS_4. R_1, measured at $\omega_0/2\pi$ = 116 MHz, refers to the rates measured in the laboratory frame of reference, $R_{1\rho}$ reflects the rates that have been recorded in the rotating frame of reference at a locking frequency of $\omega_1/2\pi$ = 20 kHz. $R_{1\rho}$ rates shown at T = 420 and 293 K, respectively, have been measured at locking frequencies of 20, 25, 30, and 40 kHz. The frequency dependence in the limit $\omega_1\tau_c \ll 1$ points to 1D diffusion. 1D diffusion is also in agreement with the large gap seen between R_1 and $R_{1\rho}$ above 440 K. It is indicated by the vertically drawn arrow. The observation that $E_{a,\ high\text{-}T}(R_1)$ on the high-T flank is given by $E_{a,\ low\text{-}T}(R_1)/2$ further supports the influence of a low-dimensional diffusion pathway on Li^+ diffusion in the β form of Li_3PS_4. Values given in eV denote activation energies E_a obtained by using linear fits to analyze the temperature dependence of the different regions the $R_{1(\rho)}$ rates pass through. In the spirit of Yang et al., curly brackets mark the charge carrier and the associated activation energy anticipated to be responsible for longitudinal (R_1) and transversal ($R_{1\rho}$) ^{7}Li NMR relaxation; see text for further discussion. (b) Stretching exponents used to parametrize the magnetization transients to extract the rates R_1 and $R_{1\rho}$, respectively.

= 1 with ω_{max} being the apex frequency and R the resistance in the limit $\omega/2\pi \rightarrow 0$, i.e., in the dc regime.

Before comparing conductivity data with results from diffusion-induced ^{7}Li NMR spin−lattice relaxation measurements, we should have a closer look at the shape of the conductivity isotherms $\sigma'(\nu)$ presented in Figure 5a. Usually the dc plateau passes into a dispersive, i.e., frequency dependent regime. In many cases, especially for disordered materials, $\sigma'(\nu)$ follows a Jonscher power law[71] dependence, $\sigma'(\nu) \propto \nu^p$; the exponent p takes values from 0.7 to 0.85 if 3D correlated diffusion governs overall ion transport.[72] Correlated motion is frequently explained as being caused by the presence of both (*i*) Coulomb interactions of the moving particles and (*ii*) structural disorder.[73−75] In a broader sense structural disorder means a heterogeneous potential landscape the ions are exposed to. Such a landscape could be the consequence of a partly filled Li sublattice with several energetically nonequivalent positions, as is the case here. In particular, values for p ranging from 0.35 to 0.55 have been interpreted in terms of low dimensional diffusion.[76] The lowest exponents are expected for 1D diffusion.[76,77]

Indeed, in the present case we see that the Jonscher exponents p in the dispersive region adopts relatively low values (0.35 to 0.43). Keep in mind that at even lower T, nearly constant loss (NCL) effects[78,79] might increasingly affect p. p_{NCL} = 1 is expected for this case. Only at sufficiently high T the NCL-free dispersive region should be used to analyze the spectra in terms of dimensionality effects. Here, values below 0.5 (see Figure 5a) are a first indication that, on a shorter length scale than probed by σ_{dc}, diffusion processes are at work being of low dimensional nature. This assumption is not in contradiction with the statement that σ_{dc} is affected by 3D motions as it senses long-range transport through the anion network of Li_3PS_4. $\sigma'(\nu)$, on the other hand, is sensitive to fast, short-ranged electrical fluctuations which might, to a certain degree, be spatially restricted. To decide whether σ_{dc} is to a larger extent also influenced by low dimensional diffusion, we used ^{7}Li nuclear spin−lattice relaxation (see Figure 6) to probe the Li^+ diffusive motions in the limit $\omega_{0(1)}\tau_c \ll 1$.

In this regime, the NMR motional correlation rate τ_c^{-1} is much larger than the Larmor (ω_0) or locking frequency (ω_1) used to sample the corresponding relaxation rates R_1 and $R_{1\rho}$. Provided $\omega_{0(1)}\tau_c \ll 1$ is valid, during one Larmor precession a series of consecutive Li^+ hopping processes take place. The NMR spin−lattice relaxation response in this so-called high-T limit of the diffusion-induced relaxation rate peak $R_{1(\rho)}(1/T)$ is usually identified as the regime that contains information on *long-range* motions.[61,80] The low-T side of such a peak is, at least in the case of R_1, affected by local or short-range Li^+ hopping processes, which also include unsuccessful forward−backward jumps.[80] The diffusion induced ^{7}Li NMR rates R_1 and $R_{1\rho}$ of nanocrystalline β-Li_3PS_4 are shown in the Arrhenius plot of Figure 6a. In Figure 6b the stretching exponents $\kappa_{(\rho)}$ are shown that determine the shape of the transients as a function of temperature.

Starting our discussion with R_1, at very low temperatures we expect the rate R_1 to be induced by so-called nondiffusive effects which depend on temperature only weakly, at least weaker than expected for thermally activated jump processes. In many cases this contribution is driven by coupling of the spins with paramagnetic impurities or phonons.[81] Above 170 K we notice that the rate, i.e., $\log_{10}(R_1)$, linearly increases with

DOI: 10.1021/acs.chemmater.8b02753
Chem. Mater. XXXX, XXX, XXX−XXX

temperature up to T = 300 K. The flank resembles that which is also seen for highly conducting garnet-type oxides.[20] The slope corresponds to an activation energy of only 0.089(2) eV. Most likely, the flank, observable over a rather broad temperature range of ΔT = 124 K, points to very fast localized ion hopping processes on the angstrom length scale. Forward−backward jumps and within-site motions may contribute to the NMR spin−lattice relaxation in this temperature range as well. Remarkably, a value of 0.089 eV is very similar to the diffusion energy barrier E_m = 0.08 eV calculated by Yang et al. for the 1D diffusion pathway along [010].[43] The activation barrier for ion transport along this pathway turned out to be 0.18 eV[43] (0.19 eV[44]) (see also Figure 1c).

Above T = 300 K the rate R_1 follows an Arrhenius line that is characterized by 0.20 eV; a similar value has recently been probed by Stöffler et al. but for coarse-grained Li_3PS_4.[82] The change in slope from 0.089 to 0.02 eV might indicate that above 300 K an additional diffusion process comes into play. The additional formation of Li_i interstitials with a formation energy E_f of 0.1 eV, leading to $E_a = E_m + E_f$ = 0.18 eV, could also explain the increase in slope. Finally, R_1 passes through a maximum at $T_{max}(R_1)$ = 420 K. At this temperature, almost independent of any relaxation model, the corresponding motional correlation time τ_c, which is within a factor of 2 identical with the Li^+ jump rate,[53] can be estimated via the relation $\omega_0\tau_c \approx 1$.[61,62] With $\omega_0/2\pi$ = 116 MHz we obtain $\tau_c = 1.37 \times 10^{-9}$ s, i.e., the residence time between two consecutive Li jumps is approximately 1.4 ns. Using a jump distance a of 2.45 Å, which is the distance between Li_i and Li(4a), the Einstein−Smoluchowski equation for 1D diffusion, $D = a^2/(2\tau)$, yields 2.2×10^{-11} m^2 s^{-1}.

Because of the superposition of two distinctly activated diffusion processes we cannot determine the temperature at which the rate R_1, when coming from the low-T regime characterized by ca. 0.089 eV, would pass through its maximum. Such a rate peak is expected at $T \geq 300$ K as indicated in Figure 6a by the dashed line serving to guide the eye. Depending on the effective jump distance, a very similar diffusion coefficient D as one can estimate for the main would be obtained but, of course, for a considerably lower temperature (see Figure 6b). D_{NMR}(420 K) = 2.2×10^{-11} m^2 s^{-1} is larger by a factor of 10 when comparing it with results from macroscopic conductivity measurements. It would correspond to a conductivity in the order of several mS/cm. The difference is clearly seen when we use the Nernst−Einstein equation, $D_\sigma = \sigma_{dc}k_BT/(Nq^2)$, to convert σ_{dc} into diffusion coefficients (see right axis of Figure 6b). Here k_B denotes Boltzmann's constant and q is the charge of the Li^+ ions; the charge carrier density was estimated to be on the order of 10^{28} m^{-3}. Worth mentioning, D_σ at 373 K (5.6×10^{-13} m^2 s^{-1}) is in perfect agreement with the diffusion coefficient derived from the pulsed field gradient (PFG) NMR carried out by Greenbaum and co-workers on nanostructured β-Li_3PS_4.[83] At 373 K they obtained a macroscopic (tracer) diffusion coefficient of $D_{PFG} = 5.4 \times 10^{-13}$ m^2 s^{-1}. Obviously, in contrast to macroscopic techniques such as conductivity spectroscopy and PFG NMR, being sensitive to through-going ion transport, spin−lattice relaxation NMR is primarily driven by very fast Li^+ spin fluctuations in β-Li_3PS_4. The latter represents only a part of the total dynamic processes being responsible for macroscopic 3D ionic conduction. Overall ion transport is expected to be limited by (slower) vacancy-type jump processes involving the Li 8d sites (see below), as well as ion-blocking grain boundaries. For soft sulfides the interfacial regions are expected to be much less blocking than for oxides. In general, the difference between D_{NMR} and D_σ has been the subject of many studies.[79,84,85] In general, the two coefficients are related to each other by $D_{NMR} = (H_r/f)\, D_\sigma$ with the Haven ratio H_r and the f ($0 < f \leq 1$) is the correlation factor that connects the macroscopic tracer diffusion coefficient with the one derived by Einstein and Smoluchowski.[61,86]

Going back to the main $R_1(1/T)$ peak showing up at 420 K (Figure 6a) we assume that it reflects zigzag Li ion diffusion as depicted in Figure 2a. The reason for this interpretation is the following. For 3D uncorrelated motion a symmetric rate peak is expected while for 3D correlated motion asymmetric peaks are obtained with the low-T flank being characterized by a lower slope than that seen on the high-T side.[53] In such a case $E_{a,\,low}$ yields an *apparent* activation energy influenced by correlation effects and short-range motions. Instead, $E_{a,\,high}$ represents long-range motion and is unaffected by correlation effects. Only for uncorrelated diffusion we have $E_{a,\,low} = E_{a,\,high}$. Phenomenologically, such correlation effects are taken into account by the parameter β in the following BPP-based[87,88] Lorentzian-type spectral density function J_{3D}:$J_{3D}(\omega_0) \propto \tau_c/(1 + (\omega_0\tau_c)^\beta)$.[49] $J(\omega_0)$ is the Fourier transform of the autocorrelation function $G(t)$ describing the incoherent diffusive motion in a solid.

In the case of uncorrelated but low-dimensional, i.e., 1D or 2D, diffusion the situation of peak asymmetry is reversed. Low dimensional ion transport affects the R_1 rates in the $\omega_0\tau_c \ll 1$ limit, i.e., in the high-T regime.[89] In some cases, the deviation from 3D behavior in this limit is rather small, thus hindering a clear-cut identification of low-dimensional effects. According to the semiempirical relaxation models first introduced by Richards and Salamon,[90] the following relationships are helpful to differentiate 1D and 2D diffusion from 3D motional processes: $E_{a,\,2D} = 0.75\, E_{a,\,3D}$ and $E_{a,\,1D} = 0.5\, E_{a,\,3D}$. To use these relationships $E_{a,\,3D}$, which is the activation energy for uncorrelated motion, needs to be known. It is only obtainable from the low-T side of the same given peak if $\beta = 2$. If $\beta < 2$, i.e., in the presence of correlated, low-dimensional diffusion, both the high-T side and the low-T side of $R_1(1/T)$ will show deviations from simple 3D behavior. In such a case, which could be the common one, *quasi* symmetric peaks can be obtained from which no conclusion about dimensionality effects can be drawn.[49] In these cases the diagnostic asymmetry for low-dimensional diffusion is simply masked. To judge whether the 1D or 2D diffusion is present we need to analyze the *frequency* dependence of the diffusion induced rate R_1 in the limit $\omega_0\tau_c \ll 1$. Semiempirical models help discriminate 1D and 2D diffusion from 3D transport. While for 3D diffusion R_1 is expected to be independent of ω_0 in the limit $\omega_0\tau_c \ll 1$, for 2D diffusion the following spectral density functions for uncorrelated motion has been introduced.[91] J_{2D} is given by $J_{2D} \propto \tau_c \ln(1 + 1/(\omega_0\tau_c)^2)$,[46,47] while for J_{1D} no sound empirical expression has been introduced so far. However, the limiting cases for 1D diffusion are known. Whereas for 2D uncorrelated diffusion a logarithmic frequency dependence $R_1 \propto -\tau_c \ln(\omega_0\tau_c)$ is obtained[89−91] in the regime $\omega_0\tau_c \ll 1$, for 1D (uncorrelated) diffusion we would expect a $\omega_0^{-0.5}$ dependence[92] of the rates R_1 on the high-T side of the $R_1(1/T)$ peak.[59]

In our case, see the main R_1 peak in Figure 6a with its maximum at T_{max} = 420 K, we definitely see that $E_{a,\,high}$ takes half the value that is seen in the range $\omega_0\tau_c \gg 1$, i.e., on the

DOI: 10.1021/acs.chemmater.8b02753
Chem. Mater. XXXX, XXX, XXX−XXX

low-T flank. If we identify the activation energy $E_{a,\,low}$ of the low-T side of the peak with that for uncorrelated motion ($E_{a,\,low} = E_{a,\,3D}$, see above) the ratio of the values $E_{a,\,high}/E_{a,\,low}$ = (0.1/0.2) eV = 0.5 strongly points to 1D channel-like diffusion. Most importantly, $E_{a,\,high}$ = 0.1 eV is also seen in spin-lock NMR (Figure 6a) for which we used angular locking frequencies in the order of ω_0 = 125 kHz.

In the regime $\omega_1\tau_c \ll 1$ and at sufficiently high T also spin-lock NMR would be sensitive to similar Li^+ exchange processes as R_1 does, thus, being able to see the same characteristic features. This similarity is, however, in contrast to what is seen in the limit $\omega_1\tau_c \gg 1$, i.e., on the right-hand side of the $R_{1\rho}(1/T)$. Only near the $R_{1\rho}(1/T)$ maximum the rates indicate that they follow a line corresponding to 0.2 eV. Below 210 K they definitely show a steeper-than-expected decrease with decreasing temperature; a similar difference between $E_{a,\,low}$ from R_1 and $R_{1\rho}$ has recently been seen for channel-structured LiB_3S_5.[60] Here, in the temperature region below 210 K, spin-lock measurements probe Li^+ motions that are characterized by an activation energy of 0.40 eV (see Figure 6a). This value is strikingly similar to that seen by conductivity spectroscopy in the dc regime. In the limit $\omega_1\tau_c \gg 1$ the motional correlation rate τ_c^{-1} is expected to me much lower than 1.25×10^5 s^{-1} and would correspond to nonangular frequencies lower than 2×10^4 Hz. This upper frequency limit marks the end of the dc plateau in the conductivity isotherms recorded at 293 K and below (Figure 5a). Hence, $\sigma_{dc}(T \leq 293\ K)$ probes ionic motions on the same time scale than $R_{1\rho}$ does. Here, we identify the motional process activated with 0.40 eV, seen at ca. T < 250 K by both methods, as the one that describes long-range ion transport in the bulk regions of β-Li_3PS_4. A very similar value (0.42 eV) is obtained if we analyze the crossover from the dc regimes to the dispersive regimes; the corresponding electrical relaxation frequencies ν_c refer to $\sigma'(\nu) = 2\sigma_{dc}$. As suggested by Marple et al., ν_c (located near the σ_{dc} plateaus) might, in some cases, sense the same transport properties as σ_{dc} does.[93] For comparison, the same activation energy (0.40 eV), as derived from NMR here, has been calculated by Yang et al. to describe Li ion hopping via the vacancy diffusion mechanism.[43]

As mentioned above, the low slope in the limit $\omega_1\tau_c \ll 1$ (and $\omega_0\tau_c \ll 1$) which yields $E_{a,\,high}/E_{a,\,low}$ = 0.5 strongly points to an (uncorrelated) 1D motional process. To underpin this view, we measured $R_{1\rho}$ not only at $\omega_1/2\pi$ = 20 kHz but varied the spin-lock frequency. Results for T = 433 K and T = 293 K are included in Figure 6a. As expected for low-dimensional effects on spin–lattice relaxation in the limit $\omega_1\tau_c \ll 1$, the rates $R_{1\rho}$ decrease with increasing locking frequency (see Figure 7). The dashed-dotted line in Figure 6a indicates the position expected for the same diffusion-induced rate peak $R_{1\rho}(1/T)$ recorded, however, at 40 kHz instead of 20 kHz. Plotting $R_{1\rho}$ as a function of frequency reveals that the rates agree with a logarithmic dependence as it is expected for 1D diffusion (Figure 7). The same dependence is found for the $R_{1\rho}$ rates recorded at T = 468 K; the rates are also in fair agreement with the respective R_1 rate measured at 166 MHz and 468 K (see Figure S3). These observations further supports our idea that the Li ions are involved in rapid 1D, snake-like motions as depicted in Figure 2a. NMR spectroscopy shows that these chain-like pathways are interconnected to enable the Li^+ to use vacant 8a Li sites to move over long distances. Macroscopic ion transport is, if we consider temperatures lower than 300 K, probed by σ_{dc} at frequencies lower than $\nu = 10^4$ Hz.

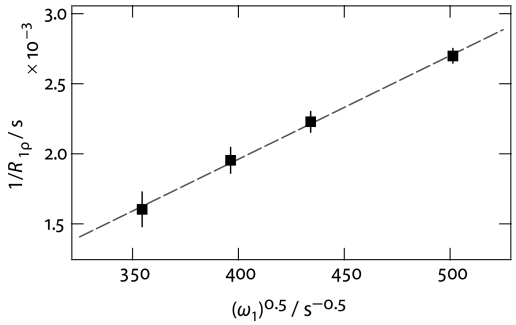

Figure 7. ^{7}Li NMR spin–lattice relaxation times $1/R_{1\rho}$ (295 K) of β-Li_3PS_4 measured in the rotating frame of reference as a function of the square root of the locking frequency applied. Diffusion-induced rates in the limit $\omega_1\tau_c \gg 1$ were measured at locking frequencies $\nu_1 = \omega_1/2\pi$ of 20, 25, 30, and 40 kHz. For 1D diffusion $1/R_1$ but also $1/R_{1\rho}$ should linearly increase with increasing $\omega_1^{0.5}$.

The frequency dependence seen and the ratio of $E_{a,\,high}/E_{a,\,low}$ = 0.5 probed reflects uncorrelated Li^+ motion. As mentioned above, for spatially restricted 1D diffusion one usually expects a highly correlated dynamics which may suffer from trapping effects[43] or blockades by foreign atoms.[60] In the present case, however, the [010] zigzag pathway uses Li interstitials and partly filled Li sites, a situation which is similar to the 1D process in the Zintl-phase $Li_{12}Si_7$ where stacked Si_5-rings guide the ions along a *quasi* linear pathway with many empty Li sites.[59] Obviously, this feature produces the signature of uncorrelated motion in diffusion-controlled ^{7}Li NMR spin–lattice relaxation.

Finally, we also estimated $D_{NMR\rho}$ at the temperature where $R_{1\rho}(1/T)$ shows its maximum. At 250 K we obtain $D_{NMR\rho} = 7.5 \times 10^{-15}$ m^2 s^{-1} which would correspond a Li ion conductivity of ca. 5×10^{-6} S cm^{-1}. Only the (local) shallow R_1 maximum assumed at 300 K, as discussed above, would point to extraordinary conductivities in the mS regime (see Figure 5b).

^{7}Li NMR spectra, when considering their shapes and widths that change with temperature, add further information to the dynamic processes in β-Li_3PS_4. In general, the line shape is sensitive to motions with τ_c^{-1} on the order of the width of the NMR line or powder pattern, i.e., the anisotropy of the spin interaction originating from interactions with other spins or the environment. In the absence of sufficiently fast Li translational motion a so-called rigid lattice line is observed. For instance, averaging of homonuclear dipolar coupling through rapid exchange processes causes the ^{7}Li NMR central line to narrow with increasing temperature. For τ_c^{-1} being much larger than the order of the nuclear spin interaction the regime of extreme narrowing is observed and no further change of the ^{7}Li NMR central line is expected. Spectra and the motional narrowing curve of β-Li_3PS_4 are shown in Figure 8.

In the rigid-lattice regime an electric quadrupole foot is visible that is superimposed by the central line. The Gaussian shaped electric quadrupole intensities indicate a coupling constant of 25 kHz if we assume an axially symmetric electric field gradient. Close inspection of the central line reveals that the line heterogeneously narrows indicating more than one diffusion process being relevant for Li ion transport in the thiophosphate. For example, the line recorded at T = 199 K is composed of a broad Gaussian-shaped line and a narrow Lorentzian one on top (see the horizontal arrows in Figure 8a).

The motional narrowing curve of β-Li_3PS_4 (Figure 8b) supports fast Li ion exchange processes able to fully average

DOI: 10.1021/acs.chemmater.8b02753
Chem. Mater. XXXX, XXX, XXX–XXX

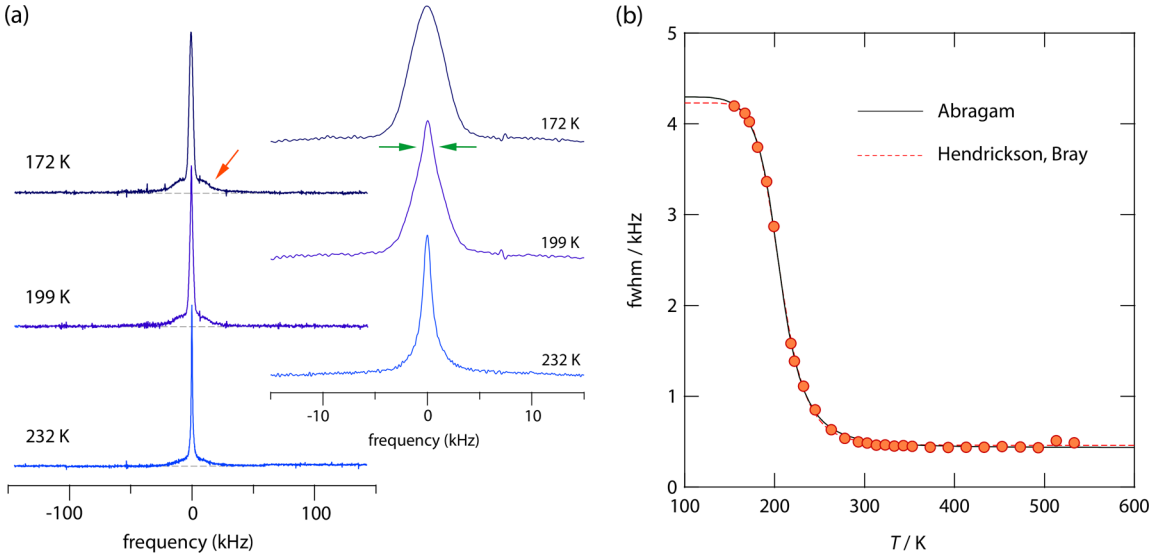

Figure 8. (a) ^{7}Li (spin-quantum number $I = 1/2$) NMR spectra of nanocrystalline β-Li_3PS_4 recorded at the temperatures indicated. The spectrum measured at 172 K represents the NMR response of the rigid lattice regime. It is composed of a central line and quadrupole intensities reflected by a broad Gaussian line. The full width of the latter points to a quadrupole coupling constant C_q of 25 kHz. With increasing temperature, both magnetic dipolar and electric quadrupolar interactions are averaged. At 300 K the quadrupole interactions are averaged as τ_c^{-1} is by many times larger than $C_q \times 2\pi$. The inset illustrates the shapes of the central lines. At 199 K we see a tapering line indicating a narrow line on top of a broader one. Most likely, the ions have access to various diffusion processes. The 1D process is assumed to represent the fastest one in β-Li_3PS_4 able to average Li interactions on 4*a* (4*c*) via interstitial hopping. (b) Motional narrowing curve constructed by reading off the full width at half-maximum (fwhm) of the central lines of the ^{7}Li NMR spectra. The lines show fits with either the Abragam formalism or the estimation procedure introduced by Hendrickson and Bray. See text for further discussion.

homonuclear dipole−dipole interactions at $T = 300$ K. At this temperature $R_{1\rho}$ tells us that τ_c^{-1} is, according to $\omega_1\tau_c = 0.5$ being valid at the peak maximum, on the order of 2.5×10^5 s^{-1}. This correlation rate clearly exceeds the rigid-lattice line width of ca. 4 kHz, i.e., it is able to completely average the spin−spin interactions. For comparison, the curves of a moderate ion conductor and a poor ion conductor are also shown in Figure 8. Extracting quantitative information from narrowing curves is fraught with difficulties as one would need a model precisely reflecting the averaging process. The model introduced by Abragam[94] on the one hand and Hendrickson and Bray[95,96] on the other hand yield activation energies of $E_{a,A} = 0.16(2)$ eV and $E_{a,HB} = 0.24(2)$ eV, respectively, although the corresponding fits have the same quality. These values are, even though they do not consider dimensionality effects, comparable to the much more precise value of 0.20 eV as seen on the low-T flank of the $R_1(1/T)$ peak in Figure 6a. We assigned the value of $E_{a,\,NMR} = 0.20$ eV to *quasi* 1D diffusion in β-Li_3PS_4 for which 0.18 eV has been calculated recently.

As Yang et al. have already pointed out,[43] the [010] pathway with its low hopping barrier cannot represent 3D Li^+ diffusion network for the overall Li ion dynamics in in β-Li_3PS_4. However, in the presence of nanoporous or nm-sized crystallites Li diffusion sensed by NMR might be caused by morphologies preferring contiguous (010) planes that cause the Li ions to preferentially diffuse along the [010] direction, at least on medium-ranged (or local) length scales.

4. SUMMARY

Theoretical considerations to explain rapid Li^+ ion dynamics in nanostructured β-Li_3PS_4 considered low-dimensional diffusion pathways. We used a complementary approach of conductivity spectroscopy and ^{7}Li NMR relaxometry to probe both (*i*) macroscopic ion transport and (*ii*) Li ion diffusion on the angstrom length scale. The dispersive regimes of the conductivity isotherms recorded indeed reveal indications for low-dimensional motional processes. ^{7}Li NMR supports this view; the diffusion-induced rate peaks pass through an asymmetric R_1 rate peaks that is most likely caused by quasi 1D, snake-like Li diffusion involving site disorder and interstitial Li ions in β-Li_3PS_4. Frequency-dependent spin-lock NMR measurements provide further evidence of this channel-like diffusion pathway, which is part of the overall ion transport in the thiophosphate. Nanostructured β-Li_3PS_4 represents one of the very rare examples where NMR was successfully used to find indications for a low-dimensional diffusion pathway, which is, at first glance, hidden in the crystal structure of the ionic conductor. This pathway is involved in overall 3D ion transport in β-Li_3PS_4. Paying attention to the dimensionality of short-ranged and medium-ranged diffusion processes might be helpful to also explain unusual transport processes in other ion conductors.

■ ASSOCIATED CONTENT

Supporting Information

The Supporting Information is available free of charge on the ACS Publications website at DOI: 10.1021/acs.chemmater.8b02753.

Illustration of crystal structures and diffusion pathways, comparison of spin-lock NMR rates with R_1 rates (PDF)

■ AUTHOR INFORMATION

Corresponding Author

*E-mail: wilkening@tugraz.at.

ORCID

Daniel Rettenwander: 0000-0002-2074-941X

Ilie Hanzu: 0000-0002-9260-9117

DOI: 10.1021/acs.chemmater.8b02753
Chem. Mater. XXXX, XXX, XXX−XXX

H. Martin R. Wilkening: 0000-0001-9706-4892

Notes

The authors declare no competing financial interest.

■ ACKNOWLEDGMENTS

We thank Tomaž Meško for his help to prepare some of the samples investigated in this study. Financial support by the DFG (Research Unit, FOR1277) and by the Austrian Federal Ministry of Science, Research and Economy, as well as the Austrian National Foundation for Research, Technology and Development is highly appreciated. Furthermore, we would like to thank financial support from the FFG (Austrian Research Promotion Agency) in the frame of the competence project "safe battery".

■ REFERENCES

(1) Larcher, D.; Tarascon, J. M. Towards greener and more sustainable batteries for electrical energy storage. *Nat. Chem.* **2015**, *7*, 19−29.

(2) Grey, C. P.; Tarascon, J. M. Sustainability and *in situ* monitoring in battery development. *Nat. Mater.* **2017**, *16*, 45−56.

(3) Hartmann, P.; Bender, C. L.; Vracar, M.; Durr, A. K.; Garsuch, A.; Janek, J.; Adelhelm, P. A rechargeable room-temperature sodium superoxide (NaO_2) battery. *Nat. Mater.* **2013**, *12*, 228−232.

(4) Bruce, P. G.; Freunberger, S. A.; Hardwick, L. J.; Tarascon, J. M. Li-O_2 and Li-S batteries with high energy storage. *Nat. Mater.* **2012**, *11*, 19−29.

(5) Kwabi, D. G.; Ortiz-Vitoriano, N.; Freunberger, S. A.; Chen, Y.; Imanishi, N.; Bruce, P. G.; Shao-Horn, Y. Materials challenges in rechargeable lithium-air batteries. *MRS Bull.* **2014**, *39*, 443−452.

(6) Goodenough, J. B. Evolution of strategies for modern rechargeable batteries. *Acc. Chem. Res.* **2013**, *46*, 1053−1061.

(7) Janek, J.; Zeier, W. G. A solid future for battery development. *Nat. Energy* **2016**, *1*, No. 16141(1), DOI: 10.1038/nenergy.2016.141.

(8) Bachman, J. C.; Muy, S.; Grimaud, A.; Chang, H. H.; Pour, N.; Lux, S. F.; Paschos, O.; Maglia, F.; Lupart, S.; Lamp, P.; Giordano, L.; Shao-Horn, Y. Inorganic solid-state electrolytes for lithium batteries: mechanisms and properties governing ion conduction. *Chem. Rev.* **2016**, *116*, 140−162.

(9) Knauth, P. Inorganic solid Li ion conductors: An overview. *Solid State Ionics* **2009**, *180*, 911−916.

(10) Thangadurai, V.; Narayanan, S.; Pinzaru, D. Garnet-type solid-state fast Li ion conductors for Li batteries: critical review. *Chem. Soc. Rev.* **2014**, *43*, 4714−4727.

(11) Zhang, B.; Tan, R.; Yang, L.; Zheng, J.; Zhang, K.; Mo, S.; Lin, Z.; Pan, F. Mechanisms and properties of ion-transport in inorganic solid electrolytes. *Energy Storage Mater.* **2018**, *10*, 139−159.

(12) Guin, M.; Tietz, F. Survey of the transport properties of sodium superionic conductor materials for use in sodium batteries. *J. Power Sources* **2015**, *273*, 1056−1064.

(13) Han, X.; Gong, Y.; Fu, K. K.; He, X.; Hitz, G. T.; Dai, J.; Pearse, A.; Liu, B.; Wang, H.; Rubloff, G.; Mo, Y.; Thangadurai, V.; Wachsman, E. D.; Hu, L. Negating interfacial impedance in garnet-based solid-state Li metal batteries. *Nat. Mater.* **2016**, *16*, 572−579.

(14) Kamaya, N.; Homma, K.; Yamakawa, Y.; Hirayama, M.; Kanno, R.; Yonemura, M.; Kamiyama, T.; Kato, Y.; Hama, S.; Kawamoto, K.; Mitsui, A. A lithium superionic conductor. *Nat. Mater.* **2011**, *10*, 682−686.

(15) Bron, P.; Dehnen, S.; Roling, B. $Li_{10}Si_{0.3}Sn_{0.7}P_2S_{12}$ − A low-cost and low-grain-boundary-resistance lithium superionic conductor. *J. Power Sources* **2016**, *329*, 530−535.

(16) Deiseroth, H. J.; Kong, S. T.; Eckert, H.; Vannahme, J.; Reiner, C.; Zaiss, T.; Schlosser, M. Li_6PS_5X: A class of crystalline Li-rich solids with an unusually high Li^+ mobility. *Angew. Chem., Int. Ed.* **2008**, *47*, 755−758.

(17) Epp, V.; Gün, O.; Deiseroth, H. J.; Wilkening, M. Highly mobile ions: low-temperature NMR directly probes extremely fast Li^+ hopping in argyrodite-type Li_6PS_5Br. *J. Phys. Chem. Lett.* **2013**, *4*, 2118−2123.

(18) Seino, Y.; Ota, T.; Takada, K.; Hayashi, A.; Tatsumisago, M. A sulphide lithium super ion conductor is superior to liquid ion conductors for use in rechargeable batteries. *Energy Environ. Sci.* **2014**, *7*, 627−631.

(19) Murugan, R.; Thangadurai, V.; Weppner, W. Fast lithium ion conduction in garnet-type $Li_7La_3Zr_2O_{12}$. *Angew. Chem., Int. Ed.* **2007**, *46*, 7778−7781.

(20) Buschmann, H.; Dolle, J.; Berendts, S.; Kuhn, A.; Bottke, P.; Wilkening, M.; Heitjans, P.; Senyshyn, A.; Ehrenberg, H.; Lotnyk, A.; Duppel, V.; Kienle, L.; Janek, J. Structure and dynamics of the fast lithium ion conductor "$Li_7La_3Zr_2O_{12}$". *Phys. Chem. Chem. Phys.* **2011**, *13*, 19378−19392.

(21) Stanje, B.; Rettenwander, D.; Breuer, S.; Uitz, M.; Berendts, S.; Lerch, M.; Uecker, R.; Redhammer, G.; Hanzu, I.; Wilkening, M. Solid electrolytes: extremely fast charge carriers in garnet-type $Li_6La_3ZrTaO_{12}$ single crystals. *Ann. Phys.* **2017**, *529*, 1700140.

(22) Rettenwander, D.; Welzl, A.; Pristat, S.; Tietz, F.; Taibl, S.; Redhammer, G. J.; Fleig, J. A microcontact impedance study on NASICON-type $Li_{1+x}Al_xTi_{2-x}(PO_4)_3$ ($0 < x < 0.5$) single crystals. *J. Mater. Chem. A* **2016**, *4*, 1506−1513.

(23) Ma, Q. L.; Xu, Q.; Tsai, C. L.; Tietz, F.; Guillon, O. A novel sol-gel method for large-scale production of nanopowders: preparation of $Li_{1.5}Al_{0.5}Ti_{1.5}(PO_4)_3$ as an example. *J. Am. Ceram. Soc.* **2016**, *99*, 410−414.

(24) Breuer, S.; Prutsch, D.; Ma, Q. L.; Epp, V.; Preishuber-Pflügl, F.; Tietz, F.; Wilkening, M. Separating bulk from grain boundary Li ion conductivity in the sol-gel prepared solid electrolyte $Li_{1.5}Al_{0.5}Ti_{1.5}(PO_4)_3$. *J. Mater. Chem. A* **2015**, *3*, 21343−21350.

(25) Epp, V.; Ma, Q. L.; Hammer, E. M.; Tietz, F.; Wilkening, M. Very fast bulk Li ion diffusivity in crystalline $Li_{1.5}Al_{0.5}Ti_{1.5}(PO_4)_3$ as seen using NMR relaxometry. *Phys. Chem. Chem. Phys.* **2015**, *17*, 32115−32121.

(26) Yu, C.; Ganapathy, S.; van Eck, E. R. H.; van Eijck, L.; Basak, S.; Liu, Y. Y.; Zhang, L.; Zandbergen, H. W.; Wagemaker, M. Revealing the relation between the structure, Li-ion conductivity and solid-state battery performance of the argyrodite Li_6PS_5Br solid electrolyte. *J. Mater. Chem. A* **2017**, *5*, 21178−21188.

(27) de Klerk, N. J. J.; Roslon, T.; Wagemaker, M. Diffusion mechanism of Li argyrodite solid electrolytes for Li-ion batteries and prediction of optimized halogen doping: the effect of Li vacancies, halogens, and halogen disorder. *Chem. Mater.* **2016**, *28*, 7955−7963.

(28) Yu, C.; Ganapathy, S.; de Klerk, N. J. J.; Roslon, I.; van Eck, E. R. H.; Kentgens, A. P. M.; Wagemaker, M. Unravelling Li-ion transport from picoseconds to seconds: bulk versus interfaces in an argyrodite Li_6PS_5Cl-Li_2S all-solid-state Li-ion battery. *J. Am. Chem. Soc.* **2016**, *138*, 11192−11201.

(29) Dietrich, C.; Weber, D. A.; Sedlmaier, S. J.; Indris, S.; Culver, S. P.; Walter, D.; Janek, J.; Zeier, W. G. Lithium ion conductivity in Li_2S-P_2S_5 glasses − building units and local structure evolution during the crystallization of superionic conductors Li_3PS_4, $Li_7P_3S_{11}$ and $Li_4P_2S_7$. *J. Mater. Chem. A* **2017**, *5*, 18111−18119.

(30) Wohlmuth, D.; Epp, V.; Wilkening, M. Fast Li ion dynamics in the solid electrolyte $Li_7P_3S_{11}$ as probed by $^{6,7}Li$ NMR spin-lattice relaxation. *ChemPhysChem* **2015**, *16*, 2582−2593.

(31) Hayashi, A.; Minami, K.; Tatsumisago, M. High lithium ion conduction of sulfide glass-based solid electrolytes and their application to all-solid-state batteries. *J. Non-Cryst. Solids* **2009**, *355*, 1919−1923.

(32) Kato, Y.; Hori, S.; Saito, T.; Suzuki, K.; Hirayama, M.; Mitsui, A.; Yonemura, M.; Iba, H.; Kanno, R. High-power all-solid-state batteries using sulfide superionic conductors. *Nat. Energy* **2016**, *1*, 16030.

(33) Funke, K. Solid State Ionics: from Michael Faraday to green energy-the European dimension. *Sci. Technol. Adv. Mater.* **2013**, *14*, 043502.

DOI: 10.1021/acs.chemmater.8b02753
Chem. Mater. XXXX, XXX, XXX−XXX

(34) Wang, Y.; Richards, W. D.; Ong, S. P.; Miara, L. J.; Kim, J. C.; Mo, Y. F.; Ceder, G. Design principles for solid-state lithium superionic conductors. *Nat. Mater.* **2015**, *14*, 1026−1031.
(35) He, X. F.; Zhu, Y. Z.; Mo, Y. F. Origin of fast ion diffusion in super-ionic conductors. *Nat. Commun.* **2017**, *8*, 15893.
(36) Chen, S.; Xie, D.; Liu, G.; Mwizerwa, J. P.; Zhang, Q.; Zhao, Y.; Xu, X.; Yao, X. Sulfide solid electrolytes for all-solid-state lithium batteries: structure, conductivity, stability and application. *Energy Storage Mater.* **2018**, *14*, 58−74.
(37) Hayashi, A.; Hama, S.; Mizuno, F.; Tadanaga, K.; Minami, T.; Tatsumisago, M. Characterization of Li_2S-P_2S_5 glass-ceramics as a solid electrolyte for lithium secondary batteries. *Solid State Ionics* **2004**, *175*, 683−686.
(38) Minami, K.; Mizuno, F.; Hayashi, A.; Tatsumisago, M. Lithium ion conductivity of the Li_2S-P_2S_5 glass-based electrolytes prepared by the melt quenching method. *Solid State Ionics* **2007**, *178*, 837−841.
(39) Wenzel, S.; Randau, S.; Leichtweiss, T.; Weber, D. A.; Sann, J.; Zeier, W. G.; Janek, J. Direct observation of the interfacial instability of the fast ionic conductor $Li_{10}GeP_2S_{12}$ at the lithium metal anode. *Chem. Mater.* **2016**, *28*, 2400−2407.
(40) Sun, Y. L.; Suzuki, K.; Hori, S.; Hirayama, M.; Kanno, R. Superionic conductors: $Li_{10+\delta}[Sn_ySi_{1-y}]_{(1+\delta)}P_{2-\delta}S_{12}$ with a $Li_{10}GeP_2S_{12}$-type structure in the Li_3PS_4-Li_4SnS_4-Li_4SiS_4 quasi-ternary System. *Chem. Mater.* **2017**, *29*, 5858−5864.
(41) Liu, Z. C.; Fu, W. J.; Payzant, E. A.; Yu, X.; Wu, Z. L.; Dudney, N. J.; Kiggans, J.; Hong, K. L.; Rondinone, A. J.; Liang, C. D. Anomalous high ionic conductivity of nanoporous β-Li_3PS_4. *J. Am. Chem. Soc.* **2013**, *135*, 975−978.
(42) Yang, J. J.; Tse, J. S. First-principles molecular simulations of Li diffusion in solid electrolytes Li_3PS_4. *Comput. Mater. Sci.* **2015**, *107*, 134−138.
(43) Yang, Y. H.; Wu, Q.; Cui, Y. H.; Chen, Y. C.; Shi, S. Q.; Wang, R. Z.; Yan, H. Elastic properties, defect thermodynamics, electrochemical window, phase stability, and Li^+ mobility of Li_3PS_4: insights from first-principles calculations. *ACS Appl. Mater. Interfaces* **2016**, *8*, 25229−25242.
(44) Lim, M. S.; Jhi, S. H. First-principles study of lithium-ion diffusion in β-Li_3PS_4 for solid-state electrolytes. *Curr. Appl. Phys.* **2018**, *18*, 541−545.
(45) Homma, K.; Yonemura, M.; Kobayashi, T.; Nagao, M.; Hirayama, M.; Kanno, R. Crystal structure and phase transitions of the lithium ionic conductor Li_3PS_4. *Solid State Ionics* **2011**, *182*, 53−58.
(46) Epp, V.; Nakhal, S.; Lerch, M.; Wilkening, M. Two-dimensional diffusion in $Li_{0.7}NbS_2$ as directly probed by frequency-dependent ^{7}Li NMR. *J. Phys.: Condens. Matter* **2013**, *25*, 195402.
(47) Epp, V.; Wilkening, M. Fast Li diffusion in crystalline $LiBH_4$ due to reduced dimensionality: frequency-dependent NMR spectroscopy. *Phys. Rev. B: Condens. Matter Mater. Phys.* **2010**, *82*, 020301 DOI: 10.1103/PhysRevB.82.020301.
(48) Stanje, B.; Epp, V.; Nakhal, S.; Lerch, M.; Wilkening, M. Li ion dynamics along the inner surfaces of layer-structured 2H-Li_xNbS_2. *ACS Appl. Mater. Interfaces* **2015**, *7*, 4089−4099.
(49) Küchler, W.; Heitjans, P.; Payer, A.; Schöllhorn, R. ^{7}Li NMR relaxation by diffusion in hexagonal and cubic Li_xTiS_2. *Solid State Ionics* **1994**, *70*, 434−438.
(50) Epp, V.; Wilkening, M. Motion of Li^+ in nanoengineered $LiBH_4$ and $LiBH_4$:Al_2O_3 comparison with the microcrystalline form. *ChemPhysChem* **2013**, *14*, 3706−3713.
(51) Wilkening, M.; Küchler, W.; Heitjans, P. From ultraslow to fast lithium diffusion in the 2D ion conductor $Li_{0.7}TiS_2$ probed directly by stimulated-echo NMR and nuclear magnetic relaxation. *Phys. Rev. Lett.* **2006**, *97*, 065901 DOI: 10.1103/PhysRevLett.97.065901.
(52) Heitjans, P.; Schirmer, A.; Indris, S. In *Diffusion in Condensed Matter − Methods, Materials, Models*, Heitjans, P.; Kärger, J., Eds. Springer: Berlin, 2005; pp 367−415.
(53) Wilkening, M.; Heitjans, P. From micro to macro: access to long-range Li^+ diffusion parameters in solids via microscopic ^{6}Li, ^{7}Li spin-alignment echo NMR spectroscopy. *ChemPhysChem* **2012**, *13*, 53−65.
(54) Volgmann, K.; Epp, V.; Langer, J.; Stanje, B.; Heine, J.; Nakhal, S.; Lerch, M.; Wilkening, M.; Heitjans, P. Solid-State NMR to Study Translational Li Ion Dynamics in Solids with Low-Dimensional Diffusion Pathways. *Z. Phys. Chem.* **2017**, *231*, 1215−1241.
(55) McDowell, A. F.; Mendelsohn, C. F.; Conradi, M. S.; Bowman, R. C.; Maeland, A. J. Two-dimensional diffusion of hydrogen in $ZrBe_2H_{1.4}$. *Phys. Rev. B: Condens. Matter Mater. Phys.* **1995**, *51*, 6336−6342.
(56) Enciso-Maldonado, L.; Dyer, M. S.; Jones, M. D.; Li, M.; Payne, J. L.; Pitcher, M. J.; Omir, M. K.; Claridge, J. B.; Blanc, F.; Rosseinsky, M. J. Computational Identification and Experimental Realization of Lithium Vacancy Introduction into the Olivine $LiMgPO_4$. *Chem. Mater.* **2015**, *27*, 2074−2091.
(57) Brinkmann, D.; Mali, M.; Roos, J.; Schweickert, E. Dimensionality effects of Li diffusion in β-eucryptite studied by single-crystal Li NMR. *Solid State Ionics* **1981**, *5*, 433−436.
(58) Singh, B.; Gupta, M. K.; Mittal, R.; Chaplot, S. L. Ab initio molecular dynamics study of 1D superionic conduction and phase transition in β-eucryptite. *J. Mater. Chem. A* **2018**, *6*, 5052−5064.
(59) Kuhn, A.; Sreeraj, P.; Pöttgen, R.; Wiemhöfer, H. D.; Wilkening, M.; Heitjans, P. Li ion diffusion in the anode material $Li_{12}Si_7$: ultrafast quasi-1D diffusion and two distinct fast 3D jump processes separately revealed by ^{7}Li NMR relaxometry. *J. Am. Chem. Soc.* **2011**, *133*, 11018−11021.
(60) Nakhal, S.; Wiedemann, D.; Stanje, B.; Dolotko, O.; Wilkening, M.; Lerch, M. $LiBi_3S_5$ − A lithium bismuth sulfide with strong cation disorder. *J. Solid State Chem.* **2016**, *238*, 60−67.
(61) Uitz, M.; Epp, V.; Bottke, P.; Wilkening, M. Ion dynamics in solid electrolytes for lithium batteries. *J. Electroceram.* **2017**, *38*, 142−156.
(62) Kuhn, A.; Narayanan, S.; Spencer, L.; Goward, G.; Thangadurai, V.; Wilkening, M. Li self-diffusion in garnet-type $Li_7La_3Zr_2O_{12}$ as probed directly by diffusion-induced ^{7}Li spin-lattice relaxation NMR spectroscopy. *Phys. Rev. B* **2011**, *83*, 094302.
(63) Kuhn, A.; Kunze, M.; Sreeraj, P.; Wiemhöfer, H. D.; Thangadurai, V.; Wilkening, M.; Heitjans, P. NMR relaxometry as a versatile tool to study Li ion dynamics in potential battery materials. *Solid State Nucl. Magn. Reson.* **2012**, *42*, 2−8.
(64) Epp, V.; Wilkening, M. In *Handbook of Solid State Batteries*; World Scientific: Singapore, 2015.
(65) Epp, V.; Gün, O.; Deiseroth, H. J.; Wilkening, M. Long-range Li^+ dynamics in the lithium argyrodite Li_7PSe_6 as probed by rotating-frame spin-lattice relaxation NMR. *Phys. Chem. Chem. Phys.* **2013**, *15*, 7123−7132.
(66) Fukushima, E.; Roeder, S. B. W. *Experimental Pulse NMR*; Addison-Wesley: Reading, 1981.
(67) Indris, S.; Heitjans, P. Heterogeneous ^{7}Li NMR relaxation in nanocrystalline Li_2O:B_2O_3 composites. *J. Non-Cryst. Solids* **2002**, *307*, 555−564.
(68) Wilkening, M.; Indris, S.; Heitjans, P. Heterogeneous lithium diffusion in nanocrystalline Li_2O Al_2O_3 composites. *Phys. Chem. Chem. Phys.* **2003**, *5*, 2225−2231.
(69) Heitjans, P.; Wilkening, M. Ion dynamics at interfaces: nuclear magnetic resonance studies. *MRS Bull.* **2009**, *34*, 915−922.
(70) Hayamizu, K.; Aihara, Y.; Watanabe, T.; Yamada, T.; Ito, S.; Machida, N. NMR studies on lithium ion migration in sulfide-based conductors, amorphous and crystalline Li_3PS_4. *Solid State Ionics* **2016**, *285*, 51−58.
(71) Jonscher, A. K. Universal dielectric response. *Nature* **1977**, *267*, 673−679.
(72) Preishuber-Pflügl, F.; Bottke, P.; Pregartner, V.; Bitschnau, B.; Wilkening, M. Correlated fluorine diffusion and ionic conduction in the nanocrystalline F^- solid electrolyte $Ba_{0.6}La_{0.4}F_{2.4}$ − ^{19}F $T_{1\rho}$ NMR relaxation vs. conductivity measurements. *Phys. Chem. Chem. Phys.* **2014**, *16*, 9580−90.
(73) Bunde, A.; Maass, P.; Meyer, M. NMR relaxation in disordered systems. *Phys. A* **1992**, *191*, 433−437.

DOI: 10.1021/acs.chemmater.8b02753
Chem. Mater. XXXX, XXX, XXX−XXX

(74) Meyer, M.; Maass, P.; Bunde, A. Spin-lattice relaxation - non-bloembergen-Purcell-Pound behavior by structural disorder and Coulomb interactions. *Phys. Rev. Lett.* **1993**, *71*, 573−576.
(75) Maass, P.; Meyer, M.; Bunde, A. Non-standard relaxation behavior in ionically conducting materials. *Phys. Rev. B: Condens. Matter Mater. Phys.* **1995**, *51*, 8164−8177.
(76) Sidebottom, D. L. Dimensionality dependence of the conductivity dispersion in ionic materials. *Phys. Rev. Lett.* **1999**, *83*, 983−986.
(77) Preishuber-Pflügl, F.; Wilkening, M. Evidence of low dimensional ion transport in mechanosynthesized nanocrystalline $BaMgF_4$. *Dalton. Trans.* **2014**, *43*, 9901−9908.
(78) Dunst, A.; Sternad, M.; Wilkening, M. Overall conductivity and NCL-type relaxation behavior in nanocrystalline sodium peroxide Na_2O_2 − consequences for Na-oxygen batteries. *Mater. Sci. Eng., B* **2016**, *211*, 85−93.
(79) Ngai, K. L. *Relaxation and diffusion in complex systems*; Springer: New York, 2011.
(80) Preishuber-Pflügl, F.; Wilkening, M. Mechanochemically synthesized fluorides: local structures and ion transport. *Dalton. Trans.* **2016**, *45*, 8675−8687.
(81) Wilkening, M.; Heitjans, P. Li jump process in *h*-$Li_{0.7}TiS_2$ studied by two-time ^{7}Li spin-alignment echo NMR and comparison with results on two-dimensional diffusion from nuclear magnetic relaxation. *Phys. Rev. B: Condens. Matter Mater. Phys.* **2008**, *77*, 024311 DOI: 10.1103/PhysRevB.77.024311.
(82) Stöffler, H.; Zinkevich, T.; Yavuz, M.; Senyshyn, A.; Kulisch, J.; Hartmann, P.; Adermann, T.; Randau, S.; Richter, F. H.; Janek, J.; Indris, S.; Ehrenberg, H. Li^+-ion dynamics in β-Li_3PS_4 observed by NMR: local hopping and long-range transport. *J. Phys. Chem. C* **2018**, *122*, 15954−15965.
(83) Gobet, M.; Greenbaum, S.; Sahu, G.; Liang, C. Structural evolution and Li dynamics in nanophase Li_3PS_4 by solid-state and pulsed-field gradient NMR. *Chem. Mater.* **2014**, *26*, 3558−3564.
(84) Ngai, K. L.; Kanert, O. Comparisons between the coupling model predictions, Monte Carlo simulations and some recent experimental data of conductivity relaxations in glassy ionics. *Solid State Ionics* **1992**, *53*−*56*, 936−946.
(85) Funke, K. Jump relaxation in solid electrolytes. *Prog. Solid State Chem.* **1993**, *22*, 111−195.
(86) Heitjans, P.; Wilkening, M. Diffusion in Nanocrystalline Ion Conductors Studied by Solid State NMR and Impedance Spectroscopy. *Defect Diffus. Forum* **2009**, *283*−*286*, 705−715.
(87) Bloembergen, N.; Purcell, E. M.; Pound, R. V. Nuclear magnetic relaxation. *Nature* **1947**, *160*, 475−476.
(88) Bloembergen, N.; Purcell, E. M.; Pound, R. V. Relaxation effects in nuclear magnetic resonance absorption. *Phys. Rev.* **1948**, *73*, 679−712.
(89) Avogadro, A.; Villa, M. Nuclear magnetic resonance in a two-dimensional system. *J. Chem. Phys.* **1977**, *66*, 2359−2367.
(90) Richards, P. M.; Salamon, M. B. Exchange narrowing of electron spin resonance in a two-dimensional system. *Phys. Rev. B* **1974**, *9*, 32−45.
(91) Richards, P. M. Effect of low dimensionality on pre-factor anomalies in superionic conductors. *Solid State Commun.* **1978**, *25*, 1019−1021.
(92) Richards, P. M., In *Topics in Current Physics*; Springer: Berlin, 1979; Vol. *15*.
(93) Marple, M. A. T.; Avila-Paredes, H.; Kim, S.; Sen, S. Atomistic interpretation of the ac-dc crossover frequency in crystalline and glassy ionic conductors. *J. Chem. Phys.* **2018**, *148*, 204507.
(94) Abragam, A. *The principles of nuclear magnetism*; Oxford University Press: Oxford, 1999.
(95) Hendrickson, J. R.; Bray, P. J. A phenomenological equation for NMR motional narrowing in solids. *J. Magn. Reson.* **1973**, *9*, 341−357.
(96) Hendrickson, J. R.; Bray, P. J. Nuclear magnetic resonance studies of ^{7}Li ionic motion in alkali silicate and borate glasses. *J. Chem. Phys.* **1974**, *61*, 2754−2764.

DOI: 10.1021/acs.chemmater.8b02753
Chem. Mater. XXXX, XXX, XXX−XXX

$LiTi_2(PS_4)_3$ – LTPS

Among current state-of-the-art lithium superionic conductors, $LiTi_2(PS_4)_3$ or LTPS has attracted particular attention due to its exceptional high Li-ion diffusivity at ambient temperature ($D = 1.2 \times 10^{-11}$ m^2/s as estimated from ^7Li pulsed field gradient (PFG) NMR measurements). The framework structure of LTPS is composed of TiS_6 octahedra sharing edge with thiophosphate (PS_4) groups (see Fig. 28 (a)). However, this Ti–P–S crystalline framework does not provide any regular octahedral or tetrahedral stable sites the Li ions could favorably occupy as usually observed in the vast majority of sulfide-based solid electrolytes. Instead lithium diffuses around the titanium sites forming rings as indicated by lithium-ion probability density plots obtained from ab initio molecular dynamics simulation (AIMD). Such a ring consists of three pocket regions of high lithium probability at lower temperatures. Further molecular dynamic simulations at different temperatures show that two diffusion processes are present in LTPS. The lithium ions can either jump between the pocket regions within a ring (intra-ring jumps) or between the individual rings (inter-ring jumps), as graphically illustrated in Fig. 28 (b). While the jump processes between the pockets are very fast and still occur at lower temperatures, jumps between the rings happen at a lower rate and preferentially take place at higher temperatures. Since diffusion along connected rings is needed for long-range ion transport, these jumps are limiting for the overall macroscopic lithium diffusion. As a consequence of the absence of regular polyhedral sites and the occupation of the pocket regions characterized by geometric frustration, lithium diffusion is not limited by jumps through narrow polyhedral faces or edges resulting in a relatively flat energy landscape with small energy barriers and numerous diffusion paths [232].

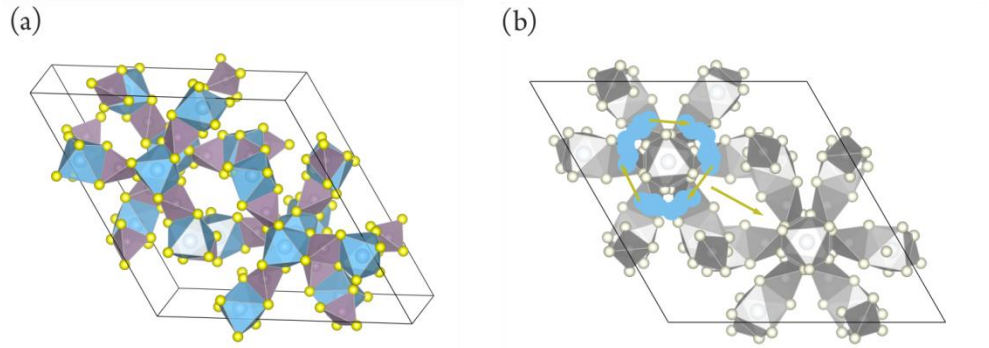

Fig. 28 **(a)** The LTPS framework consists of TiS_6 octahedra sharing edge with PS_4 groups. **(b)** The lithium ions can either jump between the pockets within a ring or between the individual rings as indicated by arrows.

In cooperation with the group of G. Hautier (University of Louvain) we investigated Li-ion dynamics in $LiTi_2(PS_4)_3$ on the angstrom length-scale taking advantage of ^7Li spin-lattice relaxation NMR experiments in both, the laboratory and rotating frame of reference. The sample was provided by Y. Kato (Toyota). The results are summarized in manuscript **M3**. Measurements using a special cryo probe head allowed us to study Li jump processes at temperatures as low as 15 K. The Li diffusion-induced parameters deduced from the relaxation rate peaks corroborate the results obtained from PFG NMR, impedance spectroscopy and molecular dynamic simulations already reported in the literature [232]. Furthermore, the diffusion process being characterized by forward-backward jumps between the pocket regions within a ring is, to our knowledge, one of the fastest exchange processes seen by NMR relaxometry so far.

M3:

^{7}Li NMR spin-lattice relaxation measurements of $LiTi_2(PS_4)_3$ (LTPS)

D. Tapler, D. Rettenwander, M. Wilkening

under preparation

^{7}Li NMR spin-lattice relaxation measurements of $LiTi_2(PS_4)_3$ (LTPS)

D. Tapler, D. Rettenwander, M. Wilkening

Institute of Chemistry and Technology of Materials, Graz University of Technology, Stremayrgasse 9, 8010 Graz, Austria

Abstract. The realization of powerful, long-lasting and safe all-solid-state batteries requires solid electrolytes that show exceptionally good ionic transport properties. Quite recently, the highest Li-ion diffusion coefficient ever reported was observed in the crystal structure of $LiTi_2(PS_4)_3$ (LTPS). Here, we used ^{7}Li NMR relaxation in both, the laboratory and rotating frame of reference to probe Li-ion dynamics in $LiTi_2(PS_4)_3$ on the angstrom-length scale over a wide temperature range. Our NMR data reveal extremely fast jump processes being present in LTPS, which occur in interconnected pocket like environments characterized by geometric frustration. The Li jump rate τ^{-1} is given by 7.3×10^{8} s^{-1}. Two jump processes with low activation energies of 0.10 and 0.14 eV can be extracted from the diffusion-induced relaxation rate peaks, which are characterized by lithium self-diffusion coefficients in the order of 2.4×10^{-11} m^{2}s^{-1} (340 K) and 6.4×10^{-12} m^{2}s^{-1} (214 K), respectively. Spin-lock NMR gives access to third diffusion process being activated at higher temperatures.

Introduction

To meet the continuing demand for high-energy and high-power rechargeable batteries, which are expected to be used for large-scale stationary energy storage or to power electric vehicles [1-4], vigorous efforts has been spent on the enhancement of capacity, power, safety and lifetime of conventional Li-ion based battery technology. Although remarkable advances has been reported for already existing systems based on liquid organic electrolytes [5], all-solid-state batteries (ASSBs), which make use of ceramic solid electrolytes, have attracted particular attention as promising and attractive next-generation technology [6-10]. These systems offer opportunities regarding improved stability, energy density and power. More precisely, the replacement of a highly flammable liquid electrolyte with a more reliable solid electrolyte removes safety hazards concerning inflammability and leakage and thus greatly improves the safety and cycle-life of the battery [6]. Furthermore, electrochemically stable and dense solid-state electrolytes allow the usage of high-capacity electrode materials such as metallic lithium as negative electrode or sulfur as positive active material, resulting in increased energy densities [11-12]. Additionally, the implementation of ceramic solid electrolytes in next-generation battery systems with higher capacities such as Li-O_2 or Li-S batteries seems to be promising. Another advantage of ASSBs is their ability to withstand higher operation temperatures, which enables their use in stationary electric energy storage and automotive applications.

A key property solids have to fulfill in order to be considered as suitable solid electrolyte for all-solid-state batteries is a high lithium-ion diffusion or conductivity at ambient temperature, at best on par with that of conventional liquid electrolytes. Thus, the search for appropriate materials that show fast ion dynamics and vanishing electronic transport has driven the development of superionic conductors to an exceptionally high level. Over the last few years various highly conducting crystalline

structure families including several oxides and sulfides such as NASICON-type structures [7], perovskites [13], garnets [14], argyrodites [15], $Li_7P_3S_{11}$ [16] and $Li_{10}GeP_2S_{12}$ [17] have been presented in the literature. Quite recently, the highest Li-ion diffusion coefficient ever reported in a crystalline solid was observed in the crystal structure of $LiTi_2(PS_4)_3$ (LTPS) [18]. So far, structural analyses, PFG NMR, impedance spectroscopy and molecular dynamic simulations data have already been made available to identify and understand the origins of the extraordinarily fast liquid-like diffusion of lithium ions in this compound. However, knowledge is scarce about the elementary steps governing Li^+ hopping on shorter length scales, which determine bulk ion transport in the underlying material and thus are responsible for the conductivity properties of a solid electrolyte. Time-domain nuclear magnetic resonance (NMR) spectroscopy, in particular NMR relaxation and line shape measurements, would present an elegant way to provide insights into very fast and slow bulk ion dynamics not only on the long-range length scale, but also on the angstrom scale. In addition, NMR spectroscopy is a contactless and non-destructive method and gives access to Li diffusion-induced parameters such as activation energies, jump rates and diffusion coefficients [19-22].

In the present study, ^{7}Li spin-lattice relaxation (SLR) NMR experiments were used to record diffusion-induced relaxation rates of $LiTi_2(PS_4)_3$ over a wide temperature range. From the rate peaks activation energies and Li ion jump rates, which can be easily converted into self-diffusion coefficients using the Einstein-Smoluchowski equation, can be deduced. In addition, line-shape measurements were performed to provide information on Li ion dynamics in LTPS. The NMR results obtained are extensively compared with those from PFG NMR, impedance spectroscopy and molecular dynamic simulations, resulting in a consistent picture of the underlying Li ion dynamic processes in $LiTi_2(PS_4)_3$.

Experimental

Due to their high moisture and air sensitivity the pressed pellets (obtained from Toyota) were fire-sealed in a glass tube prior to the NMR measurements. ^{7}Li (spin –3/2) spin-lattice relaxation(SLR) rates in the laboratory and the rotating frame of reference were recorded with a Bruker 300 Avance spectrometer combined with a shimmed cryomagnet B_0 = 7 T, which operated at a Larmor frequency of $\omega_0/2\pi$ = 116.4 MHz. We used a high-temperature ceramic NMR probe head (Bruker Biospin) for temperature measurements ranging from 175 K to 533 K together with a Eurotherm unit equipped with a type T thermocouple to control and monitor the temperature. This broadband probe allowed $\pi/2$ pulse lengths of about 2.5 μs at 200 W. Temperatures down to 15 K were measured with a cryo probe head from Bruker which was operated with evaporated liquid nitrogen and helium, respectively. The temperatures were adjusted and monitored using a LakeShore 331 unit in combination with two Cernox sensors. At 90 W the $\pi/2$ pulse lengths ranged from 3.5 to 6.5 μs.

To record the spin-lattice relaxation rates R_1 and $R_{1\rho}$ we took advantage of the well-known saturation recovery pulse sequence and the spin-lock technique, see references [23, 24] for details. The former consists of a train of ten 90° pulses (2.5 μs in length) that destroy any longitudinal magnetization in thermal equilibrium; its recovery as a function of waiting time was then recorded until full recovery has been achieved. The magnetization transients were parameterized by stretched exponentials to extract diffusion-induced spin-lattice relaxation rates R_1. The stretching exponents ranged from 1 to 0.8, thus showing only slight deviations from simple exponential recovery. For the spin-lock measurements we used a locking frequency of $\omega_1/2\pi$= 20 kHz and locking pulse durations between 22 μs and 460 ms. The recycle delay was determined with $5 \times 1/R_1$ to ensure that full longitudinal relaxation was achieved. The rates $R_{1\rho}$ were obtained by parameterizing the magnetization

transients with stretched exponentials. The stretching exponents ranged from 0.45 to 0.9 depending on the temperature. Static ^{7}Li NMR line shapes were recorded after excitation the spin ensemble with a single 90° pulse; again the recycle delay was at least $5 \times 1/R_1$ to ensure quantitative lines.

Results and Discussion

To study lithium diffusion-induced parameters, ^{7}Li spin-lattice relaxation rates were measured in both the laboratory frame of reference (R_1) and the rotating frame of reference ($R_{1\rho}$). In Fig. 1 the corresponding SLR rates are shown in an Arrhenius plot to illustrate their behavior with temperature.

At first we will look at the relaxation rates R_1 recorded at a Larmor frequency $\omega_0/2\pi$ = 116.4 MHz. Usually, the rates pass through a peak maximum, which shows up at $\omega_0\tau \cong 1$, where the Li jump rate τ^{-1} is expected in the order of the Larmor frequency ω_0. In the present case, a second rate peak appears at lower temperatures, seen as shoulder of the main peak. Thus, the R_1 rates could be best approximated with the sum of two BPP fits represented by a solid line in Fig. 1; the dashed lines indicate the two peaks (1 and 2) separately. At the temperatures of the peak maxima the mean Li jump rate can be extracted in a rather-model independent approach. Here, the rate peaks show up at $T_{max(2)}$ = 340 K and $T_{max(1)}$ = 214 K, respectively. Taking the maximum condition $\omega_0\tau \cong 1$ into consideration, the jump rate τ^{-1} at T_{max} is given by 7.3×10^{8} s^{-1}. If we assume that peak (2) represents successful jumps between the ring configurations in LTPS, which are separated by a rather long jump distance of 4 – 4.5 Å, the Einstein-Smoluchovski equation, $D = (a^2/6\tau)$ yields a diffusion coefficient for uncorrelated (3D) motion in the order of 2.4×10^{-11} m^{2}s^{-1} at 340 K. This value is in excellent agreement with the results obtained from PFG NMR measurements. The faster process represented by the peak (1) at lower temperatures could be related to more localized forward-backward jumps between the pocket regions within a ring. For this jump process a is given by ca. 2.3 Å, which results into 6.4×10^{-12} m^{2}s^{-1} at 214 K. To our knowledge, peak (1) shows one of the fastest exchange processes seen by NMR relaxometry so far. Furthermore the BPP fits yield activation energies of 0.14 eV (peak 1) and 0.10 eV (peak 2) respectively. To conclude, two types of diffusion processes (inter- and intra-ring jumps) are observed by SLR measurements in the laboratory frame of reference, which is entirely consistent with the results obtained from molelcular dynamic simulations probability analysis.

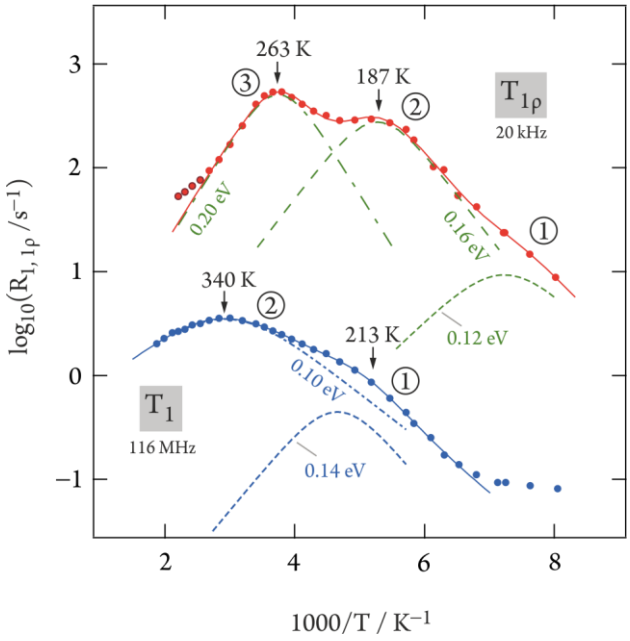

Fig. 1 Arrhenius plot of NMR spin-lattice relaxation rates R_1 and $R_{1\rho}$ recorded at $\omega_0/2\pi$ = 116.4 MHz and at $\omega_1/2\pi$ = 20 kHz. The rates R_1 pass through two relaxation rate peaks revealing complex Li self-diffusion behavior in LTPS with at least two diffusion processes running in parallel or being stepwise activated with increasing temperature. At the peak maxima the corresponding jump rates are in the order of 7.3×10^8 s^{-1}. The solid lines show a sum of two BPP-type Lorentzian shaped peaks, whereas the dashed lines indicate the two peaks separately. The $R_{1\rho}$ rates can be best approximated with the sum of three individual relaxation rate peaks indicated by the solid line. While the peak maxima (1) and (2) correspond to the two rate peaks showing up in the laboratory frame, the diffusion process represented by maximum (3) is not observed in R_1 measurements. Taking the maximum condition into account, the mean jump rate is given by 2.51×10^5 s^{-1} at 263 K and 187 K. See text for further discussion.

The upper part of the Arrhenius plot shown in Fig. 1 includes the $R_{1\rho}$ rates measured at a locking frequency of 20 kHz. Using the spin-lock technique much slower diffusion processes can be probed, since the strength of the applied spin-lock field B_1 is much lower than the external magnetic field B_0 giving rise to a much smaller Zeeman splitting. As a consequence, the peak maximum of $R_{1\rho}$, which shows up when the maximum condition $\omega_1\tau \cong 0.5$ is fulfilled, is shifted towards lower temperatures. Here, the $R_{1\rho}$ rates pass through three peak maxima in the accessible temperature range marked by (1), (2) and (3) in the figure. The relaxation processes reflected by the peak maxima (1) and (2) are attributed to inter- and intra-ring jumps in LTPS and thus correspond to the two rate peaks showing up in the laboratory frame of reference, shifted, however, to lower temperatures.

The diffusion process represented by maximum (3) is not observed in the laboratory frame at $T \geq$ 533 K. It might reflect Li^+ hopping along a different diffusion pathway being activated at higher temperatures only. To clarify this motional process further studies are needed. The $R_{1\rho}$ data can hence be best described as the sum of three independent BPP expressions. The resulting joint fit is represented by a solid line in Fig. 1, while the individual relaxation rate peaks are shown as dashed lines. The activation energies obtained from this analysis turn out to be rather low; E_A of peak 1 and 2 is given by 0.12 and 0.16 eV, whereas rate peak 3 can be best fitted with an activation energy of approximately 0.20 eV. These values can be regarded as the hopping barrier the lithium ions have to overcome in $LiTi_2(PS_4)_3$ and are quite similar to those deduced from R_1 measurements. Finally, using the maximum condition, we can estimate the mean jump rate at the temperatures $T_{max(3)}$ = 263 K and

$T_{max(2)}$ = 187 K. With $\omega_1\tau \cong 0.5$, the rate τ^{-1} is given by 2.51×10^5 s^{-1}. For peak 2 this translates to a self-diffusion coefficient D of 8.5×10^{-15} m^2s^{-1} at 187 K.

The extremely fast Li exchange process in LTPS is further confirmed by ^{7}Li NMR line shape measurements. In Fig. 2(a) selected static NMR spectra are represented, which were recorded in the temperature range from 15.4 K to 533 K. In general, the central transition of the ^{7}Li NMR line shape is dipolarly broadened at low temperatures, which can be approximated using a Gaussian function. At 15.4 K the line width (full width at half maximum, fwhm) is estimated with 2090 Hz. Only sufficiently fast Li diffusion processes are able to average dipole-dipole interactions causing pronounced motionally induced line narrowing with increasing temperature resulting in a Lorentzian-shaped signal. Here, at approximately 240 K, the NMR line already reached the extreme narrowing regime indicating rapid ionic motion. This can be clearly seen from Fig. 3(b), where the full width of half maximum of the central transition is plotted *vs.* *T*. At room temperature the line width is given by only 373 Hz. In agreement with such fast exchange processes a distinct (first order) quadrupolar powder pattern emerges at elevated *T* (also see Fig. 3(a)). The pattern is, if we simply assume an axially oriented mean electric field gradient, characterized by a coupling constant C_Q of 14.6 kHz. Another set of quadrupole singularities shows up close to the central transition with C_Q = 2.6 kHz. It indicates that the Li ions occupy several electrically inequivalent sites in LTPS that take part in overall diffusion. In contrast, at sufficiently low temperatures, in the so-called rigid lattice regime, the NMR line shapes are not affected by the ion dynamics and the corresponding line widths take constant values. Interestingly, in the present case, this regime is not yet reached at temperatures as low as 15.4 K as indicated in Fig. 3(b).

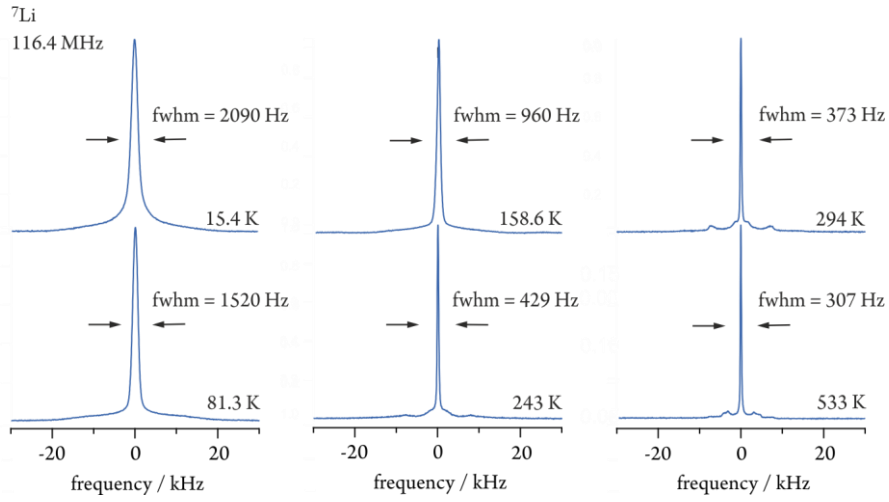

Fig. 2 Static ^{7}Li NMR spectra measured at the temperatures indicated. Motionally induced line narrowing sets in with increasing temperature due to extremely fast Li hopping processes in LTPS. A distinct quadrupolar powder pattern emerges at temperatures as high as 243 K indicating fully averaged line shapes.

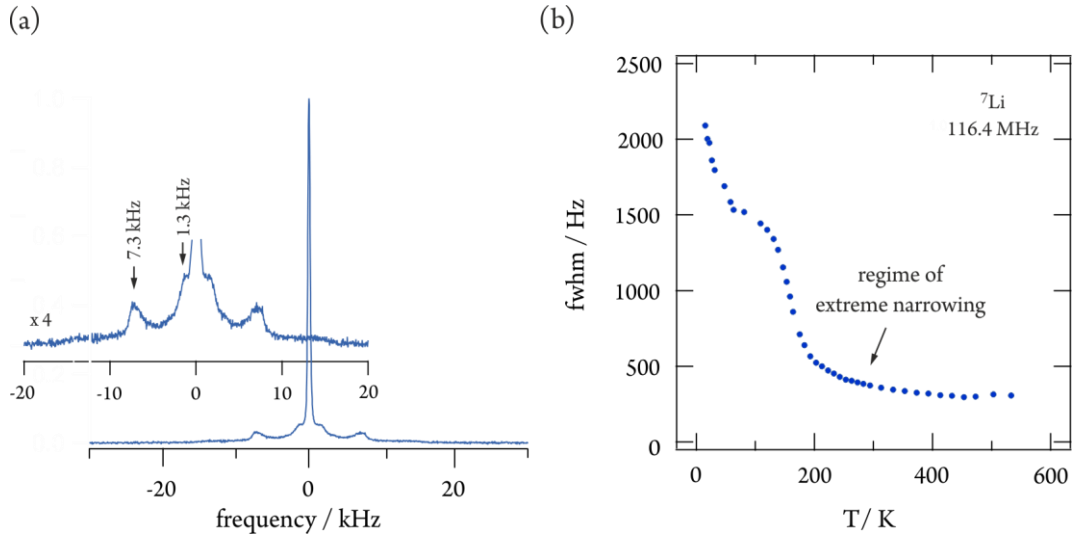

Fig. 3 (**a**) Magnification of the quadrupole singularities of the NMR line recorded at 293 K. (**b**) The full width at half maximum (fwhm) of the central ^{7}Li NMR line plotted as a function of *T*. The extreme narrowing regime is already reached at approximately 240 K. The rigid lattice regime is not observed at temperatures as low as 15.4 K.

Conclusion

In summary, bulk Li-ion dynamics in the superionic conductor $LiTi_2(PS_4)_3$ were investigated by making use of temperature-variable ^{7}Li spin-lattice relaxation and spin-lock NMR experiments. It turned out that extremely fast jump processes are present in LTPS taking place between interconnected pocket-like regions either within a ring or between the ring configurations. These two types of diffusion processes (inter- and intra-ring jumps) are attributed to the two R_1 rate peaks observed by SLR measurements in the laboratory frame of reference, which can be best approximated with the sum of two BPP fits. The Li jump rate τ^{-1} is given by 7.3×10^{8} s^{-1}. This rate transforms into a lithium self-diffusion coefficient in the order of 2.4×10^{-11} m^{2}s^{-1} (340 K) for successful jumps between the rings and 6.4×10^{-12} m^{2}s^{-1} (214 K) for the more localized forward-backward jumps between the pocket regions within a ring. The value calculated at 340 K is in excellent agreement with the results obtained from PFG NMR measurements [18]. The activation energies extracted are very low ranging from 0.10 – 0.14 eV.

^{7}Li NMR relaxometry performed in the rotating frame of reference gives access to a third rate peak showing up at higher temperatures. The diffusion process being valid in this temperature range is characterized by long-range ion dynamics and might reflect Li^+ hopping along a different diffusion pathway being activated at higher temperatures only. The mean Li jump rate is determined with 2.51×10^{5} s^{-1}. This points to a lithium self-diffusion coefficient *D* in the order of 8.5×10^{-15} m^{2}s^{-1} at 187 K. The $R_{1\rho}$ relaxation rate peaks probed can be best fitted with activation energies of 0.12, 0.16 and 0.20 eV, respectively.

The extremely fast Li exchange processes being present in LTPS are further confirmed by ^{7}Li NMR line shape measurements. Furthermore, the diffusion process being characterized by forward-backward jumps between the pocket regions within a ring is, to our knowledge, one of the fastest exchange processes seen by NMR relaxometry so far.

Acknowledgement. Financial support by the Austrian Federal Ministry for Digital and Economic Affairs and the National Foundation for Research, Technology and Development is gratefully acknowledged. We also thank the Deutsche Forschungsgemeinschaft (FOR1277, WI 3600 2-1, 4-1; SPP 1415 WI 3600 5-2) for financial support.

References

1. Tarascon, J.-M., Armand, M., *Nature*, 2001, **414**, 359.
2. Armand, M., Tarascon, J.-M., *Nature*, 2008, **451**, 652.
3. Zubi, G., et al., *Renewable and Sustainable Energy Reviews*, 2018, **89**, 292.
4. Dunn, B., Kamath, H., Tarascon, J.-M., *Science*, 2011, **334** (6058), 928.
5. Palacin, M.R., *Chemical Society Reviews*, 2009, **38** (9), 2565.
6. Knauth, P., *Solid State Ionics*, 2009, **180** (14), 911.
7. Jiang, C., Li, H. Wang, C., *Science Bulletin*, 2017, **62** (21), 1473.
8. Manthiram, A., Yu, X., Wang, S., *Nature Reviews Materials*, 2017, **2**, 16103.
9. Kim, J. G., et al., *Journal of Power Sources*, 2015, **282**, 299.
10. Sun, C., et al., *Nano Energy*, 2017, **33**, 363.
11. Li, J., et al., *Advanced Energy Materials*, 2015, **5**(4), 1401408.
12. Lin, D., Liu, Y., Cui, Y., *Nature Nanotechnology*, 2017, **62**(21), 1473.
13. Inaguma, Y., et al., *Solid State Communications*, 1993, **86** (10), 689.
14. Murugan, R., Thangadurai, V., Weppner, W., *Angewandte Chemie International Edition*, 2007, **46** (41), 7778.
15. Deiseroth, H.-J., et al., *Angewandte Chemie International Edition*, 2008, **47** (4), 755.
16. Wohlmuth, D., Epp, V., Wilkening, M., *ChemPhysChem*, 2015, **16** (12), 2582.
17. Kamaya, N., et al., *Nature Materials*, 2011, **10**, 682.
18. arXiv:1708.02997
19. Epp, V., Wilkening, M., in *Handbook Solid State Batteries*, ed. Dudney, N.J., West, W.C., Nanda, J. World Scientific, New Jersey, Hong Kong, 2015, p. 133.
20. Wilkening, M., Heitjans, P., *ChemPhysChem*, 2012, **13**, 53
21. Böhmer, R., Jeffrey, K. R., Vogel, M., *Prog. Nucl. Magn. Reson. Spectrosc.*, 2007, **50**, 87.
22. Kuhn, A., Narayanan, S., Spencer, L., Goward, G., Thangadurai, V., Wilkening, M., *Phys. Rev. B: Condens. Matter Mater. Phys.*, 2011, **83**, 0943302.
23. Epp, V., et al., Physical Chemistry Chemical Physics, 2013, 15 (19), 7123.
24. Epp, V., The Journal of Physical Chemistry Letters, 2013, 4 (13), 2118.

6.3.2 NASICON electrolytes

NASICON-type (for Na superionic conductor) compounds of the general formula $Na_{1+x}Zr_2Si_xP_{3-x}O_{12}$ ($0 \leq x \leq 3$) [91, 189] are becoming more and more attractive for energy storage applications due to their low cost, abundant resources, compositional diversity and atmospheric stability. In addition, for compositions in the range of $1.8 \leq x \leq 2.4$ the ionic conductivity reaches values close to that of liquid organic electrolytes at higher temperatures making this class of materials promising candidates as solid electrolytes for sodium batteries [233, 234]. The high Na^+ mobility in NASICON structures is based on the existence of a three-dimensional network of conduction pathways through which the sodium charge carriers can be transported. This 3D network is created by ZrO_6 octahedra sharing corners with SiO_4/PO_4 tetrahedra [235].

The most common composition is $Na_3Zr_2Si_2PO_{12}$ ($x = 2$) showing an ionic conductivity of 6.7×10^{-4} S/cm at ambient temperature [236, 237]. It displays a monoclinic symmetry (space group C2/c) and sodium can occupy three different crystallographic sites in this structure, namely 4*d*, 4*e* and 8*f*. Sodium ion migration occurs by jumping between these three positions through oxygen triangles, which represent the geometrical bottleneck for Na^+ diffusion. Partial occupation of these Na sites, which leads to a large fraction of vacant sodium positions, as well as the favorable connection of the polyhedra are crucial for the fast Na^+ mobility within this structure.

Recently, it has been shown that partial heterovalent substitution of Zr^{4+} by a trivalent cation such as Sc^{3+} greatly influences ionic conductivity by increasing the concentration of mobile sodium ions. In particular, the ionic radius of the Sc^{3+} cation is close to that of Zr^{4+}, thus substitution just results in a lack of positive charges and does not distort the crystal structure. For reasons of charge compensation, the amount of mobile Na^+ ions is increased leading to higher conductivity values [238].

In the following publication **P5**, we combined ^{23}Na spin-lattice relaxation NMR and broadband impedance spectroscopy to clarify the interrelation of long-range ion transport with the elementary steps of fast ion hopping in the scandium-substituted NASICON compound $Na_{3.4}Sc_{0.4}Zr_{1.6}SiP_4O_{12}$. The parent compound $Na_3Zr_2Si_2PO_{12}$ served as benchmark. Both samples were provided by Prof. Tietz from the Forschungszentrum Jülich. It turned out that extremely fast Na ion dynamics are present in sol-gel prepared $Na_{3.4}Sc_{0.4}Zr_{1.6}SiP_4O_{12}$ that trigger successful ion jump processes between the different crystallographic positions in the three-dimensional NASICON framework and facilitate macroscopic diffusion.

P5:

Fast Na ion transport triggered by rapid ion exchange on local length scales

S. Lunghammer, D. Prutsch, S. Breuer, D. Rettenwander, I. Hanzu, Q. Ma, F. Tietz, M. Wilkening

Sci. Rep., ***8*** *(2018) 11970.*

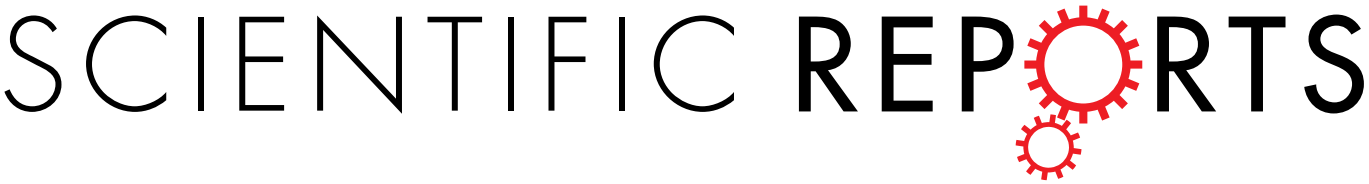

OPEN

Fast Na ion transport triggered by rapid ion exchange on local length scales

Received: 16 January 2018
Accepted: 31 July 2018
Published online: 10 August 2018

S. Lunghammer[1], D. Prutsch[1], S. Breuer[1], D. Rettenwander, I. Hanzu[1,2], Q. Ma[3], F. Tietz[3,4] & H. M. R. Wilkening[1,2]

The realization of green and economically friendly energy storage systems needs materials with outstanding properties. Future batteries based on Na as an abundant element take advantage of non-flammable ceramic electrolytes with very high conductivities. $Na_3Zr_2(SiO_4)_2PO_4$-type superionic conductors are expected to pave the way for inherently safe and sustainable all-solid-state batteries. So far, only little information has been extracted from spectroscopic measurements to clarify the origins of fast ionic hopping on the atomic length scale. Here we combined broadband conductivity spectroscopy and nuclear magnetic resonance (NMR) relaxation to study Na ion dynamics from the μm to the angstrom length scale. Spin-lattice relaxation NMR revealed a very fast Na ion exchange process in $Na_{3.4}Sc_{0.4}Zr_{1.6}(SiO_4)_2PO_4$ that is characterized by an unprecedentedly high self-diffusion coefficient of 9×10^{-12} m^2s^{-1} at −10 °C. Thus, well below ambient temperature the Na ions have access to elementary diffusion processes with a mean residence time τ_{NMR} of only 2 ns. The underlying asymmetric diffusion-induced NMR rate peak and the corresponding conductivity isotherms measured in the MHz range reveal correlated ionic motion. Obviously, local but extremely rapid Na^+ jumps, involving especially the transition sites in Sc-NZSP, trigger long-range ion transport and push ionic conductivity up to 2 mS/cm at room temperature.

In the search of safe and long-lasting energy storage systems all-solid-state batteries entered the spotlight of research[1]. One of the major outstanding challenges is to develop stable electrolytes with extraordinarily high ion conductivities at ambient conditions[2]. Since no flammable liquids are used in such batteries they are regarded as inherently safe and might easily withstand high operation temperatures[3]. In recent years, we witnessed the discovery of a couple of very fast and promising Li^+ ion conductors[4–10]. The market availability of Li might, however, narrow the widespread realization of large scale stationary applications. Sustainable batteries[11,12] with Na^+ as ionic charge carrier[3,13–15] do not carry this risk as Na is abundantly available in the earth's crust. The cost-effective realization of environmentally benign ceramic batteries, however, will need solid electrolytes with a very high ion mobility to compete with the much faster dynamic processes in the liquid state[16,17].

Although moderate to very fast ion conducting Na compounds have so far been frequently presented;[15,16,18–21] ion dynamics in non-sulfidic, *i.e.*, air-insensitive, Na^+ electrolytes with extremely high ion conductivities exceeding 1 mS/cm at room temperature have, apart from the well-known Na-β''-alumina[12], only very rarely been characterized in detail[16,18,22]. Here we present an in-depth study to explore the roots of extremely rapid 3D ion dynamics in $Na_{3.4}Sc_{0.4}Zr_{1.6}(SiO_4)_2PO_4$ (Sc-NZSP), which was prepared via a wet-chemical route[18]. The parent compound $Na_3Zr_2(SiO_4)_2PO_4$ (NZSP), following the pioneering work of Hong and Goodenough[23,24], served as benchmark. It has been shown recently that substitution of Zr by Sc in NZSP leads to an increase of ionic conductivity[22]. For the reason of charge compensation, the replacement of parts of Zr ions with an equimolar amount of Sc ions increases the number density of (mobile) Na ions. Sc-NZSP indeed exhibited Na ion bulk conductivities σ' of 2 mS/cm at room temperature with activation energies ranging from 0.13 eV to 0.31 eV. Although in the Sc-free compound σ' was somewhat lower (1 mS/cm) the grain-boundaries in NZSP turned out to be much

[1]Institute for Chemistry and Technology of Materials (NAWI Graz), and Christian Doppler Laboratory for Batteries, Stremayrgasse 9, Graz University of Technology, A-8010, Graz, Austria. [2]ALISTORE-ERI European Research Institute, 33 Rue Saint Leu, F-80039, Amiens, France. [3]Forschungszentrum Jülich GmbH, Institute of Energy and Climate Research, Materials Synthesis and Processing (IEK-1), D-52425, Jülich, Germany. [4]Helmholtz-Institute Münster, c/o Forschungszentrum Jülich GmbH, D-52425, Jülich, Germany. S. Lunghammer and D. Prutsch contributed equally to this work. Correspondence and requests for materials should be addressed to H.M.R.W. (email: wilkening@tugraz.at)

less blocking for the Na^+ ions. This feature ensured facile ion transport over distances in the µm range. Such long-range ion transport is above all the most important property for any battery application[17].

It is beyond any doubt that reporting such high conductivities[4–8,10,25–28], especially for sodium-based batteries[19–21,29,30], is of enormous importance. Understanding their roots, preferably with the help of theory[31,32], is also crucial and would enable us to safely control their dynamic properties. Yet, for many materials, however, there is still no complete picture available consistently describing the interrelation of the elementary steps of hopping with long-range ion transport. In many cases, it is not even clear which charge carrier and dynamic processes are responsible for the high conductivities reported. Such features cannot be probed by conductivity measurements alone. Instead, one should use complementary techniques that can observe dynamics over wide scales in time and length[33–35]. In this study, we combined time-domain nuclear magnetic resonance (NMR) spectroscopy with broadband conductivity spectroscopy to quantify short-range as well as long-range Na^+ ion diffusivities. Using only NMR spin-lattice relaxometry working at atomic scale[36,37] we managed to get a sneak peek at the very rapid exchange processes the Na ions are performing at temperatures very well below ambient. The data collected provide a first experimental rationale for the very high ionic conductivity observed in NZSP-type compounds.

Since our impedance measurements covered a dynamic range of more than ten decades they allowed us (i) to separate the bulk from grain boundary (g.b.) response at temperatures where batteries are usually operated and (ii) to directly compare electric relaxation with magnetic spin relaxation which was measured in the kHz and GHz range, respectively. Here, NMR relaxometry confirmed the extraordinarily high conductivity of $Na_{3.4}Sc_{0.4}Zr_{1.6}(SiO_4)_2PO_4$ and, furthermore, pointed to a distribution of activation energies including values as low as 0.13 eV and 0.16 eV. Hence, the ions are subjected not to a single but to various dynamic processes being stepwise activated with temperature or running in parallel. To our knowledge, this dynamic performance, although Na^+ ions are of course larger and therefore perhaps more sluggish than Li^+ ions, exceeds those of the best Li oxides currently discussed as ceramic electrolytes[2,38]. Considering the electrochemical stability of NZSP-type materials[39] this behaviour clearly opens the field for the development of powerful Na ion solid-state batteries.

Results and Discussion

$Na_3Zr_2(SiO_4)_2(PO_4)$ is reported to crystallize with monoclinic symmetry (space group $C2/c$, see the views along different crystallographic axes in Fig. 1a–c. In the monoclinic form of NZSP the Na^+ ions occupy three crystallographically inequivalent sites 4*d*, 4*e*, and 8*f*, which are partially occupied. The large fraction of vacant Na sites and the favourable connection of their polyhedra ensure rapid exchange of the Na^+ ions as discussed in literature[22,40]. The preparation and characterisation of the samples studied here (NZSP and Sc-NZSP) has already been described elsewhere[18,22]. The characterization also includes analyses by X-ray powder diffraction and differential scanning measurements.

Electrical conductivity: bulk vs. grain boundary responses. We used a sintered Sc-NZSP pellet (1.1 mm in thickness and 7 mm in diameter) equipped with sputtered ion-blocking electrodes of gold to ensure electrical contact for our conductivity and impedance measurements, see Fig. 1d–g. Conductivity isotherms showing the real part σ' of the complex conductivity as a function of frequency ν are displayed in Fig. 1f, see also Figs S1 and S2 for the complete temperature range covered. We used two impedance analysers to construct the isotherms, a Novocontrol Alpha analyser and an Agilent impedance bridge (see also the grey area in Fig. 1d) to reach the GHz range. If we consider the conductivities over a frequency range from the µHz to the GHz regime at least two main contributions were revealed; they are labelled (A) and (B) in Fig. 1f. While they appear as plateaus in the $\sigma'(\nu)$ plot, they manifest as two independent semicircles in the complex plane plots, *i.e.*, Nyquist illustrations, see Fig. 1e showing the responses recorded at −100 °C with the apex frequencies ω_{max} indicated; plots with equally scaled axes are shown in Figs S1 and S2. As the capacity C of plateau (A), if simply estimated via $\omega_{max}RC = 1$, is in the nF range, we attribute the semicircle in the low frequency range to the g.b. response. The spike seen at very low frequencies is attributed to ionic polarisation effects in front of the Na^+ ion blocking electrodes. Plateau (B) is assigned to the bulk response as the corresponding capacity C_{bulk} is clearly in the pF range; such capacities are diagnostic for electrical relaxation processes taking place in the grain.

Most importantly, at room temperature the bulk semicircle (see Fig. 1g), which was recorded in the GHz regime, corresponds to a specific conductivity in the mS range. At 20 °C the intercept of the $-Z''(Z')$ curve with the real axis yields a conductivity of 8.3 mS (ca. 120 Ω) which results in a specific conductivity of 2.4 mS/cm. The g.b. response yields values which are two orders of magnitude lower (see also the difference of the plateaus $\sigma'_{bulk}(\nu)$ and $\sigma'_{g.b.}(\nu)$ in Fig. 1f). The two processes can also be clearly seen if the imaginary part Z'' of the complex impedance and that of the complex modulus (M'') are analysed. The corresponding curves $-Z''(\nu)$ and $M''(\nu)$ are shown in Fig. 1d and reveal two peaks that differ in amplitude according to the capacities associated with the two processes they represent. Here we have $C_{g.b.}/C_{bulk} \approx 100$ leading to the same ratio in peak amplitudes $M''_{max./bulk}/M''_{max./g.b.}$. Since $M''_{(max.)} \propto 1/C$, bulk responses are more prominent in the modulus representation, as expected. Almost the same ratio is probed for the real part of the complex permittivity; values in the order of 10^3 or 10^4 are typically seen for g.b. contributions.

Measurements up to the GHz are indispensable to make the bulk response fully visible at temperatures above ambient, see the data points in the GHz range in Fig. 1d,f. The Nyquist curves in Fig. 1g show solely impedances measured at frequencies larger than 10^6 Hz. The curves in the complex plane plots reveal that several semicircles contribute to the overall bulk conductivity; this observation is especially indicated for the Nyquist curves recorded at 20 °C and 40 °C. The substructure of the curves of Sc-NZSP clearly points to multiple, simultaneously occurring electrical relaxation processes with very similar impedances.

Ionic vs. electronic conductivity. By reading off the conductivities of the plateaus in Fig. 1f, as indicated by the horizontally drawn arrow, we constructed an Arrhenius plot to analyse the temperature dependence of the two

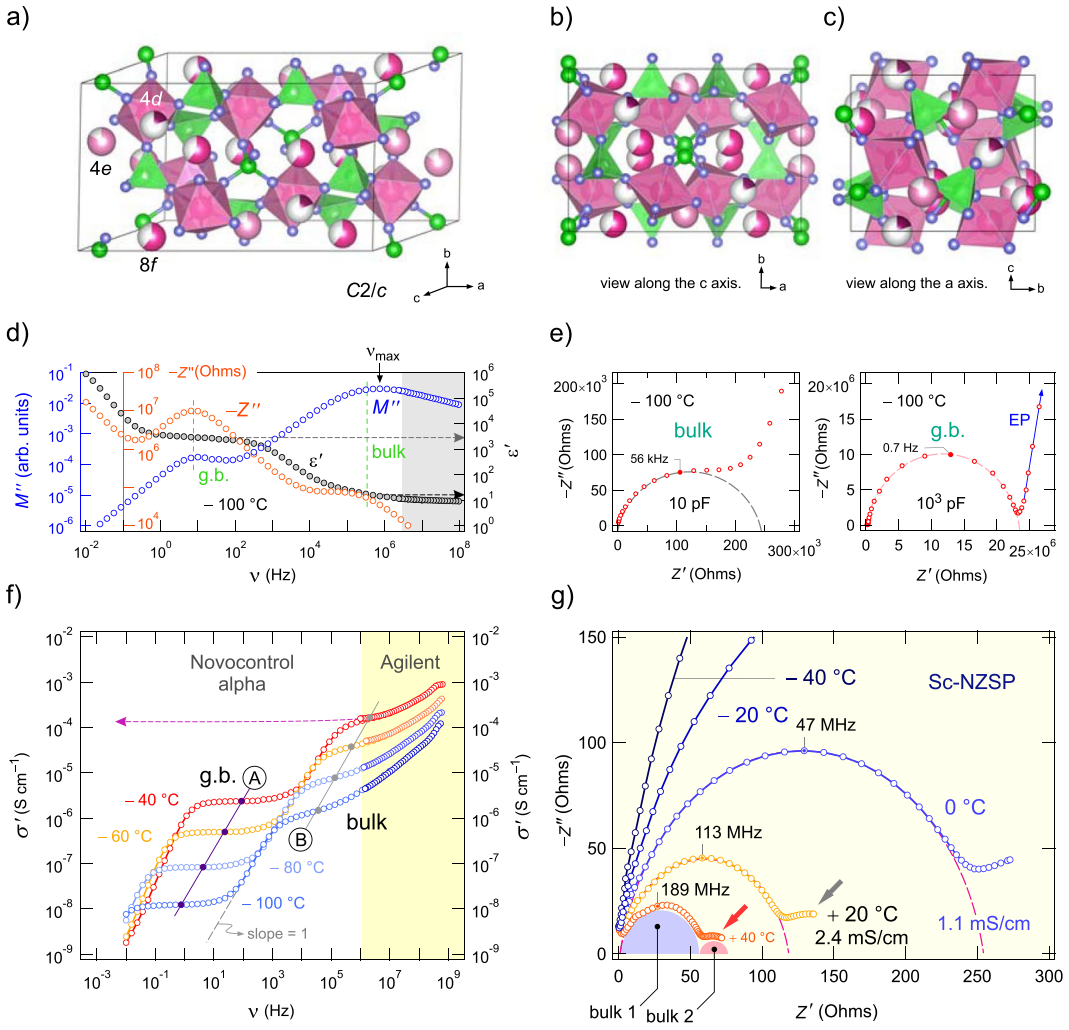

Figure 1. Crystal structure and conductivity. (**a–c**) Crystal structure of monoclinic $Na_3Zr_2(SiO_4)_2PO_4$. (**d**) Frequency dependence of the imaginary part of the complex impedance ($-Z''$) and the complex modulus (M'') of Sc-NZSP (−100 °C). For comparison, the variation of the real part ε' of the complex permittivity is also shown. $-Z''$ and M'' each reveal two maxima which correspond to the grain boundary (g.b., $\varepsilon' = 3 \times 10^3$) and bulk response, respectively; the latter is seen in the high-frequency region, ε' ranges from 10 to 20. (**e**) Complex plane plots of the impedance data (−100 °C). The depressed semicircle at high frequencies (left) represents the (overall) bulk response ($C_{bulk} = 10$ pF). The g.b. contribution is characterized by $C_{g.b.} = 10^3$ pF and a Debye-like non-depressed semicircle with its centre almost on the Z' axis (Fig. S1); piling up of the ions near the blocking electrode, *i.e.*, electrode polarization (EP), is seen as a spike at the lowest frequencies. (**f**) Conductivity isotherms of Sc-NZSP. The frequency independent regions (A) and (B) represent either the g.b. or the bulk response. The direct current g.b. response directly merges into a linear conductivity-frequency regime, $\sigma \propto \nu$ (slope = 1). The arrow points to σ' in order of 10^{-4} S/cm at −40 °C. (**g**) Nyquist plots recorded at frequencies greater than 10^6 Hz. At elevated temperatures the bulk response seems to be composed of at least two semicircles (bulk 1, bulk 2).

main electrical responses (see Fig. 2) Potentiostatic polarisation measurements, carried out prior to this analysis, ensured that the overall conductivity analysed is solely determined by ionic charge carriers. For this purpose, we used a symmetric Sc-NZSP pellet outfitted with ion blocking Au electrodes, applied a potential of 0.2 V and followed the current I over time t (Fig. 2a). After approximately 5 h a stationary state ($I_{t\to\infty} = 63(5)$ pA) is reached in which the concentration gradients are fully developed and the only net charge transport across the material is due to electrons for which the Au contacts do not act as blockade. The final current of 63 pA (Fig. 2a) corresponds to an electronic conductivity of $\sigma_{eon,\,d.c.} = 7.2(6) \times 10^{-8}$ mS/cm. This value is lower by 7 to 8 orders of magnitude compared to the total conductivity σ' measured in the direct current (d.c.) limit $\nu \to 0$, *i.e.*, for plateau (B), see Fig. 1f. Thus, Sc-NZSP must be regarded as a pure ionic conductor with the Na ion transference number t_{ion} close to 1.

Activation energies and solid-state diffusion coefficients. The total conductivities plotted in Fig. 2b reveal that the overall electric transport in Sc-NZSP is determined by activation energies ranging from 0.29 eV to 0.31 eV (−100 °C to 130 °C). The Arrhenius line of the bulk process shows slight deviations from a perfectly linear behaviour. Such a deviation is even more pronounced for the g.b. response for which we identified several regions with activation energies ranging from 0.32 eV to values as high as 0.47 eV. While for temperatures

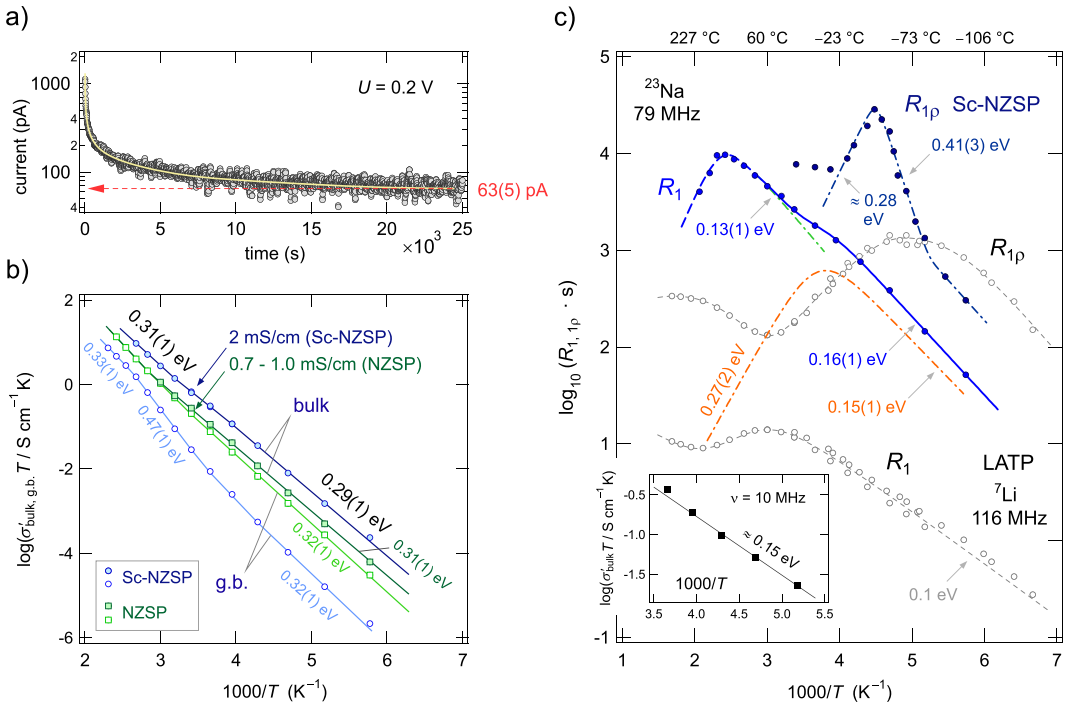

Figure 2. Electronic conductivity and temperature dependence of σ' of Sc-NZSP, ^{23}Na NMR spin-lattice relaxation. (**a**) Constant voltage (direct current) polarization curve of a sintered Sc-NZSP pellet. The high ionic conductivity translates into a rapid decay of the current at the beginning of the experiment. After a time lapse of sufficient length, the current approaches a value that is solely due to the transport of electrons. (**b**) Temperature dependence of the bulk and g.b. conductivity of Sc-NZSP ($\sigma_{bulk}(298\,K) = 2.0$ mS cm^{-1}). The results for NZSP free of Sc are also shown ($\sigma'_{bulk}(298\,K) = 1.0$ mS cm^{-1}; $\sigma'_{g.b.}(298\,K) = 0.7$ mS cm^{-1}). Filled symbols refer to bulk values, open ones represent the g.b. response. Crosses show conductivities taken from ref.[22]. (**c**) ^{23}Na spin-lattice relaxation rates (R_1, $R_{1\rho}$) of Sc-NZSP recorded in both the laboratory frame of reference (79 MHz, R_1) and the rotating-frame of reference (20 kHz, $R_{1\rho}$). The sharp diffusion-induced peak of the latter and the shoulder of the $R_1(1/T)$ curve indicate extremely rapid Na ion diffusivity with rates in the order of $\omega_0/2\pi \approx 5 \times 10^8$ s^{-1} at T as low as 260 K. Error bars of the data points are smaller than the size of the symbols used. The solid line shows a fit with two BPP-terms to approximate the R_1 rates; the dashed-dotted line highlights the asymmetric low-T peak with the activation energies 0.15 eV and 0.27 eV, respectively. The dashed-dotted line drawn through the $R_{1\rho}$ data points is to guide the eye. Unfilled symbols represent, for comparison, results from analogous measurements on a Li-analogue compound, $Li_{1.5}Al_{0.5}Ti_{1.5}(PO_4)_3$ (LATP), see ref.[49].

lower than −20 °C bulk and g.b. conductivities differ by two orders of magnitude, above −20 °C $\sigma'_{g.b.}$ increased stronger than expected and was thermally activated with 0.47 eV. At temperatures higher than 120 °C the difference between σ'_{bulk} and $\sigma'_{g.b.}$ turned out to be is less than 1 order of magnitude. A ratio $\sigma'_{bulk}/\sigma'_{g.b.}$ close to 1 is, however, observed for NZSP. At 20 °C the bulk conductivity of $Na_3Zr_2(SiO_4)_2PO_4$ is 1.0 mS/cm, for $\sigma'_{g.b.}$ we found 0.7 mS/cm (Fig. 2b, see also Fig. S2 for the corresponding Nyquist plots). A conductivity of 2.0 mS/cm for Sc-NZSP results in a room-temperature solid-state diffusion coefficient D of 2×10^{-12} m^2/s if we use the Nernst-Einstein equation to estimate D via $D = \sigma'_{bulk} k_B T/(Nq^2)$ where k_B denotes Boltzmann's constant, T the absolute temperature in K, and q the elementary charge of the Na ions. N refers to the number density of charge carriers. Values for D in the order of 10^{-12} m^2/s are comparable with the diffusion coefficients of the best ceramic Li ion conductors known today.

^{23}Na NMR spin-lattice relaxation: Na$^+$ motions on the angstrom scale. To check whether the high Na$^+$ ion mobility seen in electrical measurements for Sc-NZSP is also reflected in NMR relaxation, we carried out variable-temperature ^{23}Na spin-lattice relaxation (SLR) measurements in both the laboratory (R_1) and rotating frame of reference ($R_{1\rho}$), see Fig. 2c. The corresponding magnetization transients are shown in Fig. S3. While the first are sensitive to diffusive spin fluctuations in the MHz to GHz range, the spin-lock technique allows for the detection of slower motions in the kHz range. As we used a ^{23}Na NMR Larmor frequency of $\omega_0/(2\pi) = 79$ MHz to record the ^{23}NMR SLR rates, we expect the diffusion-induced rate R_1 to pass through a maximum at temperatures near or slightly above 20 °C. The jump rate $1/\tau_{NMR}$ at such a maximum is directly determined by the relation $\omega_0\tau_{NMR} \approx 1$ yielding $D_{NMR} = a^2/(6\tau) = 9 \times 10^{-12}$ m^2/s; for $1/\tau_{NMR}$ we obtain 5×10^8 s^{-1}. This estimation uses the Einstein-Smoluchowski equation for uncorrelated 3D diffusion and an average jump distance of 3.3 Å for the various possible exchange processes between the Na sites. In fact, we observe a complex relaxation behaviour with two R_1 rate peaks as shown in Fig. 2c. One of these peaks appears as a shoulder of the main one. It is located at approximately −10 °C if we parameterize the overall relaxation response with a sum of two spectral density

functions (for 3D diffusion) according to a modified version of the model of Bloembergen, Purcell and Pound[41,42], see Supporting Information and Table S1. Interestingly, the low-T peak indicates even faster Na ion exchange processes than seen by conductivity spectroscopy. The question of whether it is triggered by a possible phase transformation occurring below room temperature and slightly changing the Na^+ distribution in Sc-NZSP needs to be checked in further studies.

Conductivity measurements are sensitive to successful Na ion displacements in the so-called d.c. limit characterized by the respective σ'_{bulk} plateau (Fig. 1f); here the corresponding activation energy is given by $E_{a,d.c.} = 0.29(1)$ eV. The very low activation energy $E_{a,NMR}$ of 0.15 eV (see also ref.[43] for comparison) extracted from the diffusion-induced NMR rate peak $R_1(1/T)$ seen at lower T (Fig. 2c) indicates that ^{23}Na NMR SLR senses the elementary diffusion processes to which local, correlated motions do also contribute. In general, the low-T flank of a given NMR rate peak is influenced by correlation effects such as Coulomb interactions and structural disorder. The latter is present also in the form of stress the jumping ions experience while moving in a heterogeneous, irregularly shaped potential landscape[38]. This landscape contains stable as well as transitions states with shorter residence times for the Na^+ ions. We anticipate that forward-backward jumps involving interjacent bottleneck sites[22,40,44] result in highly correlated jump processes that manifests as dispersive regions in the conductivity isotherms. These dispersive regions are seen in Fig. 1f in the high frequency region (>1 MHz) of the bulk isotherms. The activation energy of the high-T flank of the $R_1(1/T)$ peak should be comparable to $E_{a,d.c.}$.

NMR and conductivity spectroscopy: a comparison. To compare activation energies from conductivity measurements directly with those from NMR relaxometry we need to analyse alternating current (a.c.) conductivities not in the limit $\nu \rightarrow 0$ but in the MHz regime, *i.e.*, on the same time scale where NMR operates. We therefore determined $\sigma'_{bulk}(\nu)$ at $\nu = 10$ MHz. At this frequency, the dispersive parts are seen fully in the temperature range from −100 °C to −50 °C, which coincides with that of the low-T flank of the first $R_1(1/T)$ peak. A plot of $\log(\sigma'_{a.c.,bulk}(10\,\text{MHz})T)$ vs. $1/T$ (see the inset of Fig. 2c) revealed an activation energy $E_{a,a.c.}$ of 0.147(5) eV which is close to that seen by ^{23}Na NMR SLR in the same temperature range, $E_{a,a.c.} = E_{a,NMR}$. The ratio $E_{a,d.c.}/E_{a,a.c.} = 1/\beta_n$ turns out to be approximately 1.97. On the other hand, $\beta_n = 1/1.97 \approx 0.5$ is related to the Jonscher power law exponent[45] describing the dispersive regime of $\sigma'_{bulk}(\nu)$ via the relation $\beta_n = 1 - n$, see ref.[46]. If NMR and a.c. conductivity spectroscopy are governed by very similar motional correlation functions in the temperature range given above, $n \approx 0.5$ should be found. In general, β_n can be used as a measure to describe the deviation from ideal Debye relaxation that relies on a pure exponential decay function. In the present case, parameterizing the corresponding a.c. isotherms with $\sigma'_{bulk} \propto \nu^n$ indeed yields $n = 0.54$ indicating similarly shaped correlation functions. This similarity does not contradict the finding that D_{NMR} is larger than D from conductivity measurements. A relatively small correlation factor f' (≤ 0.1) linking the two coefficients via $D = f' \cdot D_{NMR}$, see[47,48] would explain the difference pointing to highly correlated motions in Sc-NZSP. f' is given by the Haven ratio H_r and f. The two factors connect the tracer diffusion coefficient with either the Nernst-Einstein coefficient D or the self-diffusion coefficient $D_{(NMR)}$, see[38]. Most likely, here D_{NMR} is indeed influenced by a huge number of unsuccessful, localized jump processes which are not contained in D that is sensitive to successful ionic displacements only. These localized motions may, however, stimulate long-range ion transport leading to ionic conductivities exceeding that of the Sc-free parent compound with a lower number density of Na^+ ions.

An activation energy comparable to $E_{a,d.c.} = 0.29$ eV is seen in NMR relaxation spectroscopy only if the high-T flank of the diffusion-induced peak $R_1(1/T)$ can be reached[33]. In our case the high-T flank of the spin-lock $R_{1\rho}(1/T)$ peak recorded at a locking frequency $\omega_1/2\pi = 20$ kHz points to such a value, see Fig. 2c. However, the peak itself shows anomalous behaviour as the low-T side is characterized by a larger activation energy (0.41 eV) than that on the high-T flank. While such features might be ascribed to low-dimensional diffusion pathways, here the anomaly is supposedly caused by various superimposing jump processes. A point worth mentioning is that the conductivity spectroscopy in the d.c. limit yields an average activation energy of successful net charge transport over a long length scale. The corresponding activation energies extractable from NMR, particularly those in the low-T region of the $R_{1(\rho)}(1/T)$ peaks, specify distinct motional processes with activation energies $E_{a\,low\text{-}T}$ being smaller or even higher than $E_{a,\,d.c.}$. The modified BPP fits shown in Fig. 2c for the $R_1(1/T)$ behaviour consistently yield a high-T activation energy $E_{a\,high\text{-}T}$ of 0.27 eV being very similar to $E_{a,\,d.c.}$, see Table S1 for the NMR results. The resulting asymmetry of the peak (see Supporting Information) has frequently been assigned to correlated motion governed by a distribution of (non-)exponential motional correlation functions. The two activation energies of the peak ($E_{a\,low\text{-}T} = 0.15$ eV and $E_{a\,high\text{-}T} = 0.27$ eV) are linked to each other via $E_{a\,low\text{-}T} = (\alpha_{NMR} - 1)E_{a\,high\text{-}T}$ yielding $\alpha_{NMR} = 1.55$. $\alpha_{NMR} = 2$ would correspond to a quadratic frequency dependence, $R_1 \propto \omega_0^2$, on the low-T side and would indicate uncorrelated, isotropic motion. Furthermore, $E_{a\,high\text{-}T}$ (and $E_{a,\,d.c.}$) is in line with the activation energy if we analyse the characteristic electric relaxation frequencies $\omega_{max} = \nu_{max} \times 2\pi$ (see Fig. 1d) of the Modulus curves in the MHz to GHz regime. $1/\tau_{NMR} = 5 \times 10^8\ s^{-1}$ agrees perfectly with $\omega_{max}(1/T)$ read off from the M'' peaks, see Fig. S4. Hence, modulus spectroscopy and NMR probe the same time scale and sense the same Na^+ motional correlation function and thus the same ionic exchange process.

For comparison, in Fig. 2c also ^{7}Li NMR rates of Nasicon-type $Li_{1.5}Al_{0.5}Ti_{1.5}(PO_4)_3$ (LATP) are shown[49]. LATP crystallizes with rhombohedral structure and belongs to one the fastest Li-containing phosphates[50]. Although the peak positions of the Na compound studied here are shifted toward somewhat higher temperatures, Sc-NZSP can compete with the high Li^+ diffusivity in LATP. As for Sc-NZSP the ^{7}Li NMR relaxation response of LATP was analysed with a superposition of at least two diffusion-induced relaxation rate peaks[49]. Since the quadrupolar interactions experienced by ^{7}Li spins are much lower than those in the case of ^{23}Na, the ^{23}Na rates are shifted toward larger rates. Stretching factors of the underlying ^{23}Na R_1 magnetization transients, see Fig. S3, point to (localized) diffusion-induced quadrupolar field fluctuations that cause the recovery of the longitudinal magnetization for Sc-NZSP.

Conclusions

In summary, Na ion dynamics in sol-gel prepared $Na_{3.4}Sc_{0.4}Zr_{1.6}(SiO_4)_2PO_4$ turned out to be extremely rapid at temperatures around ambient. ^{23}Na NMR spin-lattice relaxation is governed by complex Na^+ dynamics as the relaxation rates reveal several diffusion-induced peaks. While short-range Na motion has to be characterized by activation energies ranging from 0.13 to 0.15 eV, long-range ion transport, on the other hand, follows Arrhenius behaviour with 0.29 to 0.31 eV. Facile Na ion exchange results in room-temperature ion conductivities of 2.0 mS/cm for $Na_{3.4}Sc_{0.4}Zr_{1.6}(SiO_4)_2PO_4$ and 1.0 mS/cm for the parent compound $Na_3Zr_2(SiO_4)_2PO_4$, respectively. Such high bulk conductivities correspond to solid-state diffusion coefficients in the order of 2×10^{-12} m^2/s. Indeed, for Sc-NZSP ^{23}Na spin-lattice relaxation NMR points to a self-diffusion coefficient of 9×10^{-12} m^2/s at 21 °C. Evidently, extremely rapid ion jump processes between regular and intermediate positions contribute to this high value. Such rapid movements obviously trigger the successful jump processes among the different crystallographic sites in the 3D framework of the phosphosilicate and facilitate net charge transport over macroscopic distances in Sc-NZSP.

Methods and Experimental Design

Conductivity analysis. Sintered pellets with sputtered or evaporated Au electrodes were used to measure complex conductivities at various temperatures and from 0.1 Hz up to the GHz range with a Novocontrol Concept 80 setup. The setup consists of a broadband analyser (Alpha-AN, Novocontrol), which is connected to a BDS 1200 cell in combination with an active ZGS cell interface (Novocontrol) allowing 2-electrode dielectric measurements. The temperature is automatically controlled by means of a QUATRO cryo-system (Novocontrol) making use of a heating element which builds up a specified pressure in a liquid nitrogen Dewar vessel to create a highly constant N_2 gas flow. After being heated by a gas jet, the evaporated N_2 flows directly through the sample cell that is mounted in a cryostat. With this setup, temperatures can be set with an accuracy of ±0.01 °C. To reach up to 3 GHz we used an Agilent E4991 A high-frequency analyser connected to a high frequency cell designed by Novocontrol.

Polarisation measurements. For the d.c. polarisation measurement a sintered pellet (0.89 mm thick, 7 mm in diameter) was metallised with Au on both sides by evaporation. The pellet was then mounted in an air-tight 2-electrode Swagelok-type cell and connected to the Parstat MC potentiostat equipped with a low-current option. All the preparation steps, including the metallisation, were carried out in Ar or N_2 filled gloveboxes filled with an oxygen and water content of less than 1 ppm. The polarisation experiments were performed in a Faraday cage at 23(1) °C.

^{23}Na NMR measurements. All static ^{23}Na NMR measurements were carried out using a Bruker Avance III spectrometer equipped with a shimmed cryo-magnet with a nominal magnetic field B_0 of approximately 7.04 T. This field strength corresponds to a ^{23}Na resonance frequency of $\omega_0/2\pi = 79.35$ MHz. For the NMR measurements, we used sintered pellets which were fire-sealed under vacuum in quartz glass ampoules to permanently protect them from moisture and/or air. We used a Bruker broadband probe (80 mm in diameter) designed for static variable-temperature measurements. The temperature in the sample chamber made of Teflon® was adjusted with a stream of freshly evaporated nitrogen gas. The heating coil was controlled by a Eurotherm unit connected to copper-constantan type T thermocouple placed in the immediate vicinity of the sample. To study Na ion dynamics, ^{23}Na NMR spin-lattice relaxation experiments in both in the laboratory and in the rotating frame were carried out with pulse sequences using suitable phase cycling to suppress unwanted coherences. R_1 rates were recorded with the saturation recovery pulse sequence consisting of a train of 90° pulses to destroy any longitudinal magnetization M. The subsequent recovery of M was recorded after variable delay times t_d with a 90° reading pulse. The $\pi/2$ pulse lengths ranged from 2 to 4 μs at 200 W, depending on temperature. Up to 64 scans were accumulated to obtain $M(t_d)$ for each waiting time. The area under the free induction decays was used as a measure for $M(t_d)$. The magnetization transients $M(t_d)$ were analysed with stretched exponential functions to extract the rates R_1; stretching exponents varied from 0.8 to 1. The spin-lock measurements were recorded with a locking frequency of 20 kHz. At the beginning of the pulse sequence a 90° pulse prepares the spin system. Immediately after this, the locking pulse with variable duration t_{lock} (46 μs to 46 ms) was used to observe transversal relaxation of the flipped magnetization M_ρ. The decay of M_ρ in the $(xy)_\rho$-plane of the rotating frame of reference is detected with a 90° reading pulse. The number of scans for each data point of the magnetization curve was 64. A recycle delay of at least $5 \times 1/R_1$ ensured full longitudinal relaxation. $M_\rho(t_{lock})$ could be fitted with stretched exponentials; the stretching factors ranged from 0.8 to 0.4 depending on temperature.

References

1. Janek, J. & Zeier, W. G. A solid future for battery development. *Nat. Energy* **1**, 16141 (2016).
2. Bachman, J. C. *et al.* Inorganic solid-state electrolytes for lithium batteries: mechanisms and properties governing ion conduction. *Chem. Rev.* **116**, 140–162 (2016).
3. Hueso, K. B., Armand, M. & Rojo, T. High temperature sodium batteries: status, challenges and future trends. *Energy. Environ. Sci.* **6**, 734–749 (2013).
4. Murugan, R., Thangadurai, V. & Weppner, W. Fast lithium ion conduction in garnet-type $Li_7La_3Zr_2O_{12}$. *Angew. Chem. Int. Ed.* **46**, 7778–7781 (2007).
5. Deiseroth, H. J. *et al.* Li_6PS_5X: A class of crystalline Li-rich solids with an unusually high Li^+ mobility. *Angew. Chem. Int. Ed.* **47**, 755–758 (2008).
6. Kamaya, N. *et al.* A lithium superionic conductor. *Nat. Mater.* **10**, 682–686 (2011).
7. Kato, Y. *et al.* High-power all-solid-state batteries using sulfide superionic conductors. *Nat. Energy* **1** (2016).
8. Seino, Y., Ota, T., Takada, K., Hayashi, A. & Tatsumisago, M. A sulphide lithium super ion conductor is superior to liquid ion conductors for use in rechargeable batteries. *Energy. Environ. Sci.* **7**, 627–631 (2014).

9. Bron, P., Dehnen, S. & Roling, B. $Li_{10}Si_{0.3}Sn_{0.7}P_2S_{12}$–A low-cost and low-grain-boundary-resistance lithium superionic conductor. *J. Power Sources* **329**, 530–535 (2016).
10. Kuhn, A. *et al*. A new ultrafast superionic Li-conductor: ion dynamics in $Li_{11}Si_2PS_{12}$ and comparison with other tetragonal LGPS-type electrolytes. *Phys. Chem. Chem. Phys.* **16**, 14669–14674 (2014).
11. Larcher, D. & Tarascon, J. M. Towards greener and more sustainable batteries for electrical energy storage. *Nat. Chem.* **7**, 19–29 (2015).
12. Dunn, B., Kamath, H. & Tarascon, J. M. Electrical energy storage for the grid: a battery of choices. *Science* **334**, 928–935 (2011).
13. Pan, H. L., Hu, Y. S. & Chen, L. Q. Room-temperature stationary sodium-ion batteries for large-scale electric energy storage. *Energy. Environ. Sci.* **6**, 2338–2360 (2013).
14. Hartmann, P. *et al*. A rechargeable room-temperature sodium superoxide (NaO_2) battery. *Nat. Mater.* **12**, 228–232 (2013).
15. Chu, I. H. *et al*. Room-temperature all-solid-state rechargeable sodium-ion batteries with a Cl-doped Na_3PS_4 superionic conductor. *Sci. Rep*. **6** (2016).
16. Song, S. F., Duong, H. M., Korsunsky, A. M., Hu, N. & Lu, L. A Na^+ superionic conductor for room-temperature sodium batteries. *Sci. Rep*. **6** (2016).
17. Goodenough, J. B. Evolution of strategies for modern rechargeable batteries. *Acc. Chem. Res.* **46**, 1053–1061 (2013).
18. Naqash, S., Ma, Q. L., Tietz, F. & Guillon, O. $Na_3Zr_2(SiO_4)_2(PO_4)$ prepared by a solution-assisted solid state reaction. *Solid State Ion.* **302**, 83–91 (2017).
19. Hayashi, A., Noi, K., Sakuda, A. & Tatsumisago, M. Superionic glass-ceramic electrolytes for room-temperature rechargeable sodium batteries. *Nat. Commun.* **3** (2012).
20. Zhang, L. *et al*. Na_3PSe_4: A novel chalcogenide solid electrolyte with high ionic conductivity. *Adv. Energy Mater.* **5**, 1501294 (2015).
21. Yu, C., Ganapathy, S., de Klerk, N. J. J., van Eck, E. R. H. & Wagemaker, M. Na-ion dynamics in tetragonal and cubic Na_3PS_4, a Na-ion conductor for solid state Na-ion batteries. *J. Mater. Chem. A* **4**, 15095–15105 (2016).
22. Ma, Q. L. *et al*. Scandium-Substituted $Na_3Zr_2(SiO_4)_2(PO_4)$ Prepared by a Solution Assisted Solid-State Reaction Method as Sodium-Ion Conductors. *Chem. Mater.* **28**, 4821–4828 (2016).
23. Goodenough, J. B., Hong, H. Y. P. & Kafalas, J. A. Fast Na^+-Ion transport in skeleton structures. *Mater. Res. Bull.* **11**, 203–220 (1976).
24. Hong, H. Y. P. Crystal-structures and crystal-chemistry in system $Na_{1+x}Zr_2Si_xP_{3-x}O_{12}$. *Mater. Res. Bull.* **11**, 173–182 (1976).
25. Kuhn, A., Duppel, V. & Lotsch, B. V. Tetragonal $Li_{10}GeP_2S_{12}$ and Li_7GePS_8–exploring the Li ion dynamics in LGPS Li electrolytes. *Energy. Environ. Sci.* **6**, 3548–3552 (2013).
26. Epp, V. & Wilkening, M. Fast Li diffusion in crystalline $LiBH_4$ due to reduced dimensionality: frequency-dependent NMR spectroscopy. *Phys. Rev. B* **82**, 020301 (2010).
27. Wohlmuth, D., Epp, V. & Wilkening, M. Fast Li ion dynamics in the solid electrolyte $Li_7P_3S_{11}$ as probed by ^{6,7}Li NMR spin-lattice relaxation. *Chem Phys Chem* **16**, 2582–2593 (2015).
28. Epp, V., Gün, O., Deiseroth, H. J. & Wilkening, M. Highly mobile ions: low-temperature NMR directly probes extremely fast Li^+ hopping in argyrodite-type Li_6PS_5Br. *J. Phys. Chem. Lett.* **4**, 2118–2123 (2013).
29. Richards, W. D. *et al*. Design and synthesis of the superionic conductor $Na_{10}SnP_2S_{12}$. *Nat. Commun.* **7**, 1026–1031 (2016).
30. de Klerk, N. J. J. & Wagemaker, M. Diffusion mechanism of the sodium-ion solid electrolyte Na_3PS_4 and potential improvements of halogen doping. *Chem. Mater.* **28**, 3122–3130 (2016).
31. Wang, Y. *et al*. Design principles for solid-state lithium superionic conductors. *Nat. Mater.* **14**, 1026–1031 (2015).
32. He, X. F., Zhu, Y. Z. & Mo, Y. F. Origin of fast ion diffusion in super-ionic conductors. *Nat. Commun.* **8**, 15893 (2017).
33. Wilkening, M. & Heitjans, P. From micro to macro: access to long-range Li^+ diffusion parameters in solids via microscopic ^{6}Li, ^{7}Li spin-alignment echo NMR spectroscopy. *ChemPhysChem* **13**, 53–65 (2012).
34. Preishuber-Pflügl, F., Bottke, P., Pregartner, V., Bitschnau, B. & Wilkening, M. Correlated fluorine diffusion and ionic conduction in the nanocrystalline F^- solid electrolyte $Ba_{0.6}La_{0.4}F_{2.4}$–^{19}F $T_1\rho$ NMR relaxation vs. conductivity measurements. *Phys. Chem. Chem. Phys.* **16**, 9580–9590 (2014).
35. Wilkening, M., Küchler, W. & Heitjans, P. From ultraslow to fast lithium diffusion in the 2D ion conductor $Li_{0.7}TiS_2$ probed directly by stimulated-echo NMR and nuclear magnetic relaxation. *Phys. Rev. Lett.* **97** (2006).
36. Dunst, A., Epp, V., Hanzu, I., Freunberger, S. A. & Wilkening, M. Short-range Li diffusion vs. long-range ionic conduction in nanocrystalline lithium peroxide Li_2O_2–the discharge product in lithium-air batteries. *Energy. Environ. Sci.* **7**, 2739–2752 (2014).
37. Schmidt, W. *et al*. Small change–great effect: steep increase of Li ion dynamics in $Li_4Ti_5O_{12}$ at the early stages of chemical Li insertion. *Chem. Mater.* **27**, 1740–1750 (2015).
38. Uitz, M., Epp, V., Bottke, P. & Wilkening, M. Ion dynamics in solid electrolytes for lithium batteries. *J. Electroceram.* **38**, 142–156 (2017).
39. Zhou, W. D., Li, Y. T., Xin, S. & Goodenough, J. B. Rechargeable sodium all-solid-state battery. *ACS Cent. Sci.* **3**, 52–57 (2017).
40. Park, H., Jung, K., Nezafati, M., Kim, C. S. & Kang, B. Sodium ion diffusion in NASICON ($Na_3Zr_2Si_2PO_{12}$) solid electrolytes: effects of excess sodium. *ACS Appl. Mater. Interfaces* **8**, 27814–27824 (2016).
41. Bloembergen, N., Purcell, E. M. & Pound, R. V. Relaxation effects in nuclear magnetic resonance absorption. *Phys. Rev.* **73**, 679–712 (1948).
42. Bloembergen, N., Purcell, E. M. & Pound, R. V. Nuclear magnetic relaxation. *Nature* **160**, 475–476 (1947).
43. Kaus, M. *et al*. Fast Na^+–ion conduction in NASICON-type $Na_{3.4}Sc_2(SiO_4)_{0.4}(PO_4)_{2.6}$ observed by ^{23}Na NMR relaxometry. *J. Phys. Chem. C* **121**, 1449–1454 (2017).
44. Kohler, H. & Schulz, H. Nasicon solid electrolytes - the Na^+-diffusion path and its relation to the structure. *Mater. Res. Bull.* **20**, 1461–1471 (1985).
45. Jonscher, A. K. Universal dielectric response. *Nature* **267**, 673–679 (1977).
46. Ruprecht, B., Billetter, H., Ruschewitz, U. & Wilkening, M. Ultra-slow Li ion dynamics in Li_2C_2–on the similarities of results from ^{7}Li spin-alignment echo NMR and impedance spectroscopy. *J. Phys.: Condens. Matter* **22**, 245901 (2010).
47. Kuhn, A. *et al*. NMR relaxometry as a versatile tool to study Li ion dynamics in potential battery materials. *Solid State Nucl. Magn. Reson.* **42**, 2–8 (2012).
48. Kuhn, A. *et al*. Li self-diffusion in garnet-type $Li_7La_3Zr_2O_{12}$ as probed directly by diffusion-induced ^{7}Li spin-lattice relaxation NMR spectroscopy. *Phys. Rev. B* **83**, 094302 (2011).
49. Epp, V., Ma, Q. L., Hammer, E. M., Tietz, F. & Wilkening, M. Very fast bulk Li ion diffusivity in crystalline $Li_{1.5}Al_{0.5}Ti_{1.5}(PO_4)_3$ as seen using NMR relaxometry. *Phys. Chem. Chem. Phys.* **17**, 32115–32121 (2015).
50. Breuer, S. *et al*. Separating bulk from grain boundary Li ion conductivity in the sol-gel prepared solid electrolyte $Li_{1.5}Al_{0.5}Ti_{1.5}(PO_4)_3$. *J. Mater. Chem. A* **3**, 21343–21350 (2015).

Acknowledgements

We thank our colleagues at the TU Graz for valuable discussions. Financial support from the Deutsche Forschungsgemeinschaft (DFG Research Unit 1277, grant no. WI3600/2–2 and 4–1) as also from the Austrian Federal Ministry of Science, Research and Economy, and the Austrian National Foundation for Research, Technology and Development (CD-Laboratory of Lithium Batteries: Ageing Effects, Technology and New Materials) is greatly appreciated. We also thank the FFG for financial support (project: safe battery).

Author Contributions

All authors conceived and supervised the project and also contributed to the interpretation of the data.

Additional Information

Supplementary information accompanies this paper at https://doi.org/10.1038/s41598-018-30478-7.

Competing Interests: The authors declare no competing interests.

Publisher's note: Springer Nature remains neutral with regard to jurisdictional claims in published maps and institutional affiliations.

Open Access This article is licensed under a Creative Commons Attribution 4.0 International License, which permits use, sharing, adaptation, distribution and reproduction in any medium or format, as long as you give appropriate credit to the original author(s) and the source, provide a link to the Creative Commons license, and indicate if changes were made. The images or other third party material in this article are included in the article's Creative Commons license, unless indicated otherwise in a credit line to the material. If material is not included in the article's Creative Commons license and your intended use is not permitted by statutory regulation or exceeds the permitted use, you will need to obtain permission directly from the copyright holder. To view a copy of this license, visit http://creativecommons.org/licenses/by/4.0/.

© The Author(s) 2018

7 Conclusion

Within the scope of this doctoral thesis two different topics were addressed. In the first part we considered amorphous TiO_2 nanotubes as possible anode material for Na-ion batteries. They were prepared by a conventional electrochemical oxidation (anodization) process and electrochemically characterized by techniques such as galvanostatic cycling with potential limitation and cyclic voltammetry. To enhance their functional properties or create entirely new ones these nanotubular arrays were modified by filling with different metals. In the second part we studied ion dynamics and diffusion-induced parameters of two Li-bearing sulfide-based solid electrolytes (β-Li_3PS_4 and $LiTi_2(PS_4)_3$) and one Na-ion conducting material (NASICON compound $Na_{3.4}Sc_{0.4}Zr_{1.6}SiP_4O_{12}$) on different length-scales taking advantage of impedance spectroscopy and solid-state NMR relaxation. Although at first glance these two topics are different, they converge towards the same objective – the realization of powerful, safe and reliable batteries.

TiO_2 nanotubes. These materials were most intensively studied within this doctoral thesis. Several titania nanotube samples, having different lengths and diameters, were investigated with respect to their electrochemical behavior and Na^+ insertion properties. They showed excellent cycle-life being able to withstand a large number of cycles (about 300) without significant capacity loss. Cyclic voltammetry experiments allowed the disclosure of the underlying storage mechanism. It was noticed that, in contrast to lithium insertion into TiO_2, where most of the stored Li^+ ions can be found in the bulk regions, sodium storage preferentially occurs on the surface of the titania nanotube walls. The low determined diffusion coefficient values in the order of 10^{-20} cm^2/s support the proposed interfacial storage mechanism. The interfacial layer between the liquid electrolyte and the titania nanotubes, which host most of the sodium ions, exhibit pseudocapacitive behavior making these materials suitable for supercapacitor applications.

The highly ordered geometry of the titania nanotubes allows for the introduction of a second functional material into their inner volume. We report, for the first time, on the successful filling of these nanotubular arrays with metallic tin, antimony and nickel using a pulsed-current electrodeposition approach. Electrodeposition of tin inside TiO_2 nanotubes was studied in more detail. SEM investigations of the prepared tin-titania nanocomposites revealed that deposition starts on the tube tops. This behavior disagrees with observations already published in the literature, where the tube bottoms were suggested as preferred place for nucleation and growth. Thus, we propose a quite different deposition mechanism compared to the classical one. We

assume that the growth of tin inside the tubes takes place indirectly via a redox-mediated mechanism, where the titanium substrate acts as redox mediator.

Furthermore, these tin-titania nanotubular arrays were tested for their Li^+ and Na^+ storage capability. Galvanostatic cycling experiments showed that filling of these nanotubes with Sn does not have a positive effect in terms of accessible capacity. Lower volumetric capacity values were achieved in contrast to the pristine TiO_2 nanotubes. However, the nanotubular structure prevents aggregation of tin particles and restrains volume changes during charging and discharging leading to a better cycling stability compared to a pure Sn electrode.

Solid electrolytes. The glass-ceramic β-Li_3PS_4 was the first studied solid electrolyte material in this doctoral thesis. It was prepared by high-energy ball milling followed by heat treatment at 160°C. To experimentally test the existence of low-dimensional diffusion pathways being responsible for the fast Li^+ ion dynamics in this β-modification, we used the combination of both, ^{7}Li solid-state NMR and conductivity spectroscopy. The dispersive regimes, showing up at higher frequencies of the conductivity isotherms indicate low-dimensional diffusion processes. ^{7}Li relaxometry measurements, which provide information on Li-ion dynamics on the angstrom length-scale, can support this view. The asymmetric diffusion-induced rate peak points toward a 1D Li-ion diffusion pathway in the thiophosphate, which is characterized by a low activation energy. Frequency-dependent spin-lattice relaxation measurements in the rotating frame of reference provide further evidence for the presence of this low-dimensional channel-like migration pathway. To conclude, our results support the theoretical considerations of low-dimensional migration processes in β-Li_3PS_4 involving regular and interstitial sites in the structure [239]. The predicted snake-like 1D diffusion pathway occurs in addition to vacancy-mediated Li ion transport in three dimensions, but is energetically much more favorable.

The sulfide-based superionic conductor $LiTi_2(PS_4)_3$ has already been studied by PFG NMR measurements, impedance spectroscopy and molecular dynamic simulations [232]. It turned out that extremely fast jump processes are present in LTPS taking place between interconnected pocket-like regions either within a ring or between the ring configurations. To show a further proof for these fast Li exchange processes in LTPS we made use of temperature-variable ^{7}Li spin-lattice relaxation and spin-lock NMR experiments. The two R_1 rate peaks observed by SLR measurements in the laboratory frame of reference indicate two type of diffusion processes, which are characterized by diffusion coefficients in the order of 2.4×10^{-11} m^2s^{-1} (340 K) and 6.4×10^{-12} m^2s^{-1} (214 K), respectively. The activation energies extracted are very low ranging from 0.10 – 0.14 eV. ^{7}Li NMR relaxometry performed in the rotating frame of reference gives access to a third rate peak, which is attributed to Li^+ hopping along a different diffusion pathway being activated at higher temperatures only. The extremely fast Li exchange processes are further confirmed by ^{7}Li NMR line shape measurements. Furthermore, the diffusion process being characterized by forward-backward jumps between the pocket regions within a ring is, to our knowledge, one of the fastest exchange processes seen by NMR relaxometry so far.

The scandium-substituted NASICON-type compound $Na_{3.4}Sc_{0.4}Zr_{1.6}SiP_4O_{12}$, which has been prepared via a sol gel route, served as model substance for the study of ion dynamics in a Na-ion conducting material making use of ^{23}Na spin-lattice relaxation NMR and broadband impedance spectroscopy. It turned out that extremely fast Na ion dynamics are present at ambient temperatures resulting in high ionic conductivities of 2 mS/cm. Such fast movements of the Na^+ ions in the 3D network result in successful jump processes and thus facilitate macroscopic diffusion. Additionally, several diffusion-induced rate peaks are observed by ^{23}Na NMR spin-lattice relaxation measurements pointing towards complex Na^+ ion dynamics in the three-dimensional framework of the phosphosilicate.

8 Author contributions

P1: I performed the cyclic voltammetry experiments and synthesized the samples. Together with I.H. I interpreted the results. I.H. wrote the paper with input from D.P. All authors contributed to the discussion of the results. The SEM micrographs were acquired by Sanja Simic (FELMI-ZFE).

P2: I synthesized and characterized the samples by cyclic voltammetry, galvanostatic cycling and scanning electron microscopy. Together with I.H. I analyzed and interpreted the results and wrote the paper. EDX analysis was performed by Sanja Simic (FELMI-ZFE). XRD measurements were conducted by Brigitte Bitschnau (Institute of Physical and Theoretical Chemistry). All authors contributed to the discussion of the results.

P3: H.B., V.P. and D.W. synthesized the samples. H.B. and V.P. characterized the samples by impedance spectroscopy; with the help of V.E. and B.S. I carried out the NMR experiments. Together with B.G and M.W I analyzed the data. M.W. wrote the paper with input from D.P. and B.G..

P4: D.P., S.B., M.U., P.B., J.L., S.L., M.P., P.P., V.P., B.S., A.D., D.W., H.B. and W.S. performed the experiments. Together with M.W. and I.H. the authors D.P., S.B., M.U., P.B., J.L., M.P., P.P., V.P., B.S., A.D., D.W., H.B. and W.S. analyzed and interpreted the data. M.W. and I.H. wrote the paper with input from all authors.

P5: I carried out the impedance measurements and analyzed the data; S.L. recorded ^{23}Na NMR rates and analyzed the results. S.L. performed the polarization measurements together with I.H. The sample itself has been prepared by Q.M. and F.T. All authors contributed to the interpretation of the data. M.W. wrote the paper with input of all authors.

M1: I synthesized all the samples. Together with I.H. I interpreted the results and wrote the manuscript. The SEM micrographs and EDX spectra were acquired by Sanja Simic (FELMI-ZFE). All authors contributed to the discussion of the results.

M2: I synthesized and characterized the samples by cyclic voltammetry and galvanostatic cycling. Together with I.H. I analyzed the data, interpreted the results and wrote the manuscripts. The SEM micrographs were acquired by Sanja Simic (FELMI-ZFE). All authors contributed to the discussion of the results.

M3: I carried out the NMR experiments and analyzed the data. Together with M.W. I interpreted the results and wrote the manuscript. The sample itself has been prepared and characterized by Y. Kato (Toyota). All authors contributed to the discussion of the results.

A Supporting information

A.1 Used equipment

NMR spectrometer: Bruker Avance III 300 WB connected to a shimmed-cryomagnet with a magnetic field of 7 T.
Bruker Avance III Ultrashield 500 WB Plus equipped with a magnet of 11 T.

NMR probe heads: ceramic probe head: Bruker HP BBHT 500WB Sol5 Ceramics

teflon probe head: Bruker PH HPBBHT600WB SOL10

Both probe heads use a Eurotherm unit connected with a T thermocouple to control and monitor the temperature.

cryo probe head: HP BB LT SOL5

Temperature is controlled with a LakeShore 331 element equipped with two Cernox sensors.

Impedance spectrometer: Novocontrol Concept 80 broadband analyzer connected to a BDS 1200 cell in combination with an active ZGS cell interface.
The temperature is controlled with a QUATRO cryo-system (Novocontrol).

Glove boxes: MBRAUN 150B-G and MBRAUN LABstar
(O_2 and H_2O < 1ppm)

High-energy ball mill: FRITSCH Pulverisette Premium line 7 with air-tight grinding beaker made of ZrO_2 equipped with ZrO_2 milling balls.

Powder press set: P/O/WEBER PE 30 and SPECAC

Sputter coater:	LEICA EM SCD 050
X-ray diffractometer:	BRUKER D8 Advance diffractometer with Bragg-Brentano geometry and CuK_{α} radiation.
Furnace:	REETZ LOBA 1200-45-400-1-OW tube furnace equipped with OMRON E5CK-T temperature control unit
Scanning electron microscop:	TESCAN VEGA3
Cryostat:	Julabo FP 50 ME
Potentiostat/galvanostat:	Multichannel MPG-2 and VMP-3 potentiostat from Biologic Science Instruments For electrodeposition experiments the VMP-3 was connected to a 20 A current booster from Biologic. Autolab PGSTAT100 equipped with a booster BSTR 10A
DC power supplies:	Agilent E 3612 A Voltcraft PSP 1803

A.2 Used software

Topspin 3.1 (BRUKER):	Realization of NMR experiments on BRUKER Avance III spectrometers; Fourier transformation and phase correction of the obtained NMR spectra.
WinDETA 5.73 (NOVOCONTROL):	Acquisition of impedance experiments along with data export.
EC-LAB:	Software to run experiments on the Biologic MPG-2 / VMP-3 potentiostat; evaluation of data
NOVA 1.11:	Software to run experiments on the Autolab potentiostat
VESTA 3.4.3:	Visualization of crystallographic structures.

IGOR Pro 6.3.7:	Software for processing, analysis and presentation of data.
CorelDRAW 8:	Graphical program for post-processing of figures used for presentations and publiations.
EndNote X7.3.1:	Management of references.
Microsoft Word 2010:	Text processing.

B Bibliography

1. M. Armand, and J.-M. Tarascon, *Nature*, **451** (2008) 652.
2. J.-M. Tarascon, *ChemSusChem*, **1** (2008) 777-779.
3. J.B. Goodenough and Y. Kim, *Chem. Mater.*, **22** (2010) 587-603.
4. D. Larcher and J.M. Tarascon, *Nat. Chem.*, **7** (2014) 19.
5. C.P. Grey and J.-M. Tarascon, *Nat. Mater.*, **16** (2016) 45.
6. S.Y. Hong, Y. Kim, Y. Park, A. Choi, N.-S. Choi and K.T. Lee, *Energy Environ. Sci.*, **6** (2013) 2067-2081.
7. J.-M. Tarascon and M. Armand, *Nature*, **414** (2001) 359-367.
8. M.R. Palacin, *Chem. Soc. Rev.*, **38** (2009) 2565-2575.
9. X.-P. Gao and H.-X. Yang, *Energy Environ. Sci.*, **3** (2010) 174-189.
10. G. Zubi, R. Dufo-Lopez, M. Carvahlo and G. Pasaoglu, *Renew. Sust. Energ. Rev.*, **89** (2018) 292-308.
11. B. Dunn, H. Kamath, and J.-M. Tarascon, *Science*, **334** (2011) 928-935.
12. N. Nitta, F. Wu, J. T. Lee and G. Yushin, *Mater. Today*, **18** (2015) 252-264.
13. C. Wadia, P. Albertus and V. Srinivasan, *J. Power Sources*, **196** (2011) 1593-1598.
14. V. Palomares, P. Serras, I. Villaluenga, K.B. Hueso, J. Carretero-Gonzalez, T. Rojo, *Energy Environ. Sci.*, **5** (2012) 5884-5901.
15. V. Palomares, M. Casas-Cabanas, E. Castillo-Martinez, M.H. Han, T. Rojo, *Energy Environ. Sci.*, **6** (2013) 2312-2337.
16. H. Pan, Y.-S. Hu, and L. Chen, Energy Environ. Sci., **6** (2013) 2338-2360.
17. M.D. Slater, D. Kim, E. Lee and C.S. Johnson, *Adv. Funct. Mater.*, **23** (2013) 947-958.
18. Y. Wang and W.-H. Zhong, *ChemElectroChem*, **2** (2015) 22-36.
19. P. Knauth, *Solid State Ionics*, **180** (2009) 911-916.
20. J. Li, C. Ma, M. Chi, C. Liang and N.J. Dudney, *Adv. Energy Mater.*, **5** (2015) 1401408.
21. C. Jiang, H. Li and C. Wang, *Sci. Bull.*, **62** (2017) 1473-1490.
22. A. Manthiram, X. Yu and S. Wan, *Nat. Rev. Mater.*, **2** (2017) 16103.
23. M. Uitz, V. Epp, P. Bottke and M. Wilkening, *J. Electroceram.*, **38** (2017) 142-156.
24. J.M. Tarascon and M. Armand, *Nature*, **414** (2001) 359.
25. S. Goriparti, E. Miele, F. De Angelis, E. Di Fabrizio, R. Zaccaria and C. Capiglia, J. Power Sources, **257** (2014) 421-443.
26. B.L. Ellis and L.F. Nazar, *Curr. Opin. Solid State Mater. Sci.*, **16** (2012) 168-177.
27. R. Korthauer, *Handbuch Lithium-Ionen-Batterien*. Springer Verlag Berlin Heidelberg, Berlin, 2013.
28. D. Linden and T.B. Reddy, *Handbook of batteries*, McGraw-Hill, 2002.
29. C. Daniel and J.O. Besenhard, *Handbook of Battery Materials*, Wiley-VCH Verlag, 2011.
30. P. Moreau, D. Guyomard, J. Gaubichler and F. Boucher, *Chem. Mater.*, **22** (2010) 4126-4128.
31. X. Yuan, H. Liu and J. Zhang, *Lithium-Ion Batteries: Advanced Materials and Technologies*, CRC Press, 2016.
32. M. Winter, J.O. Besenhard, M.E. Spahr and P. Novak, *Adv. Mater.*, **10** (1998) 725-763.

33. P.V. Braun, J. Cho, J. H. Pikul, W. P. King and H. Zhang, Curr. Opin. Solid State Mater. Sci., **16** (2012) 186-198.
34. J.-H. Kim, M.-J. Jung, M.-J. Kim and Y.-S. Lee, *J. Ind. Eng. Chem.*, **61** (2018) 368-380.
35. S.S. Zhang, S.S., *J. Power Sources*, **161** (2006) 1385-1391.
36. G.-N. Zhu Y.-G. Wang and Y.-Y. Xia, *Energy Environ. Sci.*, **5** (2012) 6652-6667.
37. H. Fujimoto, K. Tokumitsu, A. Mabuchi, N. Chinnasamy and T. Kasuh, *J. Power Sources*, **195** (2010) 7452-7456.
38. J. Yang, X.-Y. Zhou, J. Li, Y.-I. Zou and J.-J. Tang, *Mater. Chem. Phys.*, **135** (2012) 445-450.
39. D.A. Stevens and J.R. Dahn, *J. Electrochem. Soc.*, **148** (2001) A803-A811.
40. D.P. DiVincenzo and E.J. Mele, Phys. Rev. B, **32** (1985) 2538-2553.
41. J. Sangster, *J. Phase Equilib. Diff.*, **28** (2007) 571-579.
42. D.A. Stevens and J.R. Dahn, J. Electrochem. Soc., **147** (2000) 1271-1273.
43. S. Komaba, W. Murata, T. Ishikawa, N. Yabuuchi, Z. Ozeki, T. Nakayama, A. Ogata, K. Gotoh and K. Fujiwara, Adv. Funct. Mater., **21** (2011) 3859-3867.
44. R. Alcántara, J.M. Jiménez Mateos and J.L. Tirado, *J. Electrochem. Soc.*, **149** (2002) A201-A205.
45. M.M. Doeff, Y. Ma, S.J. Visco and L.C. DeJonghe, J. Electrochem. Soc., **140** (1993) L169-L170.
46. R. Alcántara, J.M. Jiménez-Mateos, P. Lavela and J.L. Tirado, *Electrochem. Commun.*, **3** (2001) 639-642.
47. P. Thomas and D. Billaud, *Electrochim. Acta*, **46** (2001) 3359-3366.
48. H.-G. Wang, Z. Wu, F.-I. Meng, D.-I. Ma, X.-I. Huang, L.-M. Wang and X.-B. Zhang, *ChemSusChem*, **6** (2013) 56-60.
49. K. Tang, L. Fu, R.J. White, L. Yu, M.-M. Titirici, M. Antonietti and J. Maier, *Adv. Energy Mater.*, **2** (2012) 873-877.
50. Y. Cao, L. Xiao, M. Sushko, W. Wang, B. Schwenzer, J. Xiao, Z. Nie, L.V. Saraf, Z. Yang and J. L., Nano Lett., **12** (2012) 3783-3787.
51. D. Deng, M.G. Kim, J.Y. Lee and J. Cho, *Energy Environ. Sci.*, **2** (2009) 818-837.
52. C. Jiang, I. Honma, T. Kudo and H. Zhou, *Electrochem. Solid-State Lett.*, **10** (2007) A127-A129.
53. V. Gentili, S. Brutti, L.J. Hardwick, A.R. Armstrong, S. Panero and P.G Bruce, *Chem. Mater.*, **24** (2012) 4468-4476.
54. H. Liu, Z. Bi, X.-G. Sun, R.R. Unocic, M.P. Paranthaman, S. Dai and G.M. Brown, *Adv. Mater.*, **23** (2011) 3450-3454.
55. L. Zhao, H.-L. Pan, Y.-S. Hu, H. Li and L.-Q. Chen, *Chin. Phys. B*, **21** (2012) 028201.
56. P. Senguttuvan, G. Rousse, V. Seznec, J.-M- Tarascon and M.R. Palacin, *Chem. Mater.*, **23** (2011) 4109-4111.
57. D. Prutsch, M. Wilkening and I. Hanzu, *ACS Appl. Mater. Interfaces*, 7 (2015) 25757-25769.
58. L. Wu, D. Buchholz, D. Bresser, L.G. Chagas and S. Passerini, *J. Power Sources*, **251** (2014) 379-385.
59. J.P. Huang, D.D. Yuan, H.Z. Zhang, Y.L. Cao, G.R. Li, H. X. Yang and X.P. Gao, *RSC Adv.*, **3** (2013) 12593-12597.
60. W. Jiajun, C.W.Y.c. Karen and W. Jun, *Angew. Chem. Int. Ed.*, **53** (2014) 4460-4464.
61. M. Winter and J.O. Besenhard, *Electrochim. Acta*, **45** (1999) 31-50.
62. C.K. Chan, H. Peng, G. Liu, K. McIlwarth, X.F. Zhang, R.A. Huggins and Y. Cui, *Nat. Nanotechnol.*, 3 (2007) 31.
63. C.-M. Park, J.-H. Kim, H. Kim and H.-J. Sohn, *Chem. Soc. Rev.*, **39** (2010) 3115-3141.
64. N. Liu, Z. Lu, J. Zhao, M.T. McDowell, H.-W. Lee, W. Zhao and Y. Cui, *Nat. Nanotechnol.*, **9** (2014) 187.
65. K.D. Kepler, J.T. Vaughey and M.M. Thackeray, *Electrochem. Solid-State Lett.*, **2** (1999) 307-309.
66. A.-R. Park, K.-J. Jeon and C.-M. Park, *Electrochim. Acta*, **265** (2018) 107-114.

67. I. Chumak, M. Hinterstein and H. Ehrenberg, *Prog. Solid State Chem.*, **42** (2014) 149-156.
68. S. Komaba, Y. Matsuura, T. Ishikawa, N. Yabuuchi and S.Kuze, *Electrochem. Commun.*, **21** (2012) 65-68.
69. J.W. Wang, X.H. Liu, S.X. Mao and J.Y. Huang, *Nano Lett.*, **12** (2012) 5897-5902.
70. L.D. Ellis, T.D. Hatchard and M.N. Obrovac, *J. Electrochem. Soc.*, **159** (2012) A1801-A1805.
71. A. Darwiche, C. Marino, M.T. Sougrati, B. Fraisse, L. Stievano and L. Monconduit, *J. Am. Chem. Soc.*, **134** (2012) 20805-20811.
72. J. Qian, Y. Chen, L. Wu, Y. Cao, X. Ai and H. Yang, *Chem. Commun.*, **48** (2012) 7070-7072.
73. Y. Xu, Y. Zhu, Y. Liu and C. Wang, *Adv. Energy Mater.*, **3** (2013) 128-133.
74. L. Xiao, Y. Cao, J. Xiao, W. Wang, L. Kovarik, Z. Nie and J. Liu, *Chem. Commun.*, **48** (2012) 3321-3323.
75. L. Ji, Z. Lin, M. Alcoutlabi and X. Zhang, *Energy Environ. Sci.*, **4** (2011) 2682-2699.
76. R. Alcántara, M. Jaraba, P. Lavela and J.L. Tirado, *Chem. Mater.*, **14** (2002) 2847-2848.
77. Q. Sun, Q.-Q. Ren, H. Li and Z.-W. Fu, *Electrochem. Commun.*, **13** (2011) 1462-1464.
78. B. Koo, S. Chattopadhyay, T. Shibata, V.B. Prakapenka, C.S. Johnson, T. Rajh and E.V. Shevchenko, *Chem. Mater.*, **25** (2013) 245-252.
79. S. Komaba, T. Mikumo and A. Ogata, *Electrochem. Commun.*, **10** (2008) 1276-1279.
80. J.-S. Kim, H.-J. Ahn, H.-S. Ryu, D.-J. Kim, G.-H. Cho, K.-W. Kim, T.-H. Nam and J.H. Ahn, *J. Power Sources*, **178** (2008) 852-856.
81. T.B. Kim, W.H. Jung, H.S. Ryu, K.W. Kim, J.H. Ahn, K.K. Cho, G.B. Cho, T.H. Nam, I.S. Ahn and H.J. Ahn, *J. Alloys Compd.*, **449** (2008) 304-307.
82. A.S. Nagelberg and W.L. Worrell, *J. Solid State Chem.*, **29** (1979) 345-354.
83. M. Mortazavi, C. Wang, J. Deng, V.B. Shenoy and N.V. Medhekar, *J. Power Sources*, **268** (2014) 279-286.
84. L. W Shacklette, T.R. Jow and L. Townsend, *J. Electrochem. Soc.*, **135** (1988) 2669-2674.
85. J. Molenda and A. StokŁlosa, *Solid State Ionics*, **38** (1990) 1-4.
86. S. Komaba, C. Takei, T. Nakayama, A. Ogata and N. Yabuuchi, *Electrochem. Commun.*, **12** (2010) 355-358.
87. I. Saadoune, A. Maazaz, M. Ménétrier and C. Delmas, et al., *J. Solid State Chem.*, **122** (1996) 111-117.
88. F. Sauvage, L. Laffont, J.-M. Tarascon and E. Baudrin, F., *Inorg. Chem.*, **46** (2007) 3289-3294.
89. K. West, B. Zachau-Christiansen, T. Jacobsen and S. Skaarup, *Solid State Ionics*, **28-30** (1988) 1128-1131.
90. S.-M. Oh, S.-T. Myung, J. Hassoun, B. Scrosati and Y.-K. Sun, *Electrochem. Commun.*, **22** (2012) 149-152.
91. J.B. Goodenough, H.Y.P. Hong and J.A. Kafalas, *Mater. Res. Bull.*, **11** (1976) 203-220.
92. R.A. Shakoor, D.-H. Seo, H. Kim, Y.-U. Park, J. Kim, S.-W. Kim, H. Gwon, S. Lee and K. Kang *J. Mater. Chem.*, **22** (2012) 20535-20541.
93. B.L. Ellis, W.R.M. Makahnouk, Y. Makimura, K. Toghill and L.F. Nazar, *Nat. Mater.*, **6** (2007) 749.
94. J. Barker, M.Y. Saidi and J.L. Swoyer, *Electrochem. Solid-State Lett.*, **6** (2003) A1-A4.
95. A. Ponrouch, E. Marchante, M. Courty, J.-M. Tarascon and M. R. Palacín, *Energy Environ. Sci.*, **5** (2012) 8572-8583.
96. L. Schafzahl, I. Hanzu, M. Wilkening and S.A. Freunberger, ChemSusChem, **10** (2017) 401-408.
97. C.N.R. Rao, A. Müller and A.K. Cheetham, *The Chemistry of Nanomaterials: Synthesis, Properties and Applications*, Wiley-VCH, Weinheim, Germany, 2006.
98. C.M. Lieber, *Solid State Commun.*, **107** (1998) 607-616.

99. Y. Kia, P. Yang, Y. Sun, Y. Wu, B. Mayers, B. Gates, Y. Yin, F. Kim and H. Yan, *Adv. Mater.*, **15** (2003) 353-389.
100. C.N.R. Rao and M. Nath, *Dalton Trans.*, (2003) 1-24.
101. J.L.G. Fierro, *Metal Oxides: Chemistry and Applications.*, CRC Press, 2006.
102. D.V. Bavykin, J.M. Friedrich and F.C. Walsh, *Adv. Mater.*, **18** (2006) 2807-2824.
103. P. Roy, S. Berger and P. Schmuki, *Angew. Chem. Int. Ed.*, **50** (2011) 2904-2939.
104. J.M. Macak, H. Tsuchiya, A. Ghicov, K. Yasuda, R. Hahn, S. Bauer and P. Schmuki, *Curr. Opin. Solid State Mater. Sci.*, **11** (2007) 3-18.
105. J.M. Macák, H. Tsuchiya, A. Ghicov and P. Schmuki, *Electrochem. Commun.*, **7** (2005) 1133-1137.
106. H. Xiong, M.D. Slater, M. Balasubramanian, C.S. Johnson and T. Rajh, *J. Phys. Chem. Lett.*, **2** (2011) 2560-2565.
107. M. Paulose, O.K. Varghese, G.K. Mor, C.A. Grimes and K. G. Ong, *Nanotechnology*, **17** (2006) 398.
108. J.M. Macak, F. Schmidt-Stein and P. Schmuki, *Electrochem. Commun.*, **9** (2007) 1783-1787.
109. A.L. Linsebigler, G. Lu and J.T. Yates, *Chem. Rev.*, **95** (1995) 735-758.
110. R. Wang, K. Hashimoto, A. Fujishima, M. Chikuni, E. Kojima, A. Kitamura, M. Shimohigoshi and T. Watanabe, Adv. Mater., **10** (1998) 135-138.
111. S.-H. Oh, R.R. Finones, C. Daraio, L.-H. Chen and S. Jin, *Biomaterials*, **26** (2005) 4938-4943.
112. A. Ghicov, H. Tsuchiya, R. Hahn, J.M. Macak, A.G. Muños and P. Schmuki, *Electrochem. Commun.*, **8** (2006) 528-532.
113. J.M. Macak and P. Schmuki, *Electrochim. Acta*, **52** (2006) 1258-1264.
114. S. Berger, R. Hahn, P. Roy and P. Schmuki, et al., *Self-organized TiO2 nanotubes: Factors affecting their morphology and properties. Phys. Status Solidi B*, **247** (2010) 2424-2435.
115. D. Kowalski, D. Kim and P. Schmuki, *Nano Today*, **8** (2013) 235-264.
116. S. Berger, S.P. Albu, F. Schmidt-Stein, H. Hildebrand, P. Schmuki, J.S. Hammond, D.F. Paul and S. Reichlmaier, *Surf. Sci.*, **605** (2011) L57-L60.
117. J.M. Macak, S.P. Albu and P. Schmuki, *Phys. Status Solidi (RRL)*, **1** (2007) 181-183.
118. Y.-Y. Song, R. Lynch, D. Kim, P. Roy and P. Schmuki, *Electrochem. Solid-State Lett.*, **12** (2009) C17-C20.
119. D. Kim, A. Ghicov and P. Schmuki, *Electrochem. Commun.*, **10** (2008) 1835-1838.
120. J.M. Macak, H. Hildebrand, U. Marten-Jahns and P. Schmuki, *J. Electroanal. Chem.*, **621** (2008) 254-266.
121. Z. Lockman, S. Sreekantan, S. Ismail, L. Schmidt-Mende and J.L. MacManus-Driscoll, *J. Alloys Compd.*, **503** (2010) 359-364.
122. N.-S. Peighambardoust and F. Nasirpouri, *Surf. Coat. Technol.*, **235** (2013) 27-734.
123. A. Valota, D.J. LeClere, P. Skeldon, M. Curioni, T. Hashimoto, S. Berger, J. Kunze, P. Schmuki and G.E. Thompson, *Electrochim. Acta*, **54** (2009) 4321-4327.
124. J.M. Macak, H. Tsuchiya, L. Taveira, S. Aldabergerova and P. Schmuki, *Angew. Chem. Int. Ed.*, **44** (2005) 7463-7465.
125. S.P. Albu, A. Ghicov, J.M. Macák and P. Schmuki, *Phys. Status Solidi (RRL)*, **1** (2007) R65-R67.
126. A. Khataee and G.A. Mansoori, *Nanostructured Titanium Dioxide Materials: Properties, Preparation and Applications*, World Scientific Publishing Co. Pte. Ltd., 2012.
127. Q.-J. Liu, Z. Ran, F.-S. Liu and Z.-T. Liu, *J. Alloys Compd.*, **632** (2015) 192-201.
128. Z. Su, L. Zhang, F. Jiang and M. Hong, *Prog. Nat. Sci.*, **23** (2013) 294-301.
129. J. Kunze, A. Seyeux and P. Schmuki, *Electrochem. Solid-State Lett.*, **11** (2008) K11-K13.
130. S. Bauer, A. Pittrof, H. Tsuchiya and P. Schmuki, *Electrochem. Commun.*, **13** (2011) 538-541.

131. K. Eufinger, D. Poelman, H. Poelman, R. DeGryse and G.B. Marin, *Appl. Surf. Sci.*, **254** (2007) 148-152.
132. A.G. Muñoz, Q. Chen and P. Schmuki, *J. Solid State Electrochem.*, **11** (2007) 1077-1084.
133. P. Roy, S. Berger and P. Schmuki, *Angew. Chem. Int. Ed.*, **50** (2011) 2904-2939.
134. R.P. Lynch, A. Ghicov and P. Schmuki, *J. Electrochem. Soc.*, **157** (2010) G76-G84.
135. V.V. Sergentu, I.M. Tiginyanu, V.V. Ursaki, M. Enachi, S.P. Albu and P. Schmuki, *Phys. Status Solidi (RRL)*, **2** (2008) 242-244.
136. M. Kunat, U. Burghaus and C. Wöll, *Phys. Chem. Chem. Phys.*, **6** (2004) 4203-4207.
137. S. Funk and U. Burghaus, *Catal. Lett.*, **118** (2007) 118-122.
138. B: Hokkanen, S. Funk, U. Burghaus, A. Ghicov and P. Schmuki, *Surf. Sci.*, **601** (2007) 4620-4628.
139. S. Funk, B. Hokkanen and U. Burghaus, *Nano Lett.*, **7** (2007) 1091-1094.
140. Y.-Y. Song, Z.-D. Gao, J.-H. Wang, X.-H. Xia and R. Lynch, *Adv. Funct. Mater.*, **21** (2011) 1941-1946.
141. Y.C. Nah, I. Paramasivam and P. Schmuki, *ChemPhysChem*, **11** (2010) 2698-2713.
142. R. Helmy and A.Y. Fadeev, *Langmuir*, **18** (2002) 8924-8928.
143. E. Balaur, J.M. Macak, L. Taveira and P. Schmuki, *Electrochem. Commun.*, **7** (2005) 1066-1070.
144. J.M. Macak, S. Aldabergerova, A. Ghicov and P. Schmuki, *Physica Status Solidi A*, **203** (2006) 6tgzR67-R69.
145. A. Tighineanu, S.P. Albu and P. Schmuki, *Phys. Status Solidi (RRL)*, **8** (2014) 158-162.
146. S.P. Albu, A. Ghicov, S. Aldabergenova, P. Drechsel, D. LeCLere, G.E. Thompson, J.M. Macak and P. Schmuki, *Adv. Mater.*, **20** (2008) 4135-4139.
147. Y.-Y. Song, H. Hildebrand and P. Schmuki, *Surf. Sci.*, **604** (2010) 346-353.
148. S.P. Albu, H. Tsuchiya, S. Fujimoto and P. Schmuki, *J. Inorg. Chem.*, **2010** (2010) 4351-4356.
149. A. Tighineanu, T. Ruff, S. Albu, R. Hahn and P. Schmuki, *Chem. Phys. Lett.*, **494** (2010) 260-263.
150. N.K. Shrestha, M. Yang, Y.-C. Nah, I. Paramasivam and P. Schmuki, *Electrochem. Commun.*, **12** (2010).254-257.
151. N.K. Shrestha, J.M. Macak, F. Schmidt-Stein, R. Hahn, C.T. Mierke, B. Fabry and P. Schmuki, *Angew. Chem. Int. Ed.*, **48** (2009).969-972.
152. I. Paramasivam, J.M. Macak, A.Ghicov and P. Schmuki, *Chem. Phys. Lett.*, **445** (2007) 233-237.
153. H. Mehrer, *Diffusion in Solids: Fundamentals, Methods, Materials, Diffusion-Controlled Processes.*, Springer, Berlin, 2007.
154. P. Heitjans and J. Kärger, *Diffusion in Condensed Matter - Methods, Materials, Models.*, Springer, Berlin, 2005.
155. J. Pelleg, *Diffusion in Ceramics.*,Springer, Berlin, 2016.
156. G. Kostorz, *Phase Transformations in Materials.*, WILEY-VCH, 2010.
157. J.C. Bachman, S: Muy, A. Grimaud, H.-H. Chang, N. Pour, S.F. Lux, O. Paschos, F. Maglia, S. Lupart, P. Lamp, L. Giordano and Y- Shao-Horn, *Chem. Rev.*, **116** (2016).140-162.
158. R.J.D. Tilley, *Defects in Solids.*, Wiley, 2008.
159. A.R.West, *Solid State Chemistry and Its Applications.*, Wiley, 2014.
160. H. Schmalzried, *Chemical Kinetics of Solids.*, VCH, Weinheim, Germany, 1995.
161. P. Heitjan and S. Indris,. *J. Phys.. Condens. Matter*, **15** (2003) R1257.
162. A.S. Wadhwa and H.S. Dhaliwal, *A Textbook of Engineering Material and Metallurgy.*, University Science Press, 2008.
163. D. Lin, Y. Liu and Y. Cui, *Nat. Nanotechnol.*, **12** (2017) 194.
164. J.G. Kim, B. Son, S. Mukherjee, N. Schuppert, A. Bates, O. Kwon, M.J. Choi, H.Y. Chung and S. Park, *J. Power Sources*, **282** (2015) 299-322.
165. C. Sun, J. Liu, Y. Gong, D.P. Wilkinson and J. Zhang, *Nano Energy*, **33** (2017) 363-386.

166. R. Murugan, V. Thangadurai and W. Weppner, *Angew. Chem. Int. Ed.*, **46** (2007) 7778-7781.
167. Y. Inaguma, C. Liquan, M. Itoh, T. Nakamura, T. Uchida, H. Ikuta and M. Wakihara, *Solid State Commun.*, **86** (1993) 689-693.
168. H.Y.P. Hong, *Mater. Res. Bull.*, **13** (1978) 117-124.
169. H. Aono, E. Sugimoto, Y. Sadaoka, N. Imanaka and G.-Y. Adachi, *J. Electrochem. Soci.*, **137** (1990) 1023-1027.
170. B. Zhang, R. Tan, L. Yang, J. Zheng, K. Zhang, S. Mo, Z. Lin and F. Pan, *Energy Storage Mater.*, **10** (2018) 139-159.
171. P.E. Stallworth, J.J. Fontanella, M.C. Wintersgill, C.D. Scheidler, J.J. Immel, S.G. Greenbaum, *J. Power Sources*, **81-82** (1999) 739-747.
172. D. Liu, W. Zhu, Z. Feng, A. Guerfi, A. Vijh and K. Zaghib, *Mater. Sci. and Eng., B*, **213** (2016) 169-176.
173. H.-J. Deiseroth, S.-T. Kong, H. Eckert, J. Vannahme, C. Reiner, T. Zaiß and M. Schlosser, *Angew. Chem. Int. Ed.*, **47** (2008) 755-758.
174. S. Boulineau, M. Courty, J.-M. Tarascon and V. Viallet, *Solid State Ionics*, **221** (2012) 1-5.
175. M. Murayama, N. Sonoyama, A. Yamada and R. Kanno, *Solid State Ionics*, **170** (2004) 173-180.
176. R. Kanno and M. Murayama, *J. Electrochem. Soc.*, **148** (2001) A742-A746.
177. N. Kamaya, K. Homma, Y. Yamakawa, M. Hirayama, R. Kanno, M. Yonemura, T. Kamiyama, Y: Kato, S. Hama, K. Kawamoto and A. Mitsui, *Nat. Mater.*, **10** (2011) 682.
178. A. Kuhn, O. Gerbig, C. Zhu, F. Falkenberg, J. Maier and B.V. Lotsch, *Phys. Chem. Chem. Phys.*, **16** (2014) 14669-14674.
179. P. Bron, S. Johansson, K. Zick, J. Schmedt auf der Günne, S. Dehnen and B. Roling, *J. Am. Chem. Soc.*, **135** (2013) 15694-15697.
180. F. Mizuno, A. Hayashi, K. Tadanaga and M. Tatsumisago, *Electrochem. Solid-State Lett.*, **8** (2005) A603-A606.
181. F: Mizuno, A. Hayashi, K. Tadanaga and M. Tatsumisago, *Solid State Ionics*, **177** (2006) 2721-2725.
182. F. Mizuno, A. Hayashi, K. Tadanaga and M. Tatsumisago, *Adv. Mater.*, **17** (2005) 918-921.
183. D. Wohlmuth, V. Epp and M. Wilkening, *ChemPhysChem*, **16** (2015) 2582-2593.
184. Z. Liu, W. Fu, E.A. Payzant, X. Yu, Z. Wu, N.J. Dudney, J. Kiggans, K. Hong, A.J. Rondinone and C. Liang, *J. Am. Chem. Soc.*, **135** (2013) 975-978.
185. M. Tatsumisago, M. Nagao and A. Hayashi, *J. Asian Ceram. Soc.*, **1** (2013) 17-25.
186. Y. Seino, T. Ota, K. Takada, A. Hayashi and M. Tatsumisago, *Energy Environ. Sci.*, **7** (2014) 627-631.
187. K. Homma, M. Yonemura, T. Kobayashi, M. Nagao, M. Hirayama and R. Kanno, *Solid State Ionics*, **182** (2011) 53-58.
188. K.B. Hueso, M. Armand and T. Rojo, *Energy Environ. Sci.*, **6** (2013) 734-749.
189. H.Y.P. Hong, *Mater. Res. Bull.*, **11** (1976) 173-182.
190. M. Guin, F. Tietz and O. Guillon, *Solid State Ionics*, **293** (2016) 18-26.
191. A. Hayashi, K. Noi, A. Sakuda and M. Tatsumisago, *Nat. Commun.*, **3** (2012) 856.
192. A. Hayashi, K. Noi, N. Tanibata, M. Nagao and M. Tatsumisago, *J. Power Sources*, **258** (2014) 420-423.
193. W.D. Richards, T. Tsujimura, L.J. Miara, Y. Wang, J.C. Kim, S.P. Ong, I. Uechi, N. Suzuki and G. Ceder, *Nat. Commun.*, **7** (2016) 11009.
194. Y. Wang, W.D. Richards, S.P. Ong, L.J. Miara, J.C. Kim, Y. Mo and G. Ceder, *Nat. Mater.*, **14** (2015) 1026.
195. D.A.C. Brownson and C.E. Banks, *The Handbook of Graphene Electrochemistry.*, Springer, 2014.
196. G.A. Mabbott, *J. Chem. Educ.*, **60** (1983) 697.

197. P.T. Kissinger and W.R. Heineman, *J. Chem. Educ.*, **60** (1983) 702.
198. S.-I. Pyun, H.-C. Shin, J.-W. Lee and J.-Y. Jo, *Electrochemistry of Insertion Materials for Hydrogen and Lithium.*, Springer-Verlag, Berli, Heidelberg., 2012.
199. J.-K. Park, *Principles and Applications of Lithium Secondary Batteries.*, Wiley-VCH, 2012.
200. V.F. Lvovich, *Impedance spectroscopy: Applications to Electrochemical and Dielectric Phenomena.*, Wiley, 2012.
201. E. Barsoukov and J.R. Macdonald, *Impedance Spectroscopy: Theory, Experiment, and Applications.*, Wiley, 2005.
202. M.A. Alim, *Immittance Spectroscopy: Applications to Material Systems.*,Wiley, 2018.
203. J.T.S. Irvine, D.C. Sinclair and A.R. West, *Adv. Mater.*, **2** (1990) 132-138.
204. D.L. Sidebottom, *Rev. Mod. Phys.*, **81** (2009) 999-1014.
205. A.K. Jonscher, *Nature*, **267** (1977) 673.
206. J.C. Kimball and L.W. Adams, *Phys. Rev. B*, **18** (1978) 5851-5858.
207. M.H. Levitt, *Spin Dynamics: Basics of Nuclear Magnetic Resonance.*, Wiley, 2008.
208. H. Friebolin, *Basic One-and Two-Dimensional NMR Spectroscopy.*, Wiley-VCH, 2011.
209. J. Keeler, *Understanding NMR Spectroscopy.*, Wiley, 2010.
210. A. Kuhn, M. Kunze, P. Sreeraj, H.-D. Wiemhöfer, V. Thangadurai, M. Wilkening and P. Heitjans, *Solid State Nucl. Magn. Reson.*, **42** (2012) 2-8.
211. V. Epp, Ö. Gön, H.-J. Deiseroth and M. Wilkening, *Phys. Chem. Chem. Phys.*, **15** (2013) 7123-7132.
212. N. Bloembergen, E.M. Purcell and R.V. Pound, *Phys. Rev.*, **73** (1948) 679-712.
213. M. Wilkening, *Zur Ionendynamik in Festkörpern.*, University of Hannover, 2011.
214. P.M. Richards, *Solid State Commun.*, **25** (1978) 1019-1021.
215. S. Iijima, *Nature*, **354** (1991) 56.
216. M.H. Razali and M. Yusoff, *Mater. Lett.*, **221** (2018) 168-171.
217. S. Benkara, S. Zerkout and H. Ghamri, *Mater. Sci. Semicond. Process.*, **16** (2013) 1271-1279.
218. Z. Wei, H. Mao, T. Huang and A, Yu, *J. Power Sources*, **223** (2013) 50-55.
219. X. Jiao, T. Zeng, P. Ji, Q. Peng, B. Shang and X. Hu, *J. Alloys Compd.*, **739** (2018) 1-8.
220. N. Liu, K. Lee and P. Schmuki, *Angew. Chem. Int. Ed.*, **52** (2013) 12381-12384.
221. D.V. Bavykin and F.C. Walsh, *J. Inorg. Chem.*, **2009** (2009) 977-997.
222. X. Su, Q. Wu, X. Zhan, J. Wu, S. Wei and Z. Guo, *J. Mater. Sci.*, **47** (2012) 2519-2534.
223. T. Djenizian, I. Hanzu and P. Knauth, *J. Mater. Chem.*, **21** (2011) 9925-9937.
224. H.-R. Jung, S.-G. Lee, M.-H. Kim and J.-H. Yeo, *Microelectron. Eng.*, **146** (2015)109-112.
225. H. Moriwaki, S. Kitajima, K. Shirai, K. Kiguchi and O. Yamada, *J. Hazard. Mater.*,**185** (2011) 725-731.
226. Y. Feng, L. Ling, Y. Wang, Z. Xu, F. Cao, H. Li and Z. Bian, *Nano Energy*, **40** (2017) 481-486.
227. Y. Li, C.-A. Wang, H. Xie, J. Cheng and J.B. Goodenough, *Electrochem. Commun.*, **13** (2011) 1289-1292.
228. N. Zheng, N, X. Bu and P. Feng, *Nature*, **426** (2003) 428.
229. K. Takada, *J. Power Sources*, **394** (2018) 74-85.
230. R. Mercier, J.-P. Malugani, B. Fahys and G. Robert, *Solid State Ionics*, **5** (1981) 663-666.
231. Z. Lin, Z. Liu, N.J. Dudney and C. Liang, *ACS Nano*, **7** (2013) 2829-2833.
232. arXiv: 1708.02997
233. I.K. Lloyd, T.K. Gupta and B.O. Hall, *Solid State Ionics*, **11** (1983) 39-44.
234. U. von Alpen, M.F. Bell and W. Wichelhaus, *Mater. Res. Bull.*, **14** (1979) 1317-1322.
235. N. Anantharamulu, K.K. Rao, G. Rambabu, B.V. Kumar, V. Radha and M. Vithal, *J. Mater. Sci.*, **46** (2011) 2821-2837.
236. O. Bohnke, S. Ronchetti and D. Mazza, *Solid State Ionics*, **122** (1999) 127-136.

237. J.R. Dygas, G. Fafilek and M.W. Breiter, *Solid State Ionics,* **119** (1999) 115-125.
238. Y. Saito, K. Ado, T. Asai, H. Kageyama and O. Nakamura, *Solid State Ionics,* **58** (1992) 327-331.
239. Y.H. Yang, Q. Wu, Y.H. Cui, Y.C. Chen, S.Q. Shi, R.Z. Wang and H. Yan, *ACS Appl. Mater. Interfaces,* **8** (2016) 25229-25242.

C List of publications

C.1 Articles already published in peer-reviewed journals

Long-Cycle-Life Na Ion Anodes Based on Amorphous Titania Nanotubes – Interfaces and Diffusion
D. Prutsch, M. Wilkening and I. Hanzu
ACS Appl. Mater. Interfaces, **7** (2015), 25757.

Separating bulk from grain boundary Li ion conductivity in the sol-gel prepared solid electrolyte LATP
S. Breuer, Q. Ma, D. Prutsch, V. Epp, F. Preishuber-Pflügl, F. Tietz, and M. Wilkening
J. Mater. Chem. A, **3** (2015), 21343.

Electrochemical preparation of tin-titania nanocomposite arrays
D. Prutsch, M. Wilkening and I. Hanzu
RSC Adv., **6** (2016), 98243.

Nanostructured Ceramics: Ionic Transport and Electrochemical Activity
D. Prutsch et al. D. Prutsch, S. Breuer, M. Uitz, B. Stanje, J. Langer, P. Bottke, S. Lunghammer, P. Posch, V. Pregartner, M. Philipp, A. Dunst, D. Wohlmuth, H. Brandstätter, W. Schmidt, V. Epp, A. Chadwick, I. Hanzu and M. Wilkening
Z. Phys. Chem., **231** (2017), 1361.

Fast Na ion transport triggered by rapid ion exchange on local length scales
S. Lunghammer, D. Prutsch, S. Breuer, D. Rettenwander, I. Hanzu, Q. Ma, F. Tietz, M. Wilkening
Sci. Rep., 8 (2018) 11970.

Nuclear spin relaxation in nanocrystalline β-Li_3PS_4 reveals low-dimensional Li diffusion in an isotropic matrix
D. Prutsch, B. Gadermaier, H. Brandstätter, V. Pregartner, B. Stanje, D. Wohlmuth, V. Epp, D. Rettenwander, I. Hanzu, and H. M. R. Wilkening
Chem. Mater., (2018), in press.

C.2 Manuscripts

Embedding Base Metals in Anodic Titania Nanotubes – A Potential Electrochemical Approach
D. Tapler, M. Wilkening and I. Hanzu
under preparation

Electrochemical behavior of highly ordered Sn/TiO2 nanocomposites for lithium and sodium ion batteries – Sn confinement effects and capacity evolution
D. Tapler, M. Wilkening and I. Hanzu
under preparation

Technological Aspects and Pitfalls Related to the Anodization of Porous Titanium for Larger Scale Applications
D. Tapler, M. Wilkening and I. Hanzu
under preparation

^{7}Li NMR spin-lattice relaxation measurements of $LiTi_2(PS_4)_3$ (LTPS)
D. Tapler, D. Rettenwander, M. Wilkening
under preparation

C.3 Oral presentations

Self-Organized Amorphous TiO_2 Nanotubes as Na-Ion Battery Anodes
D. Prutsch, M. Wilkening, I. Hanzu
DocDays 2016, 05.-06.04, Graz, Austria.

Sulfide Solid Electrolytes – Long-Range and Local Li-Ion Dynamics in the Glass-Ceramic Li_3PS_4
D. Prutsch, H. Brandstätter, V. Pregartner, D. Wohlmuth, V. Epp, M. Wilkening
2017 MRS Spring Meeting & Exhibit,17-21.04.2017, Phoenix, AZ, USA.

C.4 Poster presentations

Synthesis and Electrochemical Characterization of TiO_2 Nanotubes as Na-Ion Battery Anodes
D. Prutsch, M. Wilkening, I. Hanzu
nanoFIS 2014, 03.-05.12.2014, Graz, Austria.

Nanoarchitectured Titania as Anode Material for Na-Ion Batteries
D. Prutsch, M. Wilkening, I. Hanzu
LiBD 2015, 21.-26.06.2015, Arcachon, France.

Self-Organized Amorphous TiO_2 Nanotubes as Na-Ion Battery Anodes
D. Prutsch, M. Wilkening, I. Hanzu
ECSSC 15 – ^{15}th European Conference on Solid State Chemistry, 23.-26-08-2015, Vienna, Austria.

Sulfide Electrolytes: Study of Local Li-Ion Dynamics in Li_3PS_4 using ^{7}Li NMR Relaxometry
D. Prutsch, H. Brandstätter, V. Pregartner, D. Wohlmuth, V. Epp, M. Wilkening
IMLB 2016, 19.-24.06.2016, Chicago, USA

Sulfide Solid Electrolytes – Long-Range and Local Li-Ion Dynamics in the Glass-Ceramic Li_3PS_4
D. Prutsch, H. Brandstätter, V. Pregartner, D. Wohlmuth, V. Epp, M. Wilkening
2nd Graz Battery Days, 27.-28.09.2016, Graz, Austria.

Sn-filled titania nanotubes for small electrochemical devices
D. Prutsch, M. Wilkening, I. Hanzu
nanoFIS 2017, 22.-24.12.2017, Graz, Austria.

Sn-Filled Titania Nanotubes as Anode Material for Rechargeable Li and Na Batteries
D. Prutsch, B. Gadermaier, M. Wilkening, I. Hanzu
IMLB 2018, 17.-22.06.2018, Kyoto, Japan.

D Acknowledgements

The biggest thank goes to Prof. Dr. Martin Wilkening and Dr. Ilie Hanzu for giving me the opportunity to write my doctoral thesis under their supervision at the Institute of Chemistry and Technology of Materials in Graz. They were great teachers regarding scientific questions, but also supported me in all kind of things aside from scientific topics. I highly appreciated that it was possible to present my results at many international conferences from the USA to Japan.
During my time at the Institute I not only met new colleagues, but also made new friends. I would like to thank all formers and current group member for the great working atmosphere and the nice time we had together. Special thanks goes to my former and current colleagues Walter Schmidt, Veronika Pregartner, Marlena Uitz, Bernhard Gadermaier and Isabel Hanghofer with whom I shared a small office on the second floor and of course Stefan Breuer. Thank you for your support and the many fruitful discussions also aside from scientific topics. It was always a pleasure for me to spend my time with you all.
I also with to thank Liane Hochgatterer and Christina Albering for their administrative and organizational support as well as their good advices.
Sanja Simic and Dr. Brigitte Bitschnau are kindly acknowledged for their SEM micrographs and XRD measurements.
I also want to thank all my friends for the moral support during writing this doctoral thesis and the funny and relaxing time aside from university.
Finally, I would like to express my sincere thanks to my family and my husband, who have always supported and encouraged me and made this doctoral thesis possible in the first place. Thank you very much!